Modelling of a Symmetric Molten Carbonate Fuel Cell Stack

Dissertation
zur Erlangung des akademischen Grades

Doktoringenieur
(Dr.-Ing.)

von: Dipl.-Ing. Matthias André Pfafferodt
geb. am: 14. Oktober 1978
in: Magdeburg

genehmigt durch die Fakultät für Verfahrens- und Systemtechnik
der Otto-von-Guericke-Universität Magdeburg.

Begegnet uns jemand,
der uns **Dank** schuldig ist,
gleich fällt es uns ein.

Wie oft können wir jemand begegnen,
dem wir **Dank** schuldig sind,
ohne daran zu denken.

Johann Wolfgang von Goethe

Danksagung

Die vorliegende Dissertationsschrift ist das Ergebnis meiner Tätigkeit am Lehrstuhl für Systemverfahrenstechnik der Otto-von-Guericke-Universität Magdeburg und am Max-Planck-Institut für Dynamik komplexer technischer Systeme Magdeburg. Die Entstehung dieser Arbeit wurde von vielen Menschen begleitet und unterstützt. Bei ihnen möchte ich mich an dieser Stelle herzlich bedanken.

An erster Stelle möchte ich meinen Doktorvater *Professor Dr.-Ing. Kai Sundmacher* erwähnen. Er hat mir diese Arbeit möglich gemacht und mich in der Promotionszeit fortwährend gefordert und umfassend gefördert.

Ich danke *Professor Dr. rer. nat. Olaf Deutschmann* vom Karlsruher Institut für Technologie und *Professor Dr.-Ing. Dominique Thévenin* von der Otto-von-Guericke Universität Magdeburg für das Interesse an dieser Arbeit und die Erstellung der Zweitgutachten.

Weiterhin möchte ich *Dr.-Ing. Peter Heidebrecht* für die unzähligen fachlichen Diskussionen und persönlichen Gespräche von ganzem Herzen danken. Er hat die gesamte Arbeit inhaltlich begleitet, mich ohne Vorbehalt unterstützt und immer wieder angespornt. Ohne das von ihm erstellte Modell einer einzelnen Schmelzkarbonatbrennstoffzelle wäre diese Arbeit so nicht möglich gewesen.

Auch möchte ich mich bei *allen Kollegen und Doktoranden* bedanken, mit denen ich in dieser Zeit zusammenarbeiten durfte. Sie haben mir bei zahlreichen fachlichen und administrativen Fragestellungen geholfen und mich beim Lösen dieser Aufgaben unterstützt.

Mein weiterer Dank gilt *meinen Eltern und meinen Geschwistern.* Sie haben geduldig zugehört, wenn ich von meiner Arbeit erzählt habe und mich immer wieder ermuntert, mir neue Ziele zu setzen. Ohne sie wäre diese Arbeit nicht, was sie heute ist.

Schließlich danke ich noch allen Personen, die zum Gelingen dieses Projekts beigetragen haben und in dieser Danksagung versehentlich nicht erwähnt worden sind.

Table of Contents

List of Symbols

Symbols that are only of local interest in this work will be declared at the place of use and are not listed here.

Roman Letters (Dimensioned Quantities)

A	area	$[\,\mathrm{m^2}\,]$
b	width	$[\,\mathrm{m}\,]$
c_i	concentration	$[\,\mathrm{mol\,m^{-3}}\,]$
$c_{\mathrm{p}i}$	molar heat capacity of component i	$[\,\mathrm{J\,mol^{-1}\,K^{-1}}\,]$
$\overline{c_{\mathrm{p}}}$	molar heat capacity of the gas mixture	$[\,\mathrm{J\,mol^{-1}\,K^{-1}}\,]$
D_i	diffusivity	$[\,\mathrm{m^2\,s^{-1}}\,]$
$\widetilde{D}_i$	mass transport coefficient of component i	$[\,\mathrm{mol\,m^{-2}\,s^{-1}}\,]$
d	height	$[\,\mathrm{m}\,]$
g	mass flux density	$[\,\mathrm{kg\,m^{-2}\,s^{-1}}\,]$
h	enthalpy	$[\,\mathrm{J\,kg^{-1}}\,]$
i	current density	$[\,\mathrm{A\,m^{-2}}\,]$
K_j	equilibrium constant of reaction j	$[\,-\,]$
$\mathbf{K}_{\mathrm{perm}}$	permeability tensor	$[\,\mathrm{m^2}\,]$
k	heat transfer coefficient	$[\,\mathrm{W\,m^{-2}\,K^{-1}}\,]$
k_0	reaction rate coefficient	$[\,\mathrm{kg\,m^{-2}\,s^{-1}}\,]$
L	length	$[\,\mathrm{m}\,]$
M	molar mass	$[\,\mathrm{mol\,kg^{-1}}\,]$
$\widetilde{N}_i$	molar mass flux of component i	$[\,\mathrm{mol\,s^{-1}}\,]$
$\widetilde{n}_i$	molar mass flux density of component i	$[\,\mathrm{mol\,m^{-2}\,s^{-1}}\,]$
$\mathbf{n}$	boundary normal vector	$[\,\mathrm{m}\,]$
p	pressure	$[\,\mathrm{Pa}\,]$
p_0	standard pressure	$[\,\mathrm{Pa}\,]$
$\widetilde{Q}$	heat flux	$[\,\mathrm{J\,s^{-1}}\,]$
$\widetilde{r}_j^A$	surface reaction rate of reaction j	$[\,\mathrm{kg\,m^{-2}\,s^{-1}}\,]$
$\widetilde{r}_j^V$	volume reaction rate of reaction j	$[\,\mathrm{kg\,m^{-3}\,s^{-1}}\,]$
T	temperature	$[\,\mathrm{K}\,]$
$\mathbf{u}$	velocity vector $(z_1,\,z_2,\,z_3)$	$[\,\mathrm{m\,s^{-1}}\,]$
u	velocity	$[\,\mathrm{m\,s^{-1}}\,]$
V	volume	$[\,\mathrm{m^3}\,]$
w	mass fraction	$[\,-\,]$

x_i	mole fraction of component i	$[\,-\,]$
z	coordinate	$[\,\mathrm{m}\,]$

Roman Letters (Dimensionless Quantities)

Arr_j	Arrhenius number of reaction j
c	charge capacity of double layers
c_i	concentration of component i
$\overline{c_p}_l$	molar heat capacity of gas mixture in compartment l
c_{p_i}	molar heat capacity of component i
c_{p_S}	molar heat capacity of solid phase
$D_{i,l}$	mass transport coefficient of component i in gas compartment l
$Da_{j,l}$	Damköhler number of reaction j in gas compartment l
d	height
F	stoichiometric factor
f_{REC}	cathode gas recycle ratio
I_{cell}	total cell current
i	current density
l_2, l_{BP}	geometric length ratio
n_{cells}	number of fuel cells
n_i	molar mass flux density of component i
n_j	number of transported electrons of reaction j
n_t	total mass flux density
P_{blower}	electrical power of the blower
Pe_S	Peclet number of solid phase
Q	heat flux
q	heat source density
$q_{S,cell}$	heat source density in solid phase
$q_{S,conn}$	heat flux density between two solid phases
$q_{S,stack}$	heat flux density in stack direction
$r_{j,l}$	reaction rate of reaction j in gas compartment l
Sc_t	turbulent Schmidt number
St	Stanton number
U	voltage
V	volume

Greek Letters (Dimensioned Quantities)

$\Delta_R h_j$	enthalpy of reaction j	$[\,\mathrm{J\,mol^{-1}}\,]$
λ	thermal conductivity	$[\,\mathrm{W\,m^{-1}\,K^{-1}}\,]$
μ	dynamic viscosity	$[\,\mathrm{kg\,m^{-1}\,s^{-1}}\,]$
μ_t	turbulent dynamic viscosity	$[\,\mathrm{kg\,m^{-1}\,s^{-1}}\,]$
ρ	density	$[\,\mathrm{kg\,m^{-3}}\,]$

Greek Letters (Dimensionless Quantities)

γ	molar mass flux density (per cross-sectional area) in channels
Γ	molar mass flux
$\Delta_C h_i^\theta$	standard enthalpy of combustion of component i
$\Delta_R h_j^\theta$	standard enthalpy of reaction j
ε	volume fraction
ζ	spatial coordinate
ϑ	temperature
ϑ^r	reference temperature
κ_E	ion conductivity in electrolyte
$\nu_{i,j}$	stoichiometric coefficient of component i in reaction j
$\bar{\nu}_j$	sum of stoichiometric coefficients of reaction j
τ	time
ϕ_i	partial pressure of component i in electrode pores
φ	electrical potential
χ_i	mole fraction of component i

Indices

Components of the Symmetric Stack Model

A, *AC*, *AS*	anode: gas phase, catalyst, exchange with the solid phase
AIR	burned air
C, *CC*, *CS*	cathode: gas phase, catalyst, exchange with the solid phase
B	catalytic combustion chamber
BP	bipolar plate
HE, *HEA*, *HEB*	head exchanger, cold side, hot side
IIR, *IIRS*	IIR unit: gas compartment, exchange with the solid phase
IN	feed gas at the inlet
M	gas manifold
OUT	exhaust gas of the stack
RC	reversal chamber
REC	cathode gas recycle
S	solid phase

Lower Indices

conv	convective flow
diff	diffusive flux
i	chemical species, component
in	inlet
j	chemical reaction
l	compartment index
out	outlet
t	total

Upper Indices

$+|-$	forward and backward direction of mass flow
$(1\,cell)$	reference to one fuel cell
θ	standard conditions
I	fluxes *via* the phase interface in IIR unit
(k)	number of the fuel cell in the symmetric stack model
N	non-reactive phase of the IIR unit
P	catalyst pellets
R	reactive phase of the IIR unit

Reactions

ox1	electrochemical oxidation of hydrogen
ox2	electrochemical oxidation of carbon dioxide
red	electrochemical reduction of oxygen
ref1	methane steam reforming reaction
ref2	water gas shift reaction

Species

CH4	$(i = 1)$	Methane
H2O	$(i = 2)$	Water
H2	$(i = 3)$	Hydrogen
CO	$(i = 4)$	Carbon Monoxide
CO2	$(i = 5)$	Carbon Dioxide
O2	$(i = 6)$	Oxygen
N2	$(i = 7)$	Nitrogen

Abbreviations and Acronyms

CFD	Computational Fluid Dynamics
DIR	Direct Internal Reforming
ER	External Reformer
FEM	Finite Element Method
IIR	Indirect Internal Reforming
MCFC	Molten Carbonate Fuel Cell

Kurzfassung

Ziel der vorliegenden Arbeit ist die Modellierung eines Brennstoffzellensystems auf Basis der Schmelzkarbonatbrennstoffzelle (MCFC). Dieser Brennstoffzellentyp ist besonders geeignet für die stationäre Erzeugung von Wärme und Strom. Für eine weitere Optimierung von Design- und Betriebsparametern werden mathematische Modelle benötigt. Ein solches Modell des Brennstoffzellenstapels wird in dieser Arbeit vorgestellt.

Im ersten Teil der Arbeit werden wichtige Bestandteile des Brennstoffzellenstapels untersucht. Hierbei wird ein hierarchischer Modellierungsansatz verwendet, um insbesondere den Reaktor für die indirekte interne Reformierung (IIR) zu beschreiben. In diesem strukturiertem Reaktor wird das Brenngas - ein Gasgemisch welches zu einem Großteil aus Methan und Wasserdampf besteht - durch den endotherme Reformierungsprozess zu Wasserstoff und Kohlendioxid umgewandelt.

Die erste Hierarchieebene entspricht einem kleinen Ausschnitt der IIR-Einheit. In diesem Detailmodell wird die exakte 3D-Geometrie des Reaktors abgebildet. Die gewonnenen Simulationsergebnisse zeigen, dass die in dem Reaktor ablaufenden Reaktionen durch den Massentransport zwischen der reaktive Zone mit den Katalysatorpellets und der nicht-reaktive Zone limitiert werden. Ein Überschuss an Katalysatormaterial führt dazu, dass die Gesamtreaktionsrate nicht durch eine Degradation des Katalysators beeinflusst wird. Somit ermöglicht dieses Reaktorkonzept ein konstantes Temperaturprofil in der IIR-Einheit über einen langen Betriebszeitraum. Da weiterhin die für den endotherme Reformierungsprozess benötigte Wärme durch die elektrochemische Reaktionen in den benachbarten Brennstoffzellen bereitgestellt wird, kann die Temperaturverteilung in den Brennstoffzellen durch die Verteilung des Katalysatormaterials in der Reformierungseinheit beeinflusst werde.

Das Zonenmodell stellt die zweite Hierarchiestufe dar. In diesem Modell wird die komplexe Geometrie des Detailmodells durch rechtwinklige Blöcke, welche die beiden Zonen darstellen, abgebildet. Beispielhaft werden Simulationen für die bei einem existierenden MCFC-System verwendeten IIR-Einheiten durchgeführt. Die Ergebnisse zeigen, dass der Reformierungsprozess gleichmäßig über den gesamten Reaktor verteilt wird. Somit wird auch die Kühlwirkung der endothermen Reaktion auf die benachbarten Brennstoffzellen gleichmäßig verteilt.

Während die reaktive und nicht-reaktive Zone in dem Zonenmodell diskreten Gebieten zugeordnet werden können, geht diese Information bei der Reduktion zu dem Phasenmodell verloren. Die Zustände, welche die reaktive und die nicht-reaktive

Zone darstellen, werden in diesem Modell über die gesamte zweidimensionale Fläche der IIR-Einheit homogenisiert. Somit können sie als zwei Phasen interpretiert werden, welche jeweils einen Teil des Volumens beanspruchen.

Im zweiten Teil der Arbeit wird das Phasenmodell der IIR-Einheit und das Modell einer MCFC zu dem symmetrischen Stapelmodell zusammengefügt. Dieses erlaubt die Simulation eines Ausschnitts aus dem Brennstoffzellenstapels, wobei die Anzahl an MCFC's je IIR-Einheit variiert werden kann. In dem Modell sind die einzelnen Bestandteile des Stapels durch den Wärmeaustausch in Stapelrichtung, den Massentransport sowie die elektrochemischen Reaktionen miteinander verbunden. Weiterhin ermöglicht das Modell die Simulation der Zustände innerhalb des Stapels. Dabei können unter anderem die Temperaturverteilungen sowie die Stromdichteverteilung in den einzelnen Zellen betrachtet werden. Die Simulationsergebnisse zeigen einen parabolischer Temperaturverlauf in Stapelrichtung zwischen den als Wärmesenken fungierenden IIR-Einheiten. Dies führt zu unterschiedlichen Arbeitsbedingungen der einzelnen Zellen in Abhängigkeit von ihrer Entfernung zu den Reformierungsreaktoren. Eine Reduktion der Anzahl von Zellen je IIR-Einheit führt daher zu geringeren Temperaturdifferenzen innerhalb des Brennstoffzellenstapels und somit zu einer erhöhten Lebensdauer der Zellen. Dieses Ergebnis wird durch die Analyse der Energieflüsse in dem betrachteten Ausschnitt des Zellstapels gestützt. Sie zeigt, das der Wärmestrom von den Zellen in die IIR-Einheit um so höher ist, je weniger Zellen je IIR-Einheit verwendet werden.

Die aufgezeigten Beispiele belegen, dass das symmetrische Stapelmodell ein Werkzeug darstellt, mit dessen Hilfe unterschiedliche Design- und Betriebsparameter des Brennstoffzellensystems optimiert werden können. Durch die allgemeine Formulierung können neben einer Änderung der Anzahl der Zellen je IIR-Einheit inhomogene Verteilungen der Gase auf die einzelnen Zellen oder eine Verteilung des Gasstroms entlang der Eintrittsöffnung der Anoden- oder Kathodengaskanäle einfach implementiert werden.

Abstract

The focus of this work is on the modelling of a Molten Carbonate Fuel Cell stack. In Part I, the main gas compartments of the fuel cell stack, especially the Indirect Internal Reforming units (IIR), are analysed in detail.

A hierarchical modelling approach is used to describe the IIR unit. Three different levels are studied. In the detailed model, small cutout sections of the IIR unit are simulated. The exact geometry with the corrugated sheets and the individual catalyst pellets is considered. The analysis shows two main features of this reactor. First, due to the geometrical structure of the reactor, the reforming process is limited by mass transport between a reactive and a non-reactive zone. A stable repeating pattern can be observed for the temperature and velocity profiles while the concentrations show funnel-shaped profiles. Due to the excess of catalyst material, the degradation of the catalyst does not influence the overall reaction rate in the reforming reactor as long as its activity is high enough. Therefore, a constant temperature profile can be expected in the IIR unit even after long operation time. The second point is that the main heat transport route towards the cold reaction zone is from the neighbouring fuel cells through the top and bottom sheets directly into the reactive zone. Thus, the local temperature in the fuel cells can be influenced by the amount and the distribution of the reforming catalyst pellets in the IIR units.

The second level of the modelling hierarchy is represented by the zone model. It substitutes the complex geometry of the detailed model of IIR unit by rectangular zones: the reactive and the non-reactive zone. As an example, the geometry of the IIR unit as applied in the MCFC system HOTMODULE is used for the simulations. The reactive zone and the non-reactive zone are clearly visible in the temperature and concentration profiles. The results indicate that the rate of the reforming process is nearly homogeneously distributed over the IIR unit. Thus, the heat sink due to the endothermic reforming process is almost constant in these parts.

While the reactive and non-reactive zones are discrete in the zone model, this discrete geometrical information is lost in the final model reduction step to the phase model. The states representing the non-reactive and the reactive zone are homogenised over the whole (two-dimensional) area of the IIR unit. Thus, they can be interpreted as two phases, each occupying a certain fraction of the volume. The states in the phases now represent characteristic values that a corresponding zone in the specific vicinity would have. The complexity and the structure of this model correspond to the complexity and the structure of the model of a single MCFC proposed by Heidebrecht *et al.* [22].

Similar detailed models for the anode and cathode gas compartments are studied. Results show that the Direct Internal Reforming reactions in the anode gas channels are only limited by the corresponding chemical equilibrium. Furthermore, the concentration gradients perpendicular to the main gas flow direction as well as the gradients over the height of the channels are small compared to the concentration gradients in flow direction. Thus, these models confirm the assumptions used for the derivation of the model of one fuel cell.

In Part II of this work, the phase model of the IIR unit and the model of an MCFC are combined to the symmetric stack model. It allows the simulation of a representative section of a molten carbonate fuel cell stack. The coupling of all parts of the stack, mainly due to the thermal interactions, the mass flow and the corresponding electrochemical reactions at the anode and the cathode of each fuel cell are taken into account. Thus, the symmetric stack model considers the differences of the state variables in the different compartments along the stack direction. The gas phase compositions, the temperature profiles and the current density distribution in the IIR unit and each of the four fuel cells can be predicted by means of the here proposed MCFC stack model.

The functionality of the model are demonstrated by a steady state simulation. Overall, the results of the symmetric stack model correspond to those from the previously validated model by Gundermann _et al._ [18]. The differences are caused by auxiliary units of the fuel cell system that are implemented in the symmetric stack model as well as the consideration of several fuel cells. These changes allow the simulation of the temperature distribution in stack direction. The results show a parabolic temperature profile between two Indirect Internal Reforming units. Thus, the fuel cells next to the IIR unit and the fuel cells in the middle between two IIR units operate at different temperatures.

The current density distributions for all cells in the stack show similar profiles. But due to the cooling effect of the IIR unit, the cell temperatures deviate by several $10 \, \text{K}$. As overheating is one of the reasons for degradation in an MCFC system, one may expect that cells 3 and 4 are degrading fastest in this stack. This suggests that reducing the number of fuel cells per IIR unit should lead to lower temperature differences in the stack. This idea is also supported by the results of the energy flux analysis which have revealed that the advantageous heat flow from the cells into the IIR unit is higher if less fuel cells per IIR unit are used.

Due to its generalised formulation, the model can easily be extended to different numbers of fuel cells in the stack symmetry unit. Furthermore, inhomogeneous gas feed distributions to the anode or cathode gas compartments of the different fuel cells as well as different gas flows for each fuel cell can be implemented. Considering the points listed above, the presented model provides the foundation for an optimisation of design and operating parameters of MCFC systems with regard to homogenised temperature distributions and increased efficiency. Because of the number of solutions needed for such an optimisation, an additional reduction of the model complexity would be required which goes beyond the scope of this work.

At the bottom of each page of this work, simulation results for the transient behaviour of the symmetric stack model are presented. The load change from an average current density of $i_{\mathrm{avg}} = 80\,{}^{mA}/\mathrm{cm^2}$ to a current density of $i_{\mathrm{avg}} = 100\,{}^{mA}/\mathrm{cm^2}$ is shown. A detailed definition of the load change can be found in Section 6.1.5.

On odd pages, two-dimensional plots of the solid temperatures for the four fuel cells of the symmetric stack model and the temperature of the exhaust gas are displayed:
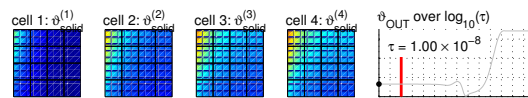
On even pages, the electrical power output provided by the fuel cell stack as well as two-dimensional plots of current density in each cell are shown.
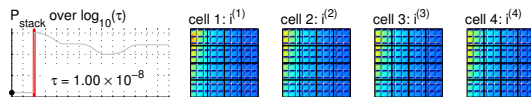
For all of these figures, a logarithmic time scale is used to account for the large differences in the time constants of the processes in the fuel cell stack.
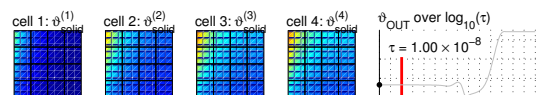
Chapter 1

Introduction

Fuel cells are efficient devices for the generation of electrical power. In contrast to the traditional power generation based on a thermodynamic cycle like the Carnot process, where the chemically stored energy is converted into thermal energy which in turn is transformed *via* kinetic energy into electricity, a direct conversion of the chemically bound energy into electrical power is accomplished by fuel cells. Thus, the fuel cell technology allows for higher efficiency, and pollution as well as noise emissions are reduced.

Considering the different types of fuel cells, high temperature fuel cells, especially the Molten Carbonate Fuel Cell (MCFC), are suitable for stationary co-generation of electricity and high-graded heat which, for example, can be used to generate steam [7, 47]. First power plants based on this technology are operated as demonstration units all over the world. Some of the challenges left to solve are the reduction of the production cost and the optimisation of the operating conditions and design parameters to increase the system efficiency.

With respect to the last mentioned point, numerical simulations of fuel cells are necessary to fully understand the physical and (electro-)chemical processes within the system and the interactions between the different processes. One state variable of a Molten Carbonate Fuel Cell, which might be the most important one, is the stack temperature. Many significant processes such as the (electro-)chemical reactions and material degradation depend on the temperature distribution in the fuel cell stack. To calculate the temperature profiles, not only the structure of the fuel cell system but also the couplings between the different parts of the stack have to be considered.

The main part of the fuel cell system consists of the fuel cell stack, which is composed of approximately two-dimensional components (the electrode, the electrolyte, and the gas compartments). Additional units, *i.e.* the gas manifold and the reversal chamber, are needed to control the gas flow. The processes inside the fuel cell system are described by coupled balances of mass, energy and charge. The non-linear characteristics of the resulting equation system is mainly due to the electrochemical reaction rate expressions at the electrodes which depend not only on the spatially distributed temperature and concentrations but also on the electrical potentials. Furthermore, the thermal coupling of all compartments in stack direction, and the external connec-

tion due to the heat exchanger, the catalytic combustion chamber and the cathode gas recycle have to be taken into account. Therefore, the basis for an optimisation of the fuel cell system is a model of the fuel cell stack, which is the focus of this work.

1.1 Working Principle of an MCFC

The working principle of Molten Carbonate Fuel Cells was first presented in the year 1960 by G. H. J. Broers and J. A. A. Ketelaar [10]. Since that time, the materials used as well as the system design have been greatly improved, but the basic principle as shown in Fig 1.1 remained the same.
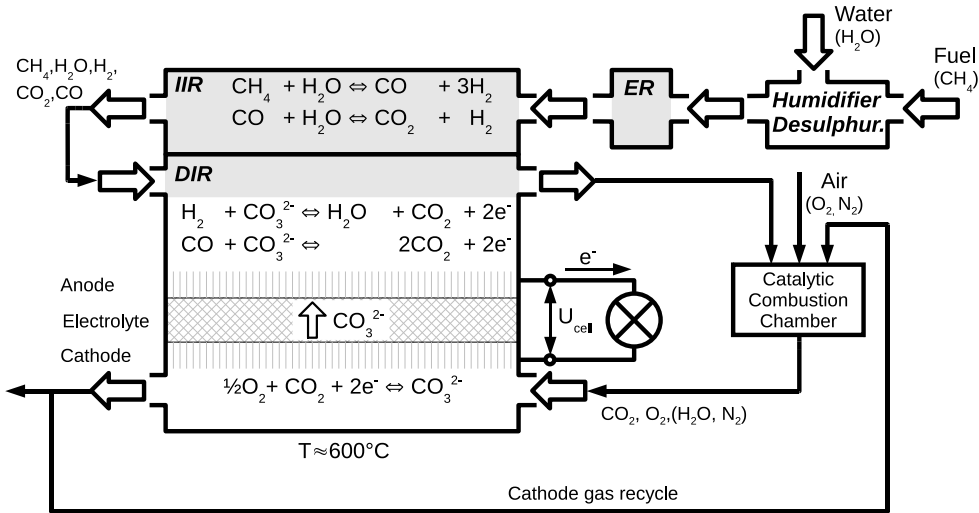

Figure 1.1.: Working principle of a Molten Carbonate Fuel Cell. The mass fluxes in the fuel cell system are indicated.

The figure shows the concept of the entire fuel cell system. It includes the humidifier and the desulphurisation as preprocessing steps for the fuel gas. The reforming of the methane rich fuel gas can take place in the External Reformer (ER), the Indirect Internal Reforming unit (IIR) or the Direct Internal Reforming (DIR) on the anode side of the fuel cell. Furthermore, the gas flow through the catalytic combustion chamber and the cathode gas recycle are displayed. The fuel cell stack itself is assembled in a planar structure consisting of IIR units (IIR in Fig. 1.1) and MCFCs. The single fuel cells, in turn, comprise three different layers: the anode gas compartment, the electrolyte with both electrodes and the cathode gas compartment. All of these components have a thickness in the order of 10^{-3} m.

The anode and cathode gas compartments are located above and below the electrodes, respectively. They serve as transport channels for the gaseous reaction educts and products. A reforming catalyst is added into the anode gas channels for the Direct
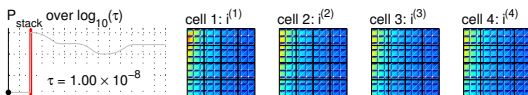
Internal Reforming (DIR) of the fuel gas. Between the single cells of the stack, the IIR units are located. These flat reactors also contain a reforming catalyst.

The typical fuel gas of an MCFC system mainly consists of natural gas, with methane as its main component. Before entering the fuel cell system, the gas is cleaned. Especially sulphur as a catalyst poison has to be removed, which is done in a separate desulfurisation unit. Furthermore, steam is added to the feed gas in a humidifier. These two units belong to the gas preprocessing which is not part of this work.

The resulting gas mixture is reformed prior to the electrochemical conversion. The methane steam reforming reaction (ref1) and the water gas shift reaction (ref2) are the dominant reactions in this process:

$$CH_4 + H_2O \rightleftharpoons CO + 3\,H_2 \tag{ref1}$$
$$CO + H_2O \rightleftharpoons CO_2 + H_2 \tag{ref2}$$

A part of the reforming is done outside the fuel cell stack in an external reformer (ER), which is not included in this work. From there, the gas mixture containing methane, water, hydrogen, carbon monoxide and carbon dioxide, is transported into the IIR unit. This gas compartment is thermally coupled to the actual fuel cell. Therefore, the heat needed for the endothermic reforming process is directly provided by the electrochemical reactions occurring in the neighbouring fuel cell [35]. At typical MCFC temperatures of about $600\,°C$, the reforming conversion is limited by the corresponding chemical equilibrium of the considered reactions.

After the IIR unit, the gas is redirected into the anode gas compartment. Within the anode gas compartment, not only the reforming reactions have to be taken into account, but also the electrochemical oxidation of hydrogen (ox1) and carbon monoxide (ox2) at the electrode. They react with carbonate ions from the electrolyte to water, carbon dioxide and electrons:

$$H_2 + CO_3^{2-} \rightleftharpoons CO_2 + H_2O + 2\,e^- \tag{ox1}$$
$$CO + CO_3^{2-} \rightleftharpoons 2\,CO_2 + 2\,e^- \tag{ox2}$$
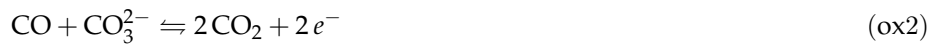
The reforming reactions ((ref1) and (ref2)) in the anode gas compartment are not only thermally coupled to the electrochemical reactions, but also connected *via* mass transport. Hydrogen and carbon monoxide are continuously removed due to these reactions. Thus, the equilibrium limited reforming reactions may reach nearly complete conversion of methane.

The anode exhaust gas, which still contains non-oxidised components such as methane, hydrogen and carbon monoxide, is mixed with air and completely burned in the catalytic combustion chamber. Beside the electrochemical oxidation the combustion taking place in the catalytic combustion chamber is an essential heat source in the system. The energy released by the combustion is directly used within this gas compartment to heat up the cold air added to the process.
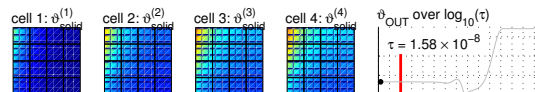
Because air is fed in excess, the exhaust gas of the combustion chamber contains a significant amount of oxygen and carbon dioxide. These gas components are needed for the electrochemical reduction at the cathode (red). Thus, the exhaust gas is redirected into the cathode gas compartment. At the cathode, new carbonate ions are produced from carbon dioxide, oxygen and electrons according to the following reaction:

$$CO_2 + \text{\textonehalf}\, O_2 + 2\, e^- \rightleftharpoons CO_3^{2-} \tag{red}$$

The formed carbonate ions are transported to the anode through the electrolyte, thereby closing the circle of charge transport. Overall, the electrochemical oxidation reactions at the anode act as an electron source while the electrochemical reduction reaction at the cathode represent an electron sink. This results in different electrical potentials at both electrodes, *i. e.* an electrical voltage. If anode and cathode are connected by an electrical consumer such as an electromotor or a light bulb, this results in an electrical current between both electrodes of the MCFC. Thus, the shortage of electrons at the cathode is compensated by the excess electrons from the anode, and the MCFC acts as a source of electrical power.

The cathode exhaust gas is split into two parts (see Fig. 1.1). While one part of the gas leaves the fuel cell system, the other fraction is used as cathode gas recycle. It is redirected into the catalytic combustion chamber in order to homogenise the temperature in the fuel cell stack.

As electrolyte, an eutectic mixture of molten Lithium and Potassium carbonate salts is used. It is placed into a porous structure, which is formed by an aluminium oxide $(\gamma - \text{LiAlO}_3)$. The electrolyte separates the anode and the cathode gas compartments and only carbonate ions (CO_3^{2-}) can cross this layer. The electrodes on both sides of the electrolyte are porous metallic structures which work as electron conductors and as catalysts for the electrochemical reactions. Due to capillary forces, the pores of the electrodes are partially filled with the electrolyte, forming the three phase boundary between the gas, the electrolyte and the electrode required for the electrochemical reactions.

Based on previous work done by the fuel cell manufacturer FuelCell Energy Inc., the MTU Onsite Energy GmbH is working on the realisation of the MCFC principle since 1990. They developed a compact MCFC system with an electrical output of 250 kW, the so-called HOTMODULE [34]. The simulation results presented in this work are obtained in the framework of a collaboration with this company. To protect the intellectual property, no exact quantitative data is given. However, qualitative data are presented for the simulated variables and their relevance for the operation of the fuel cell stack is discussed.
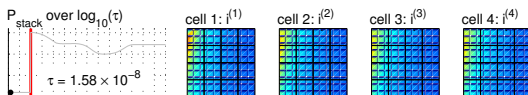
## 1.2 MCFC Models in the Scientific Literature

Although the technology of Molten Carbonate Fuel Cells is known for several decades, the knowledge about the internal states of the fuel cell stack is still limited. A direct measurement of the state variables such as the current density, the temperature or the concentration is often not possible. Therefore, MCFC systems are mostly controlled using empirical know-how aiming at a safe operation. Consequently, Mathematical models have been developed to identify and estimate non-measurable internal states of the fuel cell system [46]. The different models are classified with regard to their complexity, which especially is represented by the number of spatial dimensions considered and the description chosen for the reforming reactions as well as the electrochemical reactions. Furthermore, the aim of the modelling efforts is important.

The three-dimensional model developed by Yoshiba *et al.* [52] is based on the balances of mass and enthalpy for the gas phases as well as the energy balance in the solid parts of the fuel cell. Due to the assumption that no methane is considered in the gas phase of the anode gas compartment, the model only accounts for the water gas shift reaction. Furthermore, the equations for the cell voltage and the current density distribution are derived using an electrical resistance formulation. The model is used to compare different flow configurations of the anode and cathode gas compartments. Due to the fact that the model does not implement a catalytic combustion chamber, the properties of the cathode gas are not coupled to the anode exhaust gas.

The influence of an Indirect Internal Reforming (IIR) gas compartment on the MCFC cell was investigated by Park *et al.* [37]. They consider a counter-current flow configuration between the IIR unit and the anode gas compartment and a cross-flow design with regard to the anode and cathode gas compartment in their two-dimensional model. The methane steam reforming reaction in the IIR unit and the anode gas compartment are treated as being kinetically limited while the water gas shift reaction is assumed to be in equilibrium. The cell voltage is calculated from the Nernst equation using the electrochemical activation potential and assuming a uniform current density.

Another MCFC model with Indirect Internal Reforming was presented by Lukas *et al.* [31]. Their model is used for controlling power cycles of an MCFC plant. Therefore, a transient, spatially concentrated description is applied resulting in a small set of equations compared to the models mentioned before.

Based on mass and enthalpy balances, Bosio *et al.* developed a two-dimensional model [8]. They do consider syngas as fuel and, therefore, only the water gas shift reaction takes place in the anode gas compartment besides the electrochemical oxidation. A semi-empirical relationship is used for the description of the electrode behaviour. Thus, the phenomenological model parameters of all kinetics can be obtained by fitting experimental data. Assuming an uniform temperature at the top and bottom separator and only conductive heat transfer, several of the two-dimensional models are stacked to form a three-dimensional representation of an MCFC stack. In other
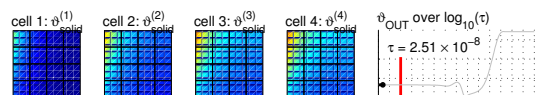
publications, the developed model is used to analyse further applications of the MCFC technology [16, 17].

A similar approach for a three-dimensional model of an MCFC stack was presented by Iora *et al.* [27]. As in the work by Bosio *et al.* [8], a two-dimensional model of one cell based on balances of mass and enthalpy is derived first. As an external reforming of the fuel gas is assumed, the fed gas for their model does not contain methane. Thus, the methane steam reforming is neglected. The water gas shift reaction is considered to be at equilibrium in the anode gas compartment. An electrochemical model is developed using the Nernst voltage and an expression for the overall cell resistance. Furthermore, as the considered MCFC system is operated under pressure, the pressure drop in the anode and cathode gas compartment is analysed. The developed model is used for a design analysis of a hybrid plant based on a MCFC and a gas-turbine [28].

A series of MCFC models has been proposed by Heidebrecht *et al.* [22, 23, 24, 25]. Kinetic rate expressions are applied for the methane steam reforming reaction and the water gas shift reaction in the anode gas chamber (DIR), and Butler-Volmer equations are used for the electrochemical reaction kinetics at the anode and cathode. Moreover, the charge balances are accounted for using a description of the electrical potential field. The model implements a catalytic combustion chamber as it is used in the MCFC system HOTMODULE. Thus, the mass flows of the anode and cathode gases are coupled.

A simple IIR unit was added to the model of Heidebrecht [22] by Gundermann *et al.* [18, 20, 21]. The resulting model that consists of one IIR unit and one representative fuel cell is applied for a validation of model parameters using measurement data from an industrial scale MCFC power plant. Furthermore, based on the model of Heidebrecht, a state estimator for the internal states of an MCFC was developed by Mangold *et al.* [32] and a simple and practical control strategy was established by Sheng *et al.* [44].

A summary of the models mentioned here is given in Table 1.1. As discussed above, especially the spatial temperature distribution is of interest when a Molten Carbonate Fuel Cell stack is modelled. Two of the just mentioned three-dimensional models describing an MCFC stack [16, 27] take into account a uniform temperature distribution at the boundary between the fuel cells. Thus, the effect of a temperature distribution in the cell plane is disregarded. Furthermore, the methane steam reforming reaction (**ref1**) at the Anode (DIR) and the Indirect Internal Reforming (IIR) are not implemented in these models. Therefore, a new stack model based on the work of Heidebrecht and Gundermann is developed in this work [38].

1.3 Objectives of this Work

As stated before, the temperature is an important state variable for the operation of high temperature fuel cells such as the MCFC [51]. Knowledge about the temperature
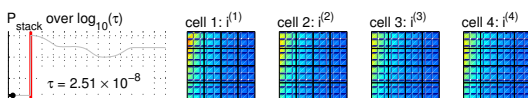
Table 1.1.: Summary of the selected MCFC models in the literature in chronological order.
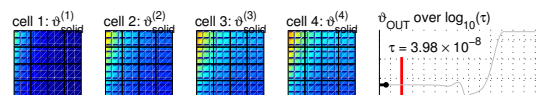
Author		Year	Dim.	Reforming Reactions	El.chemistry
Yoshiba *et al.*	[52]	1998	3D	DIR: ref2	el. resistances
Bosio *et al.*	[8]	1999	2D	DIR: ref2	el. resistances
Park *et al.*	[37]	2002	2D	DIR: ref1, ref2	el. resistances
Lukas *et al.*	[31]	2002	0D	IIR+DIR: ref1, ref2	el. resistances
Heidebrecht	[22]	2003	2D	IIR+DIR: ref1; ref2	potential field
Iora *et al.*	[27]	2007	2D/3D	DIR: ref2	el. resistances
Bosio *et al.*	[16]	2008	3D	DIR: ref2	el. resistances
Gundermann	[18]	2008	2D	IIR+DIR: ref1; ref2	potential field

profile in the fuel cell stack is required to optimise design and operating parameters of the fuel cell system. This work describes a model which provides the temperature distribution in the cell plane as well as the temperature distribution along the stack length. Additionally, the simulation results show other state variables such as the concentration profiles or the current density.

In MCFC systems, the temperature is typically around 600 °C. This temperature is high enough to allow (indirect and direct) internal reforming. Thus, the production of hydrogen from different types of fuels such as natural gas, waste gas or gas from anaerobic digestion processes is possible [50]. Also, no expensive catalysts are required due to the high temperatures; Nickel and Nickel oxide are sufficiently active to be used as reforming catalyst and simultaneously as catalysts for the electrochemical reactions. Furthermore, carbon monoxide, a catalyst poison for low temperature fuel cells, can be used as an educt for the electrochemical reactions at this temperature level.

The cell temperature is determined by several processes in the fuel cell stack. Since the reforming process is endothermic, it constitutes a heat sink. In contrast, the electrochemical reactions at both electrodes as well as the ion transport through the electrolyte release heat. The energy is transported by convection of the anode and cathode gases and by the heat conduction in the solid parts of the cell stack. The anodic and cathodic gas flows constitute directed heat transport mechanisms, while the heat conduction, which mainly occurs in the solid parts of the cell, is an omnidirectional heat transport mechanism within the cell plane and along the stack length. Together, these processes generate a 3D spatially distributed temperature profile. For an efficient and economically competitive operation, this temperature profile has to lie in a certain temperature window. On the one hand, lower temperatures decrease the local reaction rates and ion conductivity. Thus the cell voltage is decreased, which results in lower efficiency. On the other hand, higher temperatures cause fast degradation of catalyst material and material stress and, therefore, shorten the system's life time.

Reliable measurements of the temperature profile in the fuel cell system, especially inside the fuel cell stack, are difficult to perform. The high temperature, the aggres-

sive atmosphere in the stack due to the molten carbonate electrolyte and the need for electric isolation of the temperature sensors are the main problems regarding temperature measurements. Nevertheless, the internal state of the MCFC system can be studied using mathematical modelling and numerical simulation. Thus, the focus of this work is the modelling of the MCFC stack. First, the different gas compartments in the stack, especially the IIR unit, are considered.

The IIR units are flat, structured reactors located in the fuel cell stack between two fuel cells (right hand side of Fig. 1.2). Considering the IIR units used in the HotModule, they are divided into four sections with different flow directions and different spatial distributions of the reforming catalyst.
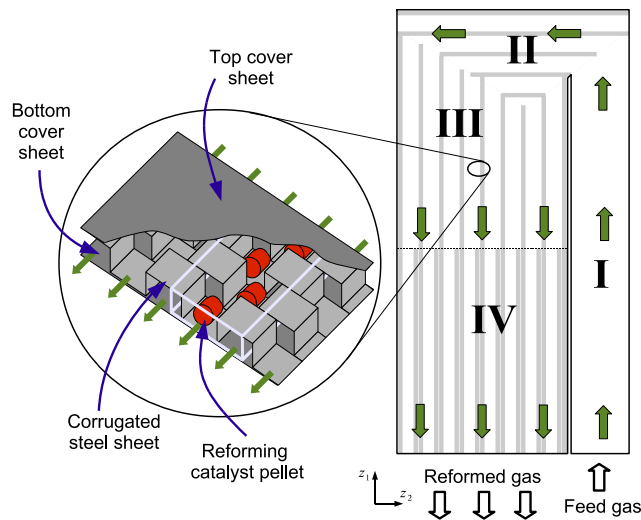

Figure 1.2.: Scheme of the entire IIR unit with gas flow directions and a cutout detail of the structure (US-Patent 6200696).

In this integrated reactor concept, heat transfer between the endothermic reforming process and the heat releasing electrochemical reactions in the neighbouring fuel cells is accomplished. Thus, the endothermic reforming process taking place at the surface of these catalyst pellets influences the temperature profile in the IIR unit and, moreover, the neighbouring fuel cells. Since the rate of the (electro-)chemical reactions as well as the rate of the undesired degradation processes strongly depend on the temperature distribution, a deeper understanding of the gas flow and the reactions in the IIR is required. In previous studies, the IIR is included as part of a lumped-parameter MCFC model [31] or it is implemented as an additional layer in two-dimensional simulations [20, 37].

However, these models do not have the level of detail needed for a further optimisation of the MCFC stack. In the above mentioned models, a flat two-dimensional representation of the different compartments of an MCFC is considered. While this is a valid approach for a first spatially distributed simulation, detailed simulations are required to further improve the accuracy of model predictions. Therefore, a small
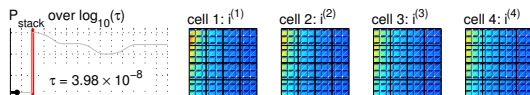
cutout section of the IIR unit is considered in this work (left hand side of Fig. 1.2) [39]. In the so-called detailed model, the exact three-dimensional geometry of the IIR unit with the corrugated sheets and the catalyst pellets is modelled.
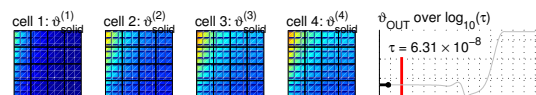
The detailed reformer model is too complex to be coupled with fuel cell models forming a stack model. Thus, its (mathematical) complexity needs to be reduced. Starting with the detailed model, physically motivated simplifications as well as spatial averaging are applied to create a reduced representation of the IIR unit which can be used in such a stack model. As a result of this model reduction, a hierarchy of IIR models is obtained and, in combination with a model of a fuel cell, the symmetric stack model.
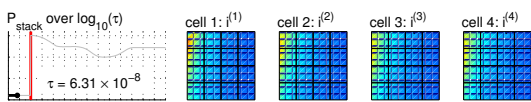
1.4 Structure of the Thesis

Besides an introduction of the working principle of an MCFC and a literature overview, this chapter presented a brief outline of the modelling approach used in the work. The following description of the various models created is split into two parts:

In Part I the main gas compartments of the fuel cell stack, the Internal Indirect Reforming (IIR) unit, the anode gas channels and the cathode gas channels are considered. The focus is on the modelling of the IIR unit, which is a structured reactor inserted into the stack between the fuel cells (Chapter 2). Models for three detail levels of this flat reactor are developed: the detailed model (Section 2.1), the zone model (Section 2.2) and the phase model (Section 2.3). Additionally, the detailed modelling of the anode and cathode gas compartments are discussed (Chapter 3).
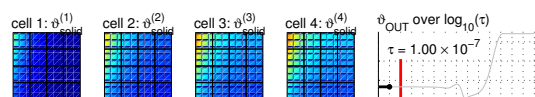
In Part II, the results of the previous chapters are used to formulate the symmetric stack model (Chapter 4). The numerical challenges of the implementation are discussed in Chapter 5 followed by the presentation of exemplary simulation results for a symmetric section of the stack (Chapter 6). At the end, the results of the work are summarised (Chapter 7).

P_{stack} over $\log_{10}(\tau)$ cell 1: $i^{(1)}$ cell 2: $i^{(2)}$ cell 3: $i^{(3)}$ cell 4: $i^{(4)}$

$\tau = 6.31 \times 10^{-8}$

Part I

Hierarchical Modelling of MCFC Compartments

Chapter 2

Modelling of the Indirect Internal Reforming Unit

In Section 1.3, a hierarchical approach for the modelling of the different gas compartments of an MCFC is proposed. The approach is used in this chapter for the modelling of the IIR unit considering three different hierarchical levels (Fig. 2.1) [39].

The so-called *detailed model* (see Fig. 2.1a) describes the reactor on a length scale in the order of 10^{-3} m. A cutout section of the structured reactor is modelled, considering the exact three-dimensional geometry as used in the HOTMODULE. The corrugated sheets as well as the cylindrical catalyst pellets are taken into account (Section 2.1).

The results of the detailed model are used to implement the so-called *zone model* (see Fig. 2.1b), which represents an entire IIR unit (Section 2.2). For this model, a physically motivated approach is applied to simplify the complex geometrical structure of the reactor. The model shows the effects observed in the detailed model on the scale of the entire IIR unit.

For the coupling of the IIR model with an existing model of a fuel cell, a further reduction of the complexity of the model is necessary. Mathematical conversion of the model equations, especially an averaging over two spacial coordinates, lead to the so-called *phase model* (see Fig. 2.1a). It is presented in Section 2.3. The complexity and mathematical structure of the model is similar to the model of a Molten Carbonate Fuel Cell developed by Heidebrecht *et al.* [23]. In Part II of this work, these two models are combined to the symmetric stack model.

2.1 The Detailed Model

2.1.1. Geometry

The IIR unit consists of corrugated sheets which are located between a top and a bottom metal sheet. On the one hand, they serve as a conductor for the electrical current through the IIR unit. On the other hand, they provide proper stiffness to
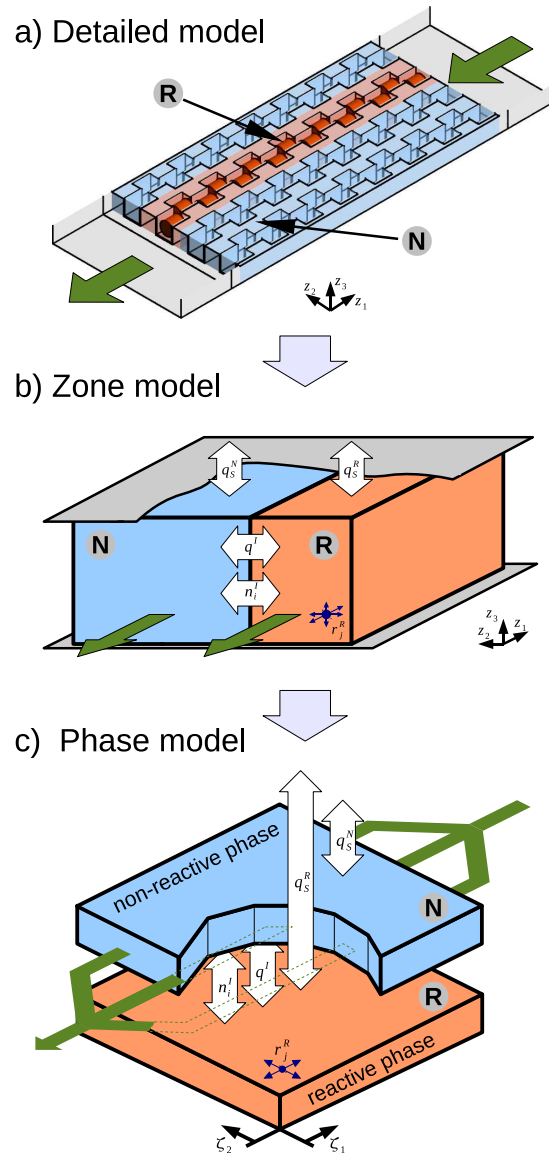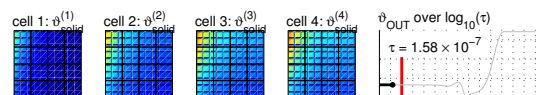
a) Detailed model

b) Zone model

c) Phase model
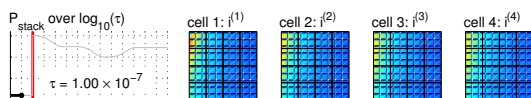
Figure 2.1.: Scheme of the model hierarchy of the IIR unit.

accept compressible load but maintain electric contact to the neighbouring fuel cells. Due to the fact that two successive punched hole in corrugated sheets are slightly displaced, they form small rectangular cages. The geometrical dimensions of these cages are of the order of 10^{-3} m. Considering the flow direction, the cages are arranged in a repeating pattern of rows. This repeating pattern is used in the entire reactor.

The reforming catalyst is available in the form of cylindrical pellets, which can be placed into the cages. In the steady state simulations it is assumed that the catalyst pellets are located in the centre of the corresponding cage with no contact to the

metal sheets. In the IIR unit, the smallest repeating pattern is represented by four rows of cages. Fig. 2.2 shows such a small section of the structure with a width of four rows of cages and a length of 15 cages.
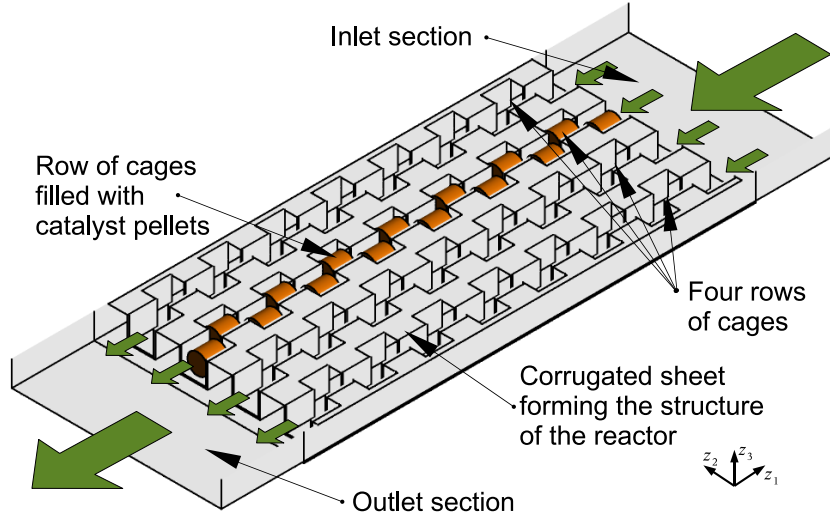

Figure 2.2.: Structure of the detailed model showing the four rows of cages (US-Patent 6200696 [2]). The top metal sheet is removed for this drawing to show the internal structure. Exemplary one row of cages is allocated with catalyst pellets.

Using this simulation domain, different placements of the catalyst pellets are possible. Allocations of one, two or three rows of cages with pellets are considered in this work. These patterns are show in Fig. 2.3a to 2.3c.
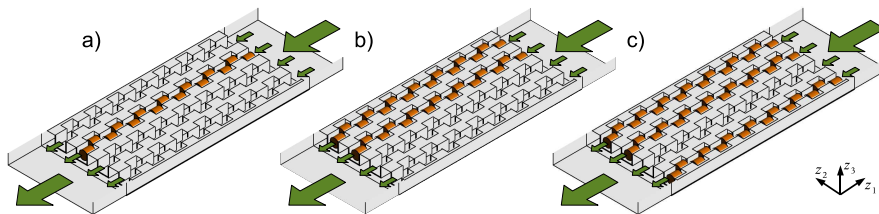

Figure 2.3.: Different allocations of the detailed model with catalyst pellets. Allocations of (a) one row, (b) two rows and (c) three rows are shown.

First simulations showed that at least an inlet section as well as a length of 5 to 6 cages are necessary to form a fully developed velocity profile which is not influenced by the gas inlet. Similar to this, an outlet section has to be implemented to reduce the influence of the increased flow area close to the gas outlet. Even with this additional section, the velocity in the last one or two cages is affected by the outlet boundary conditions. Taking into account these requirements, the simulation domain should be as long as possible. Considering the time needed for the simulation of the model, the length of the simulation domain is fixed to 15 cages.
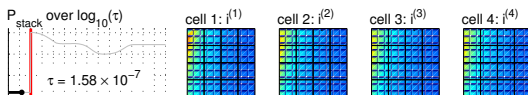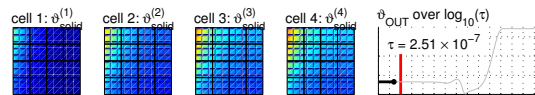
2.1.2. Assumptions

For the definition of the detailed model of the IIR unit, several assumptions are considered. A detailed discussion of the most important assumptions is given after the following overview:

a) The system is at steady state.

b) The gas is ideal and contains methane, steam, hydrogen, carbon monoxide and carbon dioxide.

c) Molecular diffusion in the gas phase is considered using a constant diffusion coefficient for each species, *i. e.* $D_i = \text{const.}$.

d) The gas flow is turbulent.

e) The reforming reactions take place at the surface of the catalyst pellets.

f) The top and bottom metal sheets have constant temperature.

With regard to molecular diffusion (assumption c)), the diffusion coefficients of the gas mixture are estimated using the correlation of Chapman-Enskog for the binary diffusion coefficients [43] and the extended approach of Wilke for the diffusion coefficients in the gas mixture [45]. The gas diffusion coefficients are determined considering a fixed temperature and a composition of the gas mixture which corresponds to the chemical equilibrium at the given temperature. Thus, the resulting constant values define the correct order of magnitude for these model parameters. An implementation of the above discussed correlations in the model would considerably increase the numerical efforts which goes beyond the scope of this work. The values for the gas diffusion coefficients used in this work are listed in Table 2.1 (Section 2.1.5).

With regard to the flow regime (assumption d)), the Reynolds number is of interest. This dimensionless number is defined as $\mathrm{Re} = \rho\, u\, d_h / \mu$. Approximating the IIR unit as a gap between two infinitely long plates, the hydraulic diameter is defined as $d_h = 2\, s$. Using the channel height of $s = 3 \times 10^{-3}\,\mathrm{m}$ and the average values for the velocity ($u = 1.4\,\mathrm{m\,s^{-1}}$) as well as the gas density ($\rho = 0.23\,\mathrm{kg\,m^{-3}}$) and the dynamic viscosity ($\mu = 1.08 \times 10^{-5}\,\mathrm{kg\,m^{-1}\,s^{-1}}$), a Reynolds number of $\mathrm{Re} = 178$ is calculated. This indicates laminar flow if a critical Reynolds number of $\mathrm{Re}_{crit.} = 2300$ for tubes is considered. But the critical Reynolds number is reduced in the IIR unit due to deviations from the tube geometry. The frequent disturbances of the gas flow by the corrugated sheet and the catalyst pellets have to be considered. Therefore, an intermediate flow regime or even turbulent flow has to be considered in parts of the simulation domain. Thus, a standard k-ε-turbulence is used for the entire detailed model. A comparison between simulations using a turbulent flow model and a laminar flow model is given in Section 2.1.6.4.

The methane steam reforming reaction:

$$CH_4 + H_2O \rightleftharpoons CO + 3\,H_2 \tag{ref1}$$

as well as the water gas shift reaction:

$$CO + H_2O \rightleftharpoons CO_2 + H_2 \tag{ref2}$$

are assumed to take place at the catalyst pellets' outer surface (assumption e). In the literature, different expressions for the kinetics of both reactions can be found [1, 12, 26, 29]. The kinetics depend on the exact chemical composition of the catalyst. Furthermore, the catalyst pellets are porous and hence the conversion of the gas includes mass transport and chemical reactions inside the pores. In this work, the catalyst pellets are assumed to be highly active so that the gas composition at the outer catalyst surface is close to the chemical equilibrium. Thus, the mass transport inside the pellets is not considered explicitly, but the pellets are assumed to be solid particles with a highly active catalytic surface. Simple mass action laws are used as reaction rate expressions which provide a good approximation of the reaction rates close to the chemical equilibrium conditions:

$$r_{\text{ref1}}^A = k_{0,\text{ref1}}^A \left[\left(\frac{p}{p^\theta} \right)^2 x_{\text{CH}_4}\, x_{\text{H}_2\text{O}} - \frac{1}{K_{\text{ref1}}(T)} \left(\frac{p}{p^\theta} \right)^4 x_{\text{CO}}\, x_{\text{H}_2}^3 \right] \tag{2.1}$$

$$r_{\text{ref2}}^A = k_{0,\text{ref2}}^A \left[\left(\frac{p}{p^\theta} \right)^2 x_{\text{CO}}\, x_{\text{H}_2\text{O}} - \frac{1}{K_{\text{ref2}}(T)} \left(\frac{p}{p^\theta} \right)^2 x_{\text{CO}_2}\, x_{\text{H}_2} \right] \tag{2.2}$$

Sufficient high values are assigned to the reaction rate constants, $k_{0,\text{ref1}}^A$ and $k_{0,\text{ref2}}^A$, to keep the gas at the pellet surface close to chemical equilibrium all the time. The equilibrium constants, $K_{\text{ref1}}(T)$ and $K_{\text{ref2}}(T)$, are calculated from thermodynamic equations via the Gibbs enthalpies of the considered reactions.

A fuel cell is located on the left and right hand side of the IIR unit in the stack. These fuel cells are not considered in the detailed model. Due to the small size of the model domain, the difference between the minimal and maximal temperature at the metal sheet separating the reforming reactor from the fuel cells is small in the modelled area. Therefore, a constant temperature for these sheets at the top and bottom of the model is assumed (assumption f)). Considering this, the heat flux through the solid domains representing the metal sheets is proportional to the difference between the temperature set at these external boundaries of these domains and the calculated gas temperature close to the wall.

2.1.3. Governing Equations

The steady state balance equations for the k-ε turbulence model are used in the simulations of the detailed model of the IIR unit. Only the basic partial differential equations for this approach to solve the Reynolds Averaged Navier-Stokes equations, as defined by the CFD software ANSYS CFX, are listed here [11]. A detailed discussion of these equations can be found in the literature [4, 30, 45, 49]. The reactions taking place at the catalyst surface are accounted for in the boundary conditions.
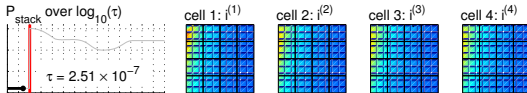
The continuity equation is given by:

$$\nabla \cdot (\rho \, \mathbf{u}) = 0 \tag{2.3}$$

while the momentum balance is defined as:

$$\nabla \cdot (\rho \, \mathbf{u} \otimes \mathbf{u}) = -\nabla \cdot \left(p' + \mu_{\text{eff}} \left(\nabla \mathbf{u} + (\nabla \mathbf{u})^T \right) \right) \tag{2.4}$$

with the effective viscosity, μ_{eff}:

$$\mu_{\text{eff}} = \mu + \mu_{\text{t}} \tag{2.5}$$

In Eq. (2.4), p' represents the modified pressure, which considers an additional pressure term due to the fluctuating velocity components of the turbulence model:

$$p' = p + \frac{2}{3}\rho \, k \tag{2.6}$$

Furthermore, the k-ε turbulence model assumes that the turbulence viscosity, μ_{t}, is linked to the turbulence kinetic energy, k, and the turbulence eddy dissipation rate, ε, *via* the relation:

$$\mu_{\text{t}} = C_\mu \, \rho \frac{k^2}{\varepsilon} \tag{2.7}$$

where C_μ is a constant for the k-ε turbulence model as defined by Ansys CFX.

The turbulence kinetic energy, k, is defined as the variance of the fluctuations in velocity while the turbulence eddy dissipation rate, ε, is the rate at which the velocity fluctuations dissipate. The corresponding differential transport equations read:

$$\nabla \cdot (\rho \, \mathbf{u} \, k) = \nabla \cdot \left[\left(\mu + \frac{\mu_{\text{t}}}{\sigma_k} \right) \nabla k \right] + p_k + \rho \, \varepsilon \tag{2.8}$$
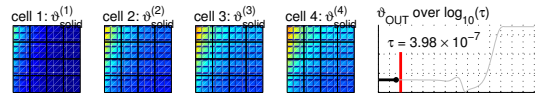
$$\nabla \cdot (\rho \, \mathbf{u} \, \varepsilon) = \nabla \cdot \left[\left(\mu + \frac{\mu_{\text{t}}}{\sigma_\varepsilon} \right) \nabla \varepsilon \right] + \frac{\varepsilon}{k} \left(C_{\varepsilon 1} p_k - C_{\varepsilon 2} \, \rho \, \varepsilon \right) \tag{2.9}$$

where $C_{\varepsilon 1}$, $C_{\varepsilon 2}$, σ_k and σ_ε are additional constants of the model.

p_k represents the turbulence production due to viscous forces, which is modelled using:

$$p_k = \mu_{\text{t}} \nabla \mathbf{u} \cdot \left(\nabla \mathbf{u} + (\nabla \mathbf{u})^T \right) - \frac{2}{3} \nabla \cdot \mathbf{u} \left(3\mu_{\text{t}} \nabla \cdot \mathbf{u} + \rho \, k \right) \tag{2.10}$$

For the energy balance, two equations are needed. On the one hand, an energy balance is defined for the gas phase including convective energy transport (left hand side) and

heat conduction as well as energy transport due to diffusion and turbulence (right hand side):

$$\nabla \cdot (\rho \, \mathbf{u} \, h) = \nabla \cdot \left(\lambda \nabla T_{\text{gas}} + \sum_i \rho \, D_i \, h_i \nabla w_i + \frac{\mu_t}{Pr_t} \nabla h \right) \tag{2.11}$$

with the turbulent Prandtl number Pr_t, which is the ratio between the kinematic viscosity due to turbulence in the gas and the turbulent thermal diffusivity.

On the other hand, the energy balance in the solid compartments, *e. g.* the corrugated sheets as well as the top and bottom metal sheets and the catalyst pellets, considers only heat conduction:

$$0 = \nabla \cdot (\lambda_{\text{solid}} \nabla T_{\text{solid}}) \tag{2.12}$$

Furthermore, the component mass balance is required. It reads:

$$\nabla \cdot (\rho \, \mathbf{u} \, w_i) = \nabla \cdot \left(\left(\rho \, D_i + \frac{\mu_t}{Sc_t} \right) \nabla w_i \right) \tag{2.13}$$

taking into account convective mass transport (left hand side) as well as molecular and turbulent diffusion (right hand side). Sc_t represents the turbulent Schmidt number, which is defined as the ratio of the kinematic viscosity due to turbulence and the turbulent diffusivity.

2.1.4. Boundary Conditions

All boundaries of the detailed model are presented in Fig. 2.4. On the one hand, there are external boundaries of the simulation domain such as the gas inlet and the gas outlet, the outer surface of the top and bottom metal sheet as well as the boundaries at the left and right hand side of the model. On the other hand, internal boundaries have to be taken into account: the surface of the catalyst pellets and the interface between the metal sheets and the gas phase.

The external boundary conditions are defined by Eqs. (2.14) to (2.21). The overall mass flux at the gas inlet, g_{in}, is used to calculate the gas velocity, considering the density of the gas at the inlet boundary (Eq. (2.14)). Furthermore, the gas temperature (Eq. (2.15)) as well as the gas composition in terms of mass fractions (Eq. (2.16)) are specified for the inlet flow:

$$[\mathbf{n} \cdot (\rho \, \mathbf{u})]_{\text{inlet}} = \frac{g_{\text{in}}}{A_{\text{inlet}}} \tag{2.14}$$

$$T_{\text{gas}}|_{\text{inlet}} = T_{\text{in}} \tag{2.15}$$

$$w_i|_{\text{inlet}} = w_{i,\text{in}} \tag{2.16}$$
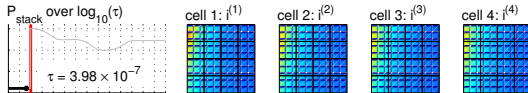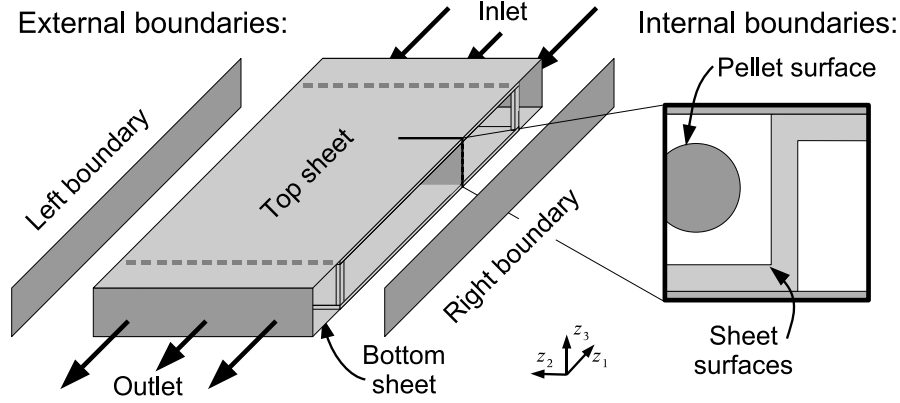
Figure 2.4.: Boundaries of the detailed model.

At the gas outlet, the relative pressure is given. It is constrained such that the area-averaged pressure value is equal to this given outlet pressure:

$$\overline{p}_{rel,\text{out}} = \frac{1}{A} \iint_A p_{rel,\text{outlet}} \, \text{d}z_2 \text{d}z_3 \tag{2.17}$$

The temperatures at the outward boundaries of the top and bottom sheets are set to a given temperature, which corresponds to an averaged temperature of the neighbouring fuel cells:

$$T_{solid}|_{\text{top}} = T_{\text{wall}} \tag{2.18}$$

$$T_{solid}|_{\text{bottom}} = T_{\text{wall}} \tag{2.19}$$

The left hand side and the right hand side of the simulation domain are coupled by a periodic domain interface using conservative interface fluxes. With regard to the solid phase, the temperature as well as the energy flux on the left and right hand side of the periodic interface have to be equal:

$$0 = \left[T_{solid} \right]_{\text{left}} - \left[T_{solid} \right]_{\text{right}} \tag{2.20}$$

$$0 = \left[\mathbf{n} \cdot (\lambda_{solid} \nabla T_{solid}) \right]_{\text{left}} - \left[\mathbf{n} \cdot (\lambda_{solid} \nabla T_{solid}) \right]_{\text{right}} \tag{2.21}$$

with the boundary normal vector, $\mathbf{n}$. Similar boundary conditions are used for the momentum balance, the energy balance and the component mass balances of the gas mixture at the periodic interface.
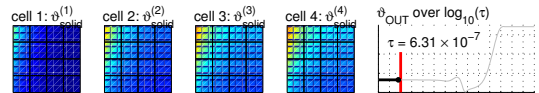
At the internal surfaces of the metal sheets, the velocity is equal to zero (no-slip condition):

$$0 = \left[\mathbf{u}\right]_{\text{sheet surface}} \tag{2.22}$$

Furthermore the temperature of the metal is equal to the temperature of the gas at these surfaces. The wall boundary layer is considered using scalable wall functions as implemented in the CFD solver ANSYS CFX [11]:

$$\left[T_{solid}\right]_{\text{sheet}} = \left[T_{gas}\right]_{\text{gas}} \tag{2.23}$$

Additionally, the heat flux across the solid-gas interface is given by:

$$\left[\mathbf{n} \cdot (\lambda_{solid}\nabla T_{solid})\right]_{\text{sheet}} = \left[\mathbf{n} \cdot \left(\lambda_{gas}\nabla T_{gas} + \sum_i \rho\, D_i\, h_i \nabla w_i + \frac{\mu_t}{Pr_t}\nabla h_{gas}\right)\right]_{\text{gas}} \tag{2.24}$$

Moreover, the sheet surface is impermeable for all gas components, that means:

$$0 = \left[\mathbf{n} \cdot \left(\left(\rho\, D_i + \frac{\mu_t}{Sc_t}\right)\nabla w_i\right)\right]_{\text{gas}} \tag{2.25}$$

At the surface of the catalyst pellets, the reforming reactions are taking place. Due to the laws of mass conservation, the mass flux density normal to the pellet surface has to be equal to zero. Orthogonal to this normal direction, the no-slip condition is applied. Thus the velocity at the catalyst surface is zero:

$$0 = \left[\mathbf{u}\right]_{\text{pellet surface}} \tag{2.26}$$

Similar to the interface between the gas and the metal sheets, equations for the temperature (Eq. (2.27)) and for the conservative energy flux (Eq. (2.28)) at the pellet surface are defined for the energy balance:

$$\left[T_{solid}\right]_{\text{pellet}} = \left[T_{gas}\right]_{\text{gas}} \tag{2.27}$$

$$\left[\mathbf{n} \cdot (\lambda_{solid}\nabla T_{solid})\right]_{\text{pellet}} = \left[\mathbf{n} \cdot \left(\lambda_{gas}\nabla T_{gas} + \sum_i \rho\, D_i\, h_i \nabla w_i + \frac{\mu_t}{Pr_t}\nabla h_{gas}\right)\right]_{\text{gas}} \tag{2.28}$$
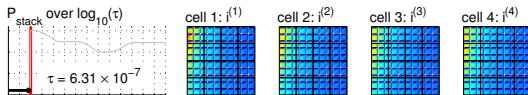
Due to the reactions taking place at the pellet surface, a component mass transfer occurs between the gas and the pellet surface (Eq. (2.29)). These component mass fluxes depend on the rates of both reforming reactions, r_j^A, and the stoichiometric coefficients, $\nu_{i,j}$.

$$0 = \left[\mathbf{n} \cdot \left(\left(\rho\, D_i + \frac{\mu_t}{Sc_t} \right) \nabla w_i \right) + \left(\sum_{j=\text{ref}} \nu_{i,j}\, M_i\, r_j^A \right) \right]_{\text{gas}} \tag{2.29}$$

The heat of reaction at the catalyst surface, $\Delta_R h_j = \sum_i \nu_{i,j}\, M_i\, r_j^A\, h_i$, is implicitly accounted for in the enthalpy balance. Therefore, it does not explicitly appear in the boundary conditions. With no turbulence at the pellet surface, *i.e.* $\mu_t = 0$ a combination of Eq. (2.28) and Eq. (2.29) results in:.

$$\left[\mathbf{n} \cdot \left(\lambda_{solid} \nabla T_{solid} \right) \right]_{\text{pellet}}$$

$$= \left[\mathbf{n} \cdot \left(\lambda_{gas} \nabla T_{gas} \right) + \sum_i \left(\sum_{j=\text{ref}} -\nu_{i,j}\, M_i\, r_j^A \right) h_i \right]_{\text{gas}}$$

$$= \left[\mathbf{n} \cdot \left(\lambda_{gas} \nabla T_{gas} \right) + \sum_j \left(-\Delta_R h_j \right) \right]_{\text{gas}} \tag{2.30}$$

2.1.5. Model Parameters

The parameters used in the model are listed in Table 2.1. For the metal sheets, the properties of steel are applied whereas the properties of nickel are used for the catalyst pellets. The values of the diffusion coefficients in the mixture are calculated considering a representative temperature and composition of the gas mixture. The thermodynamic properties of the gas such as the heat capacity, the enthalpy and the entropy are provided by the material library of the simulation tool ANSYS CFX using the NASA format [15, 33]. The values of the reaction rate constants are chosen in a way that the reforming reactions are very close to chemical equilibrium (see Section 2.1.2). The coefficients are considered as constant with regard to the temperature and gas composition. This simplifies the numerical complexity of the problem.

2.1.6. Simulation Results

Three different variants of the detailed reformer model are considered. Of the four rows of cages, one, two or three rows are filled with catalyst pellets (see Fig. 2.3). After the definition of the inlet conditions, the simulation results of the model for configurations with one row filled with catalyst pellets are discussed in detail. Further on, the results of the three different configurations are compared and the differences between turbulent and laminar flow modelling are analysed.
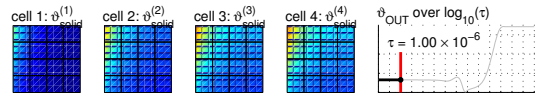
Table 2.1.: Parameters used in the detailed model of the IIR unit.

Property	Symbol	Value
metal sheets (steel)		
density	ρ_{sheet}	$7854\,\text{kg}\,\text{m}^{-3}$
specific heat capacity	$c_{p_{\text{sheet}}}$	$434\,\text{J}\,\text{kg}^{-1}\,\text{K}^{-1}$
thermal conductivity	λ_{sheet}	$60.5\,\text{W}\,\text{m}^{-1}\,\text{K}^{-1}$
catalyst pellets (nickel)		
density	ρ_{pellet}	$8903\,\text{kg}\,\text{m}^{-3}$
specific heat capacity	$c_{p_{\text{pellet}}}$	$444\,\text{J}\,\text{kg}^{-1}\,\text{K}^{-1}$
thermal conductivity	λ_{pellet}	$90.7\,\text{W}\,\text{m}^{-1}\,\text{K}^{-1}$
diffusion coefficient at 900 K		
methane	D_{CH_4}	$2 \cdot 10^{-4}\,\text{m}^2\,\text{s}^{-1}$
water	$D_{\text{H}_2\text{O}}$	$3 \cdot 10^{-4}\,\text{m}^2\,\text{s}^{-1}$
hydrogen	D_{H_2}	$5 \cdot 10^{-4}\,\text{m}^2\,\text{s}^{-1}$
carbon dioxide	D_{CO_2}	$2 \cdot 10^{-4}\,\text{m}^2\,\text{s}^{-1}$
carbon monoxide	D_{CO}	$2 \cdot 10^{-4}\,\text{m}^2\,\text{s}^{-1}$
reaction rate coefficients		
methane steam reforming reaction	$k^A_{0,\text{ref1}}$	$0.3\,\text{mol}\,\text{m}^{-2}\,\text{s}^{-1}$
water gas shift reaction	$k^A_{0,\text{ref2}}$	$1.0\,\text{mol}\,\text{m}^{-2}\,\text{s}^{-1}$

The hexagonal mesh generated for the geometry includes 593744 elements. Considering the number of equations defined, approximate 6.5 million Degrees of Freedom (DoF) have to be solved. Using ANSYS CFX, one simulation takes about 5 hours calculation time on an Intel Xeon processor with 3.2 GHz CPU speed. Up to 1.3 GB of RAM are required during the simulation procedure.

2.1.6.1. Boundary Conditions

The parameters for the boundary conditions at the gas inlet as well as for the top and bottom sheets are listed in Table 2.2. These values represent typical inlet conditions of the IIR unit considering natural gas as fuel and an average current density of $i_{avg} = 80\,m\!A/\text{cm}^2$. They are used for all simulations of the detailed model.

2.1.6.2. Results for a Catalyst Allocation of One of Four Rows

Fig. 2.5 shows the simulated velocity profile for the detailed model. The gas enters the simulation domain at the inlet boundary located at the top with the velocity calculated from the given mass flow rate. In the inlet section, the flow profile develops from a constant velocity at the inlet boundary to an inhomogeneous velocity profile at the beginning of the corrugated sheets. Fig. 2.5a shows the velocity profile at half the height of the IIR unit (z_3). Due to the reduced cross sectional area close to the catalyst pellets and the no-slip boundary condition, the gas velocity is decreased around the pellets whereas the velocity is increased in the areas without catalyst pellets.
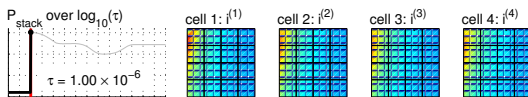
Table 2.2.: Operating conditions for the detailed model of the IIR unit.

| Property	Symbol	Value
inlet conditions		
gas temperature	T_{in}	850 K
mass flux	g_{in}	$21.945 \cdot 10^{-6}\,\mathrm{kg\,s^{-1}}$
mass fraction of methane	w_{in,CH_4}	0.196
mass fraction of water	w_{in,H_2O}	0.587
mass fraction of hydrogen	w_{in,H_2}	0.028
mass fraction of carbon monoxide	$w_{in,CO}$	0.009
mass fraction of carbon dioxide	w_{in,CO_2}	0.180
outlet conditions		
relative pressure	$\overline{p}_{rel,out}$	0 Pa
top and bottom wall		
temperature	T_{wall}	850 K
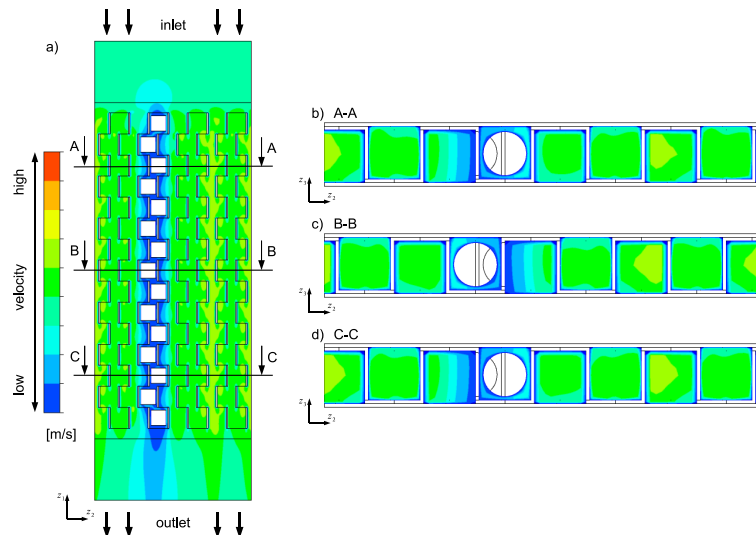
Figure 2.5.: Simulated velocity from the detailed model with 1 of 4 rows filled with catalyst pellets. a) Velocity profile at half the height of the model; b) to d) velocity profiles in a cross-section plane at the 3rd, the 8th and the 13th pellet, respectively.

In the cross section profiles (Fig. 2.5b to Fig. 2.5d), one can see that the velocity profile is repeated in an almost constant pattern after the first few catalyst pellets. In the vicinity of the catalyst pellets, the gas is meandering slowly around the pellets and it is almost stagnant compared to the gas in the other parts of the geometry. Due to the displacement of successive catalyst pellets, the velocity is also reduced in the area to the right or left hand side of the pellet. The ratio between the velocity close to the pellets and the velocity in the rest of the IIR unit is about 1:10. In the whole
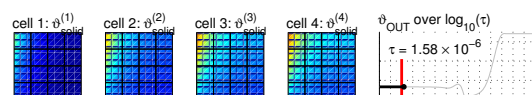
geometry, the gas flow is repeatedly disturbed by the corrugated sheet. This results in additional turbulence and mixing effects due to flow separation.

The temperature profile is displayed in Fig. 2.6. The cross section plots show that after the 6th catalyst pellet a steady repeating pattern is reached with regard to the temperature. Due to the endothermic reforming process, the temperature close to the catalyst pellets is reduced. The resulting temperature difference is the driving force for the energy fluxes from the gas phase and from the top and bottom walls towards the surface of the pellets. Considering the temperature distribution in the detailed reformer model, a distinct separation of the gas phase into two fractions can be observed. While the gas close to the catalyst pellets has a lower temperature, the gas without contact to the pellets stays at a higher temperature.
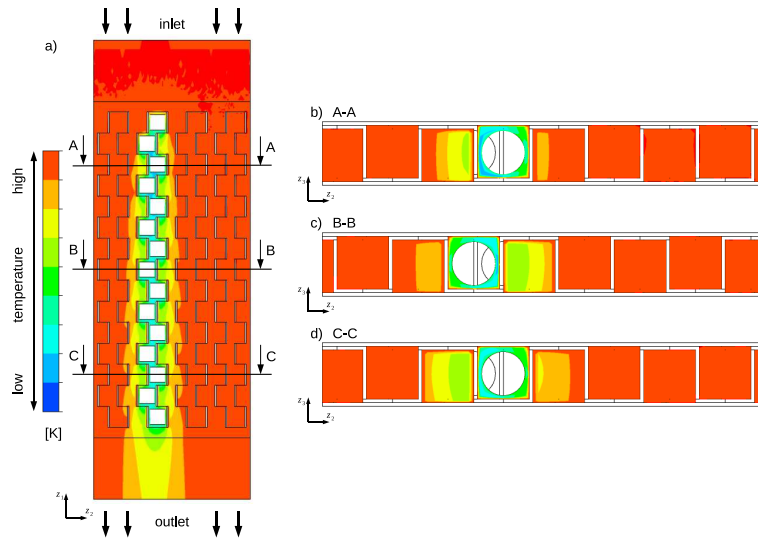

Figure 2.6.: Simulated temperature profile for the detailed model with 1 of 4 rows filled with catalyst pellets. a) Temperature distribution at half the height of the IIR unit; b) to d) temperature distribution in a cross-section plane at the 3rd, the 8th and the 13th pellet respectively.

Fig. 2.7 show a scheme of the two head flows towards the catalyst pellets. A quantitative comparison between these two heat fluxes indicates that the heat flux through the top and bottom sheets, Q_{wall}, is much higher than the energy provided by the gas phase further away from the catalyst pellets, Q_{gas}. Considering an MCFC system, a temperature change of $10\,K$ is significant with respect to degradation rates and electrochemical performance. Due to the fact that the IIR unit is intensively thermally coupled to the neighbouring fuel cells in the stack, a temperature difference of $10\,K$ in the IIR unit may also be considered as significant. The temperature difference between the gas around the catalyst pellets and the corrugated sheets or the remaining gas is several times as high as this threshold value. Thus, the endothermic reforming process in the IIR unit represents a local heat sink with regard to the neighbouring fuel cells in the stack.
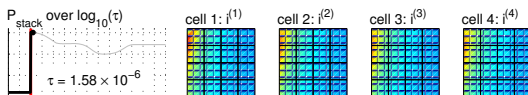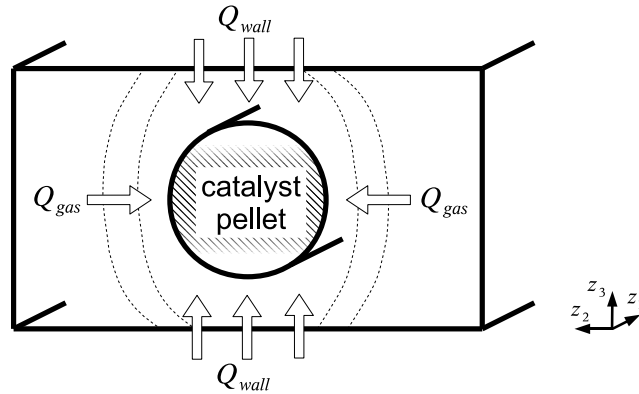
Figure 2.7.: Scheme of the energy fluxes to the catalyst pellets. The energy is provided via the top and bottom wall (Q_{wall}) as well as via gas phase (Q_{gas}) and is used for the reforming reactions at the catalytic active surface of the pellets.

The concentration profiles for methane, carbon dioxide and hydrogen are presented in Fig. 2.8. Methane is consumed by the methane steam reforming reaction at the surface of the catalyst pellets (Fig. 2.8a). Thus, the methane concentration is reduced. This results in a gradient in the methane mole fraction between the gas close to the pellet surface and the gas far from the catalyst. The difference is in the order of several mole percent. Similar gradients can be observed for the products of the reforming reactions, namely carbon dioxide (Fig. 2.8b) and hydrogen (Fig. 2.8c). The highest concentrations of these reaction products can be found close to the catalyst pellets whereas the lowest concentrations are in the free flowing gas. The turbulent characteristic of the gas flow combined with the diffusive mass transport of the educts to the catalyst pellets as well as the mass transport of the products away from the catalyst pellets result in funnel-shaped concentration profiles.

After a few catalyst pellets, the gas composition in the proximity of the pellets reaches the chemical equilibrium with respect to the reforming reactions. In this inlet region, the overall reaction rates are limited by the available catalyst surface and the activity of the catalyst. Once the gas around the pellets reaches its equilibrium composition, the reforming process is dominated by the mass transport of the reacting species towards and away from the pellet surface. Thus, after the inlet region, the rates of the reforming reactions are independent of the catalyst activity, at least as long as it is sufficiently high. It provides a constant thermal profile even in case of catalyst degradation, which is inevitable in such systems. Due to the fact that catalyst is added in excess, the degradation of the catalyst material does not influence the overall efficiency of the reforming process considering a planed life time of 5 years for a fuel cell stack with IIR units. This important feature of the presented reactor concept is a result of its geometrical structure consisting of the corrugated sheets and the catalyst pellets.
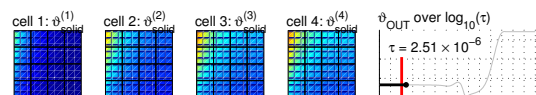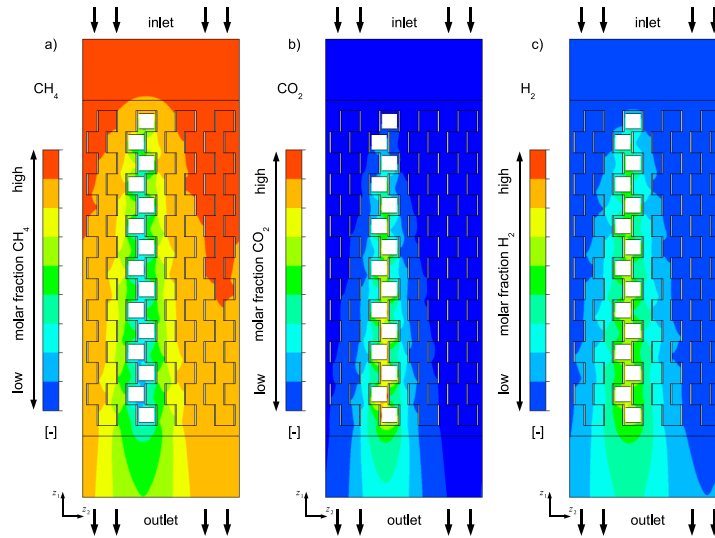
Figure 2.8.: Simulated gas compositions for the detailed model with 1 of 4 rows filled with catalyst pellets. The plots show the profiles in the main plane for the mole fraction of the following species: a) methane; b) carbon dioxide; c) hydrogen.

The concentrations profiles as well as the spatial temperature distribution and the velocity profile indicate that the reactor is divided into two zones: The first zone is a reactive zone close to the catalyst pellets. Because the flow is hindered by the pellets, the velocity is reduced in this zone. Additionally, the endothermic reforming process taking place at the surface of the catalyst pellets results in a significant temperature drop in this zone. The second zone is a non-reactive zone where the gas has no contact to the catalyst surface. Compared to the gas composition in the non-reactive zone, the concentration of the components in the reactive zone are influenced by the reactions taking place at the catalyst surface. This results in an increase of the concentrations of the reaction products and a decrease of the concentrations of the educts in this zone (Fig. 2.8). The exchange of mass and heat between the two zones due to diffusion and heat conduction determines the reaction rate of the overall system. Thus, the reactions are limited by the mass transport between the two zones defined by the corrugated sheets and the placement of the catalyst pellets.

2.1.6.3. Comparison of Different Catalyst Distributions

In addition to the model with an allocation of one row filled with catalyst pellets, simulations have also been carried out for models with two or three rows of cages filled with pellets, respectively. The additional catalyst pellets extend the size of the reactive zone and reduce the non-reactive zone. For all these simulations, the inlet conditions listed in Table 2.2 were used.
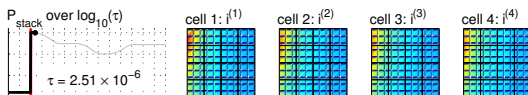
Fig. 2.9 compares the temperature profiles for the three configurations. In each of them, a similar pattern for the temperature is visible. The scale of the figures is identical and corresponds to the scale used in Fig. 2.6. A balance between the heat flux through the top and bottom sheets into the gas and the heat sink due to the reforming process is reached near the 7th catalyst pellet. After that, a constant pattern in the temperature profiles is visible. The simulations show nearly identical temperatures at the surface of the catalyst pellets for all three allocations with catalyst pellets. The more pellets are used, the more gas is converted, causing an increasing heat consumption in the reactive zone. However, the heat exchange area between the reactive and the non-reactive zone is identical in each variant. But, the heat exchange area between the top and bottom sheets and the reactive zone also grows with the number of catalyst pellets. This confirms the findings that the main heat supply to the reforming process happens directly through the outer metal sheets from the neighbouring fuel cells as discussed in Section 2.1.6.2.
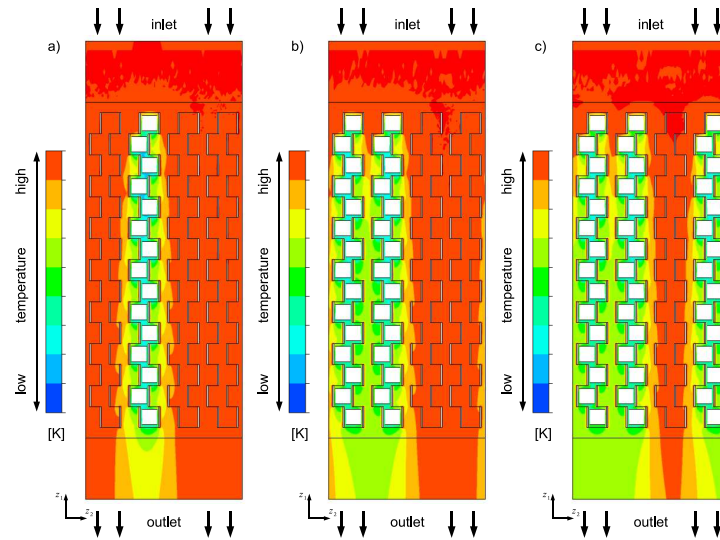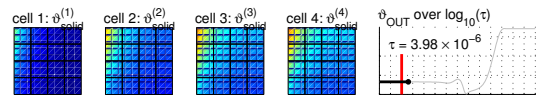

Figure 2.9.: Temperature distributions for different catalyst allocations for models with 1, 2 and 3 catalyst pellet rows. The same temperature scale is used for all three plots.

The corresponding concentration profiles for methane are shown in Fig. 2.10. The scale used in the three concentration plots is identical and corresponds to the scale used in Fig. 2.8. For each model variant, the reactive zone and non-reactive zone as well as the funnel-shaped concentration profiles are clearly visible. Mass transfer is only possible between the two zones. Therefore, the lowest methane concentrations are found in the centre of the reactive zone, where the gas is close to chemical equilibrium. Fresh, unreacted gas can only reach this area due to diffusion.

On the one hand, the yield of the reforming reactions is increasing with the number of catalyst pellets used, but on the other hand, the pressure drop rises as well. Furthermore, an increase of the number of catalysts and therefore the size of the reactive
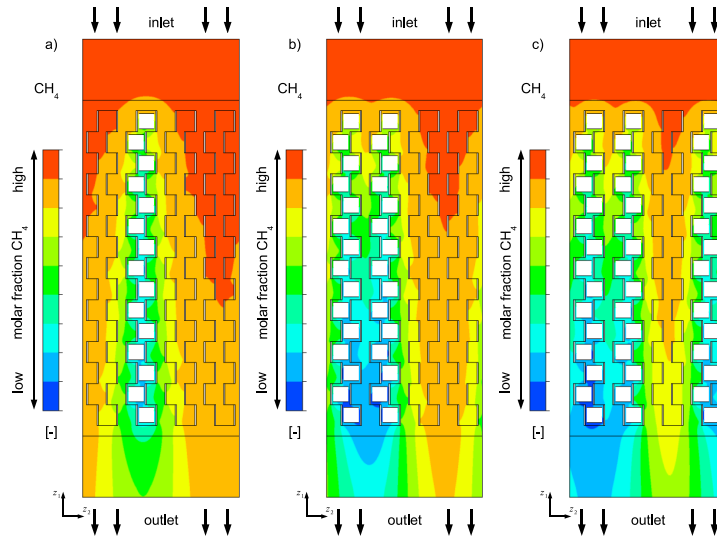
Figure 2.10.: Methane mole fraction for different catalyst allocations for models with 1, 2 and 3 catalyst pellet rows. The scale of the methane concentration is equal for all three plots. Due to the increased catalyst surface area in the reactive zone the lowest methane mole fraction can be observed if 3 of 4 rows are filled with catalyst pellets.

zone results in an increase of the overall heat flux through the top and bottom metal sheets. Thus, one can manipulate the heat transfer from the neighbouring fuel cell to the reforming reactor by changing the amount and / or the distribution of the catalyst pellets. Therefore, the catalyst density in the IIR unit can be used as a parameter to influence the local temperature in the fuel cell stack.

2.1.6.4. Comparison Between Turbulent and Laminar Flow Simulations

As stated in the assumptions (see Section 2.1.2), the k-ε-turbulence model was applied in the above discussed turbulent simulations. Fig. 2.11 compares the results for turbulent flow (images at the bottom) and for laminar flow (images at the top) for a model with a single row filled with catalyst pellets. This comparison is done for the velocity (Fig. 2.11a), the temperature (Fig. 2.11b) and the methane mole fraction (Fig. 2.11c). The images for both flow regimes use identical scales, which are equal to the scales used in the previously shown figures of the corresponding quantity.

The difference between the two flow regimes is clearly visible in the velocity profiles. The laminar velocity profile shows direct stream lines in the non-reactive zone from the inlet section towards the outlet section. Considering a turbulent flow regime results in a more homogeneous velocity profile. The difference between the velocity in the non-reactive zone and the reactive zone is increased in the laminar case.
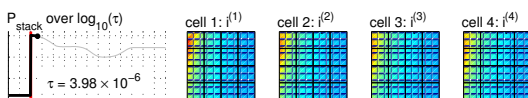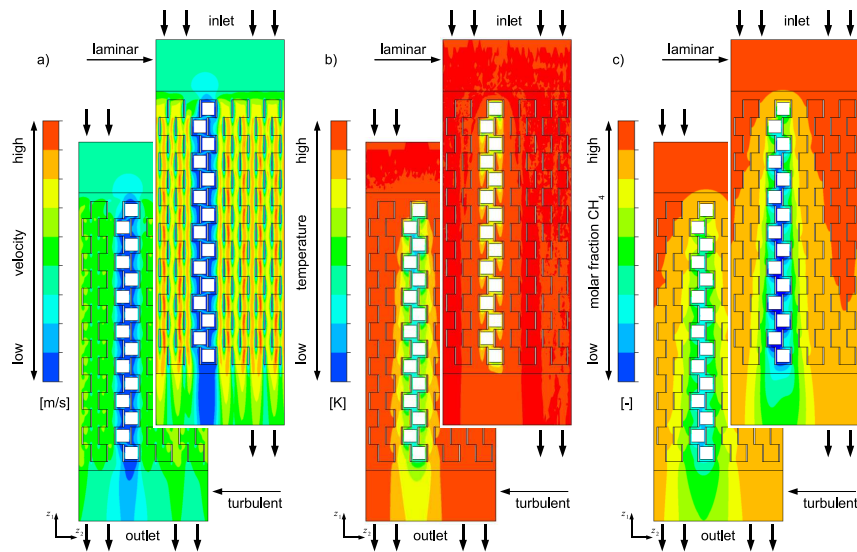
Figure 2.11.: Comparison between the results for laminar and turbulent flow for the velocity (a), the temperature (b) and the methane mole fraction (c) for a simulation with an allocation of one row with catalyst pellets.

The chemical equilibrium of the reforming reactions at the catalyst surface depends on the temperature as well as on the gas composition. If turbulence is considered, an additional transport mechanism for mass and heat between both zones is added. Therefore, the mass flow rate of methane to the catalyst surface is increased in the turbulent case. Due to the endothermic nature of the methane steam reforming reaction, this results in a lower temperature and, taking into account the chemical equilibrium, higher methane concentrations. The effect of the additional heat and mass transport is recognisable in the temperature and concentration profiles.

The simulation results do not allow an unambiguous determination of the flow regime. This indicates a flow in the transition area between the laminar and the turbulent regime. Thus, either an experimental data or models using Direct Numerical Simulation (DNS) are needed to distinguish between both possibilities. The required investigations are beyond the scope of the presented work.

2.1.7. Summary

In this section, different variants of the detailed three-dimensional model were presented by showing small cutouts of the Indirect Internal Reforming (IIR) unit. For these simulations, the exact geometry with the corrugated sheets and the individual catalyst pellets were taken into account.
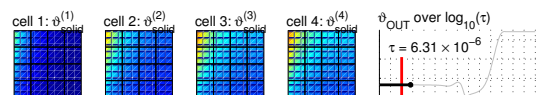
The analysis of the detailed model showed two important features of this reactor: First, due to the geometrical structure of the reactor, the reaction rate is limited by mass transport between a reactive and a non-reactive zone. A stable repeating pattern can be found for the temperature and velocity profiles while the concentration profiles show funnel-shaped profiles. Because of the excess of catalyst material, the degradation of the catalyst does not influence the overall reaction rate in the reforming reactor as long as its active surface is large enough. Therefore, a constant temperature profile can be expected in the IIR unit even after long operation time.

The second aspect is that the main heat transport route towards the cold reaction zone is from the neighbouring fuel cells through the top and bottom sheets directly into the reactive zone. Thus, the local temperature in the fuel cells can be influenced by the amount and the distribution of the catalyst pellets in the IIR units.
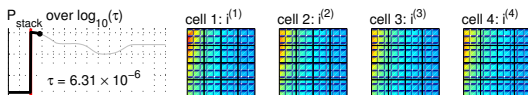
2.2 The Zone Model

2.2.1. Geometry and Assumptions

The detailed model is used to analyse a small cutout section of the reforming reactor. A modelling of the entire IIR unit on a similar detail level is not possible due to the increasing numerical effort required to solve the model. But, such a model is desirable to analyse the results found in the detailed model on the scale of an entire IIR unit. Therefore, the zone model is derived from the detailed model neglecting the exact structure of the corrugated sheets. Furthermore, the simulation domain is divided into the two zones identified in the detailed model: the non-reactive zone and the reactive zone which includes the catalyst pellets. The sizes of these zones are chosen according to the results of the detailed model (Fig. 2.12). The resulting model is used to simulate an entire IIR unit. Exemplary, a simulation representing the design of an IIR unit as used in the HotModule is created to analyse the temperature and concentration profiles [39].

A scheme of this reforming reactor is shown in Fig. 2.13. It is divided into four sections with different flow directions and different spatial distributions of the reforming catalyst. On the lower right hand side, the gas enters the IIR unit. There are no catalyst pellets in this part of the reactor (section I). Following the orientation of the corrugated sheets, the gas changes its main flow direction entering section II. In this section each forth row is filled with catalyst pellets (displayed as grey lines). After a second redirection of the gas, the last two sections follow. In section III the allocation is not changed but in section IV an alternating pattern of two rows filled with catalyst pellets and two rows without catalyst pellets is used.

The zone model of the entire IIR unit is based on the results obtained from the detailed model. First, the reactive and the non-reactive zones are represented by cuboid volumes (see Fig. 2.12). The width of the reactive zone corresponds to the width of
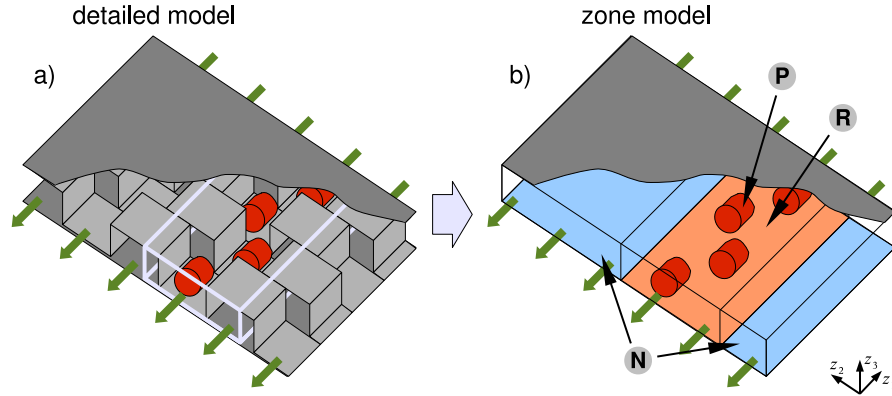
Figure 2.12.: Comparison of the structures of the detailed model and the zone model. N: non-reactive zone; R: reactive zone; P: catalyst pellet.

the zone of low gas velocities (see Fig. 2.5), which is identical to the width of the zone with low temperature (see Fig. 2.6). The exact geometry of the catalyst pellets is neglected and their volume is considered as part of the reactive zone. Furthermore, the surface reactions are replaced by a homogeneous gas phase reactions in the whole cuboid representing the reactive zone.

In a second step, the exact geometry of the corrugated sheets is neglected. To include the flow resistance of the sheets and the catalyst pellets in the model, an additional pressure drop term based on Darcy's law with anisotropic permeabilities is included in the equations. These permeabilities account for the orientation of the corrugated sheets and the additional pressure loss caused by the catalyst pellets.

The third step is to expand this simplified geometry to the size of the whole IIR unit. In this step, the orientation of the corrugated sheets and the catalyst pellet allocation of the four sections of the IIR unit are considered (see Fig. 2.13).

2.2.2. Governing Equations and Boundary Conditions

For the zone model, equations similar to for the detailed model are used including the k-ϵ-turbulence model. Only the changed equations are listed here.

As mentioned above, an additional term describing the pressure drop, S_M, is added to the momentum balance:

$$\nabla \cdot (\rho\, \mathbf{u} \otimes \mathbf{u}) = -\nabla \cdot \left(p' + \mu_{\text{eff}} \left(\nabla \mathbf{u} + (\nabla \mathbf{u})^T \right) \right) + \mathbf{S}_M \tag{2.31}$$

It is defined as follows [36]

$$\mathbf{S}_M = -\mu\, \mathbf{K}_{perm}^{-1} \cdot \mathbf{u} \tag{2.32}$$
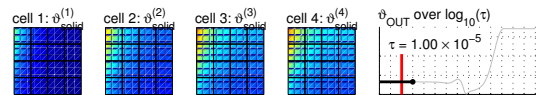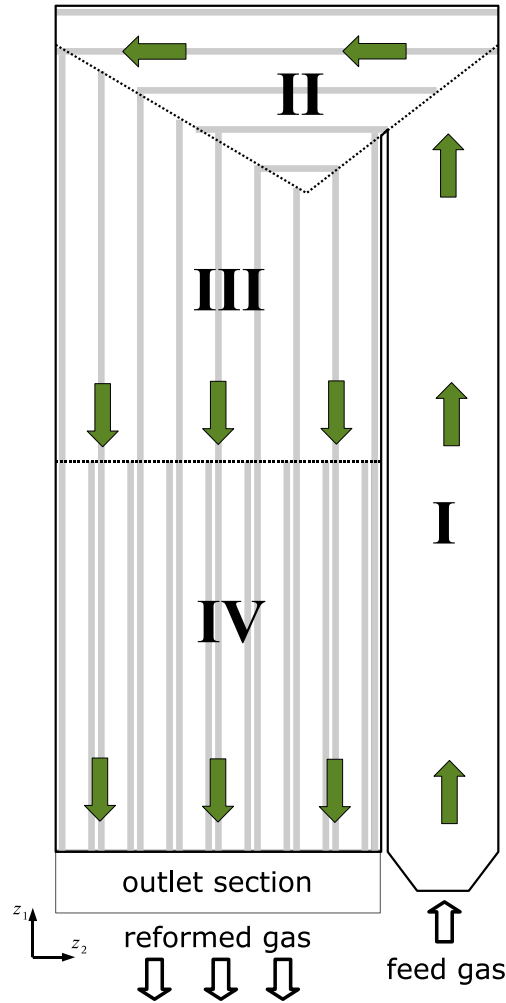
Figure 2.13.: Scheme of the IIR unit as used in the HotModule (US-Patent 6200696 [2]). For illustration of the reactor structure, the number of rows with catalyst pellets is reduced.

where μ is the dynamic viscosity of the gas mixture, $\mathbf{u}$ is the velocity vector and $\mathbf{K}_{perm}$ is the tensor describing the anisotropic permeability.

With regard to the permeability tensor, $\mathbf{K}_{perm}$, only the contributions in the two main directions, z_1 and z_2, are considered. Due to the fact, that the height (z_3-coordinate) is small compared to the other two coordinates, the permeability in this direction is neglected. Thus, the permeability tensor reads:

$$\mathbf{K}_{perm} = \begin{bmatrix} K_{perm,\parallel}^R & 0 & 0 \\ 0 & K_{perm,\perp}^R & 0 \\ 0 & 0 & 0 \end{bmatrix} \tag{2.33}$$
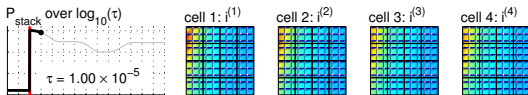
In the main flow direction of the corrugated sheets, nearly no obstacles are present while perpendicular to this direction the sheets which form the cages hamper the gas flow. Considering the reactive zone with the rows of cages filled with catalyst pallets, the additional reduction of the gas flow area results in a further pressure drop. The parameter values used in the simulations of the zone model are listed in Table 2.3.

In analogy to the energy balance of the gas phase in the detailed model (Eq. (2.11)), the energy balance reads:

$$\nabla \cdot (\rho \, \mathbf{u} \, h) = \nabla \cdot \left(\lambda_{\text{gas}} \nabla T_{\text{gas}} + \sum_i \rho \, D_i \, h_i \nabla w_i + \frac{\mu_t}{Pr_t} \nabla h \right) \tag{2.34}$$

Furthermore, the reforming reactions are incorporated in the component mass balances equations as source term (last term on the right hand side of Eq. (2.35)). This term is only considered in the reactive zones.

$$\nabla \cdot (\rho \, \mathbf{u} \, w_i) = \nabla \cdot \left(\left(\rho \, D_i + \frac{\mu_t}{Sc_t} \right) \nabla w_i \right) + \left(\sum_{j=\text{ref}} \nu_{i,j} \, M_i \, r_j^V \right) \tag{2.35}$$

The reforming reactions are considered as quasi-homogeneous gas phase reactions. Thus, the surface-related rates are transformed using the ratio of the external surface area of the catalyst pellets, A_{pellet}, and the volume of the reactive zone, V_{reactive}:

$$r_j^V = r_j^A \frac{A_{\text{pellet}}}{V_{\text{reactive}}} \tag{2.36}$$

For the zone model, temperature profiles for the top and bottom walls are required. Considering a possible experimental validation of the model, a constant temperature at the top and bottom metal sheet are assumed. At the gas inlet on the bottom right (see Fig. 2.13), the gas temperature as well as the mass flow and the gas composition are set whereas the relative pressure is given at the gas outlet. For all other walls, the no-slip boundary condition is set and thermal isolation is applied.

2.2.3. Model Parameters

In the zone model, the parameters of the detailed model, *e. g.* the diffusion coefficients, are used. The relevant thermodynamic properties of the gas, namely the heat capacity, the enthalpy as well as the entropy, are provided by the material library of the simulation tool CFX using the NASA format [15, 33]. Table 2.3 lists the additionally needed parameters. The values for the anisotropic permeability tensor in the different zones and for the different directions have been estimated by comparison of simulated and measured pressure drops on such a full scale IIR unit. Due to the fact
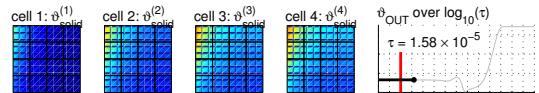
that the height of the reforming reactor is small compared to the length and width, the permeability in this direction is neglected.

Table 2.3.: Model parameters.

Property	Symbol	Value
inlet conditions		
gas temperature	T_{inlet}	$850\,K$
mass flux	g_{inlet}	$0.439 \cdot 10^{-3}\,kg\,s^{-1}$
mass fraction of methane	w_{inlet,CH_4}	0.196
mass fraction of water	w_{inlet,H_2O}	0.587
mass fraction of hydrogen	w_{inlet,H_2}	0.028
mass fraction of carbon monoxide	$w_{inlet,CO}$	0.009
mass fraction of carbon dioxide	w_{inlet,CO_2}	0.180
outlet conditions		
relative pressure	$\overline{p}_{rel,outlet}$	$0\,Pa$
top and bottom wall		
temperature	T_{wall}	$850\,K$
reaction rate coefficients		
methane steam reforming reaction	$k^V_{0,ref1}$	$192\,mol\,m^{-3}\,s^{-1}$
water gas shift reaction	$k^V_{0,ref2}$	$640\,mol\,m^{-3}\,s^{-1}$
anisotropic permeability in the non-reactive zone		
in flow direction	$K^N_{perm,\parallel}$	$2 \cdot 10^{-9}\,m^2$
orthogonal to the flow direction	$K^N_{perm,\perp}$	$20 \cdot 10^{-9}\,m^2$
anisotropic permeability in the reactive zone		
in flow direction	$K^R_{perm,\parallel}$	$100 \cdot 10^{-9}\,m^2$
orthogonal to the flow direction	$K^R_{perm,\perp}$	$20 \cdot 10^{-9}\,m^2$

2.2.4. Simulation Results

Just like the simulation results of the detailed model, the simulation results presented in this section were obtained in the framework of an industrial collaboration project. Thus, similar restrictions apply with regard to the presentation of quantitative data. Only qualitative results of the zone model are shown and their relevance for the fuel cell stack are discussed.

The hexagonal mesh generated for the zone model contains 439780 elements. Using the same computational hardware as for the detailed model (Intel Xeon 3.2 GHz), simulation results are available after several days computation time. The increased computation time is a result of the model structure, *e. g.* a great number of iterations is required to find the steady state solution. Up to 1.0 GB RAM is needed during the numerical solution.
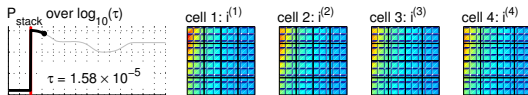
2.2.4.1. Temperature

In Fig. 2.14, the temperature distribution in the entire IIR unit according to the zone model is shown. The gas enters the simulation domain on the bottom right corner (Section I of the IIR unit; see Fig. 2.13).
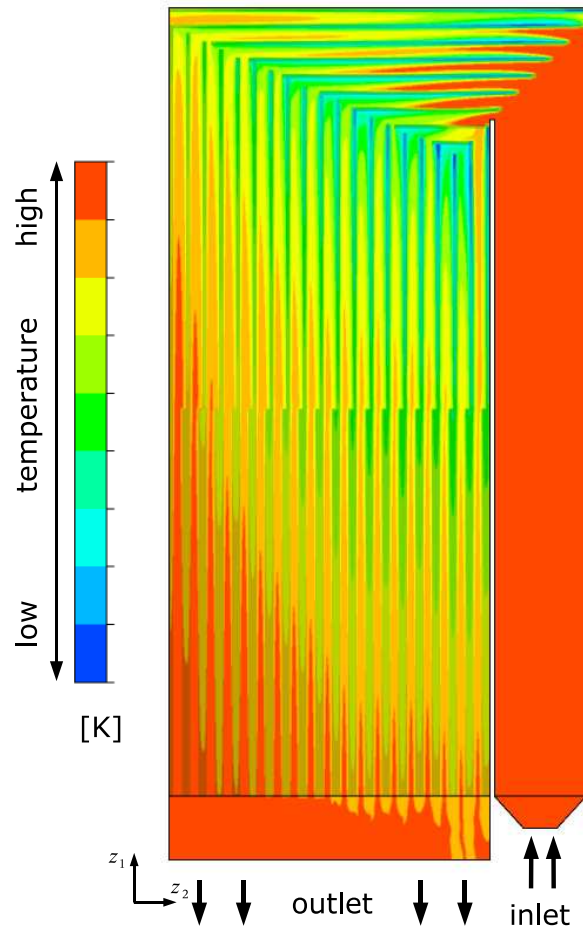
Figure 2.14.: Temperature distribution in the model of the entire IIR unit. The four sections of the IIR unit with different flow directions and different catalyst allocations are visible.

Due to the fact that the feed gas temperature is equal to the temperature of the top and bottom wall in this part of the IIR unit and no catalyst pellets are located in this section, the heat flux is zero and the gas temperature does not change. At the transition to section II, the gas hits the first catalyst pellets. As a result of the high concentration of methane as well as the high temperature, a high reaction rate for the reforming process can be found at this point. Thus, the gas mixture is quickly cooled down in the reactive zones. The temperature drop in these zones is in the range of
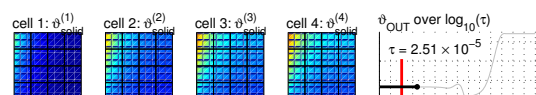
several $10\,\mathrm{K}$. The heat losses are partially compensated by the heat flux through the top and bottom wall, which is proportional to the temperature difference.

The structure of the IIR unit with separate reactive and non-reactive zones is clearly visible in the temperature profile of the last two sections. Since the methane concentration decreases along a stream line, the reaction rate and with it the heat sink decreases as well. Thus, the constant temperature of the top and bottom sheets results in a rise of the gas temperature along the flow path.

2.2.4.2. Methane Concentration

The simulated methane mole fraction is displayed in Fig. 2.15. Similar to the temperature profile, the methane mole fraction starts to change at the first contact of the gas with the reactive zones, *i. e.* in the top right corner at the first catalyst pellets. The funnel-shaped concentration profiles observed in the detailed model can also be found in the simulation of the entire IIR unit. Especially in sections III and IV, the mole fraction of methane decreases almost linearly. This corresponds to the observed temperature distribution in the IIR unit. Following the gas flow, the chemical equilibrium is nearly reached at the gas outlet taking into account the average gas temperature at this point.

As shown in the discussion of the simulation results for the detailed models, the structure of this reactor results in a limitation of the reaction rates by the mass transfer to and from the surface of the catalyst pellets and not in a limitation by the catalyst activity. Only at the first few pellets, an influence of the reaction kinetics is visible (see Fig. 2.6 and Fig. 2.8). A deactivation of the first catalyst pellets will only result in a small shift of the profiles towards the following catalyst pellets, but it will not significantly alter the temperature profile along the rest of the reactor. Thus, a temporally stable temperature profile for the neighbouring fuel cells will still be provided.

2.2.5. Summary

Using the geometry of the IIR unit used in the MCFC system HOTMODULE as example for a zone model, the concentration and temperature profiles were computed. The reactive and non-reactive zones are considered in this model and they are clearly visible in the simulation results. The results show a reduction of the temperature in the IIR unit due to the endothermic reforming process. Thus, the IIR unit acts as cooling devices for the neighbouring fuel cell in the stack.
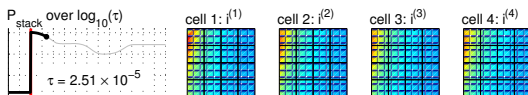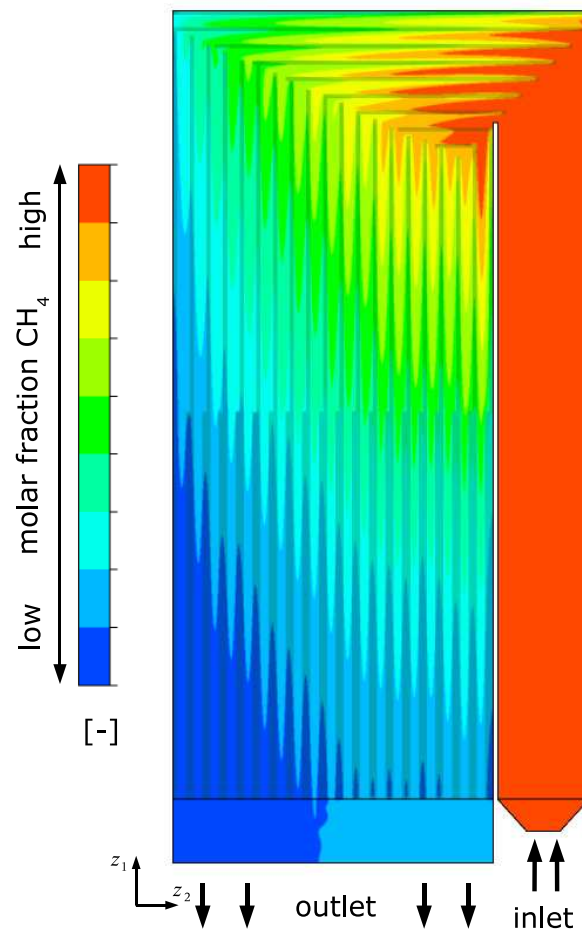
Figure 2.15.: Methane mole fraction in the model of the entire IIR unit. The mole fraction of methane is continuously reduced. The reactive and non-reactive zones in the IIR unit are clearly distinguishable.

2.3 The Phase Model

Although the zone model allows the simulation of a complete IIR unit, it is still too complex to be incorporated in a system model of a fuel cell stack. Thus, an additional reduction step is necessary (see Fig. 2.1c). In this third level of the modelling hierarchy, the essential characteristics of this structured reactor, the mass transport limitation of the reforming process, must be preserved. The complexity of the model equations is reduced using a mathematically motivated approach.
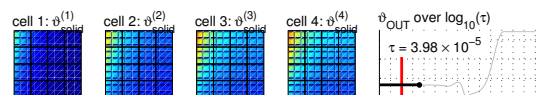
2.3.1. Geometry and Assumptions

The aim of model reduction is a representation of the zone model (Section 2.2) which is compatible to the existing fuel cell model with regard to complexity and fundamental assumptions such as:

- Ideal gas behaviour.

- Isobaric conditions.

- The heat capacity of the gas mixture depends only on its composition, but not on temperature [18]. The heat capacities of the pure components are calculated at a reference temperature of $T^r = 600\,°C$ corresponding to a dimensionless temperature of $\vartheta^r = 2.93$. This temperature represents the operating temperature of an MCFC and is, thus, chosen as linearisation point for the calculation of the thermodynamic values. A detailed description of this assumption can be found in Appendix A.2

Additional assumptions, especially with respect to the geometric structure of the IIR unit, are needed for the model reduction:

- In the zone model, the feed gas enters the IIR units in the lower right corner and it is redirected several times (see the scheme of the zone model in Fig. 2.13). Considering the absence of catalyst pellets in section I of the reactor and the small size of section II, the structure of the reactor is approximated by an unidirectional gas flow direction from the top towards the outlet at the bottom (negative z_1-direction).

- The contribution of molecular and turbulence diffusion to the mass transport in the main flow direction is small compared to convective mass transport and, thus, can be neglected. With respect to mass transport across the interface between the non-reactive and the reactive zone, the turbulent and molecular contributions are lumped to one diffusive mass transport term.

- The detailed simulations have shown that gas velocities in the reactive zone close to the catalyst pellets are at least one order of magnitude lower than the velocities in the non-reactive zone. Therefore, its contribution to the total mass transport is small compared to the convective mass transport in the non-reactive zone. Thus, a stagnant gas phase is assumed in the reactive zone.

- All gradients of state variables in z_3-direction are small compared to the gradients in flow direction and, thus, can be neglected.

Two steps are applied to reduce the complexity of the model. In the first step, the assumption of negligible gradients along the channel height is used to create an intermediate zone model in terms of two spatial dimensions only. After that, integration over the width of one half combination of a non-reactive zone and a reactive zone is performed. This results in an averaged representation of the non-reactive zone and the reactive zone as continuous phases in the entire area of the IIR unit. Since
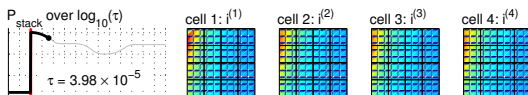
the existing fuel cell model is formulated in terms of dimensionless quantities, the reduced IIR model is converted in a dimensionless form afterwards (Fig. 2.16).
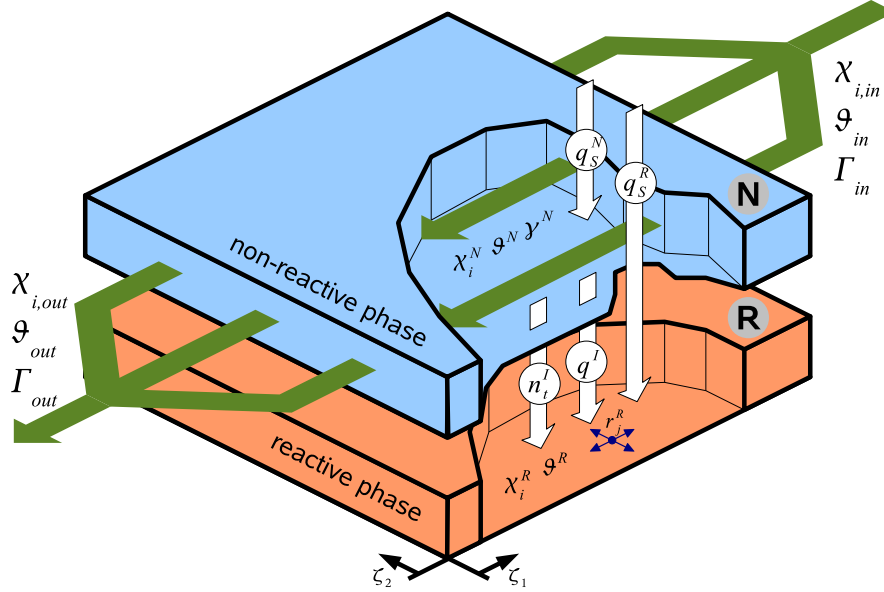
Figure 2.16.: Structure of the phase model consisting of the reactive phase (orange, index R) and the non-reactive phase (blue, index N). The heat and mass fluxes at the interface between both phases are marked by the upper index I.

2.3.2. Derivation of the Reduced Model

Fig. 2.17 shows the basic structure of the zone model. The model is divided into two parts: the non-reactive zone and the reactive zone with the catalyst pellets (see Section 2.2). In the zone model, these catalyst pellets are considered a part of the reactive zone. But in the phase model, the volume of the pellets is separated from the non-reactive zone to account for the reduced volume. The width b corresponds to the width of the four rows formed by the corrugated sheets. Thus b equals the width used in the detailed models. Considering an allocation of a single row with catalyst pellets, the non-reactive zone spans three rows of empty cages and one row filled with catalyst pellets represents the reactive zone. Due to the symmetry it is sufficient to consider only one half of this width for the derivation of the governing equations as indicated in Fig. 2.17.

In the MCFC stack used in the fuel cell system HOTMODULE, one IIR unit delivers gases for 8 fuel cells. In order to be able to easily change this ratio, one eighth of the IIR unit's height is considered as a basic height corresponding to one cell, $d^{(1\,cell)}$.
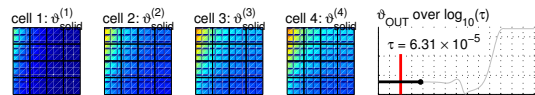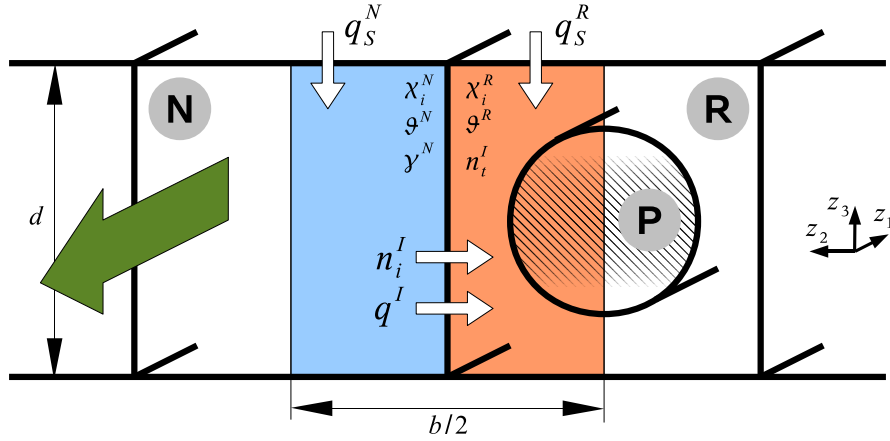
Figure 2.17.: Basic structure of the zone model of the IIR unit with the reactive zone (index R), the non-reactive zone (index N), the interface between these two zones (index I) and the catalyst pellets (index P).

Depending on the number of cells per IIR unit, n_{cells}, the height of the IIR unit, d, is scaled according to:

$$d = n_{cells}\, d^{(1\,cell)} \tag{2.37}$$

Using the partial mass balance in the non-reactive phase as an example, the procedure for the model reduction is explained in detail in the next section.

2.3.2.1. Component Mass Balances of the Non-reactive Phase

The general three-dimensional component mass balances in the IIR unit using dimensional quantities is given by:

$$\frac{\partial c_i}{\partial t} = -\nabla \cdot (\mathbf{u}\, c_i) - \nabla \widetilde{n}_{i,diff} \tag{2.38}$$

The term on the left hand side describes the mass accumulation, while the two terms on the right hand side account for convective and diffusive mass transport, respectively. The tilde for the molar diffusion fluxes, $\widetilde{n}_{i,diff}$, indicates that this is a dimensional quantity. Mass transport due to turbulence is included in the diffusive mass flux term.

In the first step, the assumption of negligible gradients in z_3-direction of the IIR gas phases is applied. Thus, the component mass balances are reduced to two dimensions:

$$\frac{\partial \hat{c}_i}{\partial t} = -\frac{\partial}{\partial z_1}\left(\hat{u}_1\, \hat{c}_i\right) - \frac{\partial}{\partial z_2}\left(\hat{u}_2\, \hat{c}_i\right) - \frac{\partial \hat{\widetilde{n}}_{i,diff,1}}{\partial z_1} - \frac{\partial \hat{\widetilde{n}}_{i,diff,2}}{\partial z_2} \tag{2.39}$$
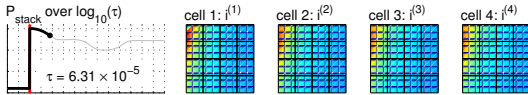
with the z_3-averaged variables for the concentrations, $\hat{c}_i$, the velocities $\hat{u}$, and the molar diffusion fluxes, $\hat{\tilde{n}}_{i,diff}$.

Fig. 2.18 presents the intermediate structure of the two-dimensional model after the integration over the z_3-coordinate. The figure shows one half width of the non-reactive zone and the reactive zone, *e. g.* a width of $\Delta z_2 = {}^b/2$. The reactive zone includes the catalysts pellets, which are completely surrounded by this zone and are depicted as dead volume in which no reaction or transport occurs. The width of these zones changes along the flow direction if the allocation of catalyst pellets changes. On the right hand side as well as on the left hand side, symmetric boundary conditions are applied, while heat and mass transport are considered at the interface between the non-reactive and reactive zones.
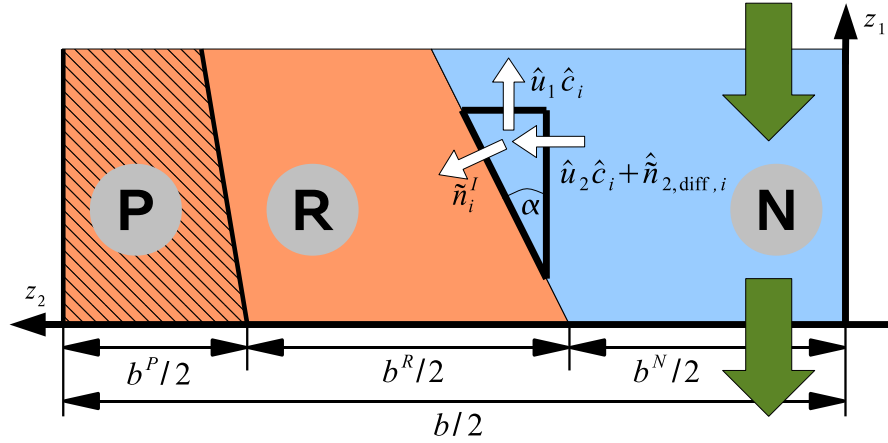
Figure 2.18.: Two-dimensional representation of the zone model as an intermediate step of model reduction.

The volume fractions of the non-reactive zone, of the reactive zone and of the catalyst pellets sum up to unity:

$$1 = \varepsilon^N + \varepsilon^R + \varepsilon^P \tag{2.40}$$

They are defined as the ratios between the width of the corresponding zones and the total width:

$$\varepsilon^P = \frac{b^P/2}{b/2} \, , \qquad\qquad \varepsilon^R = \frac{b^R/2}{b/2} \, , \qquad\qquad \varepsilon^N = \frac{b^N/2}{b/2} \tag{2.41}$$

The component mass balances of the non-reactive zone, Eq. (2.39), is further simplified. As stated above, the diffusive flux in the main flow direction, z_1, is assumed to be small compared to the convective flux in this direction and, thus, can be neglected.
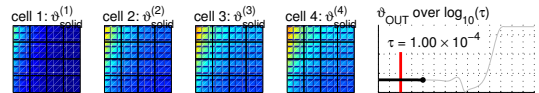
Therefore, the mass balance equations in the non-reactive zone ($0 \leq z_2 \leq {}^{b^N}/2$) can be written as:

$$\frac{\partial \hat{c}_i}{\partial t} = -\frac{\partial}{\partial z_1}\left(\hat{u}_1\,\hat{c}_i\right) - \frac{\partial}{\partial z_2}\left(\hat{u}_2\,\hat{c}_i + \hat{\tilde{n}}_{i,diff,2}\right) \tag{2.42}$$

In the second step, Eq. (2.42) is integrated over the width of the non-reactive zone, creating a homogenised gas phase for this zone with respect to the z_2-coordinate.

$$\int_0^{b^N/2} \frac{\partial \hat{c}_i}{\partial t}\,\mathrm{d}z_2 = -\int_0^{b^N/2} \frac{\partial}{\partial z_1}\left(\hat{u}_1\,\hat{c}_i\right)\mathrm{d}z_2 - \int_0^{b^N/2} \frac{\partial}{\partial z_2}\left(\hat{u}_2\,\hat{c}_i + \hat{\tilde{n}}_{i,diff,2}\right)\mathrm{d}z_2 \tag{2.43}$$

For the evaluation of the integrals in Eq. (2.43), profile assumptions are made. Since changes in z_2-direction are considered negligible compared to changes along the main direction of the flow, z_1, the concentrations, $\hat{c}_i$, and the component molar mass flux density in the non-reactive zone, $\hat{u}_1\,\hat{c}_i$, are assumed to be constant with regard to z_2.

$$\hat{c}_i(z_1, z_2) = c_i^N(z_1) \tag{2.44}$$

$$\hat{u}_1(z_1, z_2)\,\hat{c}_i(z_1, z_2) = u_1^N(z_1)\,c_i^N(z_1) = g_i^N(z_1) \tag{2.45}$$

Inserting these profile assumptions in the accumulation term as well as the convection term in z_2-direction of Eq. (2.43) yields:

$$\frac{b^N}{2}\frac{\partial c_i^N}{\partial t} = -\frac{b^N}{2}\frac{\partial g_i^N}{\partial z_1} - \left[\hat{u}_2\,c_i^N + \hat{\tilde{n}}_{i,diff,2}\right]_{z_2=0}^{z_2=b^N/2} \tag{2.46}$$

According to the symmetry condition at $z_2 = 0$, the convective and the diffusive terms become zero at that point:

$$\hat{\tilde{n}}_{i,diff,2}\Big|_{z_2=0} = 0 \tag{2.47}$$

$$\hat{u}_2\,c_i^N\Big|_{z_2=0} = 0 \tag{2.48}$$

At the right boundary of the integral, $z_2 = {}^{b^N}/2$, the balance of the molar mass fluxes at the interface between the reactive and the non-reactive zone is defined as (see Fig. 2.18):

$$0 = -\tilde{n}_i^I - \left[g_i^N\right]_{z_2=b^N/2} \times \sin\alpha + \left[\hat{u}_2\,c_i^N + \hat{\tilde{n}}_{i,diff,2}\right]_{z_2=b^N/2} \times \cos\alpha \tag{2.49}$$

with the first term describing the molar mass flux across the interface and the last two terms account for the molar mass flux in the z_1- and z_2-directions, respectively.
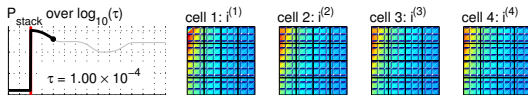
After reordering and inserting the profile assumptions (Eqs. (2.44) and (2.45)), the molar mass flux in z_2-direction at the phase interface can be expressed as:

$$\left[\hat{u}_2\, c_i^N + \hat{\tilde{n}}_{i,diff,2}\right]_{z_2=b^N/2} = \left[g_i^N\right]_{z_2=b^N/2} \times \frac{\sin\alpha}{\cos\alpha} + \frac{\tilde{n}_i^I}{\cos\alpha}$$

$$= \left[g_i^N\right]_{z_2=b^N/2} \times \frac{\partial b^N/2}{\partial z_1} + \frac{\tilde{n}_i^I}{\cos\alpha} \tag{2.50}$$

with the derivative of the width of the non-reactive phase with respect to the z_1-coordinate given by

$$\frac{\partial b^N/2}{\partial z_1} = \frac{\sin\alpha}{\cos\alpha} \tag{2.51}$$

Inserting the expressions for the right boundary (Eqs. (2.47) and (2.48)) and the left boundary (Eq. (2.50)) of the integral into Eq. (2.46) results in:

$$\frac{b^N}{2}\frac{\partial c_i^N}{\partial t} = -\frac{b^N}{2}\frac{\partial g_i^N}{\partial z_1} - g_i^N\frac{\partial\left(b^N/2\right)}{\partial z_1} - \frac{\tilde{n}_i^I}{\cos\alpha} \tag{2.52}$$

where the last term on the right hand side accounts for the molar mass flux across the interface. As the phase interface is perpendicular to the molar mass flux at the interface, $\tilde{n}_i^I$, i.e. the angle α is zero, the denominator of this term is approximately one. Thus, it can be removed from the equation.

Using the product rule of differentiation to combine the first two terms on the right hand side and inserting the volume fraction, ε^N (Eq. (2.41)), the final equation for the component mass balances in the non-reactive phase reads:

$$\varepsilon^N\frac{\partial c_i^N}{\partial t} = -\frac{\partial}{\partial z_1}\left(\varepsilon^N g_i^N\right) - \frac{2}{b}\tilde{n}_i^I \tag{2.53}$$

The total mass balance of the non-reactive phase is defined as the sum over all component mass balances (Eq. (2.53)):

$$\varepsilon^N\frac{\partial c_t^N}{\partial t} = -\frac{\partial}{\partial z_1}\left(\varepsilon^N g^N\right) - \frac{2}{b}\tilde{n}_t^I \tag{2.54}$$

with the total concentration $c_t = \sum_i c_i$, the total molar mass flux density $g^N = \sum_i g_i^N$ and the total molar mass flux density across the interface $\tilde{n}_t^I = \sum_i \tilde{n}_i^I$.

At steady state, Eq. (2.54) yields the total molar mass flux density in the non-reactive phase. If the allocation of catalyst pellets is changed, the width of the non-reactive phase and, therefore, its volume fraction is increased or decreased in a discrete step. Due to the discrete nature of the change, it does not result in a flux across the phase interface but in a corresponding change of the total molar mass flux density g^N.
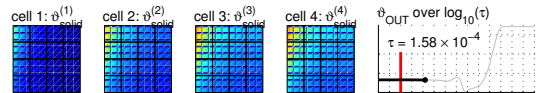
A description of the gas composition in terms of mole fractions is desired for the dimensionless formulation of the equation. The definition of the mole fraction is:

$$x_i = \frac{c_i}{c_t} \tag{2.55}$$

and the derivative of the mole fraction with respect to time reads:

$$\begin{aligned}
\frac{\partial x_i}{\partial t} = \frac{\partial}{\partial t}\left(\frac{c_i}{c_t}\right) = \ldots &= \frac{1}{c_t}\frac{\partial c_i}{\partial t} - \frac{c_i}{c_t^2}\frac{\partial c_t}{\partial t} \\
&= \frac{1}{c_t}\frac{\partial c_i}{\partial t} - \frac{x_i}{c_t}\frac{\partial c_t}{\partial t}
\end{aligned} \tag{2.56}$$

Inserting the equations for the component and the total mass balances (Eqs. (2.53) and (2.54)) yields a partial differential equation for the mole fraction in the non-reactive phase:

$$\varepsilon^N c_t^N \frac{\partial x_i^N}{\partial t} = -\varepsilon^N g^N \frac{\partial x_i^N}{\partial z_1} - \frac{2}{b}\left(\widetilde{n}_i^I - x_i^N \widetilde{n}_t^I\right) \tag{2.57}$$

After re-grouping of suitable variables to dimensionless parameters (see Appendix A.1.1), the resulting dimensionless equation reads:

$$n_{cells}\,\varepsilon^N\,V^{(1\,cell)}\frac{1}{\vartheta^N}\frac{\partial \chi_i^N}{\partial \tau} = -\varepsilon^N \gamma^N \frac{\partial \chi_i^N}{\partial \zeta_1} - \left(n_i^I - \chi_i^N n_t^I\right) \tag{2.58}$$

where n_{cells} is the number of fuel cells per IIR unit (see Eq. (2.37)).

The term on the left hand side of Eq. (2.58) describes the accumulation of species i while the two terms on the right hand side account for the convective mass transport and the mass transport across the interface.

2.3.2.2. Component Mass Balances of the Reactive Phase

For the reactive phase, the reforming reactions are added to Eq. (2.39). Furthermore, the gas is assumed to be stagnant in this phase with respect to the direction z_1. The resulting component mass balances for this phase reads:

$$\frac{\partial \hat{c}_i}{\partial t} = -\frac{\partial}{\partial z_2}\left(\hat{u}_2\,\hat{c}_i + \hat{\widetilde{n}}_{i,diff,2}\right) + \sum_j v_{i,j}\,\hat{\widetilde{r}}_j\left(\hat{c}_i, \hat{T}\right) \tag{2.59}$$
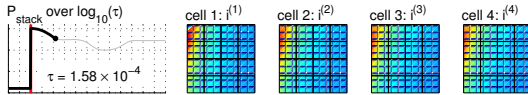
Using a similar algorithm as for the derivation of the equation for the component
mass balances of the non-reactive phase, the component mass balance of the reactive
phase is derived as:

$$\varepsilon^R \frac{\partial c_i^R}{\partial t} = \frac{2}{b}\, \widetilde{n}_i^I + \sum_j \nu_{i,j}\, \widetilde{r}_j^R \tag{2.60}$$

The summation over all species i yields the total mass balance of the non-reactive
phase (Eq. (2.60)):

$$\varepsilon^R \frac{\partial c_t^R}{\partial t} = \frac{2}{b}\, \widetilde{n}_t^I + \sum_j \overline{\nu}_j\, \widetilde{r}_j^R \tag{2.61}$$

Inserting Eqs. (2.60) and (2.61) into Eq. (2.56) results in an equation for the mole
fractions in the reactive phase:

$$\varepsilon^R c_t^R \frac{\partial x_i^R}{\partial t} = \frac{2}{b}\left(\widetilde{n}_i^I - x_i^R\, \widetilde{n}_t^I \right) + \varepsilon^R \sum_{j=\mathrm{ref}} \left(\nu_{i,j} - x_i^R\, \overline{\nu}_j \right) \widetilde{r}_j^R \tag{2.62}$$

In Eq. (2.62), the mass accumulation in the reactive phase is accounted for in the
term on the left hand side. The two terms on the right hand side consider the mass
transport across the interface as well as the concentration change due to chemical
reactions, $i.\,e.$ the methane steam reforming (ref1) and the water gas shift reaction
(ref2).

After reordering and grouping of variables (see Appendix A.1.2), the final dimension-
less equation is given by

$$n_{cells}\, \varepsilon^R\, V^{(1\,cell)} \frac{1}{\vartheta^R}\, \frac{\partial \chi_i^R}{\partial \tau} = \left(n_i^I - \chi_i^R\, n_l^I \right) + \varepsilon^R \sum_{j=\mathrm{ref}} \left(\nu_{i,j} - \chi_i^R\, \overline{\nu}_j \right) n_{cells}\, Da_j^{(1\,cell)}\, r_j \tag{2.63}$$

Similar to the basic volume of the IIR unit, $V^{(1\,cell)}$, the Damköhler numbers, $Da_j^{(1\,cell)}$,
are scaled with the theoretical height of the IIR unit for one fuel cell, $d^{(1\,cell)}$. There-
fore, these parameters are multiplied with the number of fuel cells per IIR unit, n_{cells}
(see Eq. (2.37)).

2.3.2.3.   Enthalpy Balance of the Non-reactive Phase

The equation for the enthalpy balance of the non-reactive phase can be derived anal-
ogously to the equation for the component mass balances (Eq. (2.58)). After the
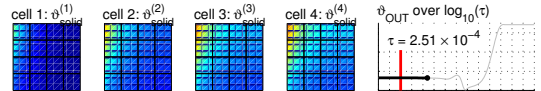
integration step and the conversion to a dimensionless form, the energy balance of the non-reactive phase reads:

$$\varepsilon^N \, n_{cells} \, V^{(1\,cell)} \frac{\overline{c}_P^N}{\vartheta^N} \frac{\partial \vartheta^N}{\partial \tau} = -\varepsilon^N \, \overline{c}_P^N \, \gamma^N \frac{\partial \vartheta^N}{\partial \zeta_1}$$

$$+ \left(\sum_i n_i^{I-} \, c_{P\,i} \right) \times \left(\vartheta^N - \vartheta^R \right) - q^I + \varepsilon^N \, q_S^N \qquad (2.64)$$

The term on the left hand side accounts for local temperature changes while the first term on the right hand side describes the convective enthalpy transport. The other terms describes the energy fluxes due to mass transport across the interface, heat flux density across the interface, q^I, and heat flux density with the neighbouring fuel cells, q_S^N, which is weighted by the corresponding heat exchange area fraction, ε^N.

2.3.2.4. Enthalpy Balance of the Reactive Phase

The dimensionless equation for the enthalpy balance of the reactive phase is similar to the corresponding equation of the non-reactive phase:

$$n_{cells} \, \varepsilon^R \, V^{(1\,cell)} \frac{\overline{c}_P^R}{\vartheta^R} \frac{\partial \vartheta^R}{\partial \tau} = \left(\sum_i n_i^{I+} \, c_{P\,i} \right) \times \left(\vartheta^N - \vartheta^R \right) + q^I$$

$$+ \varepsilon^R \sum_{j=\text{ref}} \left(-\Delta_R h_j^\theta (\vartheta^R) \right) n_{cells} \, Da_j^{(1\,cell)} \, r_j$$

$$+ \left(\varepsilon^R + \varepsilon^P \right) q_S^R \qquad (2.65)$$

Due to the assumption of a stagnant reactive gas phase, the convective term is missing and a term for the heat released by the chemical reactions appears on the right hand side. The heat flux from the reactive phase to the solid phase of the neighbouring fuel cell is given by q_S^R. The exchange area is calculated from the volumetric ratios of the reactive phase and the enclosed catalyst pellets, $(\varepsilon^R + \varepsilon^P)$.

2.3.2.5. Total Mass Balance of the Non-reactive Phase

According to the ideal gas law, the total concentration must adhere to:

$$c_t = \frac{n}{V} = \frac{p}{R \, T} \qquad (2.66)$$

With the gas constant R and the assumption of constant pressure (see Section 2.3.1), the derivative with respect to time reads:

$$\frac{\partial c_t}{\partial t} = \frac{p}{R} \frac{\partial T^{-1}}{\partial t} = -\frac{p}{R \, T^2} \frac{\partial T}{\partial t} = -\frac{c_t}{T} \frac{\partial T}{\partial t} \qquad (2.67)$$
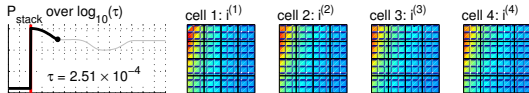
The total mass balance and the energy balance in temperature form (Eqs. (2.54) and (2.64)) are inserted into this equation. After some manipulations, the result is an ordinary differential equation in z_1-direction, which allows the calculation of the molar mass flux density, g^N, in the non-reactive phase of the IIR unit:

$$0 = -\frac{\partial}{\partial z_1}\left(\varepsilon^N g^N T^N\right)$$
$$+ \frac{1}{\overline{c}_P^N}\left(\frac{2}{b}\left(\sum_i\left(\tilde{n}_i^{I-}c_{P_i}\right)\times\left(T^N - T^R\right) - \tilde{q}^I\right) + \varepsilon^N \frac{\tilde{q}_S^N}{d}\right) - T^N\frac{2}{b}\tilde{n}_t^I \qquad (2.68)$$

The conversion of Eq. (2.68) to the dimensionless form yields

$$0 = -\frac{\partial}{\partial \zeta_1}\left(\varepsilon^N \gamma^N \vartheta^N\right)$$
$$+ \frac{1}{\overline{c}_P^N}\times\left(\sum_i\left(n_i^{I-}c_{P_i}\right)\times\left(\vartheta^N - \vartheta^R\right) - q^I + \varepsilon^N q_S^N\right) - \vartheta^N n_t^I \qquad (2.69)$$

2.3.2.6.   Total Mass Balance of the Reactive Phase

No convective flow is considered in the reactive phase of the IIR unit. Thus, the equation for the ideal gas law does not result in a partial differential equation describing the molar mass flux density but in an algebraic equation for the total molar mass flux across the interface, n_t^I. The equation is derived using an approach similar to the derivation of the corresponding equation in the non-reactive phase (Eq. (2.69)). The total concentration of the non-reactive phase, Eq. (2.61), and the enthalpy balance in temperature form for this phase, Eq. (2.65), are inserted into the derivation of the ideal gas law with respect to time (Eq. (2.67)).

$$n_t^I + \varepsilon^R \sum_{j=\text{ref}} \overline{\nu}_j\, n_{cells}\, Da_j^{(1\,cell)}\, r_j =$$
$$-\frac{1}{\vartheta^R\,\overline{c}_P^R}\times\left[\left(\sum_i n_i^{I+} c_{P_i}\right)\times\left(\vartheta^N - \vartheta^R\right) + q^I\right.$$
$$\left. + \varepsilon^R \sum_{j=\text{ref}}\left(-\Delta_R h_j^0\left(\vartheta^R\right)\right) n_{cells}\, Da_j^{(1\,cell)}\, r_j + \left(\varepsilon^R + \varepsilon^P\right) q_S^R\right] \qquad (2.70)$$

Eq. 2.70 states that the change in mole numbers due to the reforming process has to compensate the expansion effect in the reactive phase due to dynamic temperature changes. At steady state, the term on the right hand side, which represents the derivative of the temperature with respect to time, equals zero.
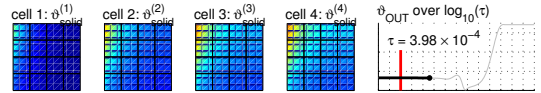
2.3.3. Heat and Mass Transport

2.3.3.1. Mass Transport

In Figure 2.16, the heat and mass flux densities between both phases of the IIR unit (n_i^I and q^I) as well as the heat transport between these gas phases and the solid phase of the neighbouring fuel cell (q_S^R and q_S^N) are indicated. Among these variables, the mass flux density across the interface requires detailed consideration. As described in the derivation of the component mass balances in the non-reactive phase (Section 2.3.2.1), the overall component molar mass flux, n_i^I, is composed of the convective and the diffusive mass transport at the interface (see Fig. 2.18):

$$n_i^I = n_{i,conv}^I + n_{i,diff}^I \tag{2.71}$$

The sum of Eq. (2.71) over all considered species results in an equation for the total molar mass flux across the phase interface, n_t^I.

$$n_t^I = n_{t,conv}^I + n_{t,diff}^I \tag{2.72}$$

Note that the sum of the diffusive component molar mass fluxes is not equal to zero due to the fact that molar mass fluxes are used.

The kinetics of the diffusive molar mass transport across the interface, $n_{i,diff}^I$, is described by a linear law:

$$n_{i,diff}^I = n_{cells}\, D_i^{I,(1\,cell)} \times \left(\chi_i^N - \chi_i^R \right) \tag{2.73}$$

with $D_i^{I,(1\,cell)}$ as the mass transport coefficient at the interface considering the height of one representative IIR unit corresponding to one fuel cell. It is scaled to the number of fuel cells used in the stack model by the factor n_{cells}.

The convective component flux of species i across the interface, $n_{i,conv}^I$, is calculated from the total convective flux, $n_{t,conv}^I$, taking into account an average mole fraction of species i at the interface, χ_i^I:

$$n_{i,conv}^I = n_{t,conv}^I \chi_i^I \qquad \text{with} \qquad \chi_i^I = \frac{\chi_i^N + \chi_i^R}{2} \tag{2.74}$$

The following expressions are used in the enthalpy balance equations of the non-reactive and reactive phase (Eqs. (2.64) and (2.65)) to distinguish the direction of the molar mass fluxes:

$$n_i^{I+} = \begin{cases} n_i^I \text{ , if } n_i^I > 0 \\ 0 \text{ , if } n_i^I \le 0 \end{cases} , \qquad n_i^{I-} = \begin{cases} 0 \text{ , if } n_i^I > 0 \\ n_i^I \text{ , if } n_i^I \le 0 \end{cases} \tag{2.75}$$
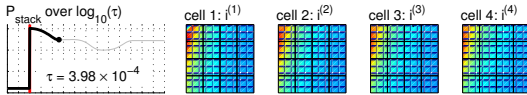
2.3.3.2. Heat Transport

Linear approaches are used for the heat flux between the non-reactive phase and the reactive phase as well as for the heat fluxes between both gas phases and the solid phase of the neighbouring fuel cell:

$$q^I = n_{cells}\, St^{I,(1\,cell)} \times \left(\vartheta^N - \vartheta^R\right) \tag{2.76}$$

$$q_S^N = St_S^N \times \left(\vartheta_S^{(1)} - \vartheta^N\right) \tag{2.77}$$

$$q_S^R = St_S^R \times \left(\vartheta_S^{(1)} - \vartheta^R\right) \tag{2.78}$$

with $St^{I,(1\,cell)}$, St_S^N and St_S^R as the dimensionless heat transfer coefficients of the corresponding heat fluxes, ϑ^N and ϑ^R as the dimensionless temperatures in the non-reactive and the reactive phase and $\vartheta_S^{(1)}$ as the temperature in the solid phase of the neighbouring fuel cell. Similar to the mass transport coefficients, the Stanton number, $St^{I,(1\,cell)}$, has to be scaled by n_{cells} to take into account the dependency of the size of the IIR unit on the number of fuel cells considered in the model.

2.3.4. Reaction Kinetics

Two reactions are considered in the reactive phase: the methane steam reforming reaction (ref1) and the water gas shift reaction (ref2). Power law kinetics are applied to describe their reaction rates [22]:

$$r_{ref1} = \exp\left[Arr_{ref1} \times \left(\frac{1}{\vartheta^r} - \frac{1}{\vartheta^R}\right)\right] \times$$
$$\left(\chi_{CH_4}^R\, \chi_{H_2O}^R - \frac{1}{K_{ref1}\left(\vartheta^R\right)}\, \chi_{CO}^R \left(\chi_{H_2}^R\right)^3\right) \tag{2.79}$$

$$r_{ref2} = \exp\left[Arr_{ref2} \times \left(\frac{1}{\vartheta^r} - \frac{1}{\vartheta^R}\right)\right] \times$$
$$\left(\chi_{CO}^R\, \chi_{H_2O}^R - \frac{1}{K_{ref2}\left(\vartheta^R\right)}\, \chi_{CO_2}^R\, \chi_{H_2}^R\right) \tag{2.80}$$

In analogy to the equations used in the anode channels of the fuel cell model [23], these equations contain an Arrhenius term. Thus, all reaction kinetics in the later symmetric stack model follow a similar structure. Furthermore, this allows not only the description of a mass transport limitation but also the description of load change scenarios where a temperature dependency of the reactions has to be considered.
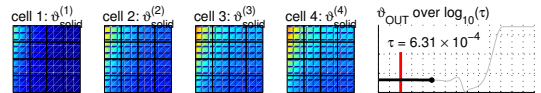
The equilibrium constants of both reactions are calculated according to:

$$K_j \left(\vartheta^R \right) = \exp \left(- \frac{\Delta_R g_j^\theta \left(\vartheta^R \right)}{\vartheta^R} \right) \tag{2.81}$$

with the standard Gibbs enthalpies of the reactions, $\Delta_R g_j^\theta$, which is calculated as described in Appendix A.2.

2.3.5. Boundary Conditions

The boundary conditions needed for the partial differential equations of the non-reactive phase correspond to the inlet conditions of the IIR unit (see Fig. 2.16). Note that the geometry of the IIR unit is simplified (Section 2.3.1). Thus, the flow direction in the IIR unit is in negative ζ_1-direction and the inlet is located at $\zeta_1 = 1$. The mole fraction, χ_i^N, and the temperature, ϑ^N, are defined at this boundary. The volume ratio of the non-reactive phase, ε^N, is considered for the inlet molar mass flux density, γ^N, in order to take into account the reduced cross-sectional area for the convective flux.

$$\chi_i^N \left(\zeta_1 = 1, \zeta_2, \tau \right) = \chi_{i,IIR,in} \left(\tau \right) \tag{2.82}$$

$$\vartheta^N \left(\zeta_1 = 1, \zeta_2, \tau \right) = \vartheta_{IIR,in} \left(\tau \right) \tag{2.83}$$

$$\gamma^N \left(\zeta_1 = 1, \zeta_2, \tau \right) = \frac{\Gamma_{IIR,in}}{\varepsilon^N} \left(\tau \right) \tag{2.84}$$

No boundary conditions are required for the equations in the reactive phase due to the fact that they do not include a convective term. Thus, they represent ODEs which are solved at each spatial point in the IIR unit.

2.3.6. Parameters of the Phase Model

The phase model includes several parameters which have to be determined. A direct measurement of these parameters is not possible due to the high temperature, the complex structure and the multiple interactions in the fuel cell stack. But some parameters, like the volume fractions ε, the dimensionless mass transport coefficients, $D_i^{I,(1\,cell)}$, and the heat transfer coefficient, $St^{I,(1\,cell)}$, can be estimated using simulation results obtained from the detailed models. The methods used for the estimation are presented in the following. Other parameters, such as the Stanton numbers St_S^N and St_S^R, which quantify the heat transfer intensity between the gas phases and the solid phase of the neighbouring fuel cell, are estimated using the results of Gundermann *et al.* [20].
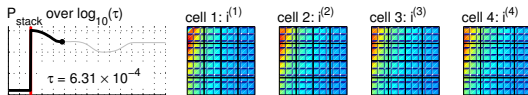
2.3.6.1. Estimation of the Volume Fractions

The exact three-dimensional structure of the IIR unit as it is used in the detailed model is shown in the top left part of Fig. 2.19. The volume of one block with four cages for catalyst pellets formed by the corrugated sheets is indicated by the blue and orange colours. Of the four cages, one is filled with a catalyst pellet. According to the zone model, the block can be divided into the volume of the non-reactive zone (blue; index N) and the volume of the reactive zone (orange; index R) which encloses the catalyst pellets (red; index P). The volume of the corrugated sheets is neglected.
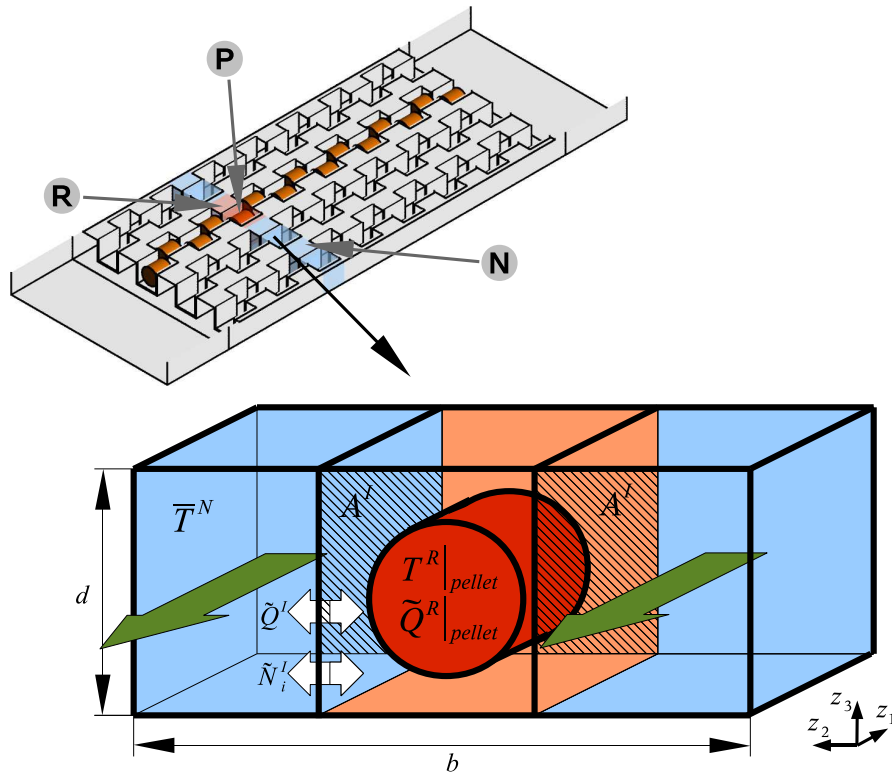
Figure 2.19.: Scheme of the detailed model used to estimate the values of the transport parameters at the interface (above). The structure of one block including one catalyst pellet is shown (below).

Considering detailed models with different allocations of catalyst pellets, the volume fractions for the two phases and the catalyst pellets can be estimated. Table 2.4 shows the resulting values for allocations of one row, two rows and three rows out of the available four rows which can be filled with catalyst pellets.

These values represent the volume fractions for the discrete allocations which are possible using the corrugated sheets. Considering an optimisation of the catalyst distribution, continuous expressions for the volume fractions are beneficial. Using the volume fraction of the non-reactive phase, ε^N, as an independent variable and
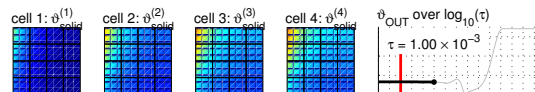
Table 2.4.: Volume fraction of the non-reactive zone, the reactive zone and the catalyst zone for different catalyst pellet allocations.

volume	rows filled with catalyst pellets		
fraction	1 of 4	2 of 4	3 of 4
ε^N	75%	50%	25%
ε^R	20%	40%	60%
ε^P	5%	10%	15%

assuming a linear correlation between the volumetric fractions, the volume fractions of the reactive phase, ε^R, and the catalyst pellets, ε^P, can be expressed as

$$\varepsilon^R = 0.8 \left(1 - \varepsilon^N \right) \tag{2.85}$$

$$\varepsilon^P = 0.2 \left(1 - \varepsilon^N \right) \tag{2.86}$$

2.3.6.2. Estimation of $St^{I,(1\,cell)}$ and $D_i^{I,(1\,cell)}$

Other important parameters for the IIR unit are the Stanton number at the interface between the non-reactive and the reactive phase, $St^{I,(1\,cell)}$, the dimensionless heat transfer coefficient between the two phases, k^I, and the mass transport coefficient between both gas phases, which is given by $\widetilde{D}_i^{I,(1\,cell)}$ or its dimensionless counter-part $D_i^{I,(1\,cell)}$. Values for these parameters can be estimated using the results of the detailed model. In the following, this procedure is exemplarily demonstrated for the Stanton number, starting with the estimation of the heat flux between both zones. To simplify the additional calculations needed for parameter estimation, only the fluid phase is considered and adiabatic boundary conditions are used, *i. e.* the heat fluxes through the top and bottom walls are set to zero (see Figure 2.7).

According to the linear heat transfer approach (Eq. (2.87)), the total heat flux across the interface, $\widetilde{Q}^I$, is given as the product of the heat transfer coefficient, k^I, the heat exchange area, $2\,A^I$, and its driving force, which is the temperature difference $(T^N - T^R)$. As shown in Fig. 2.19, the interface areas on both sides of the reactive zone have to be taken into account. The above listed variables are estimated from simulation results of the detailed model and used to identify values of k^I.

$$\widetilde{Q}^I = k^I \times 2\,A^I \left(T^N - T^R \right) \tag{2.87}$$

Because of the discontinuous geometry of the IIR unit along the main flow direction, application of the local heat flux density and the local temperature difference yields strongly varying results for k^I in this direction. Thus, the heat flux along a finite length of the interface and the average temperature difference over that length are used for the estimation. Obviously, the length of one pellet cage is a good choice as indicated in the lower scheme of Fig. 2.19.
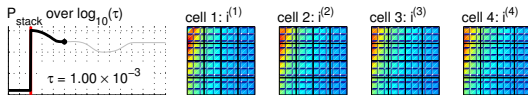
At steady state, the heat flux across the interface can be approximated by the heat flux originating at the pellet surface. This assumption is approximately fullfilled in the middle part of the detailed model (see Fig. 2.9), where the inlet and outlet effects are negligible.

$$\widetilde{Q}^I = \widetilde{Q}^R\Big|_{pellet} = \int_{A_{pellet}} \sum_{j=\mathbf{ref}} \Delta_R h_j^\theta \left(T\right) \widetilde{r}_j \, \mathrm{d}A \tag{2.88}$$

The temperature in the non-reactive zone is almost constant (see Fig. 2.9). Thus, a representative value for this phase is the average temperature in the corresponding zone of the detailed model:

$$T^N = \overline{T}^N = \frac{1}{V^N} \int_{V^N} T \, \mathrm{d}V \tag{2.89}$$

The temperature at the surface of the catalyst pellets is relevant for the reforming process. As the reactive zone is greatly influenced by these reactions, the average surface temperature of the pellets is used to represent the temperature in this zone:

$$T^R = T^R\Big|_{A_{pellet}} = \frac{1}{A_{pellet}} \int_{A_{pellet}} T \, \mathrm{d}A \tag{2.90}$$

The integrals in Eqs. (2.88) to (2.90) are obtained from the simulation results of the detailed model of the IIR unit. The values are inserted into Eq. (2.87) to estimate the heat transfer coefficient, k^I. This procedure is repeated for each block in all simulations of the detailed model.

The dimensionless heat transport coefficient between the two zones, the Stanton number $St^{I,(1\,cell)}$, is defined as:

$$St^{I,(1\,cell)} = \frac{k^I \, L_1 \, (2\,L_2\,d^{(1\,cell)})/b}{G^\theta \, c_\mathrm{p}^{\,\theta}} \tag{2.91}$$

with L_1 and L_2 as the length and the width of the fuel cell stack, $d^{(1\,cell)}$ the theoretical height of the IIR unit per fuel cell (see Eq. (2.37)), b the width of a block of four cages as shown in Fig. 2.19, and G^θ and $c_\mathrm{p}^{\,\theta}$ the characteristic gas channel flow rate and the standard heat capacity, respectively.
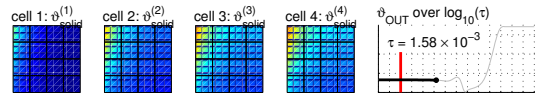
For the dimensionless mass transport coefficients, D_i^I, a similar method is applied taking into account the molar mass flux between both zones, $\widetilde{N}_i^I$, and the differences in the mole fractions, $(x_i^N - x_i^R)$.

$$\widetilde{N}_i^I = \widetilde{D}_i^I \times 2\,A^I \times \left(x_i^N - x_i^R\right) \tag{2.92}$$

$$\widetilde{N}_i^I = \left.\widetilde{N}_i^R\right|_{pellet} = \int_{A_{pellet}} \sum_{j=\mathrm{ref}} \nu_{i,j}\,\widetilde{r}_j\,\mathrm{d}A \tag{2.93}$$

$$x_i^N = \overline{x}_i^N = \frac{1}{V^N} \int_{V^N} x_i\,\mathrm{d}V \tag{2.94}$$

$$x_i^R = \left.x_i^R\right|_{pellet} = \frac{1}{A_{pellet}} \int_{A_{pellet}} x_i\,\mathrm{d}A \tag{2.95}$$

$$D_i^{I,(1\,cell)} = \frac{\widetilde{D}_i^I\,L_1\,(2\,L_2\,d^{(1\,cell)})/b}{G^\theta} \tag{2.96}$$

For the estimation of the Stanton number, $St^{I,(1\,cell)}$, and the dimensionless mass transport coefficient, $D_i^{I,(1\,cell)}$, the parameters of the detailed model are varied. On the one hand, the geometrical parameters - the volume fractions - are changed. The three allocations of catalyst pellets listed in Section 2.3.6.1 are used. On the other hand, the inlet conditions, i.e. the composition of the gas and the molar mass flux at the inlet, are varied. Representative gas concentrations close to the gas inlet, in the middle of the IIR unit and close to the gas outlet are used (Table 2.5). For the molar mass flux, a base value of $G_{\mathrm{IN}} = 1.38 \times 10^{-3}\,\mathrm{mol\,s^{-1}}$ is defined, which corresponds to the gas flow needed for 8 fuel cells and an average current density of $i_{avg} = 80\,{}^{mA}/\mathrm{cm^2}$ as used in the detailed models. Simulations are computed for 75%, 100% and 125% of this value.

Table 2.5.: Inlet gas composition used for detailed simulations applied for the parameter estimation.

location in the zone model	x_{CH_4}	x_{H_2O}	x_{H_2}	x_{CO}	x_{CO_2}
inlet	0.19	0.52	0.22	0.01	0.06
middle	0.14	0.39	0.36	0.02	0.09
outlet	0.09	0.32	0.45	0.04	0.10

Taking into account the three allocations with catalyst pellets, the three different inlet compositions for the simulations of the detailed model and the three different molar mass fluxes at the inlet, 27 different definitions of the boundary conditions are given. Furthermore, each model includes 15 blocks as shown in Fig. 2.19, for which parameter values are estimated. Exemplarily, the results for all three catalyst allocations, an inlet gas composition which corresponds to the typical gas mixture in the middle of the IIR unit and a molar mass flux of 100% are presented in Fig. 2.20.

In case of an IIR unit with each forth row filled with catalyst pellets (Fig. 2.20a), strong gradients of the calculated values for the transport parameters are visible over
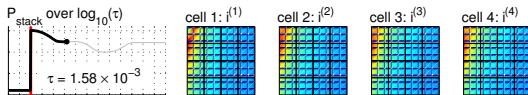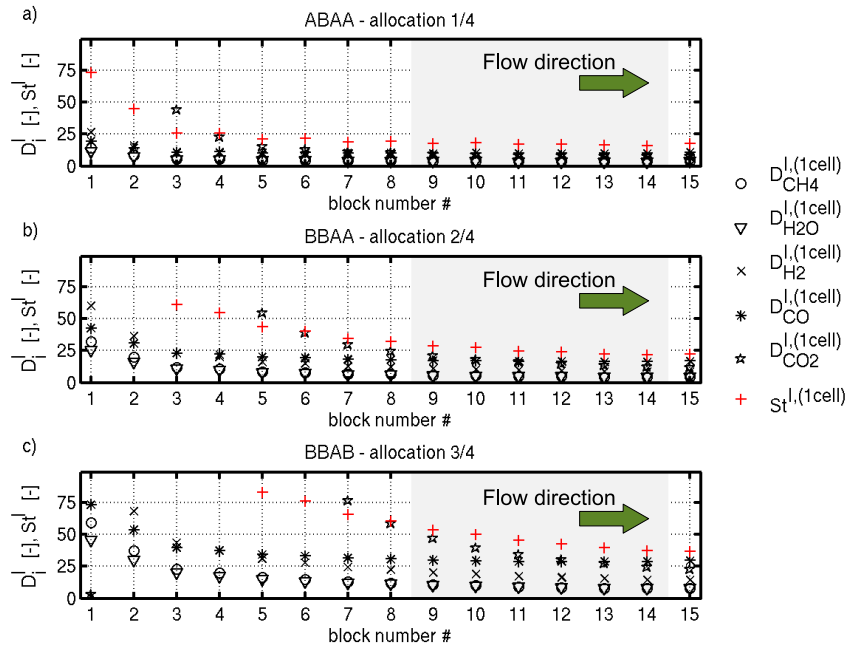
Figure 2.20.: Selected results for the dimensionless transport coefficients for an allocation of one row (a), two rows (b) and three rows (c) with catalyst pellets.

the first few pellets. The dimensionless transport parameters reach approximately constant values after the 6th pellet. At this point, the non-reactive zone and the reactive zone are fully developed. For the configuration of two out of four rows being filled with catalyst pellets (Fig. 2.20b), the inlet region is longer. A nearly constant state is reached after the 9th pellet. For an allocation of three out of four rows with catalyst pellets (Fig. 2.20c) ,the length of the detailed model is not sufficient to fully develop a repeating flow pattern. Nevertheless, for all 27 simulations, the average values of the transport parameters at the 9th to 14th pellet have been calculated and used for the parameter estimation.

A comparison of the above discussed values shows that the transport parameters are nearly independent of the considered concentration and velocity ranges. Only the catalyst allocation shows a significant influence on the transport parameters. The amount of catalyst pellets in the detailed model and therefore the volume fraction of the different phases strongly influences the transport parameters. Table 2.6 shows the average values for the dimensionless mass transport coefficients, $D_i^{I,(1\,cell)}$, and the Stanton numbers, $St^{I,(1\,cell)}$, for the considered configurations.

For the implementation of the IIR unit into the stack model, a continuous expression for the transport parameters is desirable. Assuming a linear correlation with respect
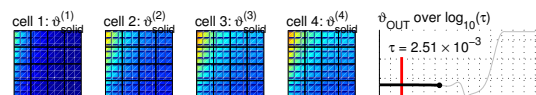
Table 2.6.: Parameter values and linearised parameters.

volume fraction	rows filled with catalyst pellets		
	1 of 4	2 of 4	3 of 4
ε^N	75%	50%	25%
$D_{CH_4}^{I,(1\,cell)}$	3.7	5.0	9.0
$D_{H_2O}^{I,(1\,cell)}$	3.4	4.8	8.8
$D_{H_2}^{I,(1\,cell)}$	7.0	9.5	17.1
$D_{CO}^{I,(1\,cell)}$	10.0	16.6	29.1
$D_{CO2}^{I,(1\,cell)}$	8.0	15.5	33.4
$St^{I,(1\,cell)}$	17.0	24.8	44.8

to the volume fraction of the non-reactive phase, the Stanton number, $St^{I,(1\,cell)}$, can be approximated by

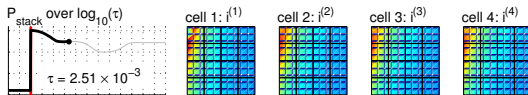$$St^{I,(1\,cell)} = 60 \left(1 - \varepsilon^N \right) \tag{2.97}$$

The dimensionless mass transport coefficient is calculated for each species, but for simplicity, one mass transport coefficient for all species is preferred. The smallest values and, thus, the strongest limitation of the mass transport are found for methane and water. Considering the mass transport limitation as the main characteristic of this reactor concept, especially the values for these two components are considered for the following linear correlation

$$D_i^{I,(1\,cell)} = 16 \left(1 - \varepsilon^N \right) \tag{2.98}$$

2.3.6.3. Validation of the Phase Model

The aim of the model hierarchy presented in this chapter is the reduction of the complexity of the model for the IIR unit of the MCFC, while preserving the mass transport limitation which is an important feature of this reactor concept. In the following, the mass transport limitation in the reduced model is analysed. For this purpose, a single full size IIR unit is simulated and the dimensionless transport parameters $D_i^{I,(1\,cell)}$ are varied to observe their influence on the methane conversion along the flow direction. Fig. 2.21 shows the methane mole fraction in both phases of the IIR unit for an allocation of one row with catalyst pellets. In the simulation, the mass transport coefficient, $D_i^{I,(1\,cell)}$, is varied between 50% and 300% of the value reported in Section 2.3.6.2.

The methane mole fractions in the non-reactive phase (N) and the reactive phase (R) show a significant sensitivity to the parameter variation (Fig. 2.21). On the one hand, if the mass transport coefficient is reduced, the transport of methane into the reactive phase is hampered and, therefore, the chemical equilibrium is not reached in the non-
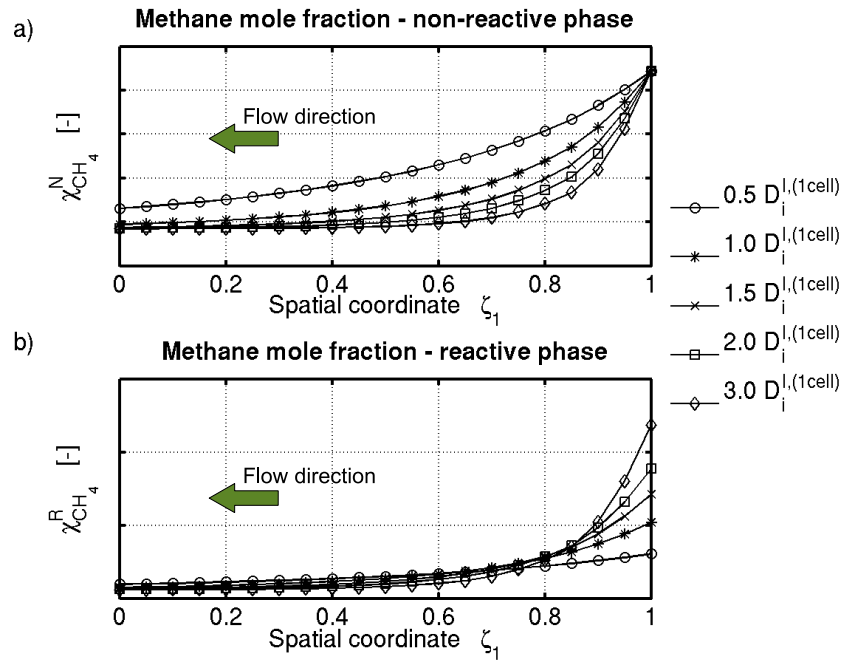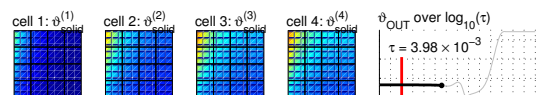
a)

Methane mole fraction - non-reactive phase

Flow direction

$\chi^N_{CH_4}$ [-]

0   0.2   0.4   0.6   0.8   1

Spatial coordinate ζ_1

b)

Methane mole fraction - reactive phase

Flow direction

$\chi^R_{CH_4}$ [-]

0   0.2   0.4   0.6   0.8   1

Spatial coordinate ζ_1

—⊙— $0.5\ D_i^{l,(1cell)}$

—✳— $1.0\ D_i^{l,(1cell)}$

—✕— $1.5\ D_i^{l,(1cell)}$

—☐— $2.0\ D_i^{l,(1cell)}$

—◇— $3.0\ D_i^{l,(1cell)}$

Figure 2.21.: Predicted concentration profiles of methane according to the phase model. The non-reactive phase (a) and the reactive phase (b) are shown for an isothermal calculation. The gas inlet is located at $\zeta_1 = 1$.

reactive phase at the outlet of the IIR unit. On the other hand, an increase of the mass transport coefficient leads to an intensified methane transport between the non-reactive and the reactive phase. The region, where methane steam reforming reaction takes place, is shifted to the inlet of the IIR unit and the equilibrium is reached earlier. Thus, the reaction rates are limited by the amount of methane transported over the phase interface

Fig. 2.22 additionally shows the temperature profiles of the non-reactive phase and the reactive phase. The temperature difference between both phases is in the order of several $10\,\mathrm{K}$. These temperature differences correlate to the results of the detailed models (Section 2.1). Due to mass transport limitation, only a slightly temperature drop is observed close to the reactor inlet. Thus, the overall temperature profile is relatively smooth.

2.4 Summary

The hierarchical modelling of the IIR unit of a molten carbonate fuel cell was presented. Using the detailed model, a small cutout section of the corrugated sheets and the catalyst pellets is analysed in detail. The simulation results show two dis-
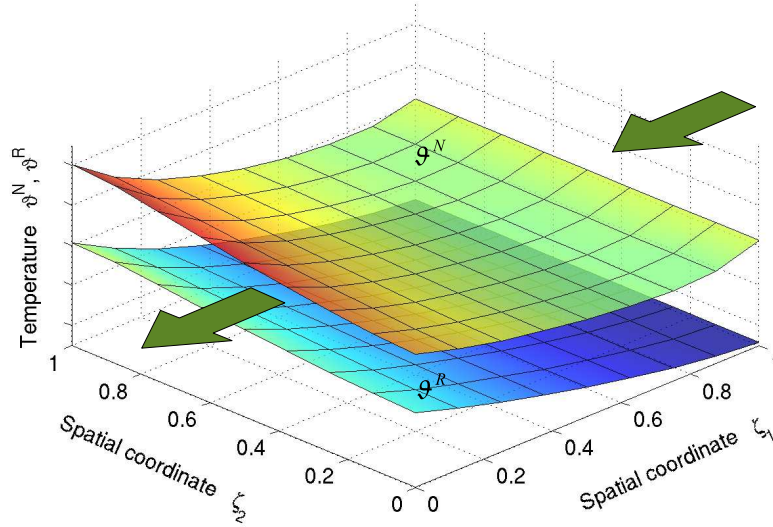
cell 1: $\vartheta^{(1)}_{solid}$ cell 2: $\vartheta^{(2)}_{solid}$ cell 3: $\vartheta^{(3)}_{solid}$ cell 4: $\vartheta^{(4)}_{solid}$ ϑ_{OUT} over $\log_{10}(\tau)$

$\tau = 3.98 \times 10^{-3}$

Figure 2.22.: Temperature distribution in the IIR unit for the non-reactive phase (ϑ^N) and the reactive phase (ϑ^R).

tinguished gas phase regions: a reactive phase close to the catalyst pellets and a non-reactive phase far away from the pellets. The structure of the reactor results in a mass transport limited reforming process.

Similar results are visible in the simulation of an entire IIR unit, which is based on the zone model. The zone model uses a simplified geometry to describe the partitioning of the reactor into the two zones. The results indicate a nearly homogeneous reaction rate for the reforming process. Thus, the IIR unit represents an almost constant heat sink for the neighbouring fuel cells.

In the zone model, the reactive and non-reactive zones are discrete: they exist at certain coordinates and have certain widths which correspond to the structure of the IIR unit. This discrete geometrical information is lost in the model reduction to the phase model. Instead, the states representing the non-reactive and the reactive zones are now distributed over the whole (two-dimensional) area of the IIR unit with mass and energy transfer between both zones (Fig. 2.16). The equations can now be interpreted as describing two phases, each occupying a certain fraction of the volume. The states in the reactive and non-reactive phases now represent characteristic values of the state variables such as the temperature and the gas composition that a corresponding zone in the specific vicinity would have.

The complexity and the structure of the phase model correspond to the complexity level and the structure of the model of a single MCFC by Heidebrecht *et al.* [22]. Therefore, both models can be combined to a common model of a molten carbonate fuel cell stack (see Part II).
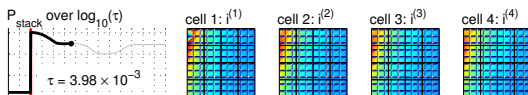
Chapter 3

Modelling of Anode and Cathode Gas Compartments

In this chapter, the anode gas compartments(Section 3.1) and the cathode gas compartment (Section 3.2) of a molten carbonate fuel cell are modelled. In analogy to the detailed model of the IIR unit, simulations for a cutout section of both types of gas compartments are carried out, taking into account the exact three-dimensional geometry.

## 3.1 Detailed Model of Anode Gas Compartment

3.1.1. Model Definition

Similar to the IIR unit, the anode gas compartment is composed of several corrugated metal sheets, which serve as current collectors and gas distributors (Fig. 3.1). The height of the arches is suitable to provide a sufficient reactant flow area as well as adequate mechanical stiffness. The catalyst for the Direct Internal Reforming (DIR) process is inserted into the structure of the gas compartment in the form of long cylinders. A pattern of one line of catalyst and one free line is used. Considering a possible variation of the catalyst distribution in the anode gas compartment, two times this width is chosen.

At the top, the gas domain is enclosed by a metal sheet acting as bipolar plate while the electrode and matrix, containing the molten carbonate electrolyte, are located at the bottom. The bottom layer is implemented as a solid domain. At the boundary between the gas and the electrode layer, the mass fluxes caused by the electrochemical reactions are considered as boundary sources.

Similar assumptions as for the detailed model of the IIR unit (Section 2.1.2) are used. Due to the different geometry of the anode gas channels as well as due to changed boundary conditions, modifications are needed. The new or modified assumptions are summarised below, followed by a detailed explanation.
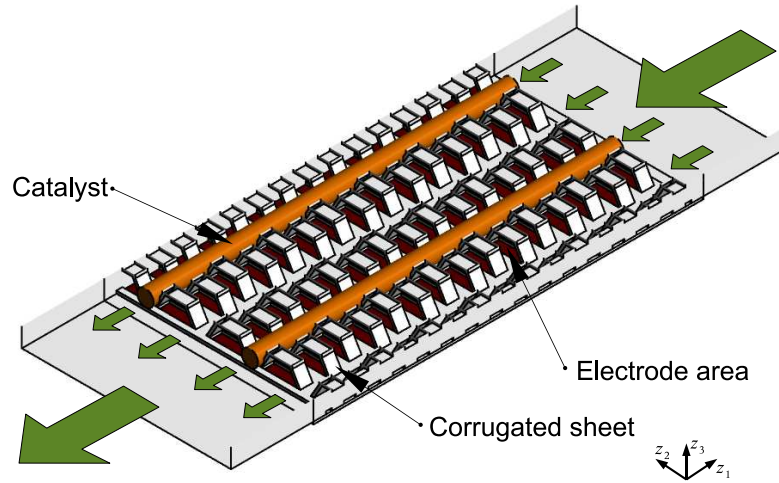
a) The gas flow is laminar.
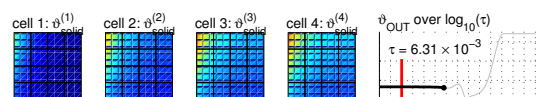
Figure 3.1.: Structure of the anode gas compartment (US-Patent 6492045 [6]).

b) The reforming reactions take place at the surface of the catalyst cylinders.

c) The heat of the reforming reactions is accounted for in the catalyst cylinders.

d) The current density is constant over the simulated area.

ad assumption a): The gas flow through the IIR unit is equally distributed to the anode gas channels of eight fuel cells. Due to a cross sectional area similar to the IIR unit, the reduction of the gas flow to one eighth results in a lower Reynolds number of approximately $Re = 32$. Thus, the equations for laminar flow are applied. For comparison, the simulations are also carried out using the k-ϵ-turbulence model. No significant differences are found between the two sets of simulation results.

ad assumption b): The methane steam reforming reaction (ref1) as well as the water gas shift reaction (ref2) take place at the surface of the DIR catalyst. In analogy to the modelling of the catalyst pellets in the IIR unit, the mass transport inside of the catalyst cylinders is not considered explicitly. It is assumed that the cylinders are solid and have a highly active external surface. The reaction rates at this surface are defined in Eq. (2.1) and Eq. (2.2), respectively.

ad assumption c): The heat of the reforming process is released in the porous solid of the catalyst cylinders. Due to the fact that the catalyst cylinders are in direct contact with the corrugated sheets, the conductive heat transfer between both materials has to be considered. The solid-solid interface between the catalysts material and the sheets is treated as ideal, *i. e.* the heat transfer resistance is not considered. The energy needed for the endothermic reforming process is mainly provided by conductive heat transport in the solid parts from the outer sheet *via* the corrugated sheets to the catalyst pellets.
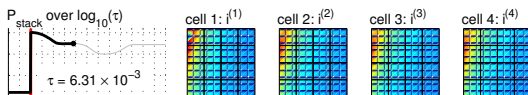
ad assumption d): In the detailed model of the anode, a constant current density is assumed. Previous models [18, 22] showed local current densities of up to twice the average current density (see also Section 6.1.2). To model these values, a current density of $i_A = 160 \, mA/cm^2$ is assumed. However, there is no information on how this current density is distributed on the two electrochemical oxidation reactions. Considering this fact, only the reaction of hydrogen with carbonate ions from the electrolyte to water and carbon dioxide (ox1) have been taken into account to simplify the model.

$$H_2 + CO_3^{2-} \rightleftharpoons H_2O + CO_2 + 2e^- \qquad \text{(ox1)}$$

The mass fluxes of the reaction educt (H_2) and the reaction products (H_2O and CO_2) are considered as boundary sources at the surface of the electrode. The resulting mass flux densities of hydrogen, water and carbon dioxide are defined as:

$$\left[\mathbf{n} \cdot (\rho \, D_i \nabla w_i) \right]_{\text{electrode}} = \nu_{i,\text{ox1}} \frac{i_A}{n \, F} M_i \qquad (3.1)$$

with the stoichiometric coefficients $\nu_{i,\text{ox1}}$.

The external boundaries are defined similar to the corresponding definitions used for the IIR model. The properties of the mass flow as well as the composition and temperature of the gas mixture are defined at the gas inlet while the relative pressure is set at the gas outlet. With regard to the bipolar plate and the electrolyte, a constant wall temperature is defined.

For the internal boundary conditions, some changes are required. While the gas-solid boundary condition at the sheet surface can be used without change, assumption c) requires a change of the numerical representation of the boundary condition at the catalyst surface. While the overall equation is equal to the equation used for the surface of the catalyst pellets in the IIR unit (see Eq. 2.28), the heat of the reforming process is accounted for in the catalyst material.

The model parameters are identical to the parameters used in the detailed model of the IIR (see Section 2.1.5). The values for the additionally needed operating parameters and the boundary conditions are listed in Table 3.1.

The mesh created for the detailed model of the anode gas compartment consists of 312103 nodes (approximately 3.5 million DoF) and is solved in 1.5 hours using ANSYS CFX version 11 [11] on a dual Xeon processor with 3.2 GHz.

3.1.2. Simulation Results

Fig. 3.2 illustrates the mole fractions of methane, carbon dioxide and hydrogen in the anode gas compartment. At the gas inlet, the gas is approximately at chemical equilibrium. Due to the methane steam reforming reaction and the water gas shift
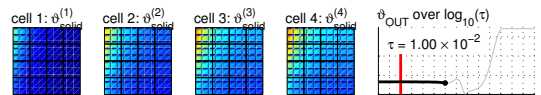
Table 3.1.: Operating conditions used for the detailed model of the anode gas compartment.

Property	Symbol	Value
electrochemical reaction		
average current density	i_{ox1}	$160\,\text{mA cm}^{-2}$
inlet conditions		
gas temperature	T_{inlet}	$900\,\text{K}$
mass flux	g_{inlet}	$3.2 \cdot 10^{-6}\,\text{kg s}^{-1}$
mass fraction of methane	$w_{\text{inlet,CH}_4}$	0.03
mass fraction of steam	$w_{\text{inlet,H}_2\text{O}}$	0.34
mass fraction of hydrogen	$w_{\text{inlet,H}_2}$	0.05
mass fraction of carbon monoxide	$w_{\text{inlet,CO}}$	0.15
mass fraction of carbon dioxide	$w_{\text{inlet,CO}_2}$	0.43
outlet conditions		
relative pressure	$\overline{p}_{rel,\text{outlet}}$	$0\,\text{Pa}$
top and bottom wall		
temperature at the top sheet / the electrode	T_{wall}	$900\,\text{K}$

reaction at the catalyst surface, the chemical equilibrium with respect to these reforming reactions is reached in the vicinity of the catalyst. Considering the electrochemical reaction, the concentration of the gas mixture is changed. As a result, the gas is no longer at chemical equilibrium and its composition is adjusted by a further conversion of methane. Thus, a lower concentration of methane can be observed close to the catalyst and, due to the mass transport in the gas phase, funnel-shaped profiles are formed. The overall change of the methane concentration between the gas inlet and gas outlet is less than 1% (see Fig. 3.2a). The difference in methane concentration at the catalyst surface and in the middle between the catalyst cylinders is only a fraction of that. Thus, the reforming reactions are not limited by mass transport but by the chemical equilibrium at the local temperature.

Carbon dioxide (Fig. 3.2b) is produced by the water gas shift reaction at the catalyst pellets as well as by the electrochemical reaction at the electrode. The electrochemical reaction is considered at the contact areas between the gas phase and the electrode. This results in a nearly linear change of the concentration due to the fact that the free electrode surfaces are distributed all over the simulation domain (Fig. 3.1). In contrast, the water gas shift reaction takes place at the catalyst pellets. Due to this reaction, similar funnel-shaped profiles as for methane can be expected for the carbon dioxide concentration. The concentration profile shown in the Fig. 3.2b is the result of the superposition of both reactions. The overall mole fraction of carbon dioxide is increased by about 4%. The concentrations at the catalyst surface and between the catalyst cylinders are almost the same, so mass transport does not limit the reaction rate.

With respect to hydrogen (Fig. 3.2c), not only the production by both reforming reactions and the consumption by the electrochemical reaction have to be considered,
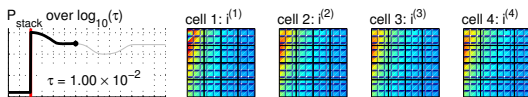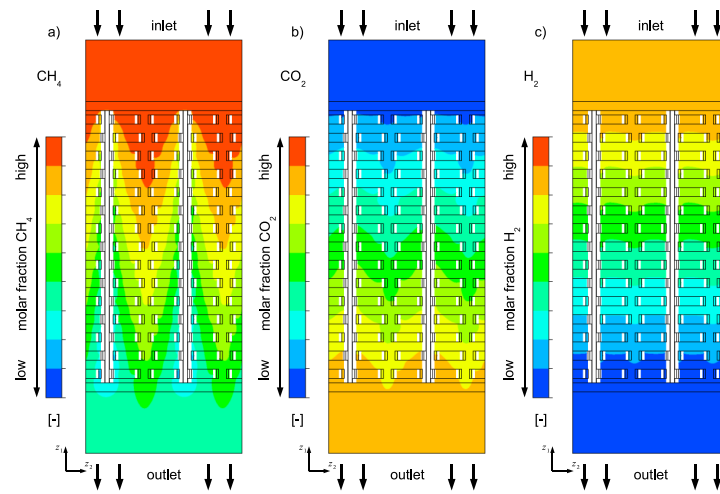
Figure 3.2.: Methane (a), carbon dioxide (b) and hydrogen (c) concentration in the anode gas compartment

but also the high mole fraction at the gas inlet. The amount of hydrogen produced by the reforming reactions is small compared to the amount of hydrogen available in the gas phase. Thus, the funnel-shaped form of the concentration profile is less chiselled and a nearly linear decrease of the hydrogen mole fraction by several percent from the inlet at the top towards the outlet at the bottom can be observed.
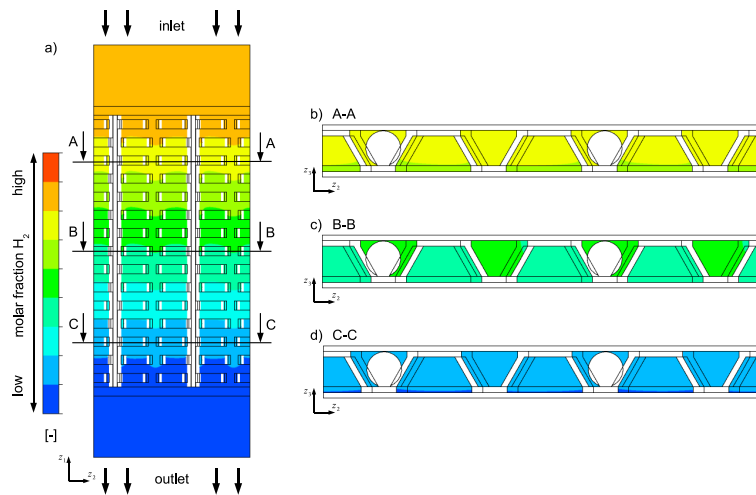
Figure 3.3.: Hydrogen mole fraction in the anode gas compartment (a). Additional cross section plots close to the inlet (b), in the middle of the model (c) and close to the outlet (d) are shown. An identical scale is used for all images.

Fig. 3.3 additionally shows cross section profiles of the hydrogen mole fraction close to the gas inlet, in the middle of the simulation domain and near the gas outlet. The

highest concentration of hydrogen can be observed in the vicinity of the reforming catalyst, where hydrogen is produced, while the lowest concentration is visible at the electrode (lower boundary of the gas domain). The concentration change over the height of the gas compartment is small compared to the concentration gradient along the f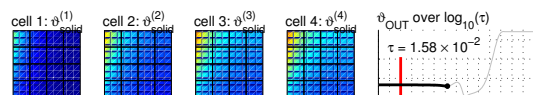low direction. This confirms the assumption of a constant concentration over the channel height, which is used in the definition of the fuel cell model [22].

3.2 Detailed Model of Cathode Gas Compartment

3.2.1. Model Definition

The geometrical structure of the detailed model for the cathode gas compartment is shown in Fig. 3.4. As in the previously discussed models, a corrugated sheet is used. It is surrounded by a bipolar plate at the top and the porous electrolyte at the bottom. The fact that no additional catalytic process has to be considered, is used to simplify the model. Only one half of the width is simulated. But, for an easier comparison of the different models, twice the simulation results are shown using the periodic boundary to visualise a similar size as the model of the IIR unit or anode gas compartment.

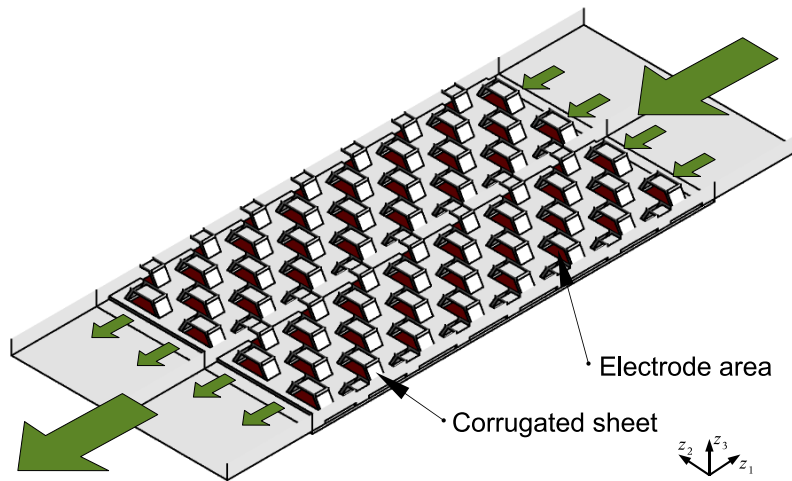**Figure 3.4.:** Structure of the cathode gas compartment (US-Patent 6492045 [6]).

For the cathode gas compartment, similar assumptions as defined for the anode gas compartment are taken into account and identical governing equations and boundary conditions are used (see Section 3.1.1). With respect to the gas mixture, water, carbon dioxide, oxygen and nitrogen are considered. The composition of the gas only
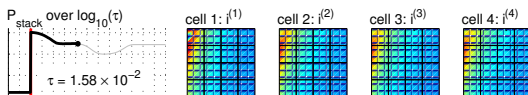
changes due to the electrochemical reduction of oxygen. The backward direction of the following electrochemical reaction takes place at the cathode:

$$CO_3^{2-} \rightleftharpoons CO_2 + 1/2\,O_2 + 2\,e^- \tag{red}$$

Similar to the electrochemical oxidation at the anode, this reaction is implemented as a mass source at the boundary between the gas phase and the electrolyte. The mass flux densities of carbon dioxide and oxygen are defined as:

$$\left[\mathbf{n} \cdot (\rho\, D_i \nabla w_i) \right]_{\text{electrode}} = \nu_{i,\text{red}} \frac{i_C}{n\,F} M_i \tag{3.2}$$

using the same current density as at the anode $i_C = i_A = 160\,mA/\text{cm}^2$.

The parameters of the detailed model for the cathode gas compartment correspond to the parameters defined for the IIR unit (see Section 2.1.5). Additionally the diffusion coefficient for nitrogen is needed, $D_{N_2} = 2 \cdot 10^{-4}\,\text{m}^2\,\text{s}^{-1}$. The boundary conditions of the model are listed in Table 3.2.

Table 3.2.: Parameters and operating conditions used for the detailed model of the cathode gas compartment.

Property	Symbol	Value
electrochemical reaction		
average current density	i_{red}	$160\,\text{mA cm}^{-2}$
inlet conditions		
gas temperature	T_{inlet}	$900\,\text{K}$
mass flux (for the geometry in Fig. 3.4)	g_{inlet}	$12 \cdot 10^{-6}\,\text{kg s}^{-1}$
mass fraction of water	w_{inlet,H_2O}	0.10
mass fraction of carbon dioxide	w_{inlet,CO_2}	0.11
mass fraction of oxygen	w_{inlet,O_2}	0.14
mass fraction of nitrogen	w_{inlet,N_2}	0.65
outlet conditions		
relative pressure	$\overline{p}_{rel,\text{outlet}}$	$0\,\text{Pa}$
top and bottom wall		
temperature at the top sheet / the electrode	T_{wall}	$900\,\text{K}$

3.2.2. Simulation Results

Fig. 3.5 presents the mole fraction of carbon dioxide in the cathode gas compartment. Carbon dioxide is an educt for the electrochemical reaction at the cathode electrode. Thus, its concentration is decreased at the boundary between the electrode and the gas phase. Due to the fact that the free electrode surfaces are equally distributed over the simulation domain (see Fig. 3.4), a nearly linear decrease of the concentration can be observed. The overall concentration difference between the gas inlet and the gas outlet is in the order of 1.5%.
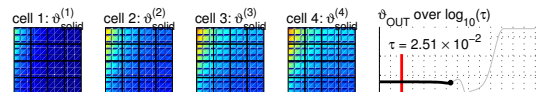
Fig 3.5b to 3.5d show cross sectional plots of the carbon dioxide mole fraction. As discussed above, the lowest concentration can be found close to the active electrode surface. Similar to the concentration gradient over the height of the anode gas channels, this concentration gradient is small compared to the concentration gradient along the flow direction. Thus, the assumption of a constant concentration over the channel height is also confirmed for the cathode gas compartment [22].
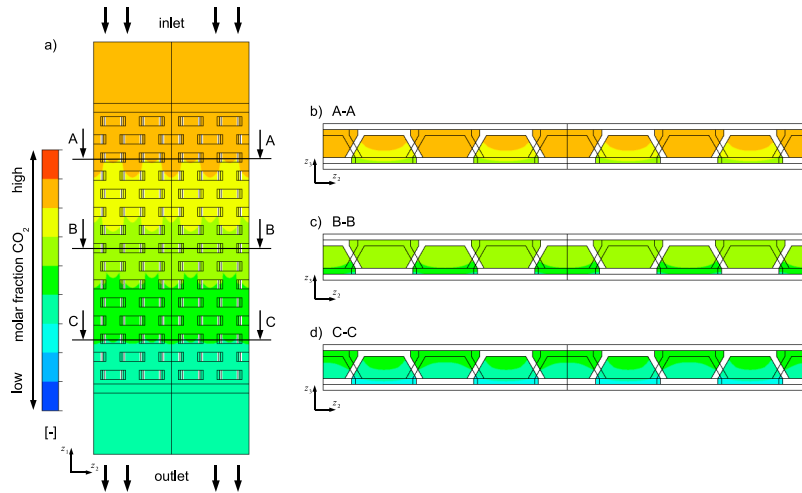
Figure 3.5.: Molar fraction of carbon dioxide in the anode gas compartment (a). Additional cross section plots close to the inlet (b), in the middle of the model (c) and close to the outlet (d) are shown.

3.3   Summary

Detailed models of the anode gas compartment and the cathode gas compartment have been presented in this chapter. In the anode gas compartment, especially the reforming process has been analysed. The simulation results show that the reforming reactions in the anode gas compartments are not governed by a mass transport limitation but by the reaction rates. Thus, a gas composition which corresponds to the chemical equilibrium at the gas temperature is maintained by the reforming process. In the cathode gas compartments, only the electrochemical reaction at the cathode takes place. All gas concentrations show a linear profile in flow direction.

Furthermore, the simulation results show that the gradients along the width as well as the gradients over the height of the channels are small compared to the concentration gradients in flow direction. Thus, the detailed models of the anode and cathode channels confirm the assumptions of negligible concentration differences in these direction used in the model by Heidebrecht [22] and in the symmetric stack model (Section 4.3).
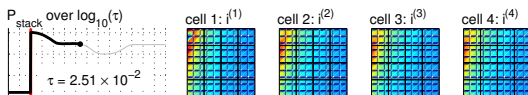
Part II

Symmetric Stack Model
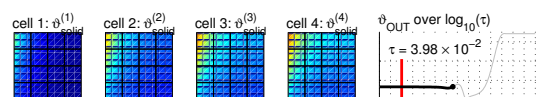
Chapter 4

Definition of the Symmetric Stack Model

In this chapter, a model for a fuel cell system based on a Molten Carbonate Fuel Cell is presented. Its structure is explained in Section 4.1 followed by a discussion of the changes and improvements compared to previous models (Section 4.2). Furthermore, the assumptions used to derive the model are presented (Section 4.3) and the equations describing the model are given in the last few sections. Besides the model equations (Section 4.4) the reaction kinetics (Section 4.5) and the equations to model the electrical potential in the bipolar plates (Section 4.6) are presented.

4.1 Geometry

In the HOTMODULE MCFC power plant, 343 fuel cells and 42 IIR units are arranged in a fuel cell stack. The structure is such that one IIR unit is inserted after 8 fuel cells. Under the following two assumptions, the stack behaviour can be represented by a symmetric section consisting of four fuel cells and one half IIR unit. The first assumption is that the thermal effects at both ends of the stack are neglected. The second assumption is that the sequence of anode and cathode channels along the stack direction has no significant impact on the temperature profile. The structure of this so-called symmetric stack model is shown in Fig. 4.1 [38].

The modelling of the IIR unit was presented in Chapter 2. In this, the phase model of the structured reactor representing the IIR unit is attached to a model of a fuel cell to form the symmetric stack model. As in the HOTMODULE a counter flow configuration with regard to the flow in the anode gas flow is used. In each of the four fuel cells, the anode and the cathode gas channels are arranged in a cross flow configuration. The solid components of the fuel cells, especially the electrolyte and the electrolyte matrix, are combined in the solid phase. In addition to the above mentioned components, the model includes further gas compartments: a heat exchanger, a gas manifold, a catalytic combustion chamber and a reversal chamber. These auxiliary components are shared by all cells of the fuel cell system.
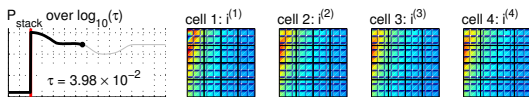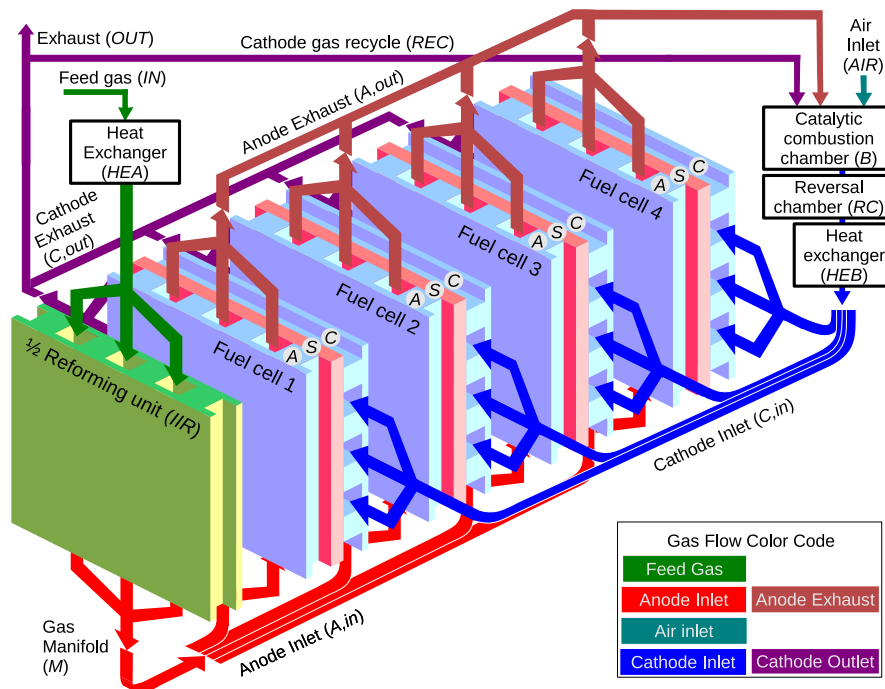
Figure 4.1.: Structure and gas flows in the symmetric MCFC stack model, consisting of four fuel cells (anode and cathode: blue; solid: red) and one half IIR unit (green).

The gas flows in the symmetric stack model are indicated in Fig. 4.1. The feed gas (IN), which is assumed to have passed through an external reformer, is heated up in the heat exchanger (HEA) by the hot gas after the catalytic combustion chamber and flows into the IIR unit (IIR, reforming reactions ($ref1$) and ($ref2$)). After the IIR unit, the gas flows into a gas manifold (M), where it is split into four streams of equal size which are redirected into the anode gas compartments of the fuel cells (A, reforming reactions ($ref1$) and ($ref2$) as well as electrochemical oxidation reactions ($ox1$) and ($ox2$)). The exhaust gases of the four anode gas compartments (A,out) is mixed with the cathode gas recycle (REC) and completely burned with air (AIR) in the catalytic combustion chamber (B).

The exhaust gas of the combustion goes into the reversal chamber (RC), where the blower is located. Following the reversal chamber, the gas is redirected into the second chamber of the heat exchanger (HEB). Within the heat exchanger, the energy of the gas is used to heat up the feed gas. In the next step, the gas flow is equally distributed to the cathode gas compartments of the four fuel cells (C, electrochemical reduction reaction (red)). A part of the cathode exhaust gas is used in the cathode gas recycle (REC) which is redirected into the catalytic combustion chamber (B), while the rest of the gas leaves the fuel cell system (OUT).
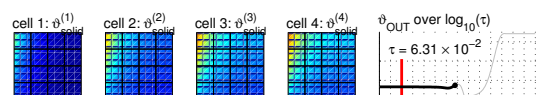
In addition to the above listed couplings of the different compartments by the convective mass flow, the thermal coupling of all components along the stack coordinate is modelled. Heat source terms are added into the corresponding equations, allowing the calculation of a temperature profile along the stack direction. Furthermore, the electrochemical reaction rates at the anode and cathode of each fuel cell are coupled by the charge balance. These dependencies between the different parts of the model increase its complexity and thus the requirements with regard to the solver (see Chapter 5).

4.2   Comparison with Previous Models

The symmetric stack model is an extension of previous works, especially the MCFC model developed by Heidebrecht [22, 24]. This model considers the physical and (electro-)chemical phenomena in a single fuel cell and is based on conservation equations of mass, enthalpy and charge. To achieve a more general description that is also valid for equivalent systems, the model is formulated in terms of dimensionless variables. An extended model including a simple IIR unit was developed by Gundermann [18]. Using this model, parameters of the MCFC system are determined and validated.

The partitioning of the stack into different compartments along the stack length is considered in this work. On the one hand, this includes the IIR unit represented by the reactive and non-reactive phase (see the definition of the phase model in Chapter 2). On the other hand, several fuel cells composed of anode, solid phase and cathode are taken into account. This way, the temperature distribution in the different compartments and thereby the temperature distribution along the stack direction can be analysed.

The model is implemented in COMSOL MULTIPHYSICS [13], a commercial solver for systems of partial differential equations which is based on the Finite Element Method (FEM). Implementation details are discussed in Chapter 5.

4.3   Model Assumptions

The main assumptions used to derive the symmetric MCFC stack are listed below. Some of these assumptions are proposed by Gundermann [18].

a) Ideal gases.

b) Isobaric conditions.

c) Symmetric boundary conditions are defined at both ends of the symmetric model in stack direction.
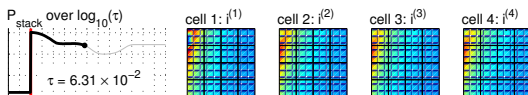
d) In the IIR unit, only the gas flow opposed to the flow direction of the anode gas compartment is considered to simplify the geometry of the reforming reactor.

e) All solid parts of a fuel cell are lumped to one solid phase, which has an average heat conductivity and a cumulated heat capacity.

f) Gas compositions in the channels of the IIR unit and the anode gas compartment are usually close to the chemical equilibrium of the reforming reactions. Therefore, power law kinetics are applied to describe their reaction rates. The electrochemical reaction rates are described by Butler-Volmer type kinetic expressions [22].

g) All concentration, temperature or velocity gradients perpendicular to the cell plane in each compartment are negligible. This reduces the geometry of the IIR unit, the anode and cathode gas compartments as well as the solid phase to two-dimensional structures.

h) The heat and mass transport between the different parts of the stack model are represented as source terms in the corresponding equations.

i) The heat capacity of the gas mixture depends only on its composition, but not on temperature [18]. The heat capacities of the pure components are calculated at the reference temperature of $T^r = 600\,°C$, corresponding to a dimensionless temperature of $\vartheta^r = 2.93$. This temperature represents the operating temperature of an MCFC and is thus chosen as linearisation point for the calculation of the thermodynamic values. A detailed description of this assumption can be found in Appendix A.2

j) The electrical potentials of each cell are independent from the potentials of the neighbouring fuel cells. This is equivalent to the assumption that in each bipolar plate between two cells, complete equalisation of the electrical potential is achieved. This is a proper assumption if the neighbouring cells show similar current density profiles. In that case, only small currents will occur in the plane of the bipolar plates, resulting in a virtually constant potential in the plates. The validity of this assumption will be checked carefully by a calculation of the potential field in the bipolar plates using the simulation results. The corresponding equations are defined in Section 4.6 and the results are presented in Section 6.1.4.

The symmetric stack model is defined on a two-dimensional plane of size 1×1, representing the dimensionless cell plane. Fig. 4.2 shows the simulation domain Ω_{stack} with the four boundaries $\partial\Omega_1$ to $\partial\Omega_4$. Furthermore, the gas flow directions in the three gas compartments of the fuel cell stack are indicated. The gas flow in the IIR unit is in the negative ζ_1-direction while the anode gas compartment is arranged in a counter-flow configuration (positive ζ_1-direction). The cathode gas flows in ζ_2-direction from the bottom to the top, a cross-flow configuration with regard to the anode gas compartment.
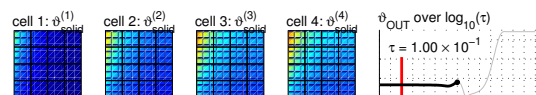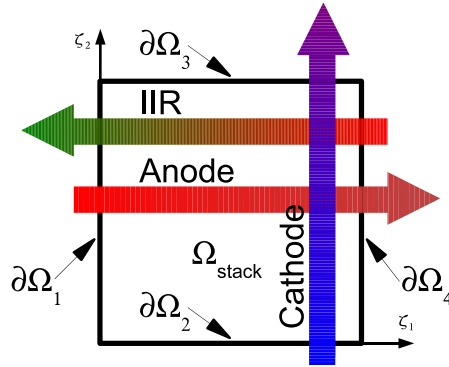
Figure 4.2.: Simulation domain of the symmetric stack model with the gas flow directions.

4.4 Governing Equations

For the mathematical description of the symmetric MCFC stack model, a system of non-linear ordinary differential equations (ODE) and non-linear partial differential equations (PDE) has been formulated. Furthermore some algebraic equations (AE) are included. In the following, the basic structure of these model equations is presented.

The description of the fuel cells is based on previous works [22, 24, 25]. For a detailed derivation of these model equations, especially the equations for the reaction kinetics and the thermodynamic expressions, the reader is referred to the corresponding publications. The equations for the anode, the solid and the cathode are slightly adapted and the changes are discussed below. Furthermore, equations for the heat exchangers, the gas manifold and the IIR unit are added and the heat transport in stack direction is implemented.

First, all gas compartments are described following the gas flow. After that, the equations for the gas composition in the electrode pores, the temperature of the solid phase and the charge balance are added. A detailed list of all dimensionless equations needed for the description of the symmetric stack model can be found in Appendix A.4.

The model can be used to simulate an arbitrary number of fuel cells, specified by n_{cells}. The standard configuration includes four fuel cells and one half IIR unit. Thus, it represents the structure of one IIR unit followed by eight fuel cells as currently realised in the industrial fuel cell stack, the HOTMODULE.

4.4.1. Feed Gas

The feed gas (*IN*) of the MCFC stack is assumed to be a partially reformed gas from an external reformer. The composition, $\chi_{i,IN}$, the temperature, ϑ_{IN}, and the molar
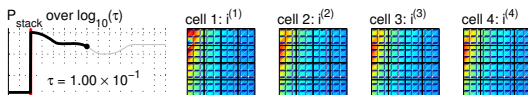
mass flux, Γ_{IN}, of the feed gas are input parameters of the symmetric stack model. They are given in Table 6.1 (Chapter 6) for the simulated load case.

4.4.2. Heat Exchanger (Cold Side)

The feed gas is heated up in a heat exchanger (*HEA*) by the exhaust gas from the catalytic combustion chamber before it reaches the IIR unit. The gas chamber of the heat exchanger is modelled as a well mixed tank. The component mass fractions, $\chi_{i,HEA}$ and the gas temperature, ϑ_{HEA}, are described by:

$$n_{cells}\, V_{HEA}^{(1\,cell)}\, \frac{1}{\vartheta_{HEA}} \frac{\partial \chi_{i,HEA}}{\partial \tau} = \Gamma_{IN} \times (\chi_{i,IN} - \chi_{i,HEA}) \tag{4.1}$$

$$n_{cells}\, V_{HEA}^{(1\,cell)}\, \frac{\overline{c}_{P\,HEA}}{\vartheta_{HEA}} \frac{\partial \vartheta_{HEA}}{\partial \tau} = \Gamma_{IN}\, \overline{c}_{P\,IN} \times (\vartheta_{IN} - \vartheta_{HEA}) - Q_{HE} \tag{4.2}$$

where Q_{HEA} denotes the heat flux between both sides of the heat exchanger (see also Section 4.4.8).

The total molar mass flux, Γ_{HEA}, is calculated as:

$$\Gamma_{HEA} = \Gamma_{IN} \times \left(1 + \frac{\overline{c}_{P\,IN}}{\overline{c}_{P\,HEA}} \times \left(\frac{\vartheta_{IN}}{\vartheta_{HEA}} - 1\right)\right) - \frac{Q_{HE}}{\overline{c}_{P\,HEA}\, \vartheta_{HEA}} \tag{4.3}$$

The heat transferred between the two gas chambers of the heat exchanger, Q_{HE}, depends on the temperature difference between the two gas flows and the Stanton number St_{HE}. It is given by

$$Q_{HE} = St_{HE} \times (\vartheta_{HEA} - \vartheta_{HEB}) \qquad . \tag{4.4}$$

4.4.3. Indirect Internal Reforming Unit

The phase model of the Indirect Internal Reforming unit (*IIR*) is presented in Section 2.3. Its mathematical complexity and structure are suited for the use in the symmetric stack model. In the following, the main equations of this model considering the non-reactive phase (index N) and the reactive phase (index R) are discussed. Their formulation is adapted for the use in the symmetric stack model.
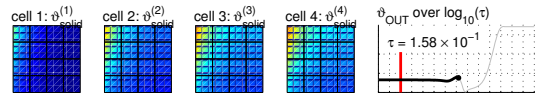
The mole fractions, $\chi^N_{i,IIR}$, and the temperature, ϑ^N_{IIR}, in the non-reactive phase are determined from Eq. (4.5) and Eq. (4.6), respectively.

$$n_{cells}\, \varepsilon^N_{IIR}\, V^{(1\,cell)}_{IIR}\, \frac{1}{\vartheta^N_{IIR}}\, \frac{\partial \chi^N_{i,IIR}}{\partial \tau} = -\varepsilon^N_{IIR}\, \gamma^N_{IIR}\, \frac{\partial \chi^N_{i,IIR}}{\partial \zeta_1} - \left[n^I_{i,IIR} - \chi^N_{i,IIR}\, n^I_{t,IIR} \right] \tag{4.5}$$

$$n_{cells}\, \varepsilon^N_{IIR}\, V^{(1\,cell)}_{IIR}\, \frac{\overline{\mathsf{c}}^N_{P\,IIR}}{\vartheta^N_{IIR}}\, \frac{\partial \vartheta^N_{IIR}}{\partial \tau} = -\varepsilon^N_{IIR}\, \overline{\mathsf{c}}^N_{P\,IIR}\, \gamma^N_{IIR}\, \frac{\partial \vartheta^N_{IIR}}{\partial \zeta_1}$$

$$+ \left(\sum_i n^{I-}_{i,IIR}\, \mathsf{c}_{Pi} \right) \times \left(\vartheta^N_{IIR} - \vartheta^R_{IIR} \right) - q^I_{IIR} + \varepsilon^N_{IIR}\, q^N_{IIRS} \tag{4.6}$$

In these equations the dimensionless volume of the IIR unit is scaled by the number of fuel cells considered in the model, n_{cells}. Thus, the flow area of the IIR unit is varied accordingly to the gas flow needed for the fuel cells.

The molar mass flux density through the non-reactive phase, γ^N_{IIR}, is described by:

$$0 = -\frac{\partial \left(\varepsilon^N_{IIR}\, \gamma^N_{IIR}\, \vartheta^N_{IIR} \right)}{\partial \zeta_1}$$

$$+ \frac{1}{\overline{\mathsf{c}}^N_{P\,IIR}} \times \left(\left(\sum_i n^{I-}_{i,IIR}\, \mathsf{c}_{Pi} \right) \times \left(\vartheta^N_{IIR} - \vartheta^R_{IIR} \right) - q^I_{IIR} + \varepsilon^N_{IIR}\, q^N_{IIRS} \right) + \vartheta^N_{IIR}\, n^I_{t,IIR}$$

$$\tag{4.7}$$

The mole fractions, $\chi^R_{i,IIR}$, and the temperature, ϑ^R_{IIR}, in the reactive phase are calculated from Eq. (4.8) and Eq. (4.9).

$$n_{cells}\, \varepsilon^R_{IIR}\, V^{(1\,cell)}_{IIR}\, \frac{1}{\vartheta^R_{IIR}}\, \frac{\partial \chi^R_{i,IIR}}{\partial \tau} = n^I_{i,IIR} - \chi^R_{i,IIR}\, n^I_{t,IIR}$$

$$+ \varepsilon^R_{IIR} \times \left(\sum_j \left(\nu_{i,j} - \chi^R_{i,IIR}\, \overline{\nu}_j \right) n_{cells}\, Da^{(1\,cell)}_{j,IIR}\, r_{j,IIR} \right) \tag{4.8}$$

$$n_{cells}\, \varepsilon^N_{IIR}\, V^{(1\,cell)}_{IIR}\, \frac{\overline{\mathsf{c}}^R_{P\,IIR}}{\vartheta^R_{IIR}}\, \frac{\partial \vartheta^R_{IIR}}{\partial \tau} = \left(\sum_i n^{I+}_{i,IIR}\, \mathsf{c}_{Pi} \right) \times \left(\vartheta^N_{IIR} - \vartheta^R_{IIR} \right) + q^I_{IIR}$$

$$+ \varepsilon^R_{IIR} \sum_{j=\mathrm{ref}} \left(-\Delta_R h^\theta_j \left(\vartheta^R_{IIR} \right) \right) \times n_{cells}\, Da^{(1\,cell)}_{j,IIR}\, r_{j,IIR}$$

$$+ \left(\varepsilon^R_{IIR} + \varepsilon^P_{IIR} \right) \times q^R_{IIRS} \tag{4.9}$$

The total molar mass flux across the interface between both phases, $n^I_{t,IIR}$, plus the change in mole numbers due to the reforming reactions have to compensate the ex-

pansion effect in the reactive phase due to dynamic temperature changes (see Section 2.3.2.6). At steady state, the right hand side of Eq. (4.10) equals zero.
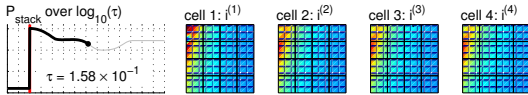
$$n_{t,IIR}^I + \varepsilon_{IIR}^R \sum_{j=\text{ref}} \overline{\nu}_j \, n_{cells} \, Da_{j,IIR}^{(1\,cell)} \, r_{j,IIR} =$$

$$-\frac{1}{\vartheta_{IIR}^R} \frac{1}{\overline{c}_{P\,IIR}^R} \times \left(\left(\sum_i n_{i,IIR}^{I+} \, c_{P\,i} \right) \times \left(\vartheta_{IIR}^N - \vartheta_{IIR}^R \right) + q_{IIR}^I \right.$$

$$+\varepsilon_{IIR}^R \sum_{j=\text{ref}} \left(-\Delta_R h_j^0 \left(\vartheta_{IIR}^R \right) \right) \times n_{cells} \, Da_{j,IIR}^{(1\,cell)} \, r_{j,IIR}$$

$$\left. + \left(\varepsilon_{IIR}^R + \varepsilon_{IIR}^P \right) \times q_{IIRS}^R \right) \tag{4.10}$$

Boundary conditions are needed for Eqs. (4.5) to (4.7). The temperature, composition and molar mass flux of the gas leaving the heat exchanger are considered at the gas inlet of the non-reactive phase ($\partial\Omega_4$ in Fig. 4.2). With regard to the molar mass flux density the volume fraction of the non-reactive phase has to be taken into account. Furthermore, as the convective flow in the IIR unit is in negative ζ_1-direction, a negative sign for the molar mass flux density occurs in Eq. (4.13).

$$\chi_{i,IIR}^N (\zeta_1 = 1, \zeta_2, \tau) = \chi_{i,IIR,in}^N = \chi_{i,HEA} \tag{4.11}$$

$$\vartheta_{IIR}^N (\zeta_1 = 1, \zeta_2, \tau) = \vartheta_{IIR,in}^N = \vartheta_{HEA} \tag{4.12}$$

$$\gamma_{IIR}^N (\zeta_1 = 1, \zeta_2, \tau) = \gamma_{IIR,in}^N = -\frac{\Gamma_{HEA}}{\varepsilon^N} \tag{4.13}$$

At the outlet of the IIR unit ($\partial\Omega_1$ in Fig. 4.2), the average outlet concentrations, $\chi_{i,IIR,out}$, the average outlet temperature, $\vartheta_{IIR,out}$, and the total outlet molar mass flux, $\Gamma_{IIR,out}$, are calculated:

$$\Gamma_{IIR,out} \, \chi_{i,IIR,out} = \int_0^1 \left[-\varepsilon^N \, \gamma_{IIR}^N \, \chi_{i,IIR}^N \right]_{\zeta_1=0,\zeta_2} \mathrm{d}\zeta_2 \tag{4.14}$$

$$\Gamma_{IIR,out} \, \overline{c}_{P\,IIR,out} \times (\vartheta_{IIR,out} - \vartheta^r) = \int_0^1 \left[-\varepsilon^N \, \gamma_{IIR}^N \overline{c}_{P\,IIR}^N \times \left(\vartheta_{IIR}^N - \vartheta^r \right) \right]_{\zeta_1=0,\zeta_2} \mathrm{d}\zeta_2 \tag{4.15}$$

$$\Gamma_{IIR,out} = \int_0^1 \left[-\varepsilon^N \, \gamma_{IIR}^N \right]_{\zeta_1=0,\zeta_2} \mathrm{d}\zeta_2 \tag{4.16}$$

In the first fuel cell, the heat flux density between the IIR unit and the solid phase is needed (Eq. (4.71) in Section 4.4.11). It is calculated using the heat flux densities
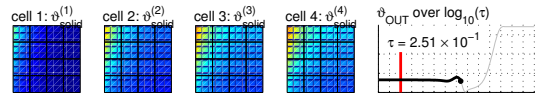
with respect to the non-reactive phase (Eq. (4.18)) and the reactive phase (Eq. (4.19)), accounting for the corresponding area fractions:

$$q_{S,IIR} = \varepsilon_{IIR}^N q_{IIRS}^N + \left(\varepsilon_{IIR}^R + \varepsilon_{IIR}^P \right) \times q_{IIRS}^R \tag{4.17}$$

$$q_{IIRS}^N = St_{IIRS}^N \times \left(\vartheta_S^{(1)} - \vartheta_{IIR}^N \right) \tag{4.18}$$

$$q_{IIRS}^R = St_{IIRS}^R \times \left(\vartheta_S^{(1)} - \vartheta_{IIRS}^R \right) \tag{4.19}$$

The heat flux density between both phases is described by

$$q_{IIR}^I = n_{cells}\, St_{IIR}^{I,(1\,cell)} \times \left(\vartheta_{IIRS}^N - \vartheta_{IIRS}^R \right) \tag{4.20}$$

The mass transport between the two phases is described in Section 2.3.3.1.

4.4.4. Gas Manifold

The gas manifold (M) is located between the IIR unit (IIR) and the anode gas compartments of the fuel cells (A). This volume is mainly used for the redirection of the gas flow. For simplicity, it is modelled as a well-mixed tank similar to the modelling of the heat exchangers (HEA and HEB). The mole fractions, $\chi_{i,M}$, and the temperature, ϑ_M, are described by Eqs. (4.21) and (4.22), respectively.

$$n_{cells}\, V_M^{(1\,cell)} \frac{1}{\vartheta_M} \frac{\partial \chi_{i,M}}{\partial \tau} = \Gamma_{IIR,out} \times (\chi_{i,IIR,out} - \chi_{i,M}) \tag{4.21}$$

$$n_{cells}\, V_M^{(1\,cell)} \frac{\overline{c_P}_M}{\vartheta_M} \frac{\partial \vartheta_M}{\partial \tau} = \Gamma_{IIR,out}\, \overline{c_P}_{IIR,out} \times (\vartheta_{IIR,out} - \vartheta_M) - Q_M \tag{4.22}$$

where Q_M denotes the energy loss to the environment.

The molar mass flux, Γ_M, is given by

$$\Gamma_M = \Gamma_{IIR,out} \times \left(1 + \frac{\overline{c_P}_{IIR,out}}{\overline{c_P}_M} \times \left(\frac{\vartheta_{IIR,out}}{\vartheta_M} - 1 \right) \right) - \frac{Q_M}{\overline{c_P}_M\, \vartheta_M} \tag{4.23}$$

In the gas manifold, a heat loss to the environment, Q_M, is considered using a linear approach:

$$Q_M = St_M \times (\vartheta_M - \vartheta_U) \tag{4.24}$$

4.4.5. Anode Gas Phase

According to the results presented in Chapter 3 for the detailed model of the anode, the model developed by Heidebrecht *et al.* is an adequate description of the anode gas phase (A). One anode gas compartment has to be modelled for each of the simulated
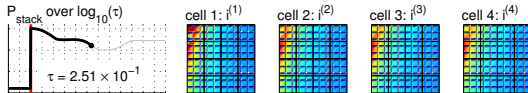
fuel cells, which are identified by the upper index k. In the anode gas channels, both reforming reactions ((ref1) and (ref2)) as well as both electrochemical oxidation reactions ((ox1) and (ox2)) are considered. The component mole fractions, $\chi_{i,A}^{(k)}$, the temperature, $\vartheta_A^{(k)}$, and the molar mass flux density, $\gamma_A^{(k)}$, are given by the component mass balances (Eq. (4.25)), the energy balance (Eq. (4.26)) and the total mass balance (Eq. (4.27)).

$$
V_A \frac{1}{\vartheta_A^{(k)}} \frac{\partial \chi_{i,A}^{(k)}}{\partial \tau} = -\gamma_A^{(k)} \frac{d\chi_{i,A}^{(k)}}{d\zeta_1} + \left[n_{i,AS}^{(k)} - \chi_{i,A}^{(k)} \sum_l n_{l,AS}^{(k)} \right]
$$
$$
+ \sum_{j=\text{ref}} \left(\nu_{i,j} - \chi_{i,A}^{(k)} \bar{\nu}_j \right) \times Da_{j,A}\, r_{j,A}^{(k)} \tag{4.25}
$$

$$
V_A \frac{\overline{c}_{PA}^{(k)}}{\vartheta_A^{(k)}} \frac{\partial \vartheta_A^{(k)}}{\partial \tau} = -\gamma_A^{(k)} \overline{c}_{PA}^{(k)} \frac{d\vartheta_A^{(k)}}{d\zeta_1} + \left(\sum_i n_{i,AS}^{(k)+}\, c_{Pi} \right) \times \left(\vartheta_S^{(k)} - \vartheta_A^{(k)} \right)
$$
$$
+ \sum_{j=\text{ref}} \left(-\Delta_R h_j^\theta \left(\vartheta_A^{(k)} \right) \right) \times Da_{j,A}\, r_{j,A}^{(k)} + q_{AS}^{(k)} \tag{4.26}
$$

$$
0 = -\frac{d\left(\gamma_A^{(k)} \vartheta_A^{(k)} \right)}{d\zeta_1} + \frac{1}{\overline{c}_{PA}^{(k)}} \times \left(\left(\sum_i n_{i,AS}^{(k)+}\, c_{Pi} \right) \times \left(\vartheta_S^{(k)} - \vartheta_A^{(k)} \right) \right.
$$
$$
\left. + \sum_{j=\text{ref}} \left(-\Delta_R h_j^\theta \left(\vartheta_A^{(k)} \right) \right) \times Da_{j,A}\, r_{j,A}^{(k)} + q_{AS}^{(k)} \right)
$$
$$
+ \vartheta_A^{(k)} \sum_i n_{i,AS}^{(k)} + \vartheta_A^{(k)} \sum_{j=\text{ref}} \bar{\nu}_j\, Da_{j,A}\, r_{j,A}^{(k)} \tag{4.27}
$$

In these equations, $n_{i,AS}^{(k)}$ denotes the component mass flux density between the anode gas channels and the electrode pores. It is defined using linear mass transport kinetics:

$$
n_{i,AS}^{(k)} = D_{i,AS} \times \left(\varphi_{i,AC}^{(k)} - \chi_{i,A}^{(k)} \right) \tag{4.28}
$$

$$
n_{i,AS}^{(k)+} = \begin{cases} n_{i,AS}^{(k)}, & \text{if } n_{i,AS}^{(k)} > 0 \\ 0, & \text{if } n_{i,AS}^{(k)} \le 0 \end{cases} \tag{4.29}
$$

with $\varphi_{i,AC}^{(k)}$ denoting the gas composition inside the electrode pores in terms of partial pressures. It is described in more detail in Section 4.4.10.

The heat flux density between the anode gas channels and the solid phase, $q_{AS}^{(k)}$, depends on the temperature difference between these phases:

$$
q_{AS}^{(k)} = St_{AS} \times \left(\vartheta_S^{(k)} - \vartheta_A^{(k)} \right) \tag{4.30}
$$
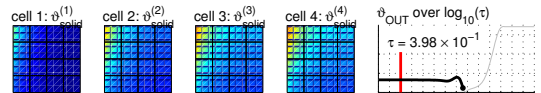
The gas from the IIR unit is equally distributed to all fuel cells. The boundary conditions for the mole fractions, the temperature and the molar mass flux density at the inlet of each anode gas compartment ($\partial\Omega_1$ in Fig. 4.2) are given by

$$\chi_{i,A}^{(k)}(\zeta_1 = 0, \zeta_2, \tau) = \chi_{i,A,in}^{(k)} = \chi_{i,M} \tag{4.31}$$

$$\vartheta_A^{(k)}(\zeta_1 = 0, \zeta_2, \tau) = \vartheta_{A,in}^{(k)} = \vartheta_M \tag{4.32}$$

$$\gamma_A^{(k)}(\zeta_1 = 0, \zeta_2, \tau) = \gamma_{A,in}^{(k)} = \frac{\Gamma_M}{n_{cells}} \tag{4.33}$$

$$\text{for } k = 1, \ldots, n_{cells}$$

At the anode outlets ($\partial\Omega_4$ in Fig. 4.2), average values for the mole fractions, $\chi_{i,A,out}$, and the temperature, $\vartheta_{A,out}$, as well as the total molar mass flux of the exhaust gas, $\Gamma_{A,out}$, are needed. They are calculated using equations similar to the equations at the outlet of the IIR unit (Eqs. (4.14) to (4.16)), but a summation over all cells is added.

$$\Gamma_{A,out}\,\chi_{i,A,out} = \sum_{k=1}^{n_{cells}} \int_0^1 \left[\gamma_A^{(k)}\,\chi_{i,A}^{(k)}\right]_{\zeta_1=1,\zeta_2} d\zeta_2 \tag{4.34}$$

$$\Gamma_{A,out}\,\overline{c}_{P_{A,out}} \times (\vartheta_{A,out} - \vartheta^r) = \sum_{k=1}^{n_{cells}} \int_0^1 \left[\gamma_A^{(k)}\overline{c}_{P_A}^{(k)} \times \left(\vartheta_A^{(k)} - \vartheta^r\right)\right]_{\zeta_1=1,\zeta_2} d\zeta_2 \tag{4.35}$$

$$\Gamma_{A,out} = \sum_{k=1}^{n_{cells}} \int_0^1 \left[\gamma_A^{(k)}\right]_{\zeta_1=1,\zeta_2} d\zeta_2 \tag{4.36}$$

4.4.6. Catalytic Combustion Chamber

In the catalytic combustion chamber (B), the anode exhaust gas (A, out) is mixed with air (AIR) and the gas from the cathode gas recycle (REC). Furthermore, all non-oxidised components of the gas are fully oxidised.

The equations for the component mass balance and the energy balance read:

$$\Gamma_B\,\chi_{i,B} = \sum_l \Gamma_l \times \left(\chi_{i,l} + \sum_{j=\text{comb}} \nu_{i,C_j}\chi_{j,l}\right) \tag{4.37}$$

$$\text{for}\quad l = A, out; REC; AIR$$

$$\Gamma_B\,\overline{c}_{P_B} \times (\vartheta_B - \vartheta^r) = \sum_l \Gamma_l \times \left(\overline{c}_{P_l} \times (\vartheta_l - \vartheta^r) + \sum_i \chi_{i,l} \times \left(-\Delta_C h_i^\theta(\vartheta^r)\right)\right) \tag{4.38}$$

$$\text{for}\quad l = A, out; REC; AIR$$
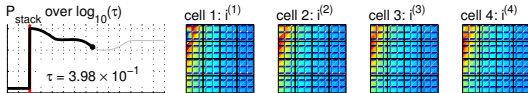
while the total mass balance is given by:

$$\Gamma_B = \sum_l \Gamma_l \times \left(1 + \sum_{j=\text{comb}} \bar{\nu}_{C_j} \chi_{j,l} \right) \tag{4.39}$$

$$\text{for} \quad l = A, out; REC; AIR$$

The air temperature, ϑ_{AIR}, the air composition, $\chi_{i,AIR}$, and the total molar mass flux of air, Γ_{AIR}, are input parameters of the model (see Table 6.1 in Section 6.1).

4.4.7. Reversal Chamber

The reversal chamber (RC) is a large volume located between the catalytic combustion chamber and the hot side of the heat exchanger. For simplicity, it is modelled as a well-mixed tank in analogy to the heat exchanger (HEA and HEB) and the gas manifold (M):

$$n_{cells} V_{RC}^{(1\,cell)} \frac{1}{\vartheta_{RC}} \frac{\partial \chi_{i,RC}}{\partial \tau} = \Gamma_B \times (\chi_{i,B} - \chi_{i,RC}) \tag{4.40}$$

$$n_{cells} V_{RC}^{(1\,cell)} \frac{\overline{c_P}_{RC}}{\vartheta_{RC}} \frac{\partial \vartheta_{RC}}{\partial \tau} = \Gamma_B \overline{c_P}_B \times (\vartheta_B - \vartheta_{RC}) - Q_{RC} + P_{blower} \tag{4.41}$$

$$\Gamma_{RC} = \Gamma_B \times \left(1 + \frac{\overline{c_P}_B}{\overline{c_P}_{RC}} \times \left(\frac{\vartheta_B}{\vartheta_{RC}} - 1 \right) \right)$$

$$- \frac{Q_{RC}}{\overline{c_P}_{RC}\, \vartheta_{RC}} + \frac{P_{blower}}{\overline{c_P}_{RC}\, \vartheta_{RC}} \tag{4.42}$$

In the reversal chamber, the energy input of the gas blower, P_{blower}, as well as the heat loss to the environment, Q_{RC}, are taken into account. A linear approach is used for the heat loss, Q_{RC}:

$$Q_{RC} = St_{RC} \times (\vartheta_{RC} - \vartheta_U) \tag{4.43}$$

while the energy input due to the gas blower, P_{blower}, is listed in Table 6.1 as an input parameter (Section 6.1).

4.4.8. Heat Exchanger (Hot Side)

The hot side of the heat exchanger (HEB) is located after the reversal chamber (B) and before the cathode gas compartments. It is modelled using analogous equations
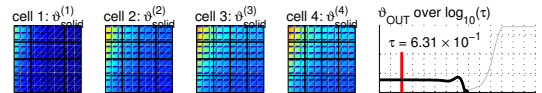
as for the cold side of the heat exchanger (HEA). The component mass fractions, $\chi_{i,HEB}$ and the gas temperature, ϑ_{HEB}, are given by:

$$n_{cells}\, V_{HEB}^{(1\,cell)} \frac{1}{\vartheta_{HEB}} \frac{\partial \chi_{i,HEB}}{\partial \tau} = \Gamma_{RC} \times (\chi_{i,HEB} - \chi_{i,HEB}) \tag{4.44}$$

$$n_{cells}\, V_{HEB}^{(1\,cell)} \frac{\overline{c_P}_{HEB}}{\vartheta_{HEB}} \frac{\partial \vartheta_{HEB}}{\partial \tau} = \Gamma_{RC}\, \overline{c_P}_{RC} \times (\vartheta_{RC} - \vartheta_{HEB}) + Q_{HE} \tag{4.45}$$

while the total molar mass flux, Γ_{HEA}, is calculated as:

$$\Gamma_{HEB} = \Gamma_{RC} \times \left(1 + \frac{\overline{c_P}_{RC}}{\overline{c_P}_{HEB}} \times \left(\frac{\vartheta_{RC}}{\vartheta_{HEB}} - 1\right)\right) + \frac{Q_{HE}}{\overline{c_P}_{HEB}\, \vartheta_{HEB}} \tag{4.46}$$

The heat flux between the two sides of the heat exchanger, Q_{HE}, is calculated according to Eq. (4.4) (Section 4.4.2).

4.4.9. Cathode Gas Phase

The cathode gas phase (C) is modelled analogously to the anode gas phase. Because anode and cathode gas flows are arranged in cross flow configuration, the main gas flow direction in the cathode follows the second spatial coordinate, ζ_2. The electrochemical reduction (red) is the only reaction considered here. Eqs. (4.47) and (4.48) describe the mole fractions, $\chi_{i,C}^{(k)}$ and the temperature, $\vartheta_C^{(k)}$, in the cathode channels.

$$V_C \frac{1}{\vartheta_C^{(k)}} \frac{\partial \chi_{i,C}^{(k)}}{\partial \tau} = -\gamma_C^{(k)} \frac{d\chi_{i,C}^{(k)}}{d\zeta_2} + \left[n_{i,CS}^{(k)} - \chi_{i,C}^{(k)} \sum_l n_{l,CS}^{(k)}\right] \tag{4.47}$$

$$V_C \frac{\overline{c_P}_C^{(k)}}{\vartheta_C^{(k)}} \frac{\partial \vartheta_C^{(k)}}{\partial \tau} = -\gamma_C^{(k)}\, \overline{c_P}_C^{(k)} \frac{d\vartheta_C^{(k)}}{d\zeta_2} + \left(\sum_i n_{i,CS}^{(k)+}\, c_{Pi}\right) \times \left(\vartheta_S^{(k)} - \vartheta_C^{(k)}\right) + q_{CS}^{(k)} \tag{4.48}$$

The total molar mass flux, $\gamma_C^{(k)}$, is given by

$$0 = -\frac{d\left(\gamma_C^{(k)}\, \vartheta_C^{(k)}\right)}{d\zeta_2} + \frac{1}{\overline{c_P}_C^{(k)}} \times \left(\left(\sum_i n_{i,CS}^{(k)+}\, c_{Pi}\right) \times \left(\vartheta_S^{(k)} - \vartheta_C^{(k)}\right) + q_{CS}^{(k)}\right)$$
$$+ \vartheta_C^{(k)} \sum_i n_{i,CS}^{(k)} \tag{4.49}$$

The equations for the mass transport to the electrode pores as well as for the boundary conditions and the calculation of average values at the outlets are similar to the
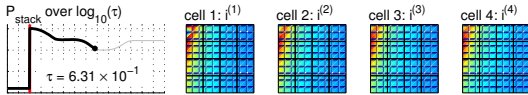
equations used for the anode (Eqs. (4.28) to (4.36)). The component molar mass flux density between the cathode gas channels and the electrode pores is defined as

$$n_{i,CS}^{(k)} = D_{i,CS} \times \left(\varphi_{i,CC}^{(k)} - \chi_{i,C}^{(k)} \right) \tag{4.50}$$

$$n_{i,CS}^{(k)+} = \begin{cases} n_{i,CS}^{(k)}, & \text{if } n_{i,CS}^{(k)} > 0 \\ 0, & \text{if } n_{i,CS}^{(k)} \leq 0 \end{cases} \tag{4.51}$$

The heat flux density between the anode and the solid phase is given by:

$$q_{CS}^{(k)} = St_{CS} \times \left(\vartheta_{S}^{(k)} - \vartheta_{C}^{(k)} \right) \tag{4.52}$$

For the inlet boundary conditions ($\partial\Omega_2$ in Fig. 4.2), the properties of the gas flow from the reversal chamber are used. The gas flow is equally distributed to all cathodes.

$$\chi_{i,C}^{(k)} (\zeta_1, \zeta_2 = 0, \tau) = \chi_{i,C,in}^{(k)} = \chi_{i,HEB} \tag{4.53}$$

$$\vartheta_{C}^{(k)} (\zeta_1, \zeta_2 = 0, \tau) = \vartheta_{C,in}^{(k)} = \vartheta_{HEB} \tag{4.54}$$

$$\gamma_{C}^{(k)} (\zeta_1, \zeta_2 = 0, \tau) = \gamma_{C,in}^{(k)} = \frac{\Gamma_{HEB}}{n_{cells}} \tag{4.55}$$

$$\text{for } k = 1, \ldots, n_{cells}$$

At the cathode outlets ($\partial\Omega_3$ in Fig. 4.2), average values for the composition of the gas, $\chi_{i,C,out}$, and the temperature of the gas, $\vartheta_{C,out}$, as well as for the total molar mass flux, $\Gamma_{C,out}$, are calculated:

$$\Gamma_{C,out} \chi_{i,C,out} = \sum_{k=1}^{n_{cells}} \int_0^1 \left[\gamma_C^{(k)} \chi_{i,C}^{(k)} \right]_{\zeta_1, \zeta_2 = 1} d\zeta_1 \tag{4.56}$$

$$\Gamma_{C,out} \overline{c}_{P_{C,out}} \times \left(\vartheta_{C,out} - \vartheta^r \right) = \sum_{k=1}^{n_{cells}} \int_0^1 \left[\gamma_C^{(k)} \overline{c}_{P_C}^{(k)} \times \left(\vartheta_C^{(k)} - \vartheta^r \right) \right]_{\zeta_1, \zeta_2 = 1} d\zeta_1 \tag{4.57}$$

$$\Gamma_{C,out} = \sum_{k=1}^{n_{cells}} \int_0^1 \left[\gamma_C^{(k)} \right]_{\zeta_1, \zeta_2 = 1} d\zeta_1 \tag{4.58}$$

A part of the cathode exhaust gas is recycled (*REC*). The cathode gas recycle ratio, f_{REC}, determines the gas fraction of cathode exhaust gas that is redirected towards
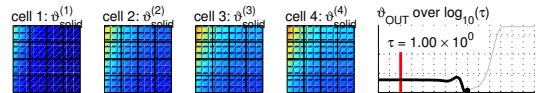
the catalytic combustion chamber (B). The value used for f_{REC} is given in Table 6.1 in Section 6.1.

$$\chi_{i,REC} = \chi_{i,C,out} \tag{4.59}$$

$$\vartheta_{REC} = \vartheta_{C,out} \tag{4.60}$$

$$\Gamma_{REC} = f_{REC}\,\Gamma_{C,out} \tag{4.61}$$

The cathode exhaust gas which is not recycled leaves the fuel cell system as exhaust gas (OUT).

$$\chi_{i,OUT} = \chi_{i,C,out} \tag{4.62}$$

$$\vartheta_{OUT} = \vartheta_{C,out} \tag{4.63}$$

$$\Gamma_{OUT} = (1 - f_{REC})\,\Gamma_{C,out} \tag{4.64}$$

4.4.10. Electrode Pores

Within the pores of anode and cathode, the electrochemical reactions take place. The spatial distribution of the gas composition along the pore is neglected. Instead, integral mass balance is used to describe the partial pressure of all gas components in the electrode pores, $\varphi_{i,AC}^{(k)}$ and $\varphi_{i,CC}^{(k)}$. The oxidation of hydrogen (ox1) and carbon monoxide (ox2) are considered in the anode pores:

$$V_{AC}\frac{1}{\vartheta_S^{(k)}}\frac{\partial \varphi_{i,AC}^{(k)}}{\partial \tau} = \sum_{j=\mathrm{ox}} \nu_{i,j}\,Da_{j,AC}\,r_{j,AC}^{(k)} - n_{i,AS}^{(k)} \tag{4.65}$$

In the cathode pores, the reduction of oxygen (red) takes place:

$$V_{CC}\frac{1}{\vartheta_S^{(k)}}\frac{\partial \varphi_{i,CC}^{(k)}}{\partial \tau} = \sum_{j=\mathrm{red}} \nu_{i,j}\,Da_{j,CC}\,r_{j,CC}^{(k)} - n_{i,CS}^{(k)} \tag{4.66}$$

The component mass fluxes between the gas channels and the electrode pores, $n_{i,AS}^{(k)}$ and $n_{i,CS}^{(k)}$, are given by Eq. (4.28) and Eq. (4.50), respectively. Regarding the enthalpy balance, the electrode pores are considered as part of the solid phase. Thus the temperature of the gas in the pores is equal to the temperature of the solid phase (Section 4.4.11).

4.4.11. Solid Phase

The enthalpy balance in the solid phase (S) of each fuel cell (Eq. (4.67)) describes heat conduction along the cell plane, enthalpy transport due to mass transfer between the anode and cathode gas channels and the electrode pores as well as different heat
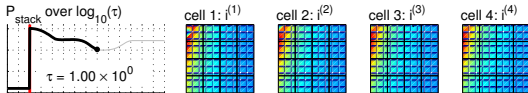
sources. Besides the non-convective heat transport between both gas phases and the solid phase, $q_{AS}^{(k)}$ and $q_{CS}^{(k)}$, the heat source due to the electrochemical reactions and the ion conduction ,$q_{S,cell}^{(k)}$, and the heat transport along the stack, $q_{S,stack}^{(k)}$, are considered.

$$
c_{PS} \frac{\partial \vartheta_S^{(k)}}{\partial \tau} = \frac{l_2}{Pe_S} \frac{\partial^2 \vartheta_S^{(k)}}{\partial \zeta_1^2} + \frac{1}{Pe_S\, l_2} \frac{\partial^2 \vartheta_S^{(k)}}{\partial \zeta_2^2} + \left(\sum_i \left(-n_{i,AS}^{(k)-} \right) c_{Pi} \right) \times \left(\vartheta_A^{(k)} - \vartheta_S^{(k)} \right)
$$

$$
+ \left(\sum_i \left(-n_{i,CS}^{(k)-} \right) c_{Pi} \right) \times \left(\vartheta_C^{(k)} - \vartheta_S^{(k)} \right) - q_{AS}^{(k)} - q_{CS}^{(k)}
$$

$$
+ q_{S,cell}^{(k)} + q_{S,stack}^{(k)} \tag{4.67}
$$

The molar mass flux densities from the anode gas channels to the solid phase are given by

$$
n_{i,AS}^{(k)-} = \begin{cases} 0, & \text{if } n_{i,AS}^{(k)} > 0 \\ n_{i,AS}^{(k)}, & \text{if } n_{i,AS}^{(k)} \leq 0 \end{cases} \tag{4.68}
$$

and for the cathode gas channels an analogous definition is used

$$
n_{i,CS}^{(k)-} = \begin{cases} 0, & \text{if } n_{i,CS}^{(k)} > 0 \\ n_{i,CS}^{(k)}, & \text{if } n_{i,CS}^{(k)} \leq 0 \end{cases} \tag{4.69}
$$

The heat source density in the solid phase, $q_{S,cell}$, includes the heat released due to the electrochemical reactions at the anode and cathode as well as Joule heating due to the ion transport:

$$
q_{S,cell}^{(k)} = \sum_{j=\text{ox}} \left(-\Delta_R h_j^\theta(\vartheta_S^{(k)}) + n_j \times \left(\phi_A^{(k),S} - \phi_A^{(k),L} \right) \right) \times Da_{j,AC}\, r_{j,AC}^{(k)}
$$

$$
+ \sum_{j=\text{red}} \left(-\Delta_R h_j^\theta(\vartheta_S^{(k)}) + n_j \times \left(\phi_C^{(k),S} - \phi_C^{(k),L} \right) \right) \times Da_{j,CC}\, r_{j,CC}^{(k)}
$$

$$
+ \left(\phi_A^{(k),L} - \phi_C^{(k),L} \right) \times i_E^{(k)} \frac{1}{F} \tag{4.70}
$$

The heat transport in stack direction, $q_{S,stack}^{(k)}$, depends on the location of the fuel cell in the symmetric stack model, i. e.:

$$
q_{S,stack}^{(k)} = \begin{cases} q_{S,IIR} - q_{S,conn}^{(k),(k+1)} & \text{, if} & k = 1 \\ q_{S,conn}^{(k-1),(k)} - q_{S,conn}^{(k),(k+1)} & \text{, if} & 1 < k < n_{cells} \\ q_{S,conn}^{(k-1),(k)} & \text{, if} & k = n_{cells} \end{cases} \tag{4.71}
$$
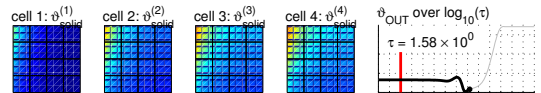
Eq. (4.71) shows that each fuel cell is thermally connected with its two neighbouring fuel cells. According to the symmetric boundary conditions on both sides of the symmetric stack model, the IIR unit is directly connected to the first fuel cell, while the last fuel cell is only connected to its predecessor.

The heat flux density between the solid phases of two neighbouring fuel cells, $q_{S,conn}^{(k),(k+1)}$, depends on the temperature difference between the corresponding solid phases:

$$q_{S,conn}^{(k),(k+1)} = St_S \times \left(\vartheta_S^{(k)} - \vartheta_S^{(k+1)} \right) \tag{4.72}$$

The heat flux density between the IIR unit and the first fuel cell, $q_{S,IIR}$, is given by Eq. (4.17) (Section 4.4.3).

The heat loss of the solid phase to the environment is not considered in the model. Thus, isolation conditions are used on all boundaries of the solid phase ($\partial\Omega_1$ to $\partial\Omega_4$ in Fig. 4.2):

$$\frac{\partial \vartheta_S^{(k)}}{\partial \zeta} = 0 \tag{4.73}$$

4.4.12. Charged Double Layer Model

The description of the electrical potential field is of essential importance for the determination of the current density distribution. For each cell, the dynamic charge balances at both charged double layers are set up and combined with a discretised form of the Poisson equation. The electrical potential in one fuel cell is shown in Fig. 4.3 [22].
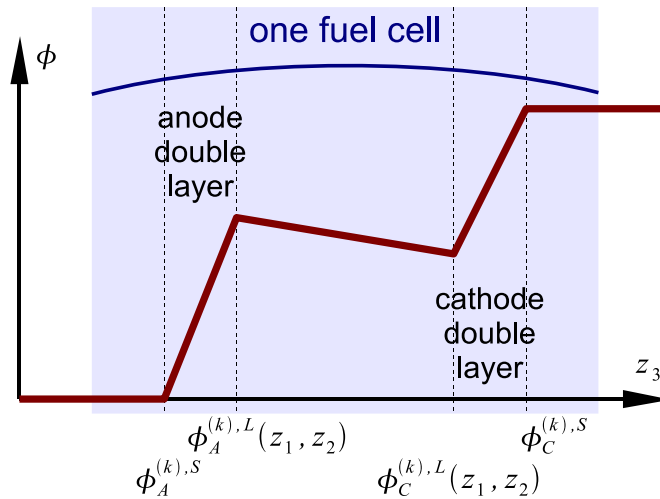

Figure 4.3.: Electrical potential in one fuel cell.
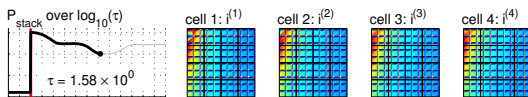
The electrical potential at the anode, $\phi_A^{(k),S}$, is arbitrarily set to zero.

$$\phi_A^{(k),S} = 0 \tag{4.74}$$

The spatially distributed potentials in the electrolyte near the anode and cathode double layer change, $\phi_A^{(k),L}$ and $\phi_C^{(k),L}$, depend on the local current density from the electrode, $i^{(k)}$, $i_A^{(k)}$ and $i_E^{(k)}$.

$$\frac{\partial \phi_A^{(k),L}}{\partial \tau} = -\frac{1}{c_A} \times \left(i^{(k)} - i_A^{(k)} \right) \tag{4.75}$$

$$\frac{\partial \phi_C^{(k),L}}{\partial \tau} = -\frac{1}{c_A} \times \left(i^{(k)} - i_A^{(k)} \right) - \frac{1}{c_E} \times \left(i^{(k)} - i_E^{(k)} \right) \tag{4.76}$$

Accordingly to the model assumption j) (Section 4.3), a spatially constant potential is defined for the cathode, $\phi_C^{(k),S}$. It depends on the differences between the overall currents in the anode, the electrolyte and the cathode ($I_A^{(k)}$, $I_E^{(k)}$ and $I_C^{(k)}$) and the given total cell current, I_{cell}.

$$\frac{\mathrm{d}\phi_C^{(k),S}}{\mathrm{d}\tau} = \frac{I_{cell} - I_A^{(k)}}{c_A} + \frac{I_{cell} - I_E^{(k)}}{c_E} + \frac{I_{cell} - I_C^{(k)}}{c_C} \tag{4.77}$$

The specific currents and current densities at the anode, through the electrolyte and at the cathode are given by the kinetics of the electrochemical reactions (Eqs. (4.79) and (4.83)) and the kinetics of the ion conduction in the electrolyte (Eq. (4.81)):

$$I_A^{(k)} = \int i_A^{(k)} \mathrm{d}\zeta \tag{4.78}$$

$$i_A^{(k)} = \sum_{j=\mathrm{ox}} n_j \, F \, Da_{j,AC} \, r_{j,AC}^{(k)} \left(\phi_A^{(k),S}, \phi_A^{(k),L} \right) \tag{4.79}$$

$$I_E^{(k)} = \int i_E^{(k)} \mathrm{d}\zeta \tag{4.80}$$

$$i_E^{(k)} = \kappa_E \times \left(\phi_A^{(k),L} - \phi_C^{(k),L} \right) \tag{4.81}$$

$$I_C^{(k)} = \int i_C^{(k)} \mathrm{d}\zeta \tag{4.82}$$

$$i_C^{(k)} = -\sum_{j=\mathrm{red}} n_j \, F \, Da_{j,CC} \, r_{j,CC}^{(k)} \left(\phi_C^{(k),S}, \phi_C^{(k),L} \right) \tag{4.83}$$

with $r_{j,AC}^{(k)}$ and $r_{j,CC}^{(k)}$ representing the Butler-Volmer kinetics at both electrodes (see Section 4.5).
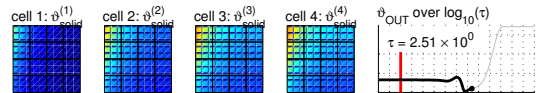
The distribution of the total current over the fuel cell electrodes is calculated depending on the specific currents and the specific current densities according to:

$$i^{(k)} = \left(\frac{1}{c_A} + \frac{1}{c_E} + \frac{1}{c_C}\right)^{-1} \times \left(\frac{i_A^{(k)}}{c_A} + \frac{i_E^{(k)}}{c_E} + \frac{i_C^{(k)}}{c_C} - \frac{I_A^{(k)}}{c_A} - \frac{I_E^{(k)}}{c_E} - \frac{I_C^{(k)}}{c_C}\right) + I_{cell} \tag{4.84}$$

The cell voltage, $U_{cell}^{(k)}$, is defined as the electrical potential difference between the cathode and anode solid phase, while the voltage of the entire stack model is calculated as the sum over all single cell voltages:

$$U_{cell}^{(k)} = \phi_C^{(k),S} - \phi_A^{(k),S} = \phi_C^{(k),S} \tag{4.85}$$

$$U_{stack} = \sum_k U_{cell}^{(k)} \tag{4.86}$$

4.5 Reaction Kinetics

The reaction rate expressions used for the methane steam reforming reaction (ref1) and the water gas shift reaction (ref2) taking place in the reactive phase of the IIR unit and in the anode gas channels are given in Section 2.3.4.

For the symmetric stack model, the reaction rates for the electrochemical reactions at the anode and the cathode have to be defined [22]. Butler-Volmer kinetics with an temperature-dependent Arrhenius term are used for the oxidation of hydrogen (ox1) and carbon monoxide (ref1) at the anode:

$$r_{A,\text{ox1}}^{(k)} = \exp\left[Arr_{\text{ox1}} \times \left(\frac{1}{\vartheta_{\text{ox1}}^{\theta}} - \frac{1}{\vartheta_S^{(k)}}\right)\right] \times \left\{\varphi_{\text{H}_2,AC}^{(k)} \exp\left(\alpha_{\text{ox1},+} n_{\text{ox1}} \frac{\eta_{A,\text{ox1}}^{(k)}}{\vartheta_S^{(k)}}\right)\right.$$
$$\left. - \varphi_{\text{H}_2\text{O},AC}^{(k)} \varphi_{\text{CO}_2,AC}^{(k)} \exp\left(-(1-\alpha_{\text{ox1},+}) \times n_{\text{ox1}} \frac{\eta_{A,\text{ox1}}^{(k)}}{\vartheta_S^{(k)}}\right)\right\} \tag{4.87}$$

$$r_{A,\text{ox2}}^{(k)} = \exp\left[Arr_{\text{ox2}} \times \left(\frac{1}{\vartheta_{\text{ox2}}^{\theta}} - \frac{1}{\vartheta_S^{(k)}}\right)\right] \times \left\{\varphi_{\text{CO},AC}^{(k)} \exp\left(\alpha_{\text{ox2},+} n_{\text{ox2}} \frac{\eta_{A,\text{ox2}}^{(k)}}{\vartheta_S^{(k)}}\right)\right.$$
$$\left. - \left(\varphi_{\text{CO}_2,AC}^{(k)}\right)^2 \exp\left(-(1-\alpha_{\text{ox2},+}) \times n_{\text{ox2}} \frac{\eta_{A,\text{ox2}}^{(k)}}{\vartheta_S^{(k)}}\right)\right\} \tag{4.88}$$

with the overpotential at the anode, $\eta_{A,j}^{(k)}$, which is defined as follows:

$$\eta_{A,j}^{(k)} = \left(\phi_A^{(k),S} - \phi_A^{(k),L}\right) - \Delta\phi_{j,0}\left(\vartheta_S^{(k)}\right) \tag{4.89}$$
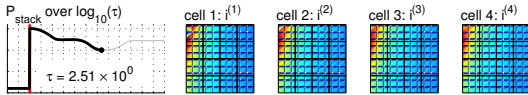
A modified Butler-Volmer kinetics [3, 40, 41] is used for the reduction of oxygen (red) taking place at the cathode:

$$
\begin{aligned}
r_{\text{red}}^{(k)} = \exp\left[Arr_{\text{red}} \times \left(\frac{1}{\vartheta_{\text{red}}^\theta} - \frac{1}{\vartheta_S^{(k)}} \right) \right] &\times \left\{ \left(\varphi_{\text{CO}_2,\text{CC}}^{(k)} \right)^{-2} \exp\left(2.5\, \frac{\eta_{C,\text{red}}^{(k)}}{\vartheta_S} \right) \right. \\
&\left. - \left(\varphi_{\text{O}_2,\text{CC}}^{(k)} \right)^{0.75} \left(\varphi_{\text{CO}_2,\text{CC}}^{(k)} \right)^{-0.5} \exp\left(-0.5\, \frac{\eta_{C,\text{red}}^{(k)}}{\vartheta_S^{(k)}} \right) \right\}
\end{aligned}
\tag{4.90}
$$

The overpotential at the cathode, $\eta_{C,j}^{(k)}$, is defined analogously to the overpotential at the anode:

$$
\eta_{C,j}^{(k)} = \left(\phi_C^{(k),S} - \phi_C^{(k),L} \right) - \Delta\phi_{j,0}\left(\vartheta_S^{(k)} \right)
\tag{4.91}
$$

The standard open circuit voltage for the electrochemical reactions is calculated from the Gibbs enthalpy of reaction:

$$
\Delta\phi_{j,0}\left(\vartheta_S^{(k)} \right) = \frac{\Delta_R g_j^\theta(\vartheta_S^{(k)})}{n_j}
\tag{4.92}
$$

$$
\text{for } j = \text{ox1}; \text{ox2}; \text{red}
$$

A description of the thermodynamic quantities used for the symmetric stack model can be found in Appendix A.2.

4.6 Modelling of the Electrical Potential in the Bipolar Plate

One assumption of the here proposed model is, that the electrical potentials of each cell is independent on the potentials of the neighbouring fuel cells (see assumption j) in Section 4.3). In an *a posteriori* calculation, the electrical potential in the bipolar plates, $\varphi_{BP}^{(k,k+1)}$, can be calculated using the previously calculated results for the current densities in the neighbouring fuel cells, $i^{(k)}$ and $i^{(k+1)}$.

Considering the current density in the bipolar plate, the three-dimensional charge balance equation for the quasi steady state is described by

$$
0 = \frac{\partial \widetilde{i}_{BP,1}^{(k,k+1)}}{\partial z_1} + \frac{\partial \widetilde{i}_{BP,2}^{(k,k+1)}}{\partial z_2} + \frac{\partial \widetilde{i}_{BP,3}^{(k,k+1)}}{\partial z_3}
\tag{4.93}
$$

where z_1 and z_2 are the length and width of the cell plane and the stack direction is denoted by z_3.
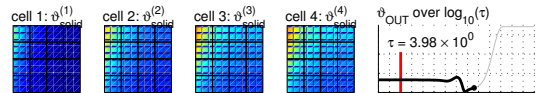
Transformed to a dimensionless form, Eq. (4.93) reads

$$0 = l_2 \frac{\partial i_{BP,1}^{(k,k+1)}}{\partial \zeta_1} + \frac{\partial i_{BP,2}^{(k,k+1)}}{\partial \zeta_2} + l_{BP} \frac{\partial i_{BP,3}^{(k,k+1)}}{\partial \zeta_3} \tag{4.94}$$

with l_2 and l_{BP} as the geometric aspect ratios between the length of the cathode channels and the length of the anode channels and between the length of the cathode channels and the thickness of the bipolar plate, respectively.

An integration of the dimensionless equation over the height of the bipolar plate (ζ_3-coordinate) results in

$$0 = l_2 \int_0^1 \frac{\partial i_{BP,1}^{(k,k+1)}}{\partial \zeta_1} d\zeta_3 + \int_0^1 \frac{\partial i_{BP,2}^{(k,k+1)}}{\partial \zeta_2} d\zeta_3 + l_{BP} \left[i_{BP,3}^{(k,k+1)} \right]_0^1 \tag{4.95}$$

The first and second term on the right hand side of Eq. 4.95 are evaluated assuming constant profiles for the current density in the bipolar plate (ζ_3-directions):

$$i_{BP,1}^{(k,k+1)} (\zeta_3) = \hat{i}_{BP,1}^{(k,k+1)} \tag{4.96}$$

$$i_{BP,2}^{(k,k+1)} (\zeta_3) = \hat{i}_{BP,2}^{(k,k+1)} \tag{4.97}$$

Ohm's law is used to describe the current densities perpendicular to the stack direction, $\hat{i}_{BP,1}^{(k,k+1)}$ and $\hat{i}_{BP,1}^{(k,k+1)}$:

$$\hat{i}_{BP,1}^{(k,k+1)} = -\kappa_{BP} \, l_2 \frac{\partial \varphi_{BP}^{(k,k+1)}}{\partial \zeta_1} \tag{4.98}$$

$$\hat{i}_{BP,2}^{(k,k+1)} = -\kappa_{BP} \frac{\partial \varphi_{BP}^{(k,k+1)}}{\partial \zeta_2} \tag{4.99}$$

with κ_{BP} as the electrical conductivity of the material of the bipolar plate.

Evaluating the last term on the right hand side of Eq. (4.95), the integration limits are given by the current densities in the neighbouring fuel cells:

$$i_{BP,3}^{(k,k+1)} \Big|_{\zeta_3=0} = i^{(k)} , \qquad\qquad i_{BP,3}^{(k,k+1)} \Big|_{\zeta_3=1} = i^{(k+1)} \tag{4.100}$$

After inserting Eqs. (4.96) to (4.100) into Eq. (4.94) and reordering, the equation for the electrical potential, $\varphi_{BP}^{(k,k+1)}$, reads

$$0 = -\kappa_{BP} \, l_2^2 \frac{\partial^2 \varphi_{BP}^{(k,k+1)}}{\partial \zeta_1^2} - \kappa_{BP} \frac{\partial^2 \varphi_{BP}^{(k,k+1)}}{\partial \zeta_2^2} - l_{BP} \times \left(i_{BP}^{(k+1)} - i_{BP}^{(k)} \right) \tag{4.101}$$
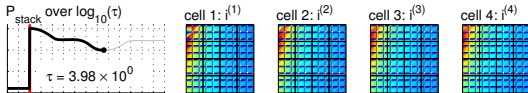
At all edges of the bipolar plate ($\partial\Omega_1$ to $\partial\Omega_4$ in Fig. 4.2), isolation boundary conditions are applied:

$$\mathbf{n} \times \frac{\partial \varphi_{BP}^{(k,k+1)}}{\partial \zeta} = 0 \quad \text{on } \partial\Omega_1 \text{ to } \partial\Omega_4 \tag{4.102}$$

The mathematical problem to solve is an ill-posed problem due to the fact that the boundary condition for the second order differential equation only fix the first derivative but not the value of the variable. Therefore, an additional condition has to be defined. In this case, the potential at the lower right corner point of the bipolar plate is set to zero, *i. e.*

$$\varphi_{BP}^{(k,k+1)} (\zeta_1 = 0, \zeta_2 = 0) = 0 \tag{4.103}$$
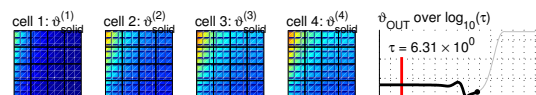
Chapter 5

Numerical Aspects

The symmetric stack model of a Molten Carbonate Fuel Cell presented in the previous chapter is implemented in the commercial simulation environment COMSOL MULTI-PHYSICS [13]. This software tool uses the Finite Element Method (FEM) to solve systems of partial differential equation (PDE).

In this chapter, the background of the Finite Element Method is shortly presented (Section 5.1) before the implementation of the stack model is discussed (Section 5.2) and the solution strategy is presented (Section 5.3). In the last section (Section 5.4), the influence of the mesh size on the quality of the solution is analysed.

5.1 Discretisation According to the Finite Element Method

Many problems in engineering and applied science are governed by differential equations or integral equations. The solution of these equations would provide an exact, closed-form solution to the particular problem being studied. However, due to complexities in the geometry and in the boundary conditions that are present in most real-world problems and due to possibly highly coupled equations, this exact solution can not be obtained or it can not be obtained in a reasonable amount of time. Therefore, numerical algorithms which calculate an approximate solution in reasonable time and with reasonable efforts are developed. The FEM is one of these approximate solution techniques.

To use the FEM, the physical formulation of the problem in the form of (partial) differential equations has to be transformed to its discrete finite element analogue. One family of methods used to numerically solve differential equations are the methods of weighted residuals with its most used variant, the Galerkin Method. The continuous geometry is partitioned into a set of discrete sub-domains of a simple shape, creating the mesh. The solution for the independent variables is approximated in each mesh element by using simple basis functions which can be described by a finite number of parameters. The sum of the parameters needed to approximate the solution in all mesh elements is called degrees of freedom (DoF). It represents a measure for the size
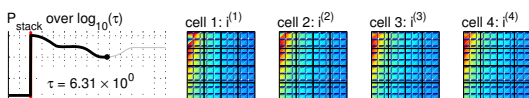
of the problem to be solved. A detailed mathematical foundation of the FEM can be found in the corresponding scientific literature [42].

The advantages of the FEM are that it can easily handle complex geometries, boundary conditions and constraints. It is used for several decades to analyse and solve engineering problems especially in the areas of mechanical engineering. With the availability of easy to use commercial tools, the FEM is one possibility to solve the complex multiphysics equation system which describes a Molten Carbonate Fuel Cell stack. Using the FEM one has to be aware that the result is an approximation of the original problem and a careful check of the physical validity of the solution is needed.

5.2 Implementation

For the implementation of the stack model in Comsol Multiphysics, second order partial differential equations are used as basic templates for all equations. For a transient problem the coefficient form of the equation template reads:

$$e_a \frac{\partial^2 \mathbf{x}}{\partial t^2} + d_a \frac{\partial \mathbf{x}}{\partial t} + \nabla \left(-c\nabla \mathbf{x} - \alpha \, \mathbf{x} + \gamma \right) + \beta \, \nabla \mathbf{x} + a \, \mathbf{x} = f \qquad \text{in } \Omega_{stack} \qquad (5.1)$$

with $\mathbf{x}$ as the independent variables and e_a, d_a, c, α, γ, β, a and f as coefficients of the equation. In the equations of the symmetric stack model, not all of these coefficients are used. The capacity with respect to the considered variable is stored in the coefficient d_a. The coefficient c is used for the Peclet number in the energy balance of the solid phase. β represents the molar mass flux density in the component mass balances and the energy balances of the gas phases. The coefficient f denotes the source term, *e. g.* the source due to Joule heating.

This template for a second order PDE is modified according to the requirements of the corresponding equations in the IIR unit, the anode and cathode gas compartments and the solid phase. The simulation domain Ω_{stack} with the boundaries $\partial\Omega_1$ to $\partial\Omega_4$ is considered (Fig. 5.1). Of the model equations only the conductive heat transport in the solid phase is described by a second order equation on this subdomain. Therefore, the four boundary conditions needed for this equation (two in each direction) can easily be defined. As stated in Eq. (4.73) (Section 4.4.11), isolation conditions are used on the four edges.

With respect to the gas flow in the non-reactive phase of the IIR unit and in the anode and cathode gas compartments, only the convective flow is considered. Furthermore, only one single gas flow direction is assumed. Therefore, the gas flows are described by first order PDEs with one boundary condition for the main flow direction. Due to the second order PDE template used for the definition of the equations, additional - neutral - boundary conditions for the other three edges have to be defined. On the one hand, isolation boundary conditions are used for the edges on the left and right hand side of the main flow direction. On the other hand, only convective gas
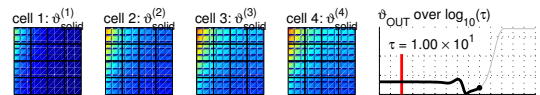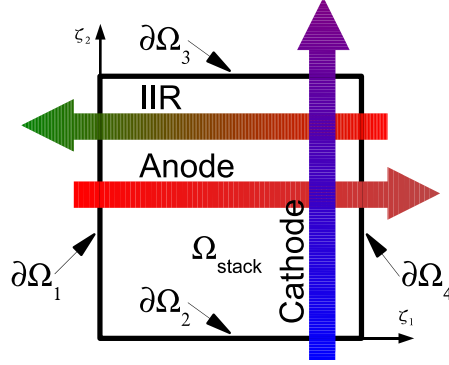
Figure 5.1.: Simulation domain of the symmetric stack model with the gas flow
directions.

flow is considered at the gas outlets. In COMSOL MULTIPHYSICS, this is done by
setting the term representing the diffusive flux in Eq. (5.1), $\nabla\left(-c\nabla\mathbf{x}\right)$, to zero at
the corresponding boundary. Due to the fact that diffusive mass transport as well as
diffusive energy transport are not accounted for in the symmetric stack model, this
term is equal to zero. Thus, this boundary condition does not influence the solution.

Exemplarily, these boundary conditions are evaluated below for the equation of the
mole fractions in the anode gas compartment (see Section. 4.4.5). In COMSOL MUL-
TIPHYSICS, the specialised application mode 'convection and diffusion' is used. It is
based on the definition of the coefficient form (Eq. 5.1) and reads

$$\delta_{ts}\frac{\partial c}{\partial t} + \nabla\left(D\,\nabla c\right) = -\mathbf{u}\nabla c + R \tag{5.2}$$

In the application mode, the variable c is replaced by the mole fraction in the anode
gas, $\chi_{i,A}^{(k)}$, and the molar mass flux density, $\gamma_A^{(k)}$, is inserted as the ζ_1-component of
the vector $\mathbf{u}$. Furthermore, the diffusive flux is neglected ($D = 0$). Considering the
variable δ_{ts} as the capacity of the anode gas compartment and R as the source terms,
the structure of the equation for the mole fraction in the anode gas compartment
(Eq. (4.25)) becomes visible.

$$\delta_{ts}\frac{\partial \chi_{i,A}^{(k)}}{\partial \tau} = -\begin{bmatrix}\gamma_A^{(k)}\\0\end{bmatrix}\nabla\chi_{i,A}^{(k)} + R \tag{5.3}$$

Eq. 5.3 is a first order partial differential equation. Thus, one boundary condition
must be defined. At the gas inlet ($\partial\Omega_1$) the mole fraction is set to the corresponding
mole fraction of the gas in the gas manifold (Eq. (4.31))

$$\chi_{i,A}^{(k)} = \chi_{i,M} \quad \text{on } \partial\Omega_1 \tag{5.4}$$
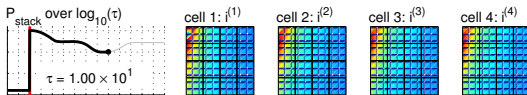
As discussed above, neutral boundary conditions are needed for the other three edges of the simulation domain. At the outlet of the anode compartment ($\partial\Omega_4$), the diffusive flux is set to zero. As discussed above, this boundary condition has not influence on the solution.

$$0 = \mathbf{n} \left(-D\nabla\chi_{i,A}^{(k)} \right) \quad \text{on } \partial\Omega_4 \tag{5.5}$$

For the edges on the left and right hand side of the gas flow ($\partial\Omega_2$ and $\partial\Omega_3$), an isolation boundary condition is used:

$$0 = \mathbf{n} \cdot \left(-D\nabla\chi_{i,A}^{(k)} + \chi_{i,A}^{(k)} \begin{bmatrix} \gamma_A^{(k)} \\ 0 \end{bmatrix} \right) \quad \text{on } \partial\Omega_2 \text{ and } \partial\Omega_3 \tag{5.6}$$

For Eq. 5.6, the directions ζ_1 and ζ_2 have to be analysed separately. The boundary normal vector at these edges is zero in the main flow direction, ζ_1. Thus, the equation is fulfilled for this coordinate. Considering the ζ_2-direction, the first term in the brackets on the right hand side is equal to zero because no diffusion is considered. Due to the fact that there is no molar mass flux density in this direction, the second term is zero as well. Therefore, the second component of the equation is also fulfilled. Thus, this boundary condition has no influence on the solution.

A special case is the equation for the total molar mass flux across the interface between the two phases of the IIR unit (Eq. 4.10). It is not a differential equation, but an implicit algebraic equation which is solved by COMSOL MULTIPHYSICS using the integral form of a partial differential equation, *i. e.* the weak form [13].

While the model has a simple geometry, complex restrains are defined. First, the integral of the current density over the subdomain Ω_{stack} has to be equal to the given cell current. Second, the total molar mass flux and average values for the temperature and gas composition have to be calculated at the outlets of all gas compartments, which requires an integration of the variable over the corresponding outlet boundary. To prevent additional terms at these boundaries due to the coupling variables used to implement these restraints, non-ideal boundary conditions are used. This means that the constraint forces at the boundary are modified to correctly describe the uni-directional fluxes at these edges.

Furthermore, the equations for the molar mass flux density in the non-reactive phase of the IIR unit, in the anode gas compartments and the cathode gas compartments (Eq. (4.7), Eq. (4.27) and Eq. (4.49)) are modified. Considering the coefficient form of a partial differential equation solved in COMSOL MULTIPHYSICS (Eq. (5.1)), only a single variable is provided in the differential terms. Thus, the product of the molar mass flux density, γ, and the gas temperature, ϑ, is replace by the new variable ω:

$$\omega = \gamma\,\vartheta \tag{5.7}$$
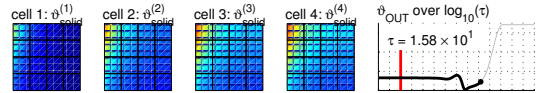
Considering the ideal gas law, a relation between the total concentration and the temperature is given by

$$\widetilde{c}_t = \frac{p}{R\,T} \tag{5.8}$$

In combination with the assumption of isobaric conditions (assumption b) in Section 4.3), Eq. (5.8) can be used to show that ω represents the dimensionless velocity of the gas:

$$\omega = \gamma\,\vartheta = \frac{g}{g^\theta} \times \frac{T}{T^\theta} = \frac{g}{g^\theta} \times \frac{p/(R\,\widetilde{c}_t)}{p/(R\,\widetilde{c}_t^\theta)} = \frac{g/\widetilde{c}_t}{g^\theta/\widetilde{c}_t^\theta} = \frac{u}{u^\theta} \tag{5.9}$$

with the definition of the velocity as the ratio of the molar mass flux density and the total concentration, $u = g/\widetilde{c}_t$.

The dimensionless velocity in the IIR unit is additionally multiplied with the volume fraction of the non-reactive phase. Thus, this variable represents the theoretical velocity in an empty IIR unit. It is independent on the catalyst distribution in the reforming reactor.

$$\omega_{IIR} = \varepsilon^N\,\omega_{IIR}^N = \varepsilon^N\,\gamma_{IIR}^N\,\vartheta_{IIR}^N \tag{5.10}$$

Ordinary Differential Equations (ODE) are used to describe the auxiliary components of the fuel cell stack. The heat exchangers as well as the gas manifold between the IIR unit and the anode gas compartment and the reversal chamber between the anode and cathode gas compartments are modelled as well mixed tanks. The corresponding equations are defined as additional DoF in COMSOL MULTIPHYSICS.

Two types of meshes are available in COMSOL MULTIPHYSICS. On the one hand, an unstructured mesh can be defined. It uses triangular elements in case of a two-dimensional geometry. On the other hand, a mapped mesh consisting of quadrilateral elements is available. Compared to an unstructured mesh, the mapped mesh is structured in a pattern where opposite edges have the same number of elements. An unstructured mesh can easily be generated for complex geometries while fairly regular shaped geometries are needed for mapped meshes. For such simple geometries, a mapped mesh will result in a lower number of DoF but a similar convergence behaviour and quality of the solution as in case of the unstructured mesh.

The symmetric stack model is based on an equidistant mapped mesh taking advantage of the simple geometry. Finite elements based on piecewise polynomials of the degree $k = 2$, the so-called the Lagrange-Quadratic elements, are used as finite elements in the simulations of the symmetric stack model. This means that node points are created at the corners, at the side midpoints and in the centre of each rectangular element. At least a 4×4 mesh of these elements is needed to solve the model. The number of elements per edge is only limited by the amount of RAM available for the calculation.
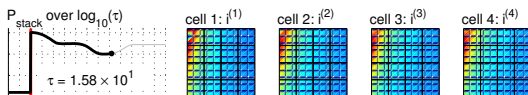
5.3 Solution Strategy

COMSOL MULTIPHYSICS provides different solvers for DAE problems resulting from the FEM discretisation of PDEs. The available set of solvers include among others stationary solvers and time-dependent solvers. They are all available for linear and non-linear problems. Depending on the selected solution type, COMSOL MULTIPHYSICS chooses the time-dependent solver for transient problems or a stationary solver if the steady state solution is requested. In that case, the solver searches for a solution where the accumulation term is zero. All of these solvers break down the given problem into the solution of one or several linear systems of equations. These in turn are solved by a direct or an iterative solver for linear systems [13].

The direct solver uses the Gaussian elimination procedure. This process is stable and reliable. But, while it requires less tuning and is often faster than iterative solvers, it also requires larger memory resources. Applying an indirect solver, the equation system is solved repeatedly, using the output of one iteration as initial guess for the next. Due to the complexity of the symmetric stack model, only the direct solvers converge. The default linear solver of COMSOL MULTIPHYSICS is used in this work (UMFPACK direct solver [48]).

The symmetric stack model is solved in several steps. In the beginning, initial values for all state variables like the temperatures and the mole fractions are defined based on a previous solution of the model. If no such solution is available, values are estimated.

COMSOL MULTIPHYSICS allows the user to define which equations of the model should be solved. The initial values or, if available, the current solution are used for all equations which are not considered. Using this feature, the symmetric stack model is solved in several steps. First, the equations for the gas phases in the IIR unit, in the anode and in the cathode gas compartment are solved on a coarse mesh (4×4) and a relative tolerance of $\mathsf{ntol} = 10^{-6}$. In the next step the equations for the solid temperature and the electrical potential are added to the list of equations to solve. In the last step, the final solution is calculated with a refined mesh (7×7) and a relative tolerance of $\mathsf{ntol} = 10^{-9}$ as convergence criterion.

Taking into account all equations (Chapter 4), the symmetric stack model consists of 114 PDEs and 26 ODEs as well as a number of algebraic equations. These equations are highly coupled to each other due to the connection of the gas compartments *via* the gas flow, the thermal interactions between all parts of the fuel cell, especially in stack direction, and the coupling of the electrochemical reaction rates at the anode and cathode of each fuel cell. Considering four fuel cells on a 7×7 mapped mesh with Lagrange-Quadratic elements, the model has 25.676 degrees of freedom (DoF).

The calculation time required to solve this model adds up to about 30 minutes on a Dual Intel Xeon CPU 3.2 GHz. The size of the models analysed in this work is restricted by the available computational memory. The largest problems solved are a
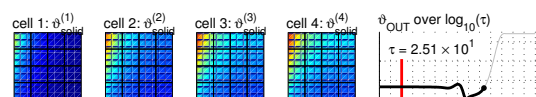
symmetric stack model with 6 fuel cells on a 8×8 mesh and a model with one fuel cell on a 18×18 mesh. Up to $8\,$GB RAM are needed to determine the solutions.

5.4   Influence of the Mesh Size

The quality of a solution depends on several factors. On the one hand, the relative tolerance of the numerical algorithm, **ntol**, defines a convergence criterion of the solution. This criterion considers the error of the numerical approximation of the solution. It is set to a constant value for the final step of all calculations (see Section 5.3). On the other hand, an energy balance as well as balances for each atomic species can be defined to test the physical correctness of the solution approximated by COMSOL MULTIPHYSICS.

Taking into account all energy fluxes or gas fluxes which enter or leave the fuel cell stack, the relative error of these balances can be used to compare solutions calculated using different mesh sizes or different numbers of fuel cells. Increasing these two factors results in an increasing number of DoF, thus increasing the memory requirements and the calculation time. But it also reduces the relative error of the solution. Therefore, one has to find a mesh size which offers a good balance between the computational effort and the numerical precision.

Fig. 5.2 shows the relative error of the enthalpy balance for different mesh sizes and different model configurations, *i. e.* numbers of fuel cells simulated in the symmetric stack model. For each model configuration, the mesh size is increased until a solution of the model is no longer possible in reasonable time or the solution process is aborted due to the fact that the memory requirement exceeds the available computational memory.
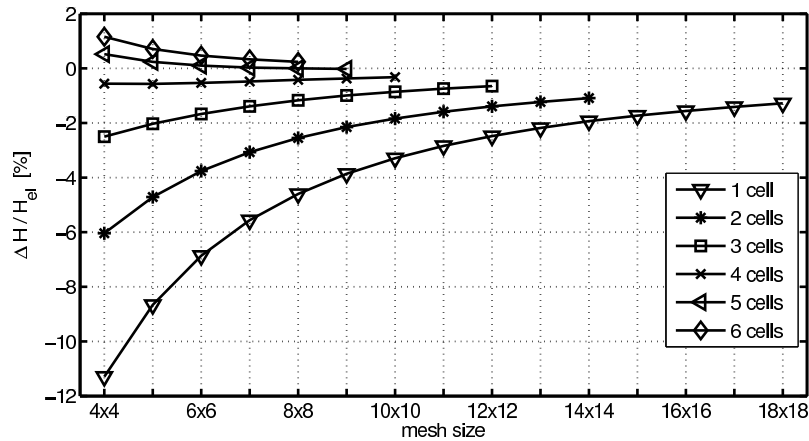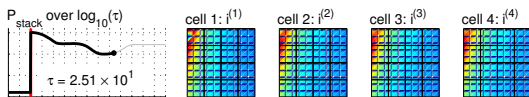

Figure 5.2.: Relative error of the energy balance for different mesh sizes and different numbers of fuel cells included in the symmetric stack model.

The relative error with respect to the energy balance of a solution is defined as the difference between energy fluxes leaving the system and the energy fluxes entering the system related to the electrical output of the simulated part of the stack. The enthalpy of the gas at the gas outlet (*OUT*), the electrical power generated by the fuel cells and the heat losses in the gas manifold and the reversal chamber are considered as energy flows leaving the system while the enthalpy of the feed gas (*IN*) and the enthalpy of the air supply (*AIR*) as well as the electrical power needed for the blower are energy flows entering the system.

$$e_{\mathrm{H}} = \frac{\Delta H}{P_{\mathrm{el}}} = \frac{(H_{OUT} + P_{\mathrm{el}} + Q_M + Q_{RC}) - (H_{IN} + H_{AIR} + P_{blower})}{P_{\mathrm{el}}} \qquad (5.11)$$

Independently of the number of fuel cells considered in the model, a finer mesh always yields a reduced relative error of the energy balance. The highest error of around 12% can be found for a model which is based on a 4×4 mesh and includes one half IIR unit and one fuel cell. For a constant mesh size, the absolute error of the enthalpy balance is reduced with increased numbers of fuel cells simulated.

The main contribution to the relative error of the energy balance comes from the energy balance of the anode (*A*). Within these parts of the model, the reforming reactions as well as the electrochemical reactions are considered. Especially at the anode inlet, high temperatures as well as a high concentration of methane and therefore high reaction rates for all reactions can be observed. Thus, strong second order gradients especially in the temperature profiles occur. These are not accurately represented by the solution approximated by COMSOL MULTIPHYSICS, resulting in the errors shown in Fig. 5.2. Nevertheless, for all variations of the model, the absolute value of the relative error of the enthalpy balance is less than 2% for the finest mesh for which results are available.

The second type of relative errors calculated considers the atomic balances. They are defined as the error between the number of atoms at the gas outlet (*OUT*) and the gas inlets (the feed gas, *IN*, and the air supply, *AIR*), related to the value at the gas outlet. The number of atoms are calculated at the selected points using the gas composition, χ_i, the gas molar mass flux density, γ, and the molecular formula of the gas species.

$$e_{\mathrm{i}} = \frac{\Delta \mathrm{atom}_i}{\mathrm{atom}_{i,OUT}} = \frac{(\mathrm{atom}_{i,OUT}) - (\mathrm{atom}_{i,IN} + \mathrm{atom}_{i,AIR})}{(\mathrm{atom}_{i,OUT})} \qquad (5.12)$$

Fig. 5.3 presents the resulting diagrams. The plots of the errors in the atom balances for carbon, hydrogen and oxygen show a behaviour similar to the relative error of the energy balance (Fig. 5.2). The relative error calculated for the balance of nitrogen is several orders of magnitude smaller. Furthermore, no differences are visible between the calculations with respect to a varying number of fuel cells. The reason is that nitrogen is only present in the reversal chamber (*RC*) and the cathode gas compartment (*C*). Thus, the reactions taking place at the anode do not influence the nitrogen
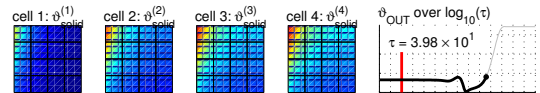
balance. Therefore, the errors in the energy balance and the atom balances of carbon, hydrogen and oxygen are mainly caused by the reactions in the anode gas channel.

(a) Relative error of the carbon atoms balance.

(b) Relative error of the hydrogen atoms balance.

(c) Relative error of the nitrogen atoms balance.

(d) Relative error of the oxygen atoms balance.
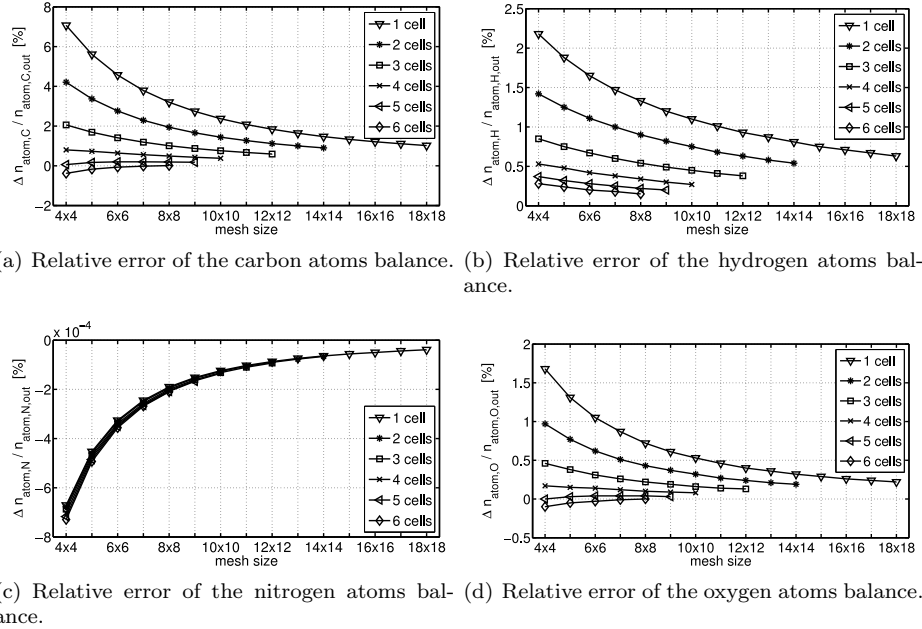
Figure 5.3.: Relative errors for the atom balances of carbon, hydrogen, nitrogen and oxygen.

A relative error below 1% is reached for all configurations of the model and for all four atomic balances if the solutions with the finest mesh is considered. Comparing the results, especially the standard model configuration of one half IIR unit and four fuel cells, a mesh size of 7×7 yields an error of less than 1% with acceptable memory requirements (less than $2\,\mathrm{GB}$) and calculation times (approx. $30\,\mathrm{min}$). Therefore, this mesh size is chosen as the final mesh size used to obtain the simulation results presented in the following chapter.
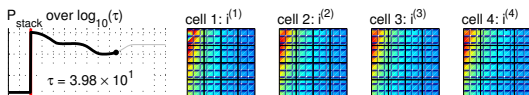
Chapter 6

Simulation Results

In this chapter the simulated results of the symmetric stack model are presented. First, the parameters of the base case are defined and simulation results for these parameters are discussed (Section 6.1). After that, these results are compared to the results of the model validation by Gundermann *et al.* [18] (Section 6.2). In the following section, the symmetric stack model is used to evaluate design variants with regard to the number of fuel cells per IIR unit (Section 6.3). The last part of this chapter, Section 6.4, analyses the energy fluxes in the MCFC system in the symmetric stack model. Exemplarily, configurations with two and eight fuel cells per IIR unit are analysed.

6.1 Base Case

In this section, selected results from the steady state solution of the symmetric stack model with one half IIR unit and four fuel cells are presented in order to demonstrate the functionality and potential of the model.

First, a set of input parameters, the so-called base case, is defined (Table 6.1). These base case conditions correspond to the values of the operating point 4 used in the model validation by Gundermann *et al.* [18, 20]. At this point the MCFC is operated at an average current density of $i_{avg} = 80 \, mA/\text{cm}^2$. The feed gas composition corresponds to a mixture of methane and steam with a steam-to-carbon ratio of about 2.4. The gas is reformed in the external reformer to about 20% conversion. In contrast to the work of Gundermann *et al.*, the here developed symmetric stack model considers the stack direction as an additional coordinate, *i. e.* the impact of the simulation of several fuel cells on the temperature profile along the stack length is shown.

The experimental data used for the model validation done by Gundermann *et al.* was measured on a HOTMODULE system built by MTU Onsite Energy, Germany for typical operating points of the fuel cell system. In order to protect the intellectual property of the industrial partner any absolute values in the following sections are omitted. Instead, the results are discussed qualitatively and conclusions are drawn from that.
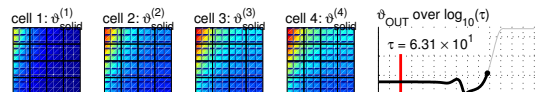
Table 6.1.: Input parameters of the symmetric stack model at base case conditions.

description	variable	dimensionless value
feed gas		
molar mass flux	Γ_{IN}	3.30
temperature	ϑ_{IN}	2.18
methane mole fraction	$\chi_{CH_4,IN}$	0.22
water mole fraction	$\chi_{H_2O,IN}$	0.57
hydrogen mole fraction	$\chi_{H_2,IN}$	0.15
carbon monoxide mole fraction	$\chi_{CO,IN}$	0.00
carbon dioxide mole fraction	$\chi_{CO_2,IN}$	0.05
air		
molar mass flux	Γ_{AIR}	21.96
temperature	ϑ_{AIR}	1.08
oxygen mole fraction	$\chi_{O_2,IN}$	0.21
nitrogen mole fraction	$\chi_{N_2,IN}$	0.79
total cell current	I_{cell}	0.45
electrical power of the blower	P_{blower}	11.10
cathode gas recycle ratio	f_{REC}	0.70
volume fraction in the IIR unit	ε_{IIR}^{N}	0.75

Below, the simulated results of the gas composition in the IIR unit as well as the anode and cathode gas compartments are discussed. Afterwards, the current densities for the four fuel cells are presented. This is followed by a discussion of the temperature distribution in the solid components of each fuel cell - the solid phase - and the resulting temperature profile in stack direction. Furthermore, the electrical potential in the bipolar plates is analysed in order to validate assumption j) of Section 4.3. At the end, results of a dynamic simulation are presented.

6.1.1. Gas Composition

Figures 6.1 to 6.3 show selected profiles of the mole fractions in various gas compartments of the symmetric stack model. In the IIR unit and the anode compartments, especially the methane mole fraction (Fig. 6.1) and the hydrogen mole fraction (Fig. 6.2) are of interest, while in the cathode channels, the mole fraction of carbon dioxide (Fig. 6.3) is more important.

In the IIR unit, about 30% of the methane present at the inlet is converted to hydrogen. The chemical equilibrium is nearly reached in the reactive phase, where the reforming process takes place. Due to the mass transport limitation across the interface, the concentration in the non-reactive phase is further away from a theoretical equilibrium composition. Thus, the composition of the exhaust gas of the IIR unit is not in chemical equilibrium. In the anode channels, the remaining methane reacts
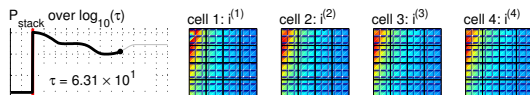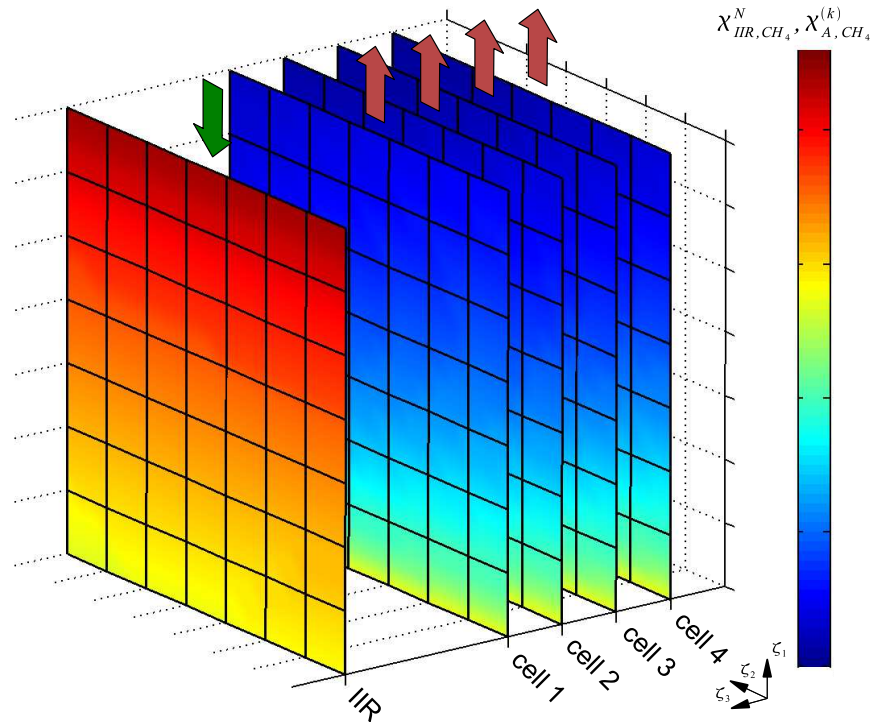
Figure 6.1.: Methane mole fraction in the non-reactive phase of the IIR unit and in the anode gas channels of the four fuel cells.

to hydrogen. The reforming products are continuously consumed by electrochemical oxidation, so the methane concentration reaches nearly zero at the anode outlets.

Fig. 6.2 shows the hydrogen mole fraction in the IIR unit and the four fuel cells. In the IIR unit, methane is converted to hydrogen by methane steam reforming. Hence, the hydrogen mole fraction increases to approximately one third at the outlet of the IIR unit. In the anode gas compartments, two processes occur. On the one hand, hydrogen is produced by steam reforming. On the other hand, hydrogen is consumed by electrochemical reactions. Thus, the hydrogen mole fraction in the anode is constant close to the anode gas inlet and after that decreases towards the gas outlet. The high concentration of hydrogen at the anode inlet also results in high electrochemical reactions rates in this case.

The hydrogen mole fraction is especially low at the anode outlet of cell 1 compared to the hydrogen mole fraction at the outlets of the other fuel cells. The opposite can be observed for the methane mole fraction. This can be attributed to the lower temperatures in cell 1 due to the cooling effect of the neighbouring IIR unit. As a result, the rates of the reforming reactions in the anode gas compartment are reduced and the equilibrium of these reactions is shifted towards the educts.
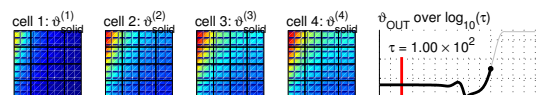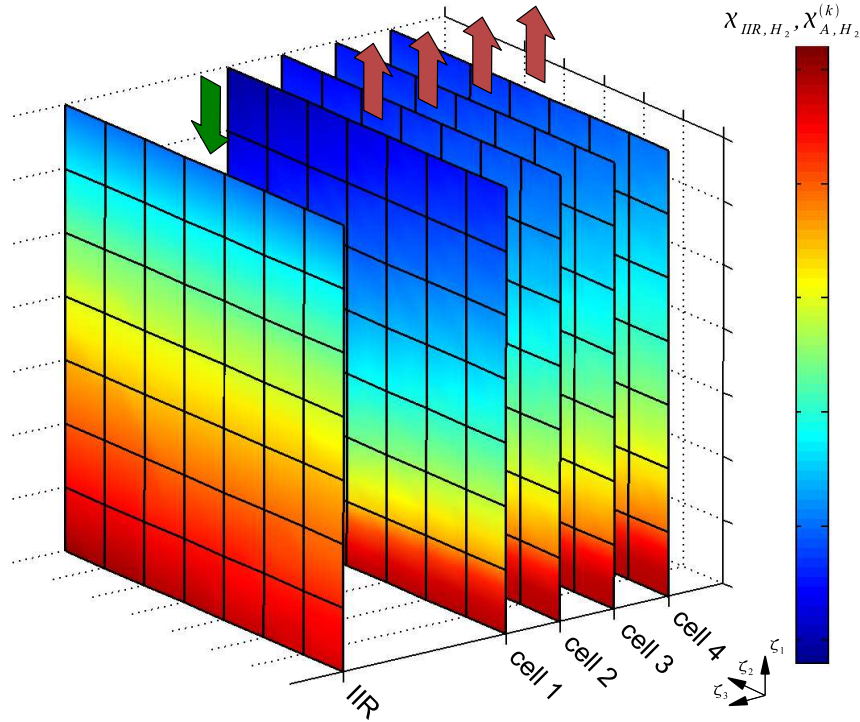
Figure 6.2.: Hydrogen mole fraction in the IIR unit and the anode gas compartments of the four fuel cells.

Carbon dioxide is an important reactant for the electrochemical reduction reaction in the cathode channels. Its mole fraction distribution is depicted in Fig. 6.3. At the cathode inlet, the mole fraction of carbon dioxide is only a few mole percent. Along the channels, carbon dioxide is consumed in the electrochemical reaction. The consumption rate is higher in the lower cathode channels due to higher electrochemical reactions rates. This almost leads to depletion of carbon dioxide near the bottom left corner, where the anode inlet and the cathode outlet are located. Due to the fact that carbon dioxide is needed as an educt for the electrochemical reduction, its concentration, especially at this point, is critical for higher fuel utilisation.

6.1.2. Current Density Distribution

Fig. 6.4 presents the current densities in the four fuel cells with an average cell current density of $i_{cell} = 80\,mA/cm^2$. All profiles are similar to each other. The maximum difference in local current density between two neighbouring cells is less than $\Delta i = 10\,mA/cm^2$, although they are calculated independently. An *a posteriori* calculation of the resulting electrical field in the bipolar plate is discussed in Section 6.1.4.

The rate of the electrochemical reactions, and therefore also the local current density, mainly depends on the temperature in the solid phase and the concentration profiles
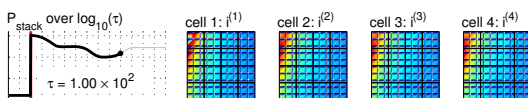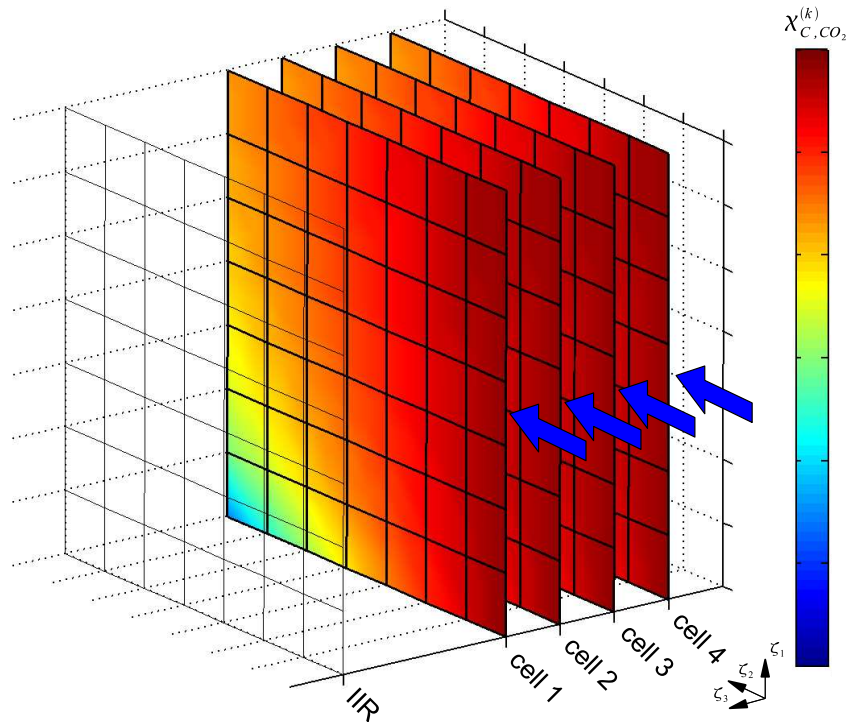
Figure 6.3.: Molar fraction of carbon dioxide in the cathode gas compartments of the four fuel cells.

of the educts of these reactions. Especially the concentrations of hydrogen in the anode channels and carbon dioxide in the cathode channels govern the current density distribution. Due to the high concentration of hydrogen at the anode inlet, the highest current densities can be found in this region.

According to the superoxide reaction mechanism proposed by Prins-Jansen *et al.* [40, 41], a negative order of reaction with respect to carbon dioxide appears in the cathodic reduction kinetics. Thus, the current density increases towards the end of the cathode channel, where the carbon dioxide fraction is low. Therefore, the current density peak is located in the vicinity of the anode inlet / cathode outlet, *i. e.* the bottom left corner of each fuel cell.

The main difference in the current density profiles of the four cells is the peak current density. The strong cooling effect in the upper half of cell 1 due to the reforming process in the IIR unit results in lower current densities in this part of the cell. But, because the total cell current is fixed, this decreased current density in the upper half has to be compensated by high current densities in the peak region. There, the current density reaches values of more than twice the average value on the cell plane.
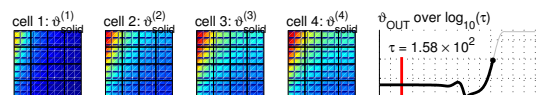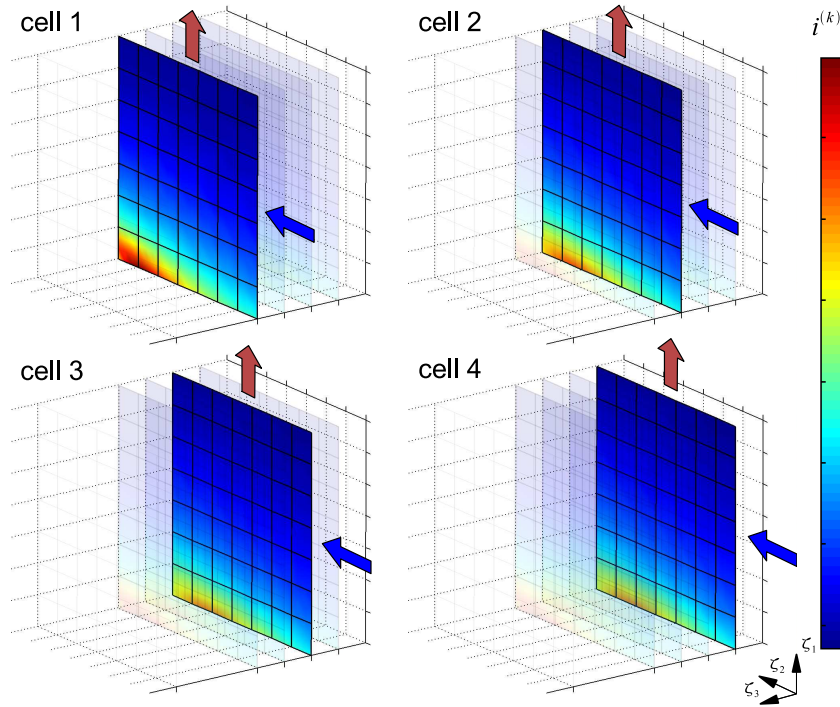
Figure 6.4.: Current densities in the four fuel cells.

6.1.3. Temperature Distribution

The temperature distribution in the solid phases of the four fuel cells is shown in Fig. 6.5. Temperatures are around $600\,°C$, with a maximum temperature difference of approximately $100\,°C$.

In each cell, the highest temperature is located near the same corner where the current density peak is observed. This is mainly because of two reasons. First, the high local current density results in a strong heat source in that area due to losses by the electrochemical reactions and by ion conduction. The second reason for the location of the temperature peak is that the cooling effect of the IIR unit is especially strong in the upper half of the symmetric stack model, which effectively lowers the cell temperature there.

The cooling effect of the IIR unit becomes evident when comparing the temperature profiles of the four fuel cells (Fig. 6.5). While the temperatures are generally lowest in cell 1, the highest temperatures are predicted in cell 4, which has the highest distance to the IIR unit. Considering the symmetry on the right hand side, this results in an approximately parabolic temperature profile in stack direction.

The temperature levels of the four fuel cells ($T_{S,min}$, $T_{S,avg}$ and $T_{S,max}$) differ by several $10\,°C$ (Fig. 6.6). Compared to the typical temperature difference in each cell, this gradient along the stack direction is significant. However, it seems that the tempera-
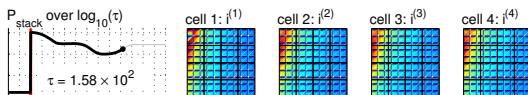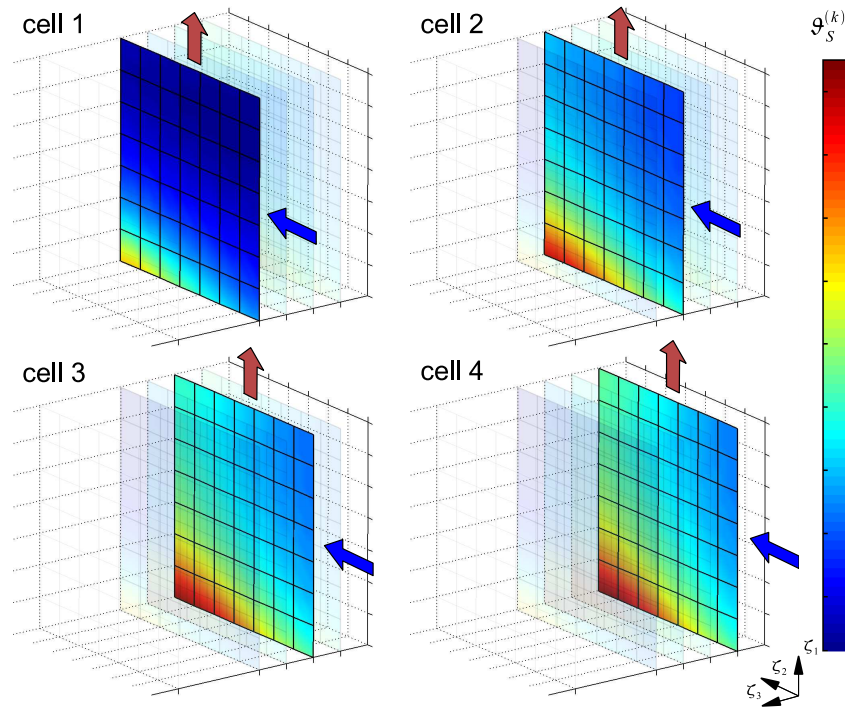
Figure 6.5.: Temperature profile in the solid phases of the four fuel cells. The IIR unit, where the endothermic reforming process takes place, is located on the left hand side of the first cell.

ture differences over each individual cell are nearly constant. So, although each cell operates at a significantly different temperature level, each cell has nearly the same temperature difference over its cell area.

With respect to cell voltages, an increase by several $10\,\text{mV}$ from the first fuel cell to the fourth fuel cell is observed (lower part of Fig. 6.6). This effect is clearly caused by the higher temperature level in cell 4. The slopes of the cell voltages and the cell temperatures are similar, indicating a dependency between these values.

From these observations, two conclusions can be drawn. First, the individual fuel cells show very similar states with respect to gas composition, voltage and current density. A reduction of the stack model to a model with one single representative cell, as in Gundermann *et al.* [21] is acceptable, if only these states are of interest. Second, concerning the cell temperature, the four cells show significant differences here (see also Section 6.3). Especially for design and optimisation purposes, where these values are very important, the temperature profile in stack direction can not be neglected. For these applications, a realistic stack model is an indispensable instrument.
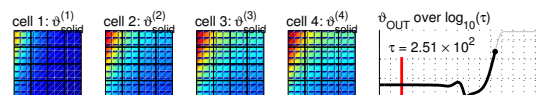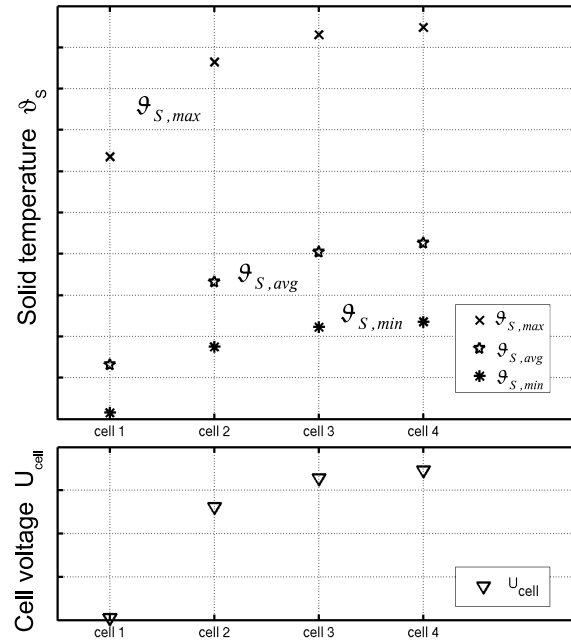
Figure 6.6.: Minimum, average and maximum temperature in the solid phase of the four fuel cells.

6.1.4. Electrical Potential in the Bipolar Plates

For the formulation of the stack model, the assumption that the electrical potentials of each cell are independent on the potentials of the neighbouring fuel cells is used (Section 4.3). A separate partial differential equation is defined to validate this assumption in an *a posteriori* investigation (Eq. 4.101 in Section 4.6). Fig. 6.7 presents simulation results for the electrical potential in the bipolar plates between the fuel cells considering base case conditions. The reference for the electrical potential is set at the lower right corner, $\varphi_{BP}^{(k,k+1))} (\zeta_1 = 0, \zeta_2 = 0) = 0$ (Eq. 4.103).

The profiles of the electrical potential show properties similar to the temperature profiles and the profiles of the current densities. The difference in the cell current densities is highest between the first two fuel cells. Thus, the highest electrical potentials can be found in the corresponding bipolar plate. Further away from the IIR unit, the cooling effect influencing the temperature profiles, decreases. This results in higher temperatures which leads to a change of the rates of the electrochemical reactions. Therefore, smaller differences between the current densities exist and a nearly homogeneous electrical field can be found in the last bipolar plate.

The maximum potential difference is observed in the bipolar plate between the first and the second fuel cell. It is in the order of $\Delta U_{BP} \approx 10^{-3}\,\mathrm{V}$. Considering the geometrical dimensions of the stack, a potential gradient of max. $E_{max} = 5 \times 10^{-3}\,V/\mathrm{m}$
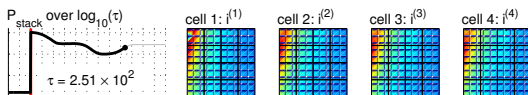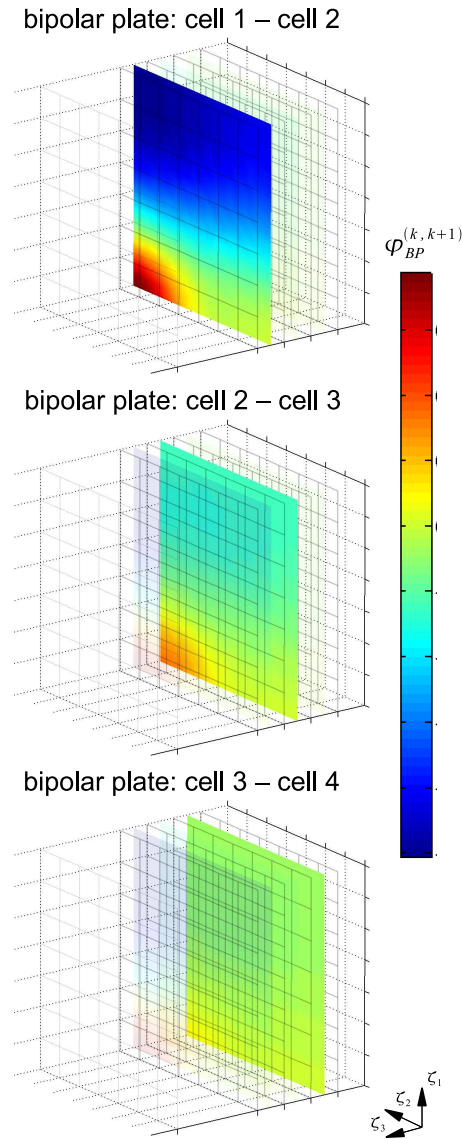
Figure 6.7.: Electric potential distribution in the bipolar plates of the MCFC symmetry unit.

is present. Thus, the assumption of homogeneous electrical potential in each bipolar plate is justified.

6.1.5. Dynamic Simulations

Using the here developed symmetric stack model, one can not only simulate the steady state operation of the fuel cell system but also the transient behaviour after
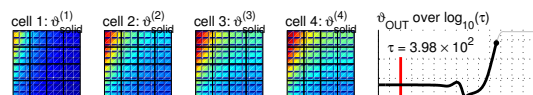
changes of operating parameters, in particular load changes. Exemplarily, a step change from the operating point 4 (80 mA/cm²) to the operating point 5 (100 mA/cm²) as defined by Gundermann [18] is briefly discussed in this section. The parameters for both operating points are listed in Table 6.2. In contrast to the simulations by Gundermann, not only the total cell current has been changed but also the parameter settings for the feed gas have been adapted. Thus, the influence of the changed feed gas flow and feed gas composition is taken into account.

Table 6.2.: Input parameters for the dynamic simulation.

| description	variable	operating point op 4 $\Rightarrow$ op 5		
feed gas				
molar mass flux	Γ_{IN}	3.30	$\Rightarrow$	3.65
temperature	ϑ_{IN}	2.18	$\Rightarrow$	2.16
methane mole fraction	$\chi_{CH_4,IN}$	0.22	$\Rightarrow$	0.23
water mole fraction	$\chi_{H_2O,IN}$	0.57	$\Rightarrow$	0.60
hydrogen mole fraction	$\chi_{H_2,IN}$	0.15	$\Rightarrow$	0.12
carbon monoxide mole fraction	$\chi_{CO,IN}$	0.00	$\Rightarrow$	0.00
carbon dioxide mole fraction	$\chi_{CO_2,IN}$	0.05	$\Rightarrow$	0.05
air				
molar mass flux	Γ_{AIR}	21.96	$\Rightarrow$	21.84
temperature	ϑ_{AIR}	1.08	$\Rightarrow$	1.07
oxygen mole fraction	$\chi_{O_2,IN}$	0.21	$\Rightarrow$	0.21
nitrogen mole fraction	$\chi_{N_2,IN}$	0.79	$\Rightarrow$	0.79
total cell current	I_{cell}	0.45	$\Rightarrow$	0.56
electrical power of the blower	P_{blower}	11.10	$\Rightarrow$	11.10
cathode gas recycle ratio	f_{REC}	0.70	$\Rightarrow$	0.70
volume fraction in the IIR unit	ε_{IIR}^{N}	0.75	$\Rightarrow$	0.75

The transient behaviour of the stack voltage, U_{stack}, is presented in Fig. 6.8. Furthermore, these simulation results are shown in the images at the bottom of each page. The operating point is changed at the dimensionless time $\tau = 10^{-6}$. The logarithmic time scale clearly shows the different characteristic time constants of the processes in the MCFC.

The charge balances in the electrochemical double layers reaches its new steady state fast. Thus, the step increase of the total cell current results in a nearly instantaneous drop of the cell voltages. In a second time range, the dynamic of the gas phase balances, especially the gas concentration and the gas temperature, can be observed. They lead to a decrease of the average cell voltage to a minimum value. After that, the system behaviour is dominated by the slow time constant of the enthalpy balance of the solid phase. The other system states follow this temperature. It changes due to the increased heat produced by the electrochemical reactions and the ion conduction as result of the increased current density. Additionally, heat is generated by the oxidation of the non-oxidised components of the feed gas in the catalytic combustion chamber.
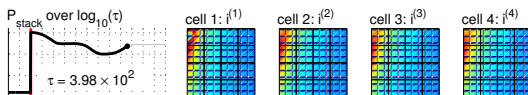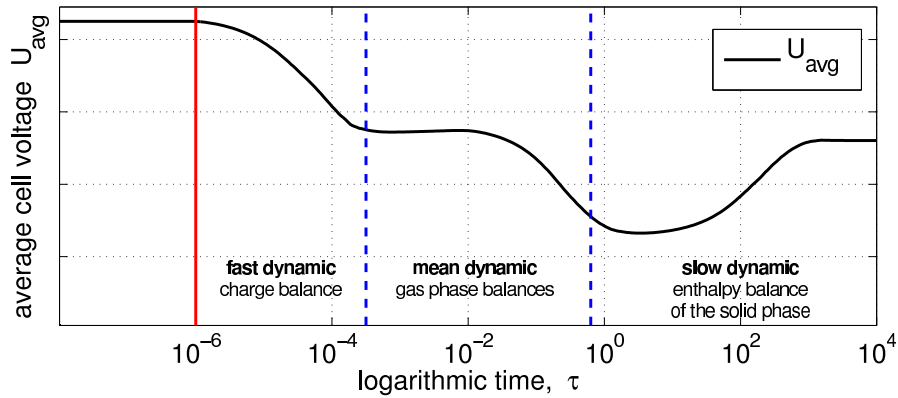
Figure 6.8.: Dynamic simulation of the stack voltage for a load change from operating point 4 to operating point 5.

6.2 Comparison with the Validated Model

The load case defined as the base case has previously been used by Gundermann [20]. In that work, it is one of four analysed load cases for which extensive sets of experimental data were available from a $250\,\text{kW}_{\text{el}}$ HOTMODULE MCFC power plant manufactured by MTU Onsite Energy, Germany [5]. These data sets are used to identify unknown parameters in a single cell model with an IIR unit. The single cell represented the average behaviour of all cells in the stack. As a result, the deviation of the model predictions by Gundermann *et al.* from the experimental data is less than or equal to the estimated measurement error [19, 21]. To demonstrate the validity of the stack model, some important values are compared to those from the simulations of the previously validated model.

The current densities in both models show similar profiles (Fig. 6.9). The figure shows the current density of the validated model (grey surface) and the current densities of the first and the fourth cell of the symmetric stack model (coloured planes). For the model of Gundermann *et al.*, a maximum current density of $i_{max} = 164\,{mA}/\text{cm}^2$ is found. In the stack model, the maximum current density varies around this value (see also Fig. 6.4). The cell voltage for both models is approximately $U_{cell} = 0.80\,\text{V}$ for an average current density of $i_{avg} = 80\,{mA}/\text{cm}^2$. Therefore, the electrical power generated by each cell of the stack model as well as their efficiencies are practically identical to the value calculated by Gundermann [18].

A variable which influences nearly all processes in the MCFC stack is the temperature of the solid phases (Fig. 6.10). The temperature profiles show similar characteristics for both models with a maximum at the anode inlet / cathode outlet and a lower temperature in the upper half of the fuel cells (see also Fig. 6.5). One can observe the influence of the IIR unit in the temperature profiles of the symmetric stack model. The solid phase temperature in the fuel cell next to the IIR unit is lower than the temperature in the solid phase of the fuel cell farthest away from this reforming reac-
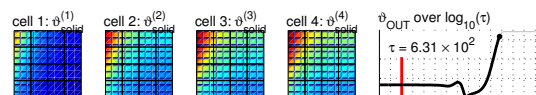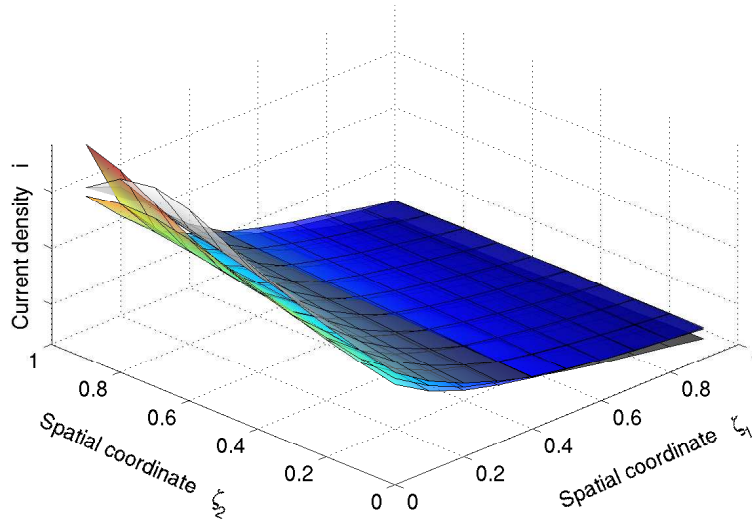
Figure 6.9.: Comparison of the current density, i, from the model of Gundermann (grey scale plot) and the current densities of the first, $i^{(1)}$, and fourth fuel cell, $i^{(4)}$, of the symmetric stack model (coloured plots).

tor. All temperatures predicted by the symmetric stack model are in the range of the solid phase temperature of the simulations of Gundermann *et al.*, where temperatures between $T_{S,min} = 553\,°C$ and $T_{S,max} = 642\,°C$ are found.

Differences between both models result from additional components of the fuel cell system considered in the symmetric stack model. While in the model of Gundermann the feed gas goes directly into the IIR unit, this gas is heated up by a heat exchanger in the symmetric stack model, resulting in higher temperatures at the inlet of the IIR unit (Fig. 6.11). Furthermore, several fuel cells are simulated in the symmetric stack model and the phase model is considered for the IIR unit. In addition to the gas temperature of the IIR unit in the validated model by Gundermann (grey scale plot), Fig. 6.11 also shows the temperature in the non-reactive phase (upper coloured plot) and the reactive phase (lower coloured plot) of the symmetric stack model. As the endothermic reforming process takes place in the reactive phase, this gas is colder than the gas in the non-reactive phase. The temperature difference between both gas phases is in the order of several $10\,K$.

All of this leads to a lower temperature difference between the gas in the IIR unit and the temperature in the solid phase of the neighbouring fuel cell compared to the corresponding temperature difference in Gundermann's model (Fig. 6.12). The temperature differences between the IIR unit and the solid phase of the validated model ($\vartheta_S - \vartheta_{IIR}$; grey scale plot) is compared to the corresponding temperature difference in the symmetric stack model, considering the temperature of the reactive
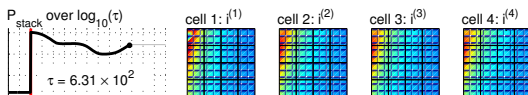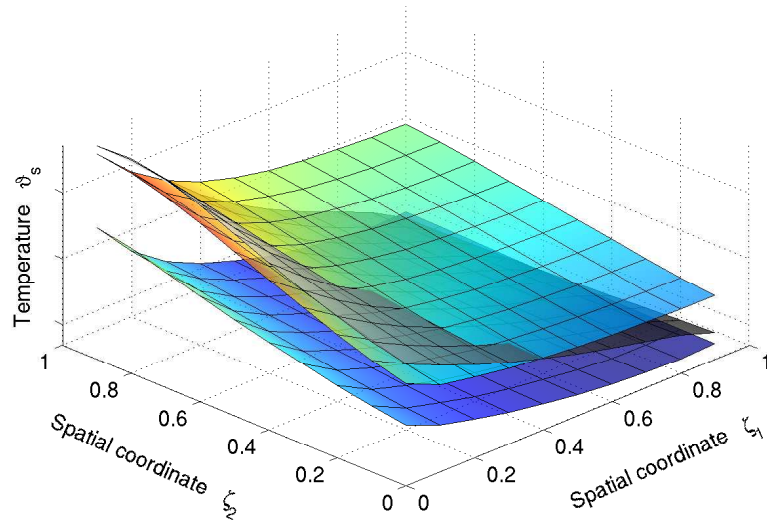
Figure 6.10.: Temperature of the solid phase, ϑ_S, in the model of Gundermann (grey scale plot) and of the first and fourth fuel cell of the symmetric stack model ($\vartheta_S^{(4)}$ and $\vartheta_S^{(1)}$; lower and upper coloured plot, respectively).
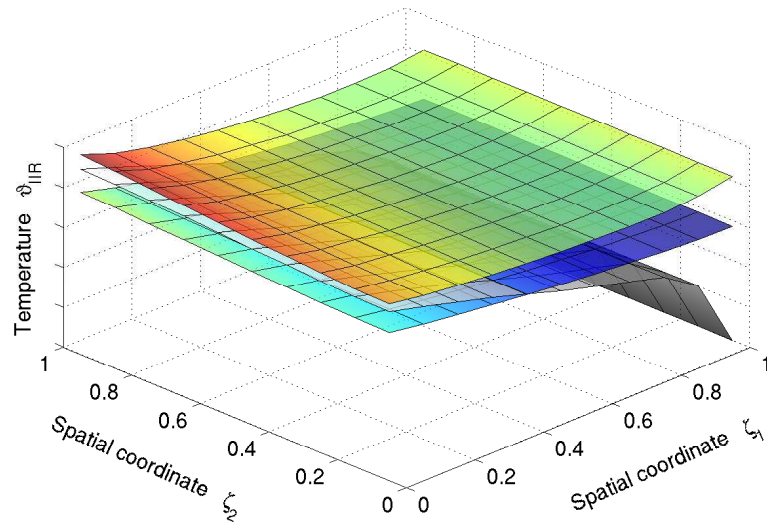
Figure 6.11.: Temperature in the IIR unit for the model of Gundermann, ϑ_{IIR}, (grey scale plot) and the non-reactive phase, ϑ_{IIR}^N, (upper coloured plot) and the reactive phase, ϑ_{IIR}^R, (lower coloured plot) of the symmetric stack model.
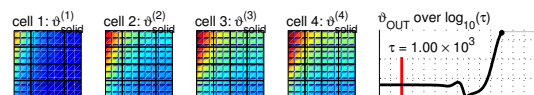
phase ($\vartheta_S^{(1)} - \vartheta_{IIR}^R$; upper coloured plot) and the non-reactive phase ($\vartheta_S^{(1)} - \vartheta_{IIR}^N$; lower coloured plot). In the model of Gundermann, the increased temperature difference results in an increased heat transport into the IIR unit which shifts the methane steam reforming reaction to a higher conversion of methane.
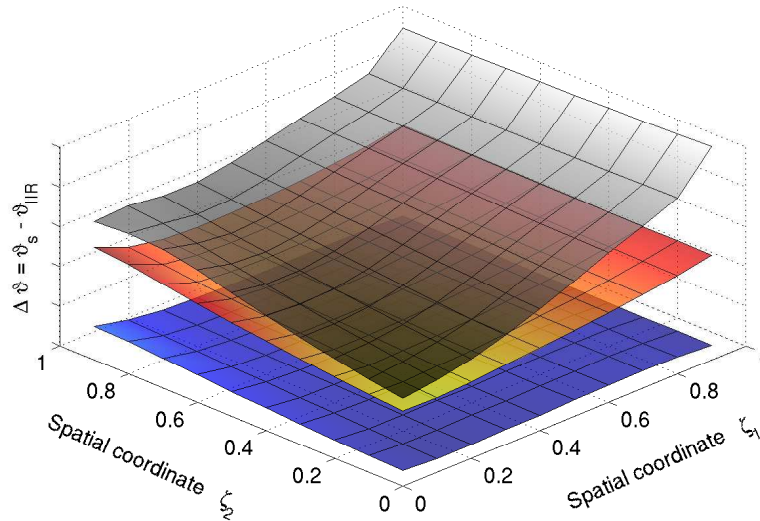
Figure 6.12.: Comparison of the temperature differences between the IIR unit and the solid phase for the validated model (grey scale plot) and the symmetric stack model, considering the temperature of the reactive phase (upper coloured plot) and the non-reactive phase (lower coloured plot).

The change of the temperature level in the IIR unit influences the reactions in this structured reactor, especially the concentrations differ between both models. The most important concentration is the mole fraction of methane shown in Fig. 6.13. Due to the higher temperature difference in the model by Gundermann *et al.*, more heat is transferred into the IIR unit providing the energy for the methane steam reforming reaction. Thus, the concentration of methane at the outlet is several percent lower than the concentration calculated by the symmetric stack model.

Overall, the results of the symmetric stack model correspond to those from the previously validated model. The differences are caused by auxiliary units of the fuel cell system implemented in the symmetric stack model as well as the consideration of several fuel cells.
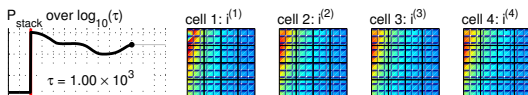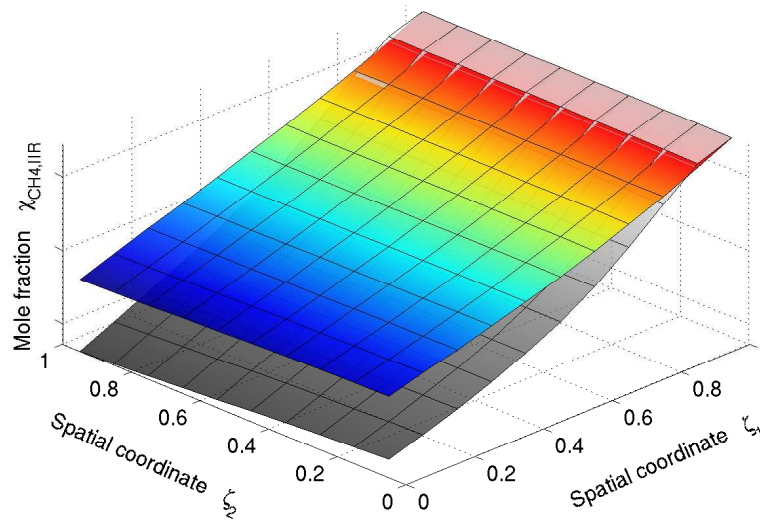
Figure 6.13.: Comparison of the methane mole fraction in the validated model (grey scale plot) and the symmetric stack model (coloured plot).

6.3 Variation of the Number of Fuel Cells

The symmetric stack model allows the simulation of an arbitrary number of fuel cells between two IIR units. The maximal number is only limited by the available computational power, especially the memory of the computer used for the simulations. In this work, simulations are carried out for one to six fuel cells connected to one half IIR unit. Besides the necessary adaption of the gas flow to the increased number of fuel cells, the height of the IIR unit also depends on the number of fuel cells simulated (see the definition of the phase model in Section 4.4.3). All of the performed simulations are using the definition of the base case as model parameters.

The average solid temperature of the individual fuel cells from the simulations with one to six cells is presented in Fig. 6.14. As discussed in Section 6.1.3, the parabolic temperature profile in stack direction due to the endothermic character of the reforming process in the IIR unit is clearly visible. The cooling effect is enhanced by the increased molar mass flux of the feed gas and the increased size of the IIR unit with increasing number of fuel cells. This results in higher reaction rates and therefore a more pronounced heat sink. Thus, the average solid temperature of the first fuel cell is decreased from a stack with one cell towards a stack with six cells.

A galvanostatic operation mode is applied in the simulations. This means that the total cell current is specified and the current density distribution and cell voltage are results of the simulations. They depend on the rates of the electrochemical reactions which in turn are influenced by the gas composition and by the temperature of the
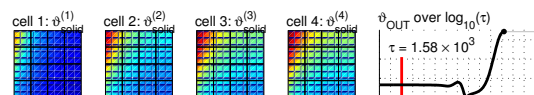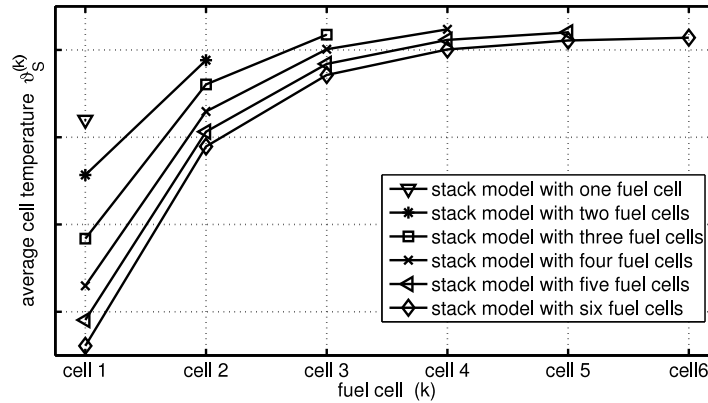
Figure 6.14.: Average solid temperature in the individual fuel cells considering the symmetric stack models with one to six cells.

electrode pores which are assumed to be equal to the solid temperatures. As a result, the slope of the cell voltages is similar to the slope of the average solid temperatures (Fig. 6.15). The differences between the cell voltages for the last fuel cell of each model, which show similar average solid temperatures, can be explained with different temperature profiles for each solid phase. On the one hand, the solid temperature is increased in the top right corner (anode outlet / cathode outlet) with increasing number of cells simulated. On the other hand, the gradient close to the anode inlet also increases, resulting in a lower temperature towards the outlet of the anode gas compartment (see also Fig. 6.5).
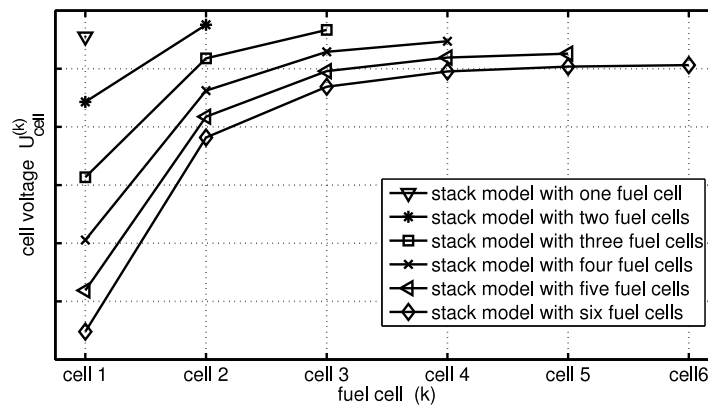
Figure 6.15.: Cell voltage in the individual fuel cells considering the symmetric stack models with one to six cells.

Fig. 6.16 shows the average cell voltage for the six models in an identical scale compared to Fig. 6.15. Due to the generally lower cell voltages in models with more fuel cells, the average cell voltage decreases with increasing number of fuel cells considered. This indicates that the highest electrical output will be available if only two fuel cells are combined with one IIR unit.
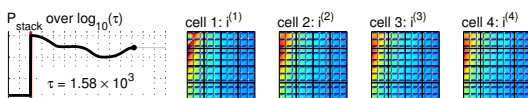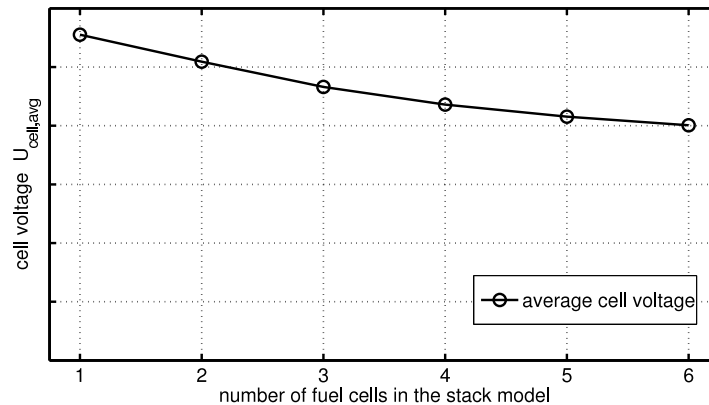
Figure 6.16.: Average cell voltages for the symmetric stack model varying the number of fuel cells between one and six. An identical scale as in Fig. 6.15 is used.

Using these simulation results, a decision guidance for the designs of the fuel cell stack can be developed. On the one hand, the average electrical output of one fuel cell is increased if the number of fuel cells per IIR units is reduced. On the other hand, this results in a increased stack length or a reduced number of fuel cells at given length, thus reducing the overall electrical power generated. An evaluation of economic aspects like material costs would be needed to define optimisation criteria with regard to the volumetric power density and the overall power output.

6.4 Energy Flux Analysis

In the Molten Carbonate Fuel Cell system, energy is transported in different forms. Besides the desired electrical power output of the fuel cell system, the chemically bound energy of the feed gas, the thermal energy of all gas mixtures and the thermal energy transported by conduction in the solid parts as well as the thermal energy losses have to be accounted for. An analysis of all energy fluxes is required to understand and optimise the design of the system [9]. Furthermore, it allows the comparison of different fuels with respect to these energy fluxes [14].

In the following sections, the energy fluxes in the stack according to two solutions of the symmetric stack model are presented and discussed [38]. First, one half IIR unit and one fuel cell are considered. Second, the default configuration of eight fuel cells per IIR unit, which corresponds to a symmetric stack model of one half IIR unit and four fuel cells, is analysed. As discussed in Section 5.4, the energy balance of the model is solved with a certain error. Here, an error of 6% or 1% has to be taken into consideration for a symmetric stack model with one or four fuel cells, respectively. Thus, the sum of the inlet and outlet energy fluxes are not identical but small deviations can be found in the energy flux diagrams.
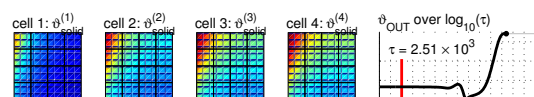
6.4.1. Symmetric Stack Model with One Fuel Cell

Fig. 6.17 shows the energy fluxes according to the solution of a stack model with a single fuel cell at base case conditions (see Table 6.1). In the figure, different kinds of energy are indicated by different colours. The energy of the feed gas, composed of the sum of the chemical bound energy usable for combustion (methane, hydrogen and carbon monoxide) and the thermal energy of the gas (relative to the reference temperature, $T_{ref} = 298.15\,\mathrm{K}$), is normalised to 100%. All energy fluxes are quantified in relation to this energy flux.
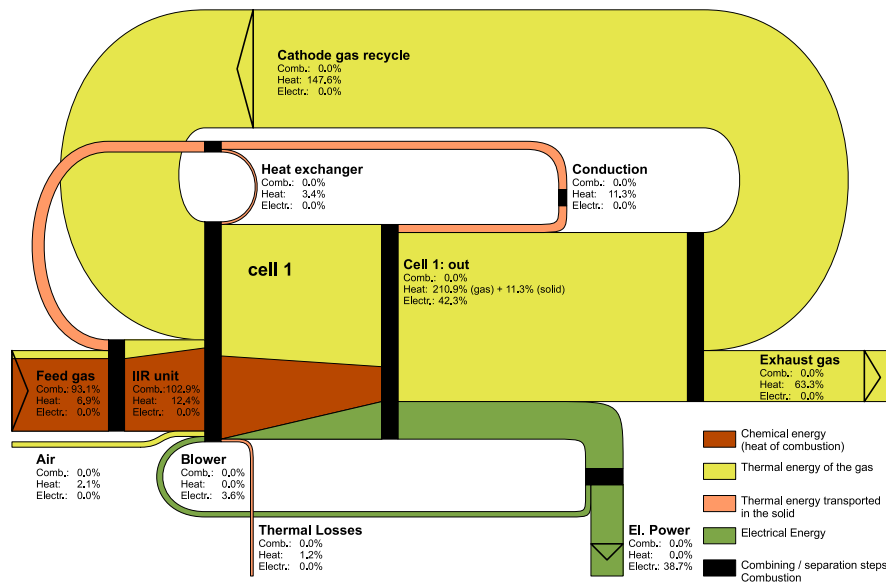
Figure 6.17.: Energy fluxes according to the base case simulation of a stack model with a single fuel cell.

The feed gas is heated up in the heat exchanger, increasing its thermal energy by 3.4%. Due to heat exchange between the fuel cell and the IIR unit, the energy of the gas is further increased by 11.3%. In the IIR unit, heat is converted to chemically bound energy by the endothermic reforming process. Thus, the ratio of this energy form is increased by approximately 10%.

The next block in the energy flux diagram represents the fuel cell. In the context of this analysis, the fuel cell is considered as one unit. No distinction is made between the anode and cathode gas flows, but one energy flux through the fuel cell is assumed. The anode feed gas is represented by the chemically bound energy and the thermal energy of the exhaust gas of the IIR unit. With respect to the cathode gas flow, the thermal energy of the air and the cathode gas recycle as well as the electrical energy of the blower, which is converted to thermal energy due to friction, are added. While the air flow and the blower contribute only a small amount of energy, the thermal energy
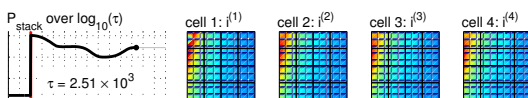
of the cathode gas recycle is 1.5 times the energy of the feed gas. This is mainly a result of the high recycle ratio of 70% used in the symmetric stack model.

The energy needed for the heat exchangers (3.4%) and the sum of all heat losses (1.2%) are subtracted from the energy flux. Thus, the total energy of the cathode and anode gas flows is composed of 102.9% chemically bound energy and 161.6% thermal energy. In the fuel cell, the chemically bound energy of the anode gas is converted to electrical energy (42.3%) and heat by the electrochemical reaction. Furthermore, energy is transported to the IIR unit due to heat conduction. After the fuel cell, the remaining chemically bound energy of the gas is transformed to thermal energy due to the combustion of all non-oxidised components in the catalytic combustion chamber.

The electrical power produced by the fuel cell is reduced by the energy needed for the blower, resulting in an electrical output of 38.7%. This is not equal to the efficiency of the fuel cell system, because it is related to the pre-reformed gas fed into the symmetric stack model. If only the conversion of the chemically bound energy of the gas fed into the symmetric stack model is considered, an electrical efficiency of 45.4% is obtained.

The diagram shows two fluxes which flow "backwards", *i. e.* from the right to the left hand side. On the one hand, a part of the cathode exhaust gas is circulated in the cathode gas recycle. This results in a homogenised temperature profile in the solid phase of the fuel cell. But it also requires additional power, *i. e.* a larger blower due to the higher pressure drop.

On the other hand, energy is transferred into the IIR unit from the fuel cell by heat conduction in the solid parts and, to a lesser extend, by the energy exchanged between the cathode exhaust gas and the feed gas in the heat exchanger. The additional energy is converted in the IIR unit into chemically bound energy by the reforming process. An optimisation of the conductive energy transport in the solid parts allows a reduction of the ratio of the cathode gas used in the cathode gas recycle. Thus, the size of the blower can be reduced and the efficiency of the system can be increased.

6.4.2. Symmetric Stack Model with Four Fuel Cells

A similar analysis as for the symmetric stack model with a single fuel cell can be done for a model with four fuel cells. For easier comparison with the previous results, the energy of the entire feed gas, which is four times as high as in the previous example, is similarly normalised to 100% (Fig. 6.18).

The amount of energy feed into the IIR unit *via* the heat exchangers is similar to the previous case, but the energy transported along the stack direction due to heat conduction contributes only 6.1%. The reason is that only one fuel cell is in direct contact to the IIR unit. The heat exchange between the IIR unit and the fuel cells 2 to 4 is indirect *via* the cells in between. Thus, the amount of thermal energy transported into the IIR unit decreases from 3.9% for cell 1 to 0.3% for cell 4. As a
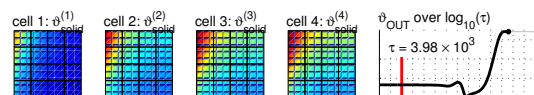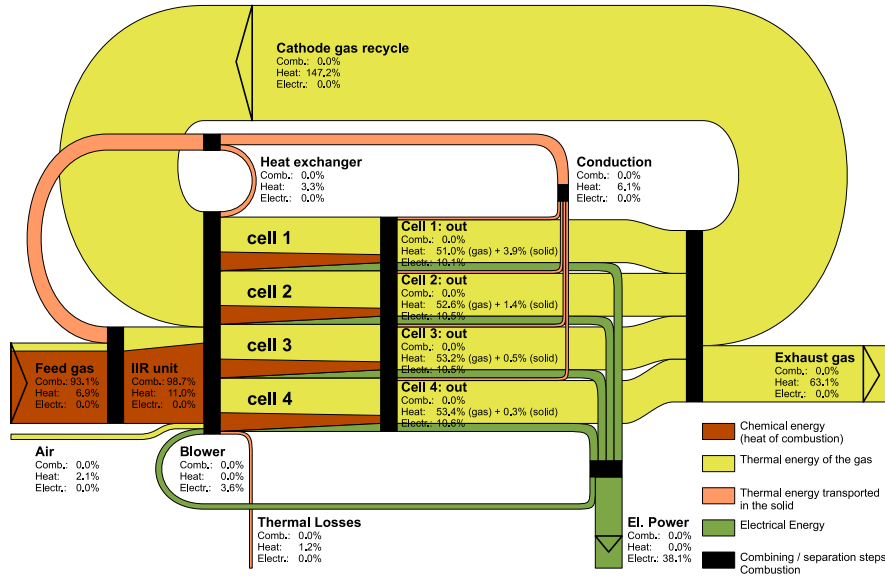
Figure 6.18.: Energy fluxes according to the base case simulation of a stack model
with four fuel cells.

result of the reduced conductive energy transport into the IIR unit, the amount of
chemically bound energy in the IIR is increased by only 5.6%.

The molar mass flux at the anode and cathode gas inlets for each fuel cell are iden-
tical and also the composition and temperature are the same. Nevertheless, due to
the differences in the average solid temperatures and therefore different rates of the
electrochemical reactions, the first fuel cell provides 10.1% electrical energy while the
last fuel cells provides up to 10.6%. Overall, the electrical power generated in the
case of four fuel cells per IIR unit is slightly lower than in the simulation with only a
single fuel cell. Thus, similar to the results presented in Section 6.3, the energy flux
diagrams support a stack design which uses a smaller number of fuel cells per IIR unit
if the volumetric power density should be increased.
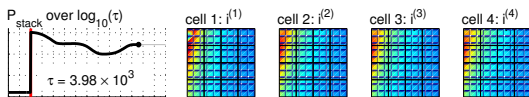
Chapter 7

Conclusions

The focus of this work is on the modelling of a Molten Carbonate Fuel Cell stack. In Part I, the main gas compartments of the fuel cell stack, especially the Indirect Internal Reforming units (IIR), are analysed in detail.

A hierarchical modelling approach has been used to describe the IIR unit. Three different levels have been studied. In the *detailed model*, small cutout sections of the IIR unit are simulated. The exact geometry with the corrugated sheets and the individual catalyst pellets is considered. The analysis shows two main features of this reactor. First, due to the geometrical structure of the reactor, the reforming process is limited by mass transport between a reactive and a non-reactive zone. A stable repeating pattern can be observed for the temperature and velocity profiles while the concentrations show funnel-shaped profiles. Due to the excess of catalyst material, the degradation of the catalyst does not influence the overall reaction rate in the reforming reactor as long as its activity is high enough. Therefore, a constant temperature profile can be expected in the IIR unit even after long operation time. The second point is that the main heat transport route towards the cold reaction zone is from the neighbouring fuel cells through the top and bottom sheets directly into the reactive zone. Thus, the local temperature in the fuel cells can be influenced by the amount and the distribution of the reforming catalyst pellets in the IIR units.

The second level of the modelling hierarchy is represented by the *zone model*. It substitutes the complex geometry of the detailed model of IIR unit by rectangular zones: the reactive and the non-reactive zone. As an example, the geometry of the IIR unit as applied in the MCFC system HOTMODULE is used for the simulations. The reactive zone and the non-reactive zone are clearly visible in the temperature and concentration profiles. The results indicate that the rate of the reforming process is nearly homogeneously distributed over the IIR unit. Thus, the heat sink due to the endothermic reforming process is almost constant in these parts.

While the reactive and non-reactive zones are discrete in the zone model, this discrete geometrical information is lost in the final model reduction step to the *phase model*. The states representing the non-reactive and the reactive zone are homogenised over the whole (two-dimensional) area of the IIR unit. Thus, they can be interpreted as two phases, each occupying a certain fraction of the volume. The states in the phases now

represent characteristic values that a corresponding zone in the specific vicinity would have. The complexity and the structure of this model correspond to the complexity and the structure of the model of a single MCFC proposed by Heidebrecht *et al.* [22].

Similar detailed models for the anode and cathode gas compartments have been studied. Results show that the Direct Internal Reforming reactions in the anode gas channels are only limited by the corresponding chemical equilibrium. Furthermore, the concentration gradients perpendicular to the main gas flow direction as well as the gradients over the height of the channels are small compared to the concentration gradients in flow direction. Thus, these models confirm the assumptions used for the derivation of the model of one fuel cell.

In Part II of this work, the phase model of the IIR unit and the model of an MCFC are combined to the symmetric stack model. It allows the simulation of a representative section of a molten carbonate fuel cell stack. The coupling of all parts of the stack, mainly due to the thermal interactions, the mass flow and the corresponding electrochemical reactions at the anode and the cathode of each fuel cell are taken into account. Thus, the symmetric stack model considers the differences of the state variables in the different compartments along the stack direction. The gas phase compositions, the temperature profiles and the current density distribution in the IIR unit and each of the four fuel cells can be predicted by means of the here proposed MCFC stack model.

The functionality of the model has been demonstrated by a steady state simulation. Overall, the results of the symmetric stack model correspond to those from the previously validated model by Gundermann *et al.* [18]. The differences are caused by auxiliary units of the fuel cell system that are implemented in the symmetric stack model as well as the consideration of several fuel cells. These changes allow the simulation of the temperature distribution in stack direction. The results show a parabolic temperature profile between two Indirect Internal Reforming units. Thus, the fuel cells next to the IIR unit and the fuel cells in the middle between two IIR units operate at different temperatures.

The current density distributions for all cells in the stack show similar profiles. But due to the cooling effect of the IIR unit, the cell temperatures deviate by several $10\,\mathrm{K}$. As overheating is one of the reasons for degradation in an MCFC system, one may expect that cells 3 and 4 are degrading fastest in this stack. This suggests that reducing the number of fuel cells per IIR unit should lead to lower temperature differences in the stack. This idea is also supported by the results of the energy flux analysis which have revealed that the advantageous heat flow from the cells into the IIR unit is higher if less fuel cells per IIR unit are used.

Due to its generalised formulation, the model can easily be extended to different numbers of fuel cells in the stack symmetry unit. Furthermore, inhomogeneous gas feed distributions to the anode or cathode gas compartments of the different fuel cells as well as different gas flows for each fuel cell can be implemented. Considering the points listed above, the presented model provides the foundation for an optimisation

of design and operating parameters of MCFC systems with regard to homogenised temperature distributions and increased efficiency. Because of the number of solutions needed for such an optimisation, an additional reduction of the model complexity would be required which goes beyond the scope of this work.

P_{stack} over $\log_{10}(\tau)$ cell 1: $i^{(1)}$ cell 2: $i^{(2)}$ cell 3: $i^{(3)}$ cell 4: $i^{(4)}$

$\tau = 1.00 \times 10^4$

Appendix

Appendix A

Formulation of the Stack Model

A.1 Derivation of the IIR Unit Balance Equations in Dimensionless Form

In the following, the dimensionless formulation of the component mass balances for the non-reactive phase and for the reactive phase in the IIR unit are exemplarily derived. The definition of the required dimensionless quantities is listed in Table A.1. The equations for the enthalpy balances and the total mass balances are analogously deduced. Additional information about the formulation of the dimensionless equations can be found in the work of Heidebrecht [22].

Table A.1.: Definition of dimensionless quantities.

Variable and Definition	Dimensionless quantity
$Da_j^{(1\,cell)} = \dfrac{r_j^\theta\, L_1\, L_2\, d^{(1\,cell)}}{G^\theta}$	Damköhler number of reaction j (per fuel cell)
$n_{cells} = \dfrac{d}{d^{(1\,cell)}}$	number of fuel cells per IIR unit
$n_i = \dfrac{\widetilde{n}_i^I\, L_1\left(\frac{2d}{b}\, L_2\right)}{G^\theta}$	molar mass flux of component i at the interface
$n_t = \dfrac{\widetilde{n}_t^I\, L_1\left(\frac{2d}{b}\, L_2\right)}{G^\theta}$	total molar mass flux at the interface
$r_j^R = \dfrac{\widetilde{r}_j^R}{r_j^\theta}$	reaction rate of reaction j in the reactive phase
$V^{(1\,cell)} = \dfrac{L_1\, L_2\, d^{(1\,cell)}}{V^\theta}$	volume of the IIR unit (per fuel cell)
$\gamma^N = \dfrac{g^N\, L_2\, d}{G^\theta}$	molar mass flux in the non-reactive phase
$\zeta_1 = \dfrac{z_1}{L_1}$	space coordinate
$\vartheta = \dfrac{T}{T^\theta} = \dfrac{R\,T}{p}\dfrac{p}{R\,T^\theta} = \dfrac{c_t^\vartheta}{c_t}$	temperature
$\tau = \dfrac{t}{t^\theta}$	time
$\chi_i = x_i$	mole fraction of component i

A.1.1. Component Mass Balances of the Non-reactive Phase

The partial differential equation for the mole fraction in the non-reactive phase reads (Eq. (2.57) in Section 2.3.2.1):

$$\varepsilon^N c_t^N \frac{\partial x_i^N}{\partial t} = -\varepsilon^N g^N \frac{\partial x_i^N}{\partial z_1} - \frac{2}{b} \left(\widetilde{n}_i^I - x_i^N \widetilde{n}_t^I \right) \tag{A.1}$$

The time, t, is made dimensionless by division with the standard time t^θ, which is defined as:

$$t^\theta = \frac{V^\theta c_t^\theta}{G^\theta} \tag{A.2}$$

and the total concentration, c_t^N, is made dimensionless by the standard total concentration, c_t^θ. Thus, the complete equation is multiplied with the term:

$$\frac{t^\theta}{c_t^\theta} = \frac{V^\theta}{G^\theta} \tag{A.3}$$

Eq. (A.1) reads now:

$$\varepsilon^N \frac{c_t^N}{c_t^\theta} \frac{\partial x_i^N}{\partial t/t^\theta} = -\varepsilon^N \frac{g^N}{G^\theta} \frac{L_2 d}{L_1 L_2 d^{(1\,cell)}} \frac{V^\theta}{d} \frac{d^{(1\,cell)}}{\partial z_1/L_1} \frac{\partial x_i^N}{}$$
$$- \frac{V^\theta}{L_1 L_2 d^{(1\,cell)}} \frac{d^{(1\,cell)}}{d} \left[\frac{\widetilde{n}_i^I L_1 \left(\frac{2\,d}{b} L_2 \right)}{G^\theta} - x_i^N \frac{\widetilde{n}_t^I L_1 \left(\frac{2\,d}{b} L_2 \right)}{G^\theta} \right] \tag{A.4}$$

with all variables grouped into dimensionless terms with specific physical interpretations as listed in Table A.1. Inserting the dimensionless variables and reordering results in (see Eq. (2.58)):

$$n_{cells} \, \varepsilon^N V^{(1\,cell)} \frac{1}{\vartheta^N} \frac{\partial \chi_i^N}{\partial \tau} = -\varepsilon^N \gamma^N \frac{\partial \chi_i^N}{\partial \zeta_1} - \left(n_i^I - \chi_i^N n_t^I \right) \tag{A.5}$$

A.1.2. Component Mass Balances of the Reactive Phase

The partial differential equation for the mole fraction in the reactive phase is given by (Eq. (2.62) in Section 2.3.2.1):

$$\varepsilon^R c_t^R \frac{\partial x_i^R}{\partial t} = \frac{2}{b} \left(\widetilde{n}_i^I - x_i^R \widetilde{n}_t^I \right) + \varepsilon^R \sum_{j=\text{ref}} \left(v_{i,j} - x_i^R \bar{v}_j \right) \widetilde{r}_j^R \tag{A.6}$$

The conversion to a dimensionless equation is achieved by multiplication with the same standard values as in the case of the non-reactive phase:

$$
\varepsilon^R \frac{c_t^R}{c_t^\theta} \frac{\partial x_i^R}{\partial t/t^\theta} = \frac{V^\theta}{L_1\,L_2\,d^{(1\,cell)}}\frac{d^{(1\,cell)}}{d} \left(\frac{\widetilde{n}_i^I\,L_1\,(2\,L_2\,d)/b}{G^\theta} - x_i^R\,\frac{\widetilde{n}_t^I\,L_1\,(2\,L_2\,d)/b}{G^\theta} \right)
$$
$$
+ \varepsilon^R \sum_{j=\mathrm{ref}} \left(\nu_{i,j} - x_i^R\,\overline{\nu}_j \right) \frac{r_j^\theta\,L_1\,L_2\,d^{(1\,cell)}}{G^\theta}\frac{V^\theta}{L_1\,L_2\,d^{(1\,cell)}}\frac{\widetilde{r}_j^R}{r_j^\theta} \tag{A.7}
$$

Using the definition of the dimensionless quantities as defined in Table A.1, the dimensionless equation reads (see Eq. (2.63)):

$$
n_{cells}\,\varepsilon^R\,V^{(1\,cell)}\frac{1}{\vartheta^R}\frac{\partial \chi_i^R}{\partial \tau} = \left(n_i^I - \chi_i^R\,n_i^I \right)
$$
$$
+ \varepsilon^R \sum_{j=\mathrm{ref}} \left(\nu_{i,j} - \chi_i^R\,\overline{\nu}_j \right) n_{cells}\,Da_j^{(1\,cell)}\,r_j \tag{A.8}
$$

A.2 Thermodynamic Relations

In the phase model of the IIR unit (Section 2.3) and the symmetric stack model (Chapter 4) it is assumed, that the heat capacity of the gas mixture depends on gas composition but not on gas temperature [18].

$$
\overline{\varsigma_P} = \sum_i \chi_i\,\varsigma_{P_i} \tag{A.9}
$$

The heat capacities of the pure components are calculated at a reference temperature of $T^r = 600\,°C$, which represents the operating temperature of an MCFC. The value corresponds to a dimensionless temperature of $\vartheta^r = 2.93$.

$$
\varsigma_{P_i} = \varsigma_{P_i}(\vartheta^r) = \mathrm{const.} \tag{A.10}
$$

A polynomial approach with four coefficients is used [22]:

$$
\varsigma_{P_i}(\vartheta) = A_{i,1} + A_{i,2}\,\vartheta + \frac{A_{i,3}}{\vartheta^2} + A_{i,4}\,\vartheta^2 \tag{A.11}
$$

Taking into account the above listed assumption of a constant heat capacity, the enthalpy of the component i is given by

$$
h_{f,i}^\theta(\vartheta) = h_{f,i}^\theta(\vartheta^r) + \int_{\vartheta^r}^{\vartheta} \varsigma_{P_i}(\Psi)\,\mathrm{d}\Psi = h_{f,i}^\theta(\vartheta^r) + \varsigma_{P_i}(\vartheta - \vartheta^r) \tag{A.12}
$$

and its entropy is given by

$$s_{f,i}^{\theta}(\vartheta) = s_{f,i}^{\theta}(\vartheta^r) + \int_{\vartheta^r}^{\vartheta} \frac{c_{p_i}}{\Psi}(\Psi)\,\mathrm{d}\Psi = s_{f,i}^{\theta}(\vartheta^r) + c_{p_i}\ln\frac{\vartheta}{\vartheta^r} \tag{A.13}$$

Using Eqs. (A.12) and (A.13) the reaction enthalpy and the reaction entropy can be determined

$$\Delta_R h_j^{\theta}(\vartheta) = \sum_i v_{i,j}\, h_{f,i}^{\theta}(\vartheta) = \Delta_R h_j^{\theta}(\vartheta^r) + \Delta_R c_{p_j}(\vartheta - \vartheta^r) \tag{A.14}$$

$$\Delta_R s_j^{\theta}(\vartheta) = \sum_i v_{i,j}\, s_{f,i}^{\theta}(\vartheta) = \Delta_R s_j^{\theta}(\vartheta^r) + \Delta_R c_{p_j}\ln\frac{\vartheta}{\vartheta^r} \tag{A.15}$$

with

$$\Delta_R c_{p_j} = \sum_i v_{i,j} c_{p_i} \tag{A.16}$$

$$\Delta_R h_j^{\theta} = \sum_i v_{i,j} h_{f,i}^{\theta} \tag{A.17}$$

$$\Delta_R s_j^{\theta} = \sum_i v_{i,j} s_{f,i}^{\theta} \tag{A.18}$$

Considering the reaction enthalpy and the reaction entropy, the Gibbs' enthalpy, needed to calculate the standard open circuit voltage for the electrochemical reactions and the equilibrium constants for the reforming reactions, can be calculated.

$$\Delta_R g_j^{\theta}(\vartheta) = \Delta_R h_j^{\theta}(\vartheta) - \vartheta\,\Delta_R s_j^{\theta}(\vartheta) \tag{A.19}$$

A.3 Reaction Kinetics

Within the IIR unit and the anode gas channels, the reforming process has to be considered. The methane steam reforming reaction (ref1) and the water gas shift reaction (ref2) are taken into account. At the electrodes of the fuel cell, the electrochemical oxidation of hydrogen (ox1) and carbon monoxide (ox2) on the anode side while at the cathode carbon dioxide is electrochemically reduced (red).

The equilibrium constants for all reactions are calculated according to

$$K_j(\vartheta) = \exp\left(-\frac{\Delta_R g_j^{\theta}(\vartheta)}{\vartheta}\right) \tag{A.20}$$

with the Gibbs enthalpy of the reactions, $\Delta_R g_j^{\theta}(\vartheta)$, given in section A.2.

A.3.1. Reforming Reactions

The reforming process in the IIR unit and in the anode channels is described by two reactions. Besides the methane steam reforming (ref1):

$$CH_4 + H_2O \rightleftharpoons CO + 3\,H_2 \tag{ref1}$$

also the water gas shift reaction (ref2) is taken into account:

$$CO + H_2O \rightleftharpoons CO_2 + H_2 \tag{ref2}$$

Power law kinetics are applied for both reactions:

$$r_{\text{ref1}} = \exp\left[Arr_{\text{ref1}} \times \left(\frac{1}{\vartheta_{\text{ref1}}^r} - \frac{1}{\vartheta}\right)\right] \times \left(\chi_{CH_4}\,\chi_{H_2O} - \frac{1}{K_{\text{ref1}}(\vartheta)}\,\chi_{CO}\,(\chi_{H_2})^3\right) \tag{A.21}$$

$$r_{\text{ref2}} = \exp\left[Arr_{\text{ref2}} \times \left(\frac{1}{\vartheta_{\text{ref2}}^r} - \frac{1}{\vartheta}\right)\right] \times \left(\chi_{CO}\,\chi_{H_2O} - \frac{1}{K_{\text{ref2}}(\vartheta)}\,\chi_{CO_2}\,\chi_{H_2}\right) \tag{A.22}$$

A.3.2. Anode Reactions

The oxidation of hydrogen (ox1) and carbon monoxide (ox2) take place at the anode electrodes.

$$H_2 + CO_3^{2-} \rightleftharpoons CO_2 + H_2O + 2\,e^- \tag{ox1}$$
$$CO + CO_3^{2-} \rightleftharpoons 2\,CO_2 + 2\,e^- \tag{ox2}$$

For the electrochemical reactions at the anode Butler-Volmer kinetics with an temperature dependent Arrhenius terms are used:

$$r_{\text{ox1}} = \exp\left[Arr_{\text{ox1}}\left(\frac{1}{\vartheta_{\text{ox1}}^\theta} - \frac{1}{\vartheta_S}\right)\right] \times \left\{\varphi_{H_2,AC} \exp\left(\alpha_{\text{ox1},+}\,n_{\text{ox1}}\frac{\Delta\phi_{A,\text{ox1}}}{\vartheta_S}\right)\right.$$
$$\left. -\varphi_{H_2O,AC}\,\varphi_{CO_2,AC} \exp\left(-(1-\alpha_{\text{ox1},+})\,n_{\text{ox1}}\frac{\Delta\phi_{A,\text{ox1}}}{\vartheta_S}\right)\right\} \tag{A.23}$$

$$r_{\text{ox2}} = \exp\left[Arr_{\text{ox2}}\left(\frac{1}{\vartheta_{\text{ox2}}^\theta} - \frac{1}{\vartheta_S}\right)\right] \times \left\{\varphi_{CO,AC} \exp\left(\alpha_{\text{ox2},+}\,n_{\text{ox2}}\frac{\Delta\phi_{A,\text{ox2}}}{\vartheta_S}\right)\right.$$
$$\left. -(\varphi_{CO_2,AC})^2 \exp\left(-(1-\alpha_{\text{ox2},+})\,n_{\text{ox2}}\frac{\Delta\phi_{A,\text{ox2}}}{\vartheta_S}\right)\right\} \tag{A.24}$$

Where

$$\Delta\phi_{A,j} = \left(\phi_A^S - \phi_A^L\right) - \Delta\phi_{j,0}(\vartheta_S) \tag{A.25}$$

and

$$\Delta\phi_{j,0}\left(\vartheta_S\right) = \frac{\Delta_R g_j^\theta(\vartheta_S)}{n_j}$$ (A.26)

$$\text{for } j = \text{ox1; ox2}$$

define the overpotential and the equilibrium potential of the reaction.

A.3.3. Cathode Reaction

The reduction of oxygen (red) takes place at the cathode:

$$CO_3^{2-} \rightleftharpoons CO_2 + {}^1\!/\!2\, O_2 + 2\, e^-$$ (red)

A modified Butler-Volmer kinetic expression [40, 41, 3] is used to describe the rate of this reaction.

$$r_{\text{red}} = \exp\left[Arr_{\text{red}}\left(\frac{1}{\vartheta_{\text{red}}^\theta} - \frac{1}{\vartheta_S}\right)\right] \times \left\{ \left(\varphi_{CO_2,CC}\right)^{-2} \exp\left(2.5\,\frac{\Delta\phi_{C,\text{red}}}{\vartheta_S}\right)\right.$$
$$\left. - \left(\varphi_{O_2,CC}\right)^{0.75}\left(\varphi_{CO_2,CC}\right)^{-0.5}\exp\left(-0.5\,\frac{\Delta\phi_{C,\text{red}}}{\vartheta_S}\right)\right\}$$ (A.27)

with the overpotential and the equilibrium potential defined as

$$\Delta\phi_{C,\text{red}} = \left(\phi_C^S - \phi_C^L\right) - \Delta\phi_{\text{red},0}\left(\vartheta_S\right)$$ (A.28)

and

$$\Delta\phi_{\text{red},0}\left(\vartheta_S\right) = \frac{\Delta_R g_{\text{red}}^\theta(\vartheta_S)}{n_{\text{red}}} \quad .$$ (A.29)

A.4 Governing Equations

On the following pages the governing equations of the symmetric stack model are summarised (Table A.2). The (partial) differential equations or algebraic expressions for the component mass balances, the energy balance and the total mass balance are listed and the boundary conditions are defined. This is followed by a list of additional equations needed for the considered part of the model.

The derivation of the dimensionless equations for the IIR unit can be found in Section 2.3 while the derivation of the equations for one fuel cell is explained in detail in the PhD thesis of Heidebrecht [22].

Table A.2.: Equations of the symmetric stack model.

Gas		

Feed Gas

$\chi_{i,IN}$:	$\chi_{i,IN} = $ (given as model parameter)	
ϑ_{IN}:	$\vartheta_{IN} = $ (given as model parameter)	
Γ_{IN}:	$\Gamma_{IN} = n_{cells}\,\Gamma_{IN}^{(1\,cell)}$; $\Gamma_{IN}^{(1\,cell)} = $ (given as model parameter)	

Heat Exchanger (Cold Side)

$\chi_{i,HEA}$:	$n_{cells}\,V_{HEA}^{(1\,cell)}\,\frac{1}{\vartheta_{HEA}}\,\frac{\partial \chi_{i,HEA}}{\partial \tau} = \Gamma_{IN} \times \left(\chi_{i,IN} - \chi_{i_{HEA}} \right)$	(4.1)
ϑ_{HEA}:	$n_{cells}\,V_{HEA}^{(1\,cell)}\,\frac{\overline{\mathrm{c}}_{P_{HEA}}}{\vartheta_{HEA}}\,\frac{\partial \vartheta_{HEA}}{\partial \tau} = \Gamma_{IN}\,\overline{\mathrm{c}}_{P_{IN}} \times \left(\vartheta_{IN} - \vartheta_{HEA} \right) - Q_{HE}$	(4.2)
Γ_{HEA}:	$\Gamma_{HEA} = \Gamma_{IN} \times \left(1 + \frac{\overline{\mathrm{c}}_{P_{IN}}}{\overline{\mathrm{c}}_{P_{HEA}}} \left(\frac{\vartheta_{IN}}{\vartheta_{HEA}} - 1 \right) \right) - \frac{Q_{HE}}{\overline{\mathrm{c}}_{P_{HEA}}\,\vartheta_{HEA}}$	(4.3)
	$Q_{HE} = n_{cells}\,St_{HE}^{(1\,cell)} \times \left(\vartheta_{HEA} - \vartheta_{HEB} \right)$	

Indirect Internal Reforming Unit

$\chi_{i,IIR}^N$:	$n_{cells}\,\varepsilon_{IIR}^N\,V_{IIR}^{(1\,cell)}\,\frac{1}{\vartheta_{IIR}^N}\,\frac{\partial \chi_{i,IIR}^N}{\partial \tau} = -\varepsilon_{IIR}^N\,\gamma_{IIR}^N\,\frac{\partial \chi_{i,IIR}^N}{\partial \zeta_1} - \left(n_{i,IIR}^I - \chi_{i,IIR}^N\,n_{t,IIR}^I \right)$	(4.5)
	$\chi_{i,IIR}^N \left(\zeta_1 = 1, \zeta_2, \tau \right) = \chi_{i,IIR,in}^N \left(\tau \right) = \chi_{i,HEA}$ on $\partial \Omega_4$; $\Gamma_{IIR,out}\,\chi_{i,IIR,out} = \int\limits_0^1 \left[-\varepsilon_{IIR}^N\,\gamma_{IIR}^N\,\chi_{i,IIR}^N \right]_{\zeta_1=0,\zeta_2} \mathrm{d}\zeta_2$ on $\partial \Omega_1$	
ϑ_{IIR}^N:	$n_{cells}\,\varepsilon_{IIR}^N\,V_{IIR}^{(1\,cell)}\,\frac{1}{\vartheta_{IIR}^N}\,\frac{\partial \vartheta_{IIR}^N}{\partial \tau} = -\varepsilon_{IIR}^N\,\gamma_{IIR}^N\,\frac{\partial \vartheta_{IIR}^N}{\partial \zeta_1} + \frac{1}{\overline{\mathrm{c}}_{P_{IIR}}^N} \times \left(\left(\sum_i n_{i,IIR}^{I-}\,\mathrm{c}_{P_i} \right) \times \left(\vartheta_{IIR}^N - \vartheta_{IIR}^R \right) - q_{IIR}^I + \varepsilon_{IIR}^N\,q_{IIRS}^N \right)$	(4.6)
	$\vartheta_{IIR}^N \left(\zeta_1 = 1, \zeta_2, \tau \right) = \vartheta_{IIR,in}^N \left(\tau \right) = \vartheta_{HEA}$ on $\partial \Omega_4$; $\Gamma_{IIR,out}\,\overline{\mathrm{c}}_{P_{IIR,out}} \left(\vartheta_{IIR,out} - \vartheta^r \right) = \int\limits_0^1 \left[-\varepsilon_{IIR}^N\,\gamma_{IIR}^N\,\overline{\mathrm{c}}_{P_{IIR}}^N \left(\vartheta_{IIR}^N - \vartheta^r \right) \right]_{\zeta_1=0,\zeta_2} \mathrm{d}\zeta_2$ on $\partial \Omega_1$	
γ_{IIR}^N:	$0 = -\frac{\mathrm{d}}{\mathrm{d}\zeta_1} \left(\varepsilon_{IIR}^N\,\gamma_{IIR}^N\,\vartheta_{IIR}^N \right) + \frac{1}{\overline{\mathrm{c}}_{P_{IIR}}^N} \times \left(\sum_i \left(n_{i,IIR}^{I-}\,\mathrm{c}_{P_i} \right) \times \left(\vartheta_{IIR}^N - \vartheta_{IIR}^R \right) - q_{IIR}^I + \varepsilon_{IIR}^N\,q_{IIRS}^N \right) - \vartheta_{IIR}^N\,n_{t,IIR}^I$	(4.7)
	$\gamma_{IIR}^N \left(\zeta_1 = 1, \zeta_2, \tau \right) = \gamma_{IIR,in}^N \left(\tau \right) = -\frac{\Gamma_{HEA}}{\varepsilon^N}$ on $\partial \Omega_4$; $\Gamma_{IIR,out} = \int\limits_0^1 \left[-\varepsilon_{IIR}^N\,\gamma_{IIR}^N \right]_{\zeta_1=0,\zeta_2} \mathrm{d}\zeta_2$ on $\partial \Omega_1$	

Table A.2.: Equations of the symmetric stack model (continued).

$\chi_{i,IIR}^R$:
$$n_{cells}\,\varepsilon_{IIR}^R\,V_{IIR}\,\frac{1}{\vartheta_{IIR}^R}\,\frac{\partial \chi_{i,IIR}^R}{\partial \tau} = n_{i,IIR}^I - \chi_{i,IIR}^R\,n_{l,IIR}^I + \varepsilon_{IIR}^R \sum_{j=\text{ref}} \left(\nu_{i,j} - \chi_{i,IIR}^R\,\overline{\nu}_j \right) n_{cells}\,Da_{j,IIR}^{(1\,cell)}\,r_j \tag{4.8}$$

ϑ_{IIR}^R:
$$n_{cells}\,\varepsilon_{IIR}^R\,V_{IIR}^{(1\,cell)}\,\frac{\mathfrak{c}_{P_{IIR}}^R}{\vartheta_{IIR}^R}\,\frac{\partial \vartheta_{IIR}^R}{\partial \tau} = \left(\sum_i n_{i,IIR}^{I+}\,\mathfrak{c}_{P\,i} \right) \times \left(\vartheta_{IIR}^N - \vartheta_{IIR}^R \right) + q_{IIR}^I + \varepsilon_{IIR}^R \sum_{j=\text{ref}} \left(-\Delta_R h_j^\theta(\vartheta_{IIR}^R) \right) n_{cells}\,Da_{j,IIR}^{(1\,cell)}\,r_j + \left(\varepsilon_{IIR}^R + \varepsilon_{IIR}^P \right) q_{IIRS}^R \tag{4.9}$$

$n_{t,IIR}^I$:
$$0 = n_{t,IIR}^I + \varepsilon_{IIR}^R \sum_{j=\text{ref}} \overline{\nu}_j\,n_{cells}\,Da_{j,IIR}^{(1\,cell)}\,r_j + \frac{1}{\vartheta_{IIR}^R}\,\frac{1}{\mathfrak{c}_{P_{IIR}}^R} \times \left(\left(\sum_i n_{i,IIR}^{I+}\,\mathfrak{c}_{P\,i} \right) \times \left(\vartheta_{IIR}^N - \vartheta_{IIR}^R \right) + q_{IIR}^I + q_{IIR,\text{ref}}^R + \left(\varepsilon_{IIR}^R + \varepsilon_{IIR}^P \right) \times q_{IIRS}^R \right) \tag{4.10}$$

$$n_{i,IIR}^I = n_{i,IIR,conv}^I + n_{i,IIR,diff}^I \;\; ; \;\; n_{i,IIR,conv}^I = \left(n_{t,IIR}^I - \sum_i n_{i,IIR,diff}^I \right) \frac{\chi_{i,IIR}^N + \chi_{i,IIR}^R}{2} \;\; ; \;\; n_{i,IIR,diff}^I = n_{cells}\,D_{i,IIR}^{I,(1\,cell)} \times \left(\chi_{i,IIR}^R - \chi_{i,IIR}^N \right)$$

$$n_{i,IIR}^{I+} = \begin{cases} n_{i,IIR}^I \,, & \text{if } n_{i,IIR}^I > 0 \\ 0 \,, & \text{if } n_{i,IIR}^I \le 0 \end{cases} \;\; ; \;\; n_{i,IIR}^{I-} = \begin{cases} 0 \,, & \text{if } n_{i,IIR}^I > 0 \\ n_{i,IIR}^I \,, & \text{if } n_{i,IIR}^I \le 0 \end{cases} \;\; ; \;\; n_{t,IIR,conv}^I = n_{t,IIR}^I - \sum_i n_{i,IIR,diff}^I$$

$$q_{IIR}^I = n_{cells}\,St_{IIR}^{I,(1\,cell)} \times \left(\vartheta_{IIR}^N - \vartheta_{IIR}^R \right) \;\; ; \;\; q_{IIRS}^N = St_{IIRS}^N \times \left(\vartheta_S^{(1)} - \vartheta_{IIR}^N \right) \;\; ; \;\; q_{IIRS}^R = St_{IIRS}^R \times \left(\vartheta_S^{(1)} - \vartheta_{IIR}^R \right)$$

$$q_{IIR,\text{ref}}^R = \varepsilon_{IIR}^R \sum_{j=\text{ref}} \left(-\Delta_R h_j^\theta(\vartheta_{IIR}^R) \right) n_{cells}\,Da_{j,IIR}^{(1\,cell)}\,r_j \;\; ; \;\; q_{IIRS} = \varepsilon_{IIR}^N\,q_{IIRS}^N + \left(\varepsilon_{IIR}^R + \varepsilon_{IIR}^P \right) \times q_{IIRS}^R$$

Gas Manifold

$\chi_{i,M}$:
$$n_{cells}\,V_M^{(1\,cell)}\,\frac{1}{\vartheta_M}\,\frac{\partial \chi_{i,M}}{\partial \tau} = \Gamma_{IIR,out} \times \left(\chi_{i,IIR,out} - \chi_{i,M} \right) \tag{4.21}$$

ϑ_M:
$$n_{cells}\,V_M^{(1\,cell)}\,\frac{\overline{\mathfrak{c}}_{P_M}}{\vartheta_M}\,\frac{\partial \vartheta_M}{\partial \tau} = \Gamma_{IIR,out}\overline{\mathfrak{c}}_{P_{IIR,out}} \times \left(\vartheta_{IIR,out} - \vartheta_M \right) - Q_M \tag{4.22}$$

Γ_M:
$$\Gamma_M = \Gamma_{IIR,out} \times \left(1 + \frac{\overline{\mathfrak{c}}_{P_{IIR,out}}}{\overline{\mathfrak{c}}_{P_M}} \left(\frac{\vartheta_{IIR,out}}{\vartheta_M} - 1 \right) \right) - \frac{Q_M}{\overline{\mathfrak{c}}_{P_M}\,\vartheta_M} \tag{4.23}$$

$$Q_M = n_{cells}\,St_M^{(1\,cell)} \times \left(\vartheta_M - \vartheta_U \right)$$

Anode Gas Phase

$\chi_{i,A}^{(k)}$:
$$V_A\,\frac{1}{\vartheta_A^{(k)}}\,\frac{\partial \chi_{i,A}^{(k)}}{\partial \tau} = -\gamma_A^{(k)}\,\frac{d\chi_{i,A}^{(k)}}{d\zeta_1} + n_{i,AS}^{(k)} - \chi_{i,A}^{(k)} \sum_l n_{l,AS}^{(k)} + \sum_{j=\text{ref}} \left(\nu_{i,j} - \chi_{i,A}^{(k)}\overline{\nu}_j \right) Da_{j,A}\,r_j^{(k)} \tag{4.25}$$

$$\chi_{i,A}^{(k)}\left(\zeta_1 = 0, \zeta_2, \tau \right) = \chi_{i,A,in}^{(k)}(\tau) = \chi_{i,M} \quad \text{on } \partial\Omega_1 \;\; ; \;\; \Gamma_{A,out}\,\chi_{i,A,out} = \sum_{k=1}^{n_{cells}} \int_0^1 \left[\gamma_A^{(k)}\,\chi_{i,A}^{(k)} \right]_{\zeta_1=1,\zeta_2} d\zeta_2 \quad \text{on } \partial\Omega_4$$

Table A.2.: Equations of the symmetric stack model (continued).

$\vartheta_A^{(k)}$:

$$V_A \, \frac{\overline{c}_{P_A}^{(k)}}{\vartheta_A^{(k)}} \, \frac{\partial \vartheta_A^{(k)}}{\partial \tau} = -\gamma_A^{(k)} \, \overline{c}_{P_A}^{(k)} \, \frac{\mathrm{d}\vartheta_A^{(k)}}{\mathrm{d}\zeta_1} + \left(\sum_i n_{i,AS}^{(k)+} \, c_{P_i} \right) \times \left(\vartheta_S^{(k)} - \vartheta_A^{(k)} \right) + \sum_{j=\text{ref}} \left(-\Delta_R h_j^\theta (\vartheta_A^{(k)}) \right) Da_{j,A} \, r_j^{(k)} + q_{AS}^{(k)}$$ (4.26)

$$\vartheta_A^{(k)} \, (\zeta_1 = 0, \zeta_2, \tau) = \vartheta_{A,in}^{(k)} (\tau) = \vartheta_M \quad \text{on } \partial\Omega_1 \quad ; \quad \Gamma_{A,out} \, \overline{c}_{P_{A,out}} \, (\vartheta_{A,out} - \vartheta^r) = \sum_{k=1}^{n_{cells}} \int_0^1 \left[\gamma_A^{(k)} \, \overline{c}_{P_A}^{(k)} \, \left(\vartheta_A^{(k)} - \vartheta^r \right) \right]_{\zeta_1 = 1, \zeta_2} \mathrm{d}\zeta_2 \quad \text{on } \partial\Omega_4$$

$\gamma_A^{(k)}$:

$$0 = -\frac{\mathrm{d}}{\mathrm{d}\zeta_1} \left(\gamma_A^{(k)} \, \vartheta_A^{(k)} \right) + \frac{1}{\overline{c}_{P_A}^{(k)}} \times \left(\left(\sum_i n_{i,AS}^{(k)+} \, c_{P_i} \right) \times \left(\vartheta_S^{(k)} - \vartheta_A^{(k)} \right) + q_{A,\text{ref}}^{(k)} + q_{AS}^{(k)} \right) + \vartheta_A^{(k)} \times \left(n_{t,AS}^{(k)} + \sum_{j=\text{ref}} \overline{v}_j \, Da_{j,A} \, r_j^{(k)} \right)$$ (4.27)

$$\gamma_A^{(k)} \, (\zeta_1 = 0, \zeta_2, \tau) = \gamma_{A,in}^{(k)} (\tau) = \frac{1}{n_{cells}} \Gamma_M \quad \text{on } \partial\Omega_1 \quad ; \quad \Gamma_{A,out} = \sum_{k=1}^{n_{cells}} \int_0^1 \left[\gamma_{IIR}^{(k)} \right]_{\zeta_1 = 1, \zeta_2} \mathrm{d}\zeta_2 \quad \text{on } \partial\Omega_4$$

$$q_{A,\text{ref}}^{(k)} = \sum_{j=\text{ref}} \left(-\Delta_R h_j^\theta \left(\vartheta_A^{(k)} \right) \right) \times Da_{j,A} \, r_j^{(k)} \quad ; \quad q_{AS}^{(k)} = St_{AS}^{(k)} \times \left(\vartheta_S^{(k)} - \vartheta_A^{(k)} \right)$$

$$n_{i,AS}^{(k)} = D_{i,AS} \times \left(\varphi_{i,AC}^{(k)} - \chi_{i,A}^{(k)} \right) \quad ; \quad n_{t,AS}^{(k)} = \sum_i n_{i,AS}^{(k)} \quad ; \quad n_{i,AS}^{(k)+} = \begin{cases} n_{i,AS}^{(k)} \, , \text{ if } n_{i,AS}^{(k)} > 0 \\ 0 \, , \text{ if } n_{i,AS}^{(k)} \le 0 \end{cases} \quad ; \quad n_{i,AS}^{(k)-} = \begin{cases} 0 \, , \text{ if } n_{i,AS}^{(k)} < 0 \\ n_{i,AS}^{(k)} \, , \text{ if } n_{i,AS}^{(k)} \le 0 \end{cases}$$

Electrode Pores (anode)

$\varphi_{i,AC}^{(k)}$:

$$V_{AC} \, \frac{1}{\vartheta_S^{(k)}} \, \frac{\partial \varphi_{i,AC}^{(k)}}{\partial \tau} = \sum_{j=\text{ox}} v_{i,j} \, Da_{j,AC} \, r_j^{(k)} - n_{i,AS}^{(k)}$$ (4.65)

Air

$\chi_{i,AIR}$: $\quad \chi_{i,AIR} = \text{(given as model parameter)}$

ϑ_{AIR}: $\quad \vartheta_{AIR} = \text{(given as model parameter)}$

Γ_{AIR}: $\quad \Gamma_{AIR} = n_{cells} \, \Gamma_{AIR}^{(1\,cell)} \quad ; \quad \Gamma_{AIR}^{(1\,cell)} = \text{(given as model parameter)}$

Catalytic Combustion Chamber

$\chi_{i,B}$:

$$\Gamma_B \, \chi_{i,B} = \sum_l \Gamma_l \times \left(\chi_{i,l} + \sum_{j=\text{comb}} v_{i,C_j} \chi_{i,l} \right)$$ (4.37)

ϑ_B:

$$\Gamma_B \, \overline{c}_{P_B} \times (\vartheta_B - \vartheta^r) = \sum_l \Gamma_l \left(\overline{c}_{P_l} \times (\vartheta_l - \vartheta^r) + \sum_i \chi_{i,l} \times \left(-\Delta_C h_i^\theta (\vartheta^r) \right) \right)$$ (4.38)

Table A.2.: Equations of the symmetric stack model (continued).

Γ_B:	$\Gamma_B = \sum\limits_l \Gamma_l \times \left(1 + \sum\limits_{j=\text{comb}} \bar{\nu}_{C_j} \chi_{j,l}\right)$	(4.39)
	with: $l = A, out; REC; AIR$	

Reversal Chamber

$\chi_{i,RC}$:	$n_{cells} V_{RC}^{(1\,cell)} \frac{1}{\vartheta_{RC}} \frac{\partial \chi_{i,RC}}{\partial \tau} = \Gamma_B \times \left(\chi_{i,B} - \chi_{i,RC}\right)$	(4.40)
ϑ_{RC}:	$n_{cells} V_{RC}^{(1\,cell)} \frac{\overline{c}_{P_{RC}}}{\vartheta_{RC}} \frac{\partial \vartheta_{RC}}{\partial \tau} = \Gamma_B\, \overline{c}_{P_B} \times \left(\vartheta_B - \vartheta_{RC}\right) - Q_{RC} + P_{blower}$	(4.41)
Γ_{RC}:	$\Gamma_{RC} = \Gamma_B \times \left(1 + \frac{\overline{c}_{P_B}}{\overline{c}_{P_{RC}}} \times \left(\frac{\vartheta_B}{\vartheta_{RC}} - 1\right)\right) - \frac{Q_{RC}}{\overline{c}_{P_{RC}} \vartheta_{RC}} + \frac{P_{blower}}{\overline{c}_{P_{RC}} \vartheta_{RC}}$	(4.42)
	$Q_{RC} = n_{cells}\, St_{RC}^{(1\,cell)} \times \left(\vartheta_{RC} - \vartheta_U\right)$	

Heat Exchanger (Hot Side)

$\chi_{i,HEB}$:	$n_{cells} V_{HEB}^{(1\,cell)} \frac{1}{\vartheta_{HEB}} \frac{\partial \chi_{i,HEB}}{\partial \tau} = \Gamma_{RC} \left(\chi_{i,RC} - \chi_{i,HEB}\right)$	(4.44)
ϑ_{HEB}:	$n_{cells} V_{HEB}^{(1\,cell)} \frac{\overline{c}_{P_{HEB}}}{\vartheta_{HEB}} \frac{\partial \vartheta_{HEB}}{\partial \tau} = \Gamma_{RC}\, \overline{c}_{P_{RC}} \left(\vartheta_{RC} - \vartheta_{HEB}\right) + Q_{HE}$	(4.45)
Γ_{HEB}:	$\Gamma_{HEB} = \Gamma_{RC} \left(1 + \frac{\overline{c}_{P_{RC}}}{\overline{c}_{P_{HEB}}} \left(\frac{\vartheta_{RC}}{\vartheta_{HEB}} - 1\right)\right) + \frac{Q_{HE}}{\overline{c}_{P_{HEB}} \vartheta_{HEB}}$	(4.46)

Cathode Gas Phase

$\chi_{i,C}^{(k)}$:	$V_C \frac{1}{\vartheta_C^{(k)}} \frac{\partial \chi_{i,C}^{(k)}}{\partial \tau} = -\gamma_C^{(k)} \frac{d\chi_{i,C}^{(k)}}{d\zeta_2} + n_{i,CS}^{(k)} - \chi_{i,C}^{(k)} \sum\limits_l n_{l,CS}^{(k)}$	(4.47)
	$\chi_{i,C}^{(k)} \left(\zeta_1, \zeta_2 = 0, \tau\right) = \chi_{i,C,in}^{(k)} \left(\tau\right) = \chi_{i,HEB}$ on $\partial\Omega_2$; $\Gamma_{C,out} \chi_{i,C,out} = \sum\limits_{k=1}^{n_{cells}} \int\limits_0^1 \left[\gamma_C^{(k)} \chi_{i,IIR}^{(k)}\right]_{\zeta_1, \zeta_2 = 1} d\zeta_1$ on $\partial\Omega_3$	
$\vartheta_C^{(k)}$:	$V_C \frac{\overline{c}_{P_C}^{(k)}}{\vartheta_C^{(k)}} \frac{\partial \vartheta_C^{(k)}}{\partial \tau} = -\gamma_C^{(k)} \overline{c}_{P_C}^{(k)} \frac{d\vartheta_C^{(k)}}{d\zeta_2} + \left(\sum\limits_i n_{i,CS}^{(k)+} c_{P_i}\right) \times \left(\vartheta_S^{(k)} - \vartheta_C^{(k)}\right) + q_{CS}^{(k)}$	(4.48)
	$\vartheta_C^{(k)} \left(\zeta_1, \zeta_2 = 0, \tau\right) = \vartheta_{C,in}^{(k)} \left(\tau\right) = \vartheta_{HEB}$ on $\partial\Omega_2$; $\Gamma_{C,out} \overline{c}_{P_{C,out}} \left(\vartheta_{C,out} - \vartheta^r\right) = \sum\limits_{k=1}^{n_{cells}} \int\limits_0^1 \left[\gamma_C^{(k)} \overline{c}_{P_C}^{(k)} \times \left(\vartheta_C^{(k)} - \vartheta^r\right)\right]_{\zeta_1, \zeta_2 = 1} d\zeta_1$ on $\partial\Omega_3$	

Table A.2.: Equations of the symmetric stack model (continued).

$\gamma_C^{(k)}$:	$0 = -\dfrac{\mathrm{d}}{\mathrm{d}\zeta_2}\left(\gamma_C^{(k)}\,\vartheta_C^{(k)}\right) + \dfrac{1}{c_{P_C}^{(k)}} \times \left(\left(\sum_i n_{i,CS}^{(k)+}\,c_{P_i}\right)\times\left(\vartheta_S^{(k)} - \vartheta_C^{(k)}\right) + q_{CS}^{(k)}\right) + \vartheta_C^{(k)}\,n_{t,CS}^{(k)}$	(4.49)

$$\gamma_C^{(k)}\,(\zeta_1, \zeta_2 = 0, \tau) = \gamma_{C,in}^{(k)}\,(\tau) = \frac{1}{n_{cells}}\Gamma_{HEB} \quad \text{on } \partial\Omega_2 \quad ; \quad \Gamma_{C,out} = \sum_{k=1}^{n_{cells}}\int_0^1 \left[\gamma_C^{(k)}\right]_{\zeta_1,\zeta_2=1}\mathrm{d}\zeta_1 \quad \text{on } \partial\Omega_3$$

$$q_{CS}^{(k)} = St_{CS}^{(k)} \times \left(\vartheta_S^{(k)} - \vartheta_C^{(k)}\right) \;;\; n_{i,CS}^{(k)} = D_{i,CS} \times \left(\varphi_{i,CC}^{(k)} - \chi_{i,C}^{(k)}\right) \;;\; n_{t,CS}^{(k)} = \sum_i n_{i,CS}^{(k)}$$

$$n_{i,CS}^{(k)+} = \begin{cases} n_{i,CS}^{(k)} \text{, if } n_{i,CS}^{(k)} > 0 \\ 0 \text{, if } n_{i,CS}^{(k)} \leq 0 \end{cases} \;;\; n_{i,CS}^{(k)-} = \begin{cases} 0 \text{, if } n_{i,CS}^{(k)} > 0 \\ n_{i,CS}^{(k)} \text{, if } n_{i,CS}^{(k)} \leq 0 \end{cases}$$

Electrode Pores (cathode)

$\varphi_{i,CC}^{(k)}$:	$V_{CC}\,\dfrac{1}{\vartheta_S^{(k)}}\dfrac{\partial\varphi_{i,CC}^{(k)}}{\partial\tau} = \sum_{j=\text{red}}\nu_{i,j}\,Da_{j,CC}\,r_j^{(k)} - n_{i,CS}^{(k)}$	(4.66)

Cathode gas recycle

$\chi_{i,REC}$:	$\chi_{i,REC} = \chi_{i,C,out}$
ϑ_{REC}:	$\vartheta_{REC} = \vartheta_{C,out}$
Γ_{REC}:	$\Gamma_{REC} = f_{REC}\,\Gamma_{C,out}$

Solid

Solid Phase

$\vartheta_S^{(k)}$:	$c_{P_S}\dfrac{\partial\vartheta_S^{(k)}}{\partial\tau} = \dfrac{l_2}{Pe_S}\dfrac{\partial^2\vartheta_S^{(k)}}{\partial\zeta_1^2} + \dfrac{1}{Pe_S\,l_2}\dfrac{\partial^2\vartheta_S^{(k)}}{\partial\zeta_2^2} + \sum_i\left(-n_{i,AS}^{(k)-}\,c_{P_i}\right)\times\left(\vartheta_S^{(k)} - \vartheta_A^{(k)}\right) + \sum_i\left(-n_{i,CS}^{(k)-}\,c_{P_i}\right)\times\left(\vartheta_S^{(k)} - \vartheta_C^{(k)}\right) - q_{AS}^{(k)} - q_{CS}^{(k)} + q_{S,cell}^{(k)} + q_{S,stack}^{(k)}$	(4.67)

$$\left.\dfrac{\partial\vartheta_S^{(k)}}{\partial\zeta}\right|_{\zeta_1=0,\zeta_2} = \left.\dfrac{\partial\vartheta_S^{(k)}}{\partial\zeta}\right|_{\zeta_1=1,\zeta_2} = \left.\dfrac{\partial\vartheta_S^{(k)}}{\partial\zeta}\right|_{\zeta_1,\zeta_2=0} = \left.\dfrac{\partial\vartheta_S^{(k)}}{\partial\zeta}\right|_{\zeta_1,\zeta_2=1} = 0 \quad \text{on } \partial\Omega$$

$$q_{S,cell}^{(k)} = q_{S,ox}^{(k)} + q_{S,red}^{(k)} + i_E^{(k)}\frac{1}{F}\times\left(\phi_A^{L(k)} - \phi_C^{L(k)}\right)$$

$$q_{S,ox}^{(k)} = \sum_{j=\text{ox}}\left(-\Delta_R h_j^\theta(\vartheta_S^{(k)}) + n_j\times\left(\phi_A^{S(k)} - \phi_A^{L(k)}\right)\right)\times Da_{j,AC}\,r_j^{(k)}$$

Table A.2.: Equations of the symmetric stack model (continued).

$$q_{S,\text{red}}^{(k)} = \sum_{j=\text{red}} \left(-\Delta_R h_j^\theta(\vartheta_S^{(k)}) + n_j \times \left(\phi_C^{S(k)} - \phi_C^{L(k)} \right) \right) \times Da_{j,CC}\, r_j^{(k)}$$

$$q_{S,stack}^{(k)} = \begin{cases} q_{S,IIR} - q_{S,conn}^{(k),(k+1)} & ,\text{ if } \quad 1 = k \\ q_{S,conn}^{(k-1),(k)} - q_{S,conn}^{(k),(k+1)} & ,\text{ if } \quad 1 < k < n_{cells} \quad ;\quad q_{S,conn}^{(k),(k+1)} = St_S \times \left(\vartheta_S^{(k)} - \vartheta_S^{(k+1)} \right) \\ q_{S,conn}^{(k-1),(k)} & ,\text{ if } \quad\quad k = n_{cells} \end{cases}$$

Charged Double Layer Model

$\phi_A^{S(k)}:$ $\quad \phi_A^{S(k)} = 0$ $\hfill (4.74)$

$\phi_A^{L(k)}:$ $\quad \dfrac{\partial \phi_A^{L(k)}}{\partial \tau} = -\dfrac{1}{c_A} \times \left(i^{(k)} - i_A^{(k)} \right)$ $\hfill (4.75)$

$\phi_C^{L(k)}:$ $\quad \dfrac{\partial \phi_C^{L(k)}}{\partial \tau} = -\dfrac{1}{c_A} \times \left(i^{(k)} - i_A^{(k)} \right) - \dfrac{1}{c_E} \times \left(i^{(k)} - i_E^{(k)} \right)$ $\hfill (4.76)$

$\phi_C^{S(k)}:$ $\quad \dfrac{\mathrm{d}\phi_C^{S(k)}}{\mathrm{d}\tau} = \dfrac{I_{cell} - I_A^{(k)}}{c_A} + \dfrac{I_{cell} - I_E^{(k)}}{c_E} + \dfrac{I_{cell} - I_C^{(k)}}{c_C}$ $\hfill (4.77)$

$$I_A^{(k)} = \int_A i_A^{(k)} \mathrm{d}\zeta \;\; ;\;\; i_A^{(k)} = \sum_{j=\text{ox}} n_j\, F\, Da_{j,AC}\, r_j^{(k)} \left(\phi_A^{S(k)}, \phi_A^{L(k)} \right)$$

$$I_E^{(k)} = \int_A i_E^{(k)} \mathrm{d}\zeta \;\; ;\;\; i_E^{(k)} = \kappa_E \times \left(\phi_A^{L(k)} - \phi_C^{L(k)} \right)$$

$$I_C^{(k)} = \int_A i_C^{(k)} \mathrm{d}\zeta \;\; ;\;\; i_C^{(k)} = \sum_{j=\text{red}} n_j\, F\, Da_{j,CC}\, r_j^{(k)} \left(\phi_C^{S(k)}, \phi_C^{L(k)} \right)$$

$$i^{(k)} = \left(\frac{1}{c_A} + \frac{1}{c_E} + \frac{1}{c_C} \right)^{-1} \times \left(\frac{i_A^{(k)}}{c_A} + \frac{i_E^{(k)}}{c_E} + \frac{i_C^{(k)}}{c_C} - \left(\frac{I_A^{(k)}}{c_A} + \frac{I_E^{(k)}}{c_E} + \frac{I_C^{(k)}}{c_C} \right) \right) + I_{cell}$$

$$U_{cell}^{(k)} = \phi_C^{S(k)} - \phi_A^{S(k)} = \phi_C^{S(k)} \;\; ;\;\; U_{stack} = \sum_k U_{cell}^{(k)}$$

Modelling of the Electrical Potential in the Bipolar Plate

$\varphi_{BP}^{(k,k+1)}:$ $\quad 0 = -\kappa_{BP}\, l_2^2 \dfrac{\partial^2 \varphi_{BP}^{(k,k+1)}}{\partial \zeta_1^2} - \kappa_{BP} \dfrac{\partial^2 \varphi_{BP}^{(k,k+1)}}{\partial \zeta_2^2} - l_{BP} \times \left(i^{(k+1)} - i^{(k)} \right)$ $\hfill (4.94)$

$$\left.\frac{\partial \varphi^{(k,k+1)}}{\partial \zeta}\right|_{\zeta_1=0,\zeta_2} = \left.\frac{\partial \varphi^{(k,k+1)}}{\partial \zeta}\right|_{\zeta_1=1,\zeta_2} = \left.\frac{\partial \varphi^{(k,k+1)}}{\partial \zeta}\right|_{\zeta_1,\zeta_2=0} = \left.\frac{\partial \varphi^{(k,k+1)}}{\partial \zeta}\right|_{\zeta_1,\zeta_2=1} = 0 \quad \text{on } \partial\Omega \quad ; \quad \varphi^{(k,k+1)}\left(\zeta_1=0, \zeta_2=0 \right) = 0$$

A.5 Model Parameters

Thermodynamic Parameters

	CH_4	H_2O	H2	CO	CO_2	O_2	N_2
$h^{\theta}_{f,i}(\vartheta^r)$	-18.35	-88.95	6.82	-37.34	-147.68	7.39	7.19
$s^{\theta}_{f,i}(\vartheta^r)$	28.66	27.45	19.50	27.78	31.75	28.74	27.03
$c_{P,i}$	7.92	4.89	3.63	3.94	6.38	4.06	3.89
ϑ^r	2.93	2.93	2.93	2.93	2.93	2.93	2.93

Reaction Kinetic Parameters

$Da^{(1\,cell)}_{\mathrm{ref1},IIR}$	$Da^{(1\,cell)}_{\mathrm{ref2},IIR}$	$Da_{\mathrm{ref1},A}$	$Da_{\mathrm{ref1},A}$	$Da_{\mathrm{ox1},AC}$	$Da_{\mathrm{ox2},AC}$	$Da_{\mathrm{red},CC}$
200	200	200	200	7	7	0.15
$Arr_{\mathrm{ref1},IIR}$	$Arr_{\mathrm{ref2},IIR}$	$Arr_{\mathrm{ref1},A}$	$Arr_{\mathrm{ref1},A}$	$Arr_{\mathrm{ox1},AC}$	$Arr_{\mathrm{ox2},AC}$	$Arr_{\mathrm{red},CC}$
84.4	6.2	84.4	6.2	21.6	21.6	31.2
				$\alpha_{\mathrm{ox1},+}$	$\alpha_{\mathrm{ox2},+}$	
				0.5	0.5	
				$\alpha_{\mathrm{ox1},-}$	$\alpha_{\mathrm{ox2},-}$	
				0.5	0.5	

Stoichiometric Coefficients of the Reforming Reactions and the Electrochemical Reactions

$\nu_{i,j}$	ref1	ref2	ox1	ox2	red
CH_4	-1	0	0	0	0
H_2O	-1	-1	1	0	0
H2	3	1	-1	0	0
CO	1	-1	0	-1	0
CO_2	0	1	1	2	1
O_2	0	0	0	0	1/2
N_2	0	0	0	0	0
n_j	-	-	2	2	2
F	3.5/8				

Stoichiometric Coefficients of the Combustion

ν_{i,C_j}	C_{CH_4}	C_{H_2O}	C_{H2}	C_{CO}	C_{CO_2}	C_{O_2}	C_{N_2}
CH_4	-1	0	0	0	0	0	0
H_2O	2	0	1	0	0	0	0
$H2$	0	0	-1	0	0	0	0
CO	0	0	0	-1	0	0	0
CO_2	0	0	0	1	0	0	0
O_2	-2	0	1/2	1/2	0	0	0
N_2	0	0	0	0	0	0	0

Heat Transport Parameters

$St_{HE}^{(1\,cell)}$	$St_{IIR}^{I,(1\,cell)}$	St_{IIRS}^{N}	St_{IIRS}^{R}	$St_{M}^{(1\,cell)}$	$St_{RC}^{(1\,cell)}$	St_{AS}	St_{CS}
50	15	200	200	0.01	0.5	40	140

St_S	Pe_S	ϑ_U
100	2.5	1.0

Mass Transport Parameters

$D_{i,IIR}^{I,(1\,cell)}$	$D_{i,AS}$	$D_{i,AS}$	κ_E
4	100	100	1

Geometric Parameters

$V_{HEA}^{(1\,cell)}$	$V_{IIR}^{(1\,cell)}$	V_M	V_A	V_{AC}	$V_{HEB}^{(1\,cell)}$	$V_{RC}^{(1\,cell)}$	V_C	V_{CC}
0.1	0.2	2	1	0.01	0.1	5	1	0.01

l_2	l_{BP}
2/3	2000

Additional Parameters

ε_{IIR}^{N}	$c_{P\,S}$	c_A	c_E	c_C	κ_{BP}	f_{REC}
0.75	10000	1.0×10^{-5}	1.0×10^{-5}	1.0×10^{-5}	150	0.7

Appendix B

Bibliography

[1] M. E. E. Abashar. Coupling of steam and dry reforming of methane in catalytic fluidized bed membrane reactors. *International Journal of Hydrogen Energy*, 29(8):799–808, 2004.

[2] J. Allen, M. Farooque, and L. Novacco. Internal reforming fuel cell assembly with simplified fuel feed, 2001. US-Patent 6200696, http://www.patentgenius.com/patent/6200696.html.

[3] M. Bednarz. *Mechanistische Untersuchung und Modellierung der Kathodenreaktion in Karbonatbrennstoffzellen (MCFC)*. Deutsche Nationalbibliothek, 2002. Dissertation, http://www.sub.uni-hamburg.de/disse/975/dissertation.pdf.

[4] R. B. Bird, W. E. Stewart, and E. N. Lightfoot, editors. *Transport phenomena*. John Wiley & Sons, Inc., 2nd edition, 2002.

[5] M. Bischoff. Molten carbonate fuel cells: A high temperature fuel cell on the edge to commercialization. *Journal of Power Sources*, 160(2):842–845, 2006.

[6] S. Blanchet, J. Doyon, and L. Novacco. Corrugated current collector for direct internal reforming fuel cells, 2002. US-Patent 6492045, http://www.patentgenius.com/patent/6200696.html.

[7] M. Bode. MTU's HotModule enters dual-fuel operation. *Fuel Cells Bulletin*, 2005(1):12 – 14, 2005.

[8] B. Bosio, P. Costamagna, and F. Parodi. Modeling and experimentation of molten carbonate fuel cell reactors in a scale-up process. *Chemical Engineering Science*, 54(13-14):2907–2916, 1999.

[9] R. Braun, R. Gaggioli, and W. Dunbar. Improvements of a molten carbonate fuel cell power plant via exergy analysis. *Journal of Energy Resources Technology*, 121(4):277–285, 1999.

[10] G. Broers and J. Ketelaar. High Temperature Fuel Cells. *Industrial and Engineering Chemistry*, 52(4):303–306, 1960.

[11] *Ansys CFX 11.0 Handbook*, 2008. CFX 11.0.

[12] Y. Choi and H. G. Stenger. Water gas shift reaction kinetics and reactor modeling for fuel cell grade hydrogen. *Journal of Power Sources*, 124(2):432–439, 2003.

[13] *COMSOL Multiphysics Reference Manual (Version 3.5)*. Stockholm, 2008. http://www.comsol.com.

[14] G. Donolo, G. De Simon, and M. Fermeglia. Steady state simulation of energy production from biomass by molten carbonate fuel cells. *Journal of Power Sources*, 158(2):1282–1289, 2006.

[15] S. Gordon and B. J. McBride. Computer program for calculation of complex chemical equilibrium compositions and applications: I. analysis. *NASA Reference Publication*, 1311, 1994. http://gltrs.grc.nasa.gov/cgi-bin/GLTRS/browse.pl?1996/RP-1311-P2.html.

[16] P. Greppi, B. Bosio, and E. Arato. A steady-state simulation tool for MCFC systems suitable for on-line applications. *International Journal of Hydrogen Energy*, 33(21):6327–6338, 2008.

[17] P. Greppi, B. Bosio, and E. Arato. Feasibility of the integration of a molten carbonate fuel-cell system and an integrated gasification combined cycle. *International Journal of Hydrogen Energy*, 34(20):8664–8669, 2009.

[18] M. Gundermann. *Parameteridentifikation und Reduktion des mathematischen Modells einer industriellen Schmelzkarbonatbrennstoffzellenanlage*. Shaker Verlag, Aachen, 2008. Dissertation.

[19] M. Gundermann, P. Heidebrecht, and K. Sundmacher. Validation of a mathematical model using an industrial MCFC plant. *JOURNAL OF FUEL CELL SCIENCE AND TECHNOLOGY*, 3(3):303–307, AUG 2006. Conference on European Fuel Cell Technology and Applications, Rome, ITALY, DEC 14-16, 2005.

[20] M. Gundermann, P. Heidebrecht, and K. Sundmacher. Parameter identification of a dynamic MCFC model using a full-scale fuel cell plant. *Industrial & Engineering Chemistry Research*, 47(8):2728–2741, 2008.

[21] M. Gundermann, P. Heidebrecht, and K. Sundmacher. Physically motivated reduction of a 2D dynamic model for molten carbonate fuel cells (MCFC). *Fuel Cells*, 8(2):96–110, 2008.

[22] P. Heidebrecht. *Modelling, Analysis and Optimisation of a Molten Carbonate Fuel Cell with Direct Internal Reforming (DIR-MCFC)*. VDI-Verlag, Düsseldorf, 2005. Dissertation.

[23] P. Heidebrecht and K. Sundmacher. Molten carbonate fuel cell (MCFC) with internal reforming: model-based analysis of cell dynamics. *Chemical Engineering Science*, 58(3-6):1029–1036, 2003.

[24] P. Heidebrecht and K. Sundmacher. Dynamic model of a cross-flow molten carbonate fuel cell with direct internal reforming. *Journal of The Electrochemical Society*, 152(11):A2217–A2228, 2005.

[25] P. Heidebrecht and K. Sundmacher. Optimization of reforming catalyst distribution in a cross-flow molten carbonate fuel cell with direct internal reforming. *Industrial & Engineering Chemistry Research*, 44(10):3522–3528, 2005.

[26] K. Hou, M. Fowles, and R. Hughes. The effect of hydrogen removal during methane steam reforming in membrane reactors in the presence of hydrogen sulphide. *Catalysis Today*, 56(1-3):13–20, 2000.

[27] P. Iora and S. Campanari. Development of a three-dimensional molten carbonate fuel cell model and application to hybrid cycle simulations. *Journal of Fuel Cell Science and Technology*, 4(4):501–510, 2007.

[28] P. Iora, S. Campanari, and A. Salogni. Off-Design Analysis of a MCFC-Gas Turbine Hybrid Plant. *Journal of Fuel Cell Science and Technology*, 7(3), 2010.

[29] K. Jarosch, T. El Solh, and H. I. de Lasa. Modelling the catalytic steam reforming of methane: discrimination between kinetic expressions using sequentially designed experiments. *Chemical Engineering Science*, 57(16):3439–3451, 2002.

[30] M. Jischa. *Konvektiver Impuls-, Wärme und Stoffaustausch*. Vieweg Verlag, 1982.

[31] M. Lukas, K. Lee, and H. Ghezel-Ayagh. Modeling and cycling control of carbonate fuel cell power plants. *Control Engineering Practice*, 10(2):197–206, 2002.

[32] M. Mangold, M. Grotsch, M. Sheng, and A. Kienle. State estimation of a molten carbonate fuel cell by an extended Kalman filter. In Meurer, T. and Graichen, K. and Gilles, E.D., editor, *Control And Observer Design For Nonlinear Finite And Infinite Dimensional Systems*, volume 322 of *Lecture Notes In Control And Information Sciences*, pages 93–109. Springer-Verlag Berlin, 2005.

[33] B. J. McBride and S. Gordon. Computer program for calculation of complex chemical equilibrium compositions and applications: Ii. users manual and program description. *NASA Reference Publication*, 1311, 1996. http://gltrs.grc.nasa.gov/cgi-bin/GLTRS/browse.pl?1994/RP-1311.html.

[34] MTU Onsite Energy :: Fuel Cell System. http://www.mtu-online.com/mtuonsiteenergy/products/fuel-cell-systems/ (2010/04/14).

[35] A. Musa, H. J. Steeman, and M. De Paepe. Performance of internal and external reforming molten carbonate fuel cell systems. *Journal of Fuel Cell Science and Technology*, 4(1):65–71, 2007.

[36] J. A. Ochoa-Tapia and S. Whitaker. Momentum transfer at the boundary between a porous medium and a homogeneous fluid - I. Theoretical development. *Int. J. Heat Mass Transfer*, 38(14):2635–2646, 1995.

[37] N. Park, Y. Lee, M. Kim, G. Chung, S. Nam, S. Hong, T. Lim, and H. Lim. Studies of the effects of the reformer in an internal-reforming molten carbonate fuel cell by mathematical modeling. *Journal Of Power Sources*, 104(1):140–147, 2002.

[38] M. Pfafferodt, P. Heidebrecht, and K. Sundmacher. Stack Modelling of a Molten Carbonate Fuel Cell (MCFC). *Fuel Cells*, 10(4):619–635, 2010.

[39] M. Pfafferodt, P. Heidebrecht, K. Sundmacher, U. Wuertenberger, and M. Bednarz. Multiscale simulation of the indirect internal reforming unit (IIR) in a molten carbonate fuel cell (MCFC). *Industrial & Engineering Chemistry Research*, 47(13):4332–4341, 2008.

[40] J. A. Prins-Jansen, K. Hemmes, and J. H. W. de Wit. An extensive treatment of the agglomerate model for porous electrodes in molten carbonate fuel cells–i. qualitative analysis of the steady-state model. *Electrochimica Acta*, 42(23-24):3585 – 3600, 1997.

[41] J. A. Prins-Jansen, K. Hemmes, and J. H. W. de Wit. An extensive treatment of the agglomerate model for porous electrodes in molten carbonate fuel cells–ii. quantitative analysis of time-dependent and steady-state model. *Electrochimica Acta*, 42(23-24):3601 – 3618, 1997.

[42] B. D. Reddy, editor. *Introductory functional analysis : with applications to boundary value problems and finite elements.* Springer Verlag, New York, 1998.

[43] R. C. Reid, editor. *The properties of gases and liquids.* McGraw-Hill, Inc., 1987.

[44] M. Sheng, M. Mangold, and A. Kienle. A strategy for the spatial temperature control of a molten carbonate fuel cell system. *Journal of Power Sources*, 162(2):1213–1219, 2006.

[45] J. C. Slattery, editor. *Advanced transport phenomena.* Cambridge University Press, 1999.

[46] K. Sundmacher, A. Kienle, H. J. Pesch, J. F. Berndt, and G. Huppmann, editors. *Molten Carbonate Fuel Cells: Modeling, Analysis, Simulation, and Control.* Wiley-VCH, Weinheim, 1 edition, June 2007.

[47] P. Tomczyk. MCFC versus other fuel cells - Characteristics, technologies and prospects. *Journal of Power Sources*, 160(2):858–862, 2006.

[48] UMFPACK: unsymmetric multifrontal sparse LU factorization package. http://www.cise.ufl.edu/research/sparse/umfpack/ (2010/04/14).

[49] H. K. Versteeg and W. Malalasekera, editors. *An introduction to computational fluid dynamics : the finite volume method.* Longman Scientific & Technical, 1995.

[50] T. Watanabe, Y. Izaki, Y. Mugikura, H. Morita, M. Yoshikawa, M. Kawase, F. Yoshiba, and K. Asano. Applicability of molten carbonate fuel cells to various fuels. *Journal of Power Sources*, 160(2):868–871, 2006.

[51] N. Woudstra, T. van der Stelt, and K. Hemmes. The thermodynamic evaluation and optimization of fuel cell systems. *Journal of Fuel Cell Science and Technology*, 3(2):155–164, 2006.

[52] F. Yoshiba, N. Ono, Y. Izaki, T. Watanabe, and T. Abe. Numerical analyses of the internal conditions of a molten carbonate fuel cell stack: comparison of stack performances for various gas flow types. *Journal of Power Sources*, 71(1-2):328–336, 1998.